

Microstructural Investigation of Alloys Used for Power Generation Industries

Ram Krishna

A thesis submitted for the degree of

Doctor of Philosophy

May 2010

Preface

This dissertation is submitted for the degree of Doctor of Philosophy at the Department of Engineering, University of Leicester. The research reported herein was conducted under the supervision of Professor Sarah Hainsworth in the Mechanics of Materials Research Group, Department of Engineering, University of Leicester.

This work is to the best of my knowledge original, except where acknowledgement and references are made to previous work. Neither this, nor any substantially similar dissertation has been or is being submitted for any degree, diploma or other qualification at any other university or institution.

Part of the work described herein has been published in the following publications:

1. **R. Krishna**, S.V. Hainsworth, S.P.A. Gill, A. Strang and H. V. Atkinson. 'Microstructural evolution in creep exposed IN617' 2nd International Creep Conference Zurich, SWITZERLAND, 21-23 April, 2009. Creep & Fracture in High Temperature Components: Design & Life Assessment Issues, Proceedings, Shibli IA; Holdsworth SR (Eds.) 2009, Pages 1223- 1235.

2. **R. Krishna**, S.V. Hainsworth, H.V. Atkinson and A. Strang. 'Microstructural analysis of creep exposed IN617 alloy'. Special Issue of Material Science and Technology, 2009. (In Press).

Ram Krishna

09/05/2010

Acknowledgements

It is a great pleasure to express my sincere gratitude and indebtedness to my supervisor Prof. Sarah Hainsworth for her inspiration, immense support, continuous encouragement and her constant guidance throughout the course of this work. Her help and constant enthusiasm have been very much appreciated during the past years.

I sincerely express thanks and gratitude to Prof. Helen Atkinson, Head of Mechanics of Materials Research Group, for her valuable suggestions and continued support in different instances apart from quarterly and monthly meetings. I acknowledge her for her effort and generosity with her time to evaluate my work.

I express my deepest admiration and great sense of regard to Prof. Andrew Strang for his immense guidance and for learning the high temperature creep mechanism in material from his extraordinary experience.

I would like to extend my appreciation and thanks to Prof. P. J. Ennis for his valuable comments at many instance during this work and to provide ready information on materials.

I sincerely thank and acknowledge the modelling team of Dr Simon Gill and Dr Tianxiang Liu for their constructive suggestions and help for thermodynamic calculations on different high temperature materials.

I would like to thank Dr G McColvin, Alstom Power Ltd, and Prof. V. Vodárek, Pohraniční, Czech Republic, who have generously provided me relevant technical information about the material and beneficial discussion during this work.

I warmly acknowledge the ever willing cooperation and help extended to me by Dr Gouthama, IIT Kanpur, in understanding intricacy of TEM.

I would like to express my gratitude and acknowledge the UK Government's Technology Strategy Board for providing financial support to carry out this work.

I sincerely thank and acknowledge ALSTOM Power Ltd. and Doosan Babcock Energy Ltd., for supplying creep exposed Inconel & Nimonic alloys specimens.

I wish to thank Mr. Barry Kirkland and for his co-operation and help. I am very grateful to Mr. Graham Clarke for his willing assistance and co-operation during this work. I would like to acknowledge Dr Simon Lawes, Experimental Officer, for his help in AFM characterisation. I would also like to thank our engineering workshop staff Mr. Tony Forryan and Mr. Alan Wale, in helping me with cutting and preparing specimens for the dissolution technique.

I express my sincere gratitude to my beloved parents, and I am greatly indebted to my family, well wishers and all the people who rendered their support and co-operation in completing this work.

Last, but not least, I would like to thank my wife and best friend, Shanti, for being supportive and helpful.

Abstract

Nickel based superalloys are currently being investigated for high temperature applications in advanced steam power plant operating at temperatures of 700°C and above. Three nickel-based superalloys Inconel 617, Inconel 625 and Nimonic 263 alloys, which are of primary interest for boiler technology components such as furnace walls, superheater tubes, header and steam pipes, etc and for steam turbine technology components such as HP & IP cylinders, rotor forgings, casing and valve chest, blading, etc., have been evaluated for long and short term creep performance. Creep deformation processes occurring at high temperatures and stresses lead to the evolution of microstructures in the form of precipitation, precipitate coarsening and recovery effects. The deterioration in mechanical properties as a result of this microstructural change has been evaluated by hardness testing. This work discusses the microstructural evolution occurring in alloys in samples that have been creep exposed at a series of temperatures from 650°C to 775°C and for durations from 1000 to 45,000 hours using advanced FEGSEM, TEM, XRD and phase extraction techniques. The fractions and morphology of different phases, their locations during exposure to higher temperatures and probable creep fracture mechanism in these alloys are illustrated and discussed.

Keywords: solid-solution strengthening, creep, intergranular, grain boundary precipitates, volume fraction, fractography, carbon replica, thin foil, $M_{23}C_6$, SEM, TEM, Inconel 617, Inconel 625 and Nimonic 263 alloys

Contents

	Page No
Preface	i
Acknowledgements	ii
Abstract	iv
CHAPTER 1 Introduction	1
1.1 Background	1
1.1.1 Austenitic Superalloys	3
1.1.2 Nickel Base Superalloys	4
1.1.3 Multi-component Ni-base Superalloys	9
1.1.4 Creep-rupture Mechanism	14
1.1.5 Alloy Stability & Microstructural Degradation	20
1.1.6 Carbide Reactions	22
1.1.7 Inter- & Intragranular Precipitates	23
1.1.8 Effect of Precipitates on Dislocations	25
1.1.9 Role of Grain Boundaries during Creep	26
1.2 Objective of the Thesis	28
1.3 Structure of the Thesis	29
References	30
CHAPTER 2 Literature Review	33
2.1 Background	33
2.1.1 Research Activities on Inconel Alloy 617	34
2.1.2 Research Activities on Inconel Alloy 625	44
2.1.3 Research Activities on Nimonic Alloy 263	49
Summary	56
References	57
CHAPTER 3 Materials and Experimental Procedure	65
3.1 Inconel 617 Alloy	66

3.2	Inconel 625 Alloy	67
3.3	Nimonic 263 Alloy	68
3.4	Specimen Preparation technique	70
3.4.1	Optical microscopy	71
3.4.2	Scanning electron microscopy (FEGSEM)	71
3.4.3	Electron backscattered diffraction (EBSD)	72
3.4.4	Transmission electron microscopy (TEM)	72
3.4.4.1	Twin-Jet Polishing	72
3.4.4.2	Carbon-replica technique	73
3.5	Characterisations of Alloys	73
3.5.1	X-ray diffractometry (XRD) and peaks separation	74
3.5.2	Extraction techniques for x-ray diffraction (XRD)	74
3.5.3	Mechanical property i.e. bulk hardness determination	74
3.5.4	Average grain size measurement	75
3.6	Estimation of area fraction of precipitates	75
3.7	Estimation of volume fraction of precipitates from TEM Images	77
	Summary	79
	References	80
CHAPTER 4	Inconel 617 alloys	81
4.1	'As-received' specimen	81
4.1.2	Grain Morphology	81
4.1.3	Phase Identification	83
4.1.4	Precipitate Morphology and Location	85
4.1.5	Transmission Electron Microscopy (TEM) Observations	87
4.2	'Creep-exposed specimen' (T0003) (650°C/ 574Hrs / 350MPa)	94
4.2.1	Fractography	94
4.2.2	Grain Morphology	95
4.2.3	Phase Identification	97
4.2.4	Precipitate Morphology and Location	98
4.2.5	Transmission Electron Microscopy (TEM) Observations	100

4.3	'Creep-exposed specimen' (T0008) (650°C/45,000Hrs/275MPa)	109
4.3.1	Fractography	109
4.3.2	Grain Morphology	110
4.3.3	Phase Identification	112
4.3.4	Precipitate Morphology and Location	113
4.3.5	Transmission Electron Microscopy (TEM) Observations	115
4.4	'Creep-exposed specimen' (T0151) (700°C/ 4,000Hrs / 200MPa)	123
4.4.1	Fractography	123
4.4.2	Grain Morphology	124
4.4.3	Phase Identification	126
4.4.4	Precipitate Morphology and Location	127
4.4.5	Transmission Electron Microscopy (TEM) Observations	129
4.5	'Creep-exposed specimen' (T0154) (700°C/ 32,000Hrs / 145MPa)	135
4.5.1	Fractography	135
4.5.2	Grain Morphology	136
4.5.3	Phase Identification	138
4.5.4	Precipitate Morphology and Location	139
	References	142
CHAPTER 5	Inconel 625 alloys	144
5.1	'As-received' specimen	144
5.1.1	Grain Morphology	144
5.1.2	Phase Identification	146
5.1.3	Precipitate Morphology and Location	147
5.1.4	Transmission Electron Microscopy (TEM) Observations	150
5.2	'Creep-exposed specimen' (S9980) (650°C/ 33,000Hrs)	156
5.2.1	Grain Morphology	156
5.2.2	Fractography	158
5.2.3	Phase Identification	160
5.2.4	Precipitate Morphology and Location	161
5.2.5	Transmission Electron Microscopy (TEM) Observations	163

5.3	'Creep-exposed specimen' (S9976) (650°C/ 1,000Hrs)	170
5.3.1	Grain Morphology	170
5.3.2	Fractography	171
5.3.3	Phase Identification	172
5.3.4	Precipitate Morphology and Location	173
5.3.5	Transmission Electron Microscopy (TEM) Observations	175
	References	182
CHAPTER 6	Nimonic 263 alloys	183
6.1	Grain Morphology	183
6.2	Fractography	188
6.3	Phase Identification	190
6.4	Precipitate Morphology and Location	190
	Summary	195
CHAPTER 7	Discussions	196
7.1	Discussion on IN617 Alloy	196
7.2	Discussion on IN625 Alloy	204
7.3	Discussion on Nimonic 263 Alloy	209
	Summary	210
	References	211
CHAPTER 8	Conclusions & Future work	212

Future generation fossil fuelled power plants are being envisaged to operate with steam conditions of temperatures as high as 760°C and pressures of 37.5MPa. The increased operating temperatures and pressures have a substantial effect on raising the thermal efficiency from 45%, with present typical steam conditions of 600°C/30MPa, to 60%. The higher temperatures will reduce harmful emissions of gases such as SO_x, NO_x, CO, CO₂, CH₄ etc, with abundant fuel savings (Tancret et al, 2003). The need for greater efficiency and reduction of polluting emissions has prompted utilities to consider ultra supercritical steam conditions (USSC) i.e. steam conditions up to 760°C/37.5MPa (Zhao et al, 2003 and Viswanathan et al, 2005). The long term creep strength requirements that are required for operating under these conditions challenge the capacity of currently used ferritic/austenitic steels and other related alloys for steam turbines and their components. To maintain the structural integrity for safe and economic operation for future fossil fuelled power plants, Nickel base superalloys are currently being evaluated as the prime candidate material for operating temperatures in excess of 650°C. The high-temperature strengthening characteristics of these alloys are based on the principle of a stable face-centered cubic matrix combined with solid solution strengthening and some additional strengthening through precipitation. In this chapter, the fundamental understanding for long term service properties of Nickel base superalloys and their correlation with composition/microstructure will be discussed (Meetham, 1986).

1.1 Background

The high temperature creep-rupture strength and creep life of Nickel base superalloys is significantly affected by their strengthening mechanisms; solid-solution strengthening and precipitation strengthening through precipitation of coherent creep-resistant intermetallic phase gamma prime (γ'). The solid-solution strengthening mechanism is an important contributor to creep resistance in these alloys, and it improves the elevated temperature strength from alloying element interactions. The alloying elements diffuse into the matrix

heterogeneously to form a 'solid solution'. The strengthening effect is from the matrix strain around different size of solute atoms, which impedes easy dislocation motion. At certain concentrations the alloying elements form precipitates of a second phase. The second phase precipitates impede the movement of dislocations. The magnitude of precipitation strengthening depends on the precipitate size and their spacing. Inconel 617 and 625 alloys are from the family of solid-solution strengthened nickel based superalloys. Their chemical composition provides uniform microstructure for application at high temperature up to 600°C. In the early stages of creep, solid-solution strengthening gives the greatest contribution to creep resistance, however, as service-exposed (ageing time) time progresses; the precipitation of carbides (primarily $M_{23}C_6$) has a more significant contribution to the creep resistance. As ageing time progresses still further, the strengthening effect from carbide precipitation is reduced, as the carbides get coarsened (Ostwald ripening). In the solid-solution strengthened alloy an increase in temperature increases the diffusion rates of solute atoms from the dislocation atmospheres, and weakens the structure. The mechanism of creep deformation is the climb of dislocations over precipitates, and the precipitates therefore control creep deformation.

Precipitation-hardened alloys are strengthened by intermetallic [γ' : $Ni_3(Al, Ti)$] precipitation. High temperature creep strength can be optimized by controlling the volume fraction, morphology and spacing of the γ' phase. Titanium and aluminium are the γ' precipitating agents. Other elements, notably niobium, tantalum and chromium also enter γ' . γ' has a superlattice that possesses the Cu_3Au ($L1_2$)-type structure, which exhibits long-range order to its melting point of 1385°C. A high temperature exposure causes solutionization of the precipitates in the precipitation-hardened alloys. At intermediate temperature, precipitates can coarsen and become less effective impediments to dislocation motion. High temperature, stress and high-strain cycle loading lead to accelerated softening and pre-mature failure of the alloys.

A typical creep property requirement for Nickel base superalloys is creep rupture life of 100,000 hours at 750°C under a stress of 100 MPa (Reed, 2007).

1.1.1 Austenitic Superalloys

Austenitic superalloys are very complex in nature. The alloy chemical composition defines the phases present and these in turn create the microstructure. Therefore, the chemical composition, phase constitution and microstructure physically define superalloys. The phases have significant effects on strengthening in superalloys. Some phases can be deleterious to behaviour. The high-temperature strength capability of all superalloys is based on stable matrix consisting of closed-packed FCC austenite (known as γ -phase) combined with solid-solution strengthening and/or precipitation hardening. The major strengthening phases in the austenitic matrix are coherently ordered fcc γ' , metal carbides (MC, $M_{23}C_6$), and the BCT (body-centered-tetragonal) gamma double-prime $\{\gamma'', Ni_3(Nb, Mo, Al, Ti)\}$. Other phases that are generally undesirable and observed in nickel base superalloys arise from variations in composition or processing or due to high-temperature exposure. Phases in this group are the orthorhombic δ -phase (Ni_3Nb), rhombohedral μ -phase $\{(Fe, Co)_7 Mo_6\}$ and the hexagonal close-packed (hcp) η -phase (Ni_3Ti). The compositions of austenitic alloys are complex and challenging. *Table 1.1.1* summarises the functions of elements in particular to nickel base superalloys (Davis, 1999).

Effects		Nickel base
Solid-solution strengtheners		Co, Cr, Mo, Fe, W, Nb
Carbide form:	MC	Ti
	$M_{23}C_6$	Cr, Mo
	M_6C	Mo, Fe, Co, W
Carbonitrides: M(CN)		Ti, C, N
$\gamma' Ni_3(Al, Ti)$		Ni, Al, Ti
Raises solvus temperature of γ'		Co
Hardening precipitates and/or intermetallics		Al, Ti, Nb, Mo
Oxidation resistance (oxide scale)		Al, Cr
Sulfidation resistance		Cr, Co, Si
Improves creep properties & rupture strength		C, B
Grain-boundary refiners		B, C

Boron and carbon (called grain-boundary refiners) lead to borides and carbides precipitation, typically at the grain boundaries, which limit the grain growth. It has beneficial effect on creep rupture resistance. The low thermal expansion coefficient (α) and high thermal conductivity of nickel base superalloys (compared to iron and cobalt) accommodates their use in turbine components to close tolerances to achieve maximum efficiency. Their outstanding strength over the temperature ranges at which turbine components operate are the prime reason for the existence of superalloys. Their close-packed FCC lattice has the capability to maintain relatively high and reliable tensile, rupture, creep and thermomechanical fatigue properties to homologous temperatures that are much higher than for equivalent BCC systems. The high modulus of austenitic FCC lattice, many operative slip systems, low diffusivity for secondary elements, large solubility of secondary elements and their thermo-chemical characteristics enabling precipitation of intermetallic compounds (such as γ' and γ'') are contributing factors to their strength. The superalloys always contain substantial alloying additions in solid solution to provide strengthening effects by solid solution hardening, carbide precipitation, grain boundary control, creep resistance and resistance to surface degradation (oxidation and corrosion resistance). When significant resistance to loading under static, fatigue and creep-conditions is required, the nickel base superalloys have emerged as the materials of choice for high-temperature applications (Betteridge and Shaw, 1987; Sims et al, 1987 and Green et al. 2004).

1.1.2 Nickel base Superalloys

Nickel base superalloys are high-temperature structural materials due to their remarkable ability to maintain their properties at elevated temperatures under considerable load for extended period of life. Their uses are many and varied but primarily the alloys discussed in this work include nickel base superalloys used in components of steam boilers and turbines, heat exchangers, rotor forgings, blades, pipes, tubes, headers, HP & IP valve chest, superheat tubing, hot gas ducting (transition piece) and bolting etc. Nickel base alloys contain

20-23% Cr, 6-9% Mo, up to 20% Co, up to 1% Al, up to 2.2% Ti, up to 3.7% Nb, up to 2.2% Fe and traces of C and W, which provides solid solution strengthening and precipitation hardening to the austenitic γ matrix. Nickel base superalloys can either be solid solution or precipitation strengthened. The solid-solution strengthened alloys such as Inconel 617, Inconel 625 etc are used for intermediate strength applications. They are used in steam boiler components such as the HP/IP valve chest, rotor forgings, blades, pipes, tubes, headers etc. The precipitation strengthened alloys such as Nimonic 263 etc is used in applications requiring high strength. It is used in the hottest sections of steam boilers and turbines such as superheater tubes, outlet headers, steam lines, hot gas ducting (transition piece) and bolting etc. The solute elements in nickel base superalloys are categorised as (i) elements partitioned to γ -matrix such as Ni, Co, Cr, Mo, Nb, Fe; (ii) elements partitioned to γ' -phase such as Ti, Al, Nb; (iii) elements partitioned to carbide formers such as Cr, Mo, Nb, W, Ti; (iv) elements partitioned to grain boundaries such as C, B; and (v) elements partitioned to oxide formers, which develop adherent diffusion-resistant oxides to protect the alloys from environment such as Cr, Al.

The ambient temperature microstructure consists of major phases as follows:

(i) Austenitic gamma (γ) Matrix: The γ -matrix is favoured by most turbine designers for the most severe condition of environments, high temperatures and stresses. All nickel base alloys contain this phase as the matrix. The γ constitutionally consists of nickel, cobalt, chromium, iron, titanium, aluminium and refractory metal such as molybdenum.

(ii) Gamma Prime (γ') Precipitate: Nickel matrix favours (due to nearly filled third electron shell of nickel) precipitation of FCC A_3B (superlattice structure of Cu_3Au : $L1_2$ - type) precipitates γ' . The compatibility of the γ' FCC crystal structure and lattice constant (approximately 0.1% mismatch) with γ allows homogeneous nucleation of a precipitate with low surface energy and extraordinary long-time stability. Coherency between γ' and γ is maintained by tetragonal distortion. The γ' is a unique intermetallic phase. It contributes remarkable high temperature strengthening and creep resistance by dislocation interaction to

γ' . Al and Ni atoms are randomly distributed in the γ' FCC atomic sites. The passage of dislocations through γ' precipitates does not change the overall structure. However, when dislocations come across the γ' precipitates, the dislocations dissociated in two unit dislocations for glide. The dissociation leads to disorder in the structure called anti phase boundary (APB) fault. The dissociated dislocations tend to move in pairs to restore the order of the structure. The high value of APB fault energy restricts the slip along the planes and hence γ' precipitates are resistant to dislocation motion. γ' was found to have different morphology (spherical, cubic and plates), depending on the value of the matrix/precipitates lattice mismatch, in different nickel base superalloys. Their volume percent influences alloy strength. A low volume percent weakens faster than high volume percent at service temperature.

(iii) Carbides: Grain boundaries are the preferred location sites for the carbides to appear. In nickel base superalloys carbon typically varies from 0.03 to 0.06 wt%. It combines with reactive and refractory elements, such as chromium, titanium, niobium, molybdenum, cobalt to form metal carbides. The common nickel base superalloys carbides are MC, $M_{23}C_6$ and/or M_6C . These carbides are a closely-packed dense FCC structure. Carbides have significant effect on nickel superalloys properties.

The MC carbides occur as discrete, blocky and regular geometric particles distributed heterogeneously throughout the alloy, both in intergranular and transgranular positions. MC carbides are a major source of carbon for subsequent phase reactions during heat treatment and service expose conditions. During heat treatment and service exposure, MC carbides tend to decompose and generate other carbides, such as $M_{23}C_6$, which tend to form at grain boundaries. The typical formula for MC is TiC.

The $M_{23}C_6$ carbides are grain-boundary carbides, which strengthen the grain boundaries, and promote a significant effect on rupture strength, apparently through inhibition of grain boundary sliding. They usually occur as irregular and discontinuous precipitates, although plates and regular geometric forms have been also observed. Eventually, however, rupture failure can initiate either by fracture of these same grain boundary $M_{23}C_6$ particles or by

decohesion of the $M_{23}C_6$ interface. If fine carbides are precipitated in the matrix, strengthening results. The $M_{23}C_6$ precipitates form during lower temperature heat treatment and in service exposed to 760-980°C, both from the degeneration of MC carbide and from soluble residual carbon in the alloy matrix. Although, usually seen at grain boundaries, they occasionally occur along twin bands, stacking faults, and at twin ends. When molybdenum is present, the approximate composition of $M_{23}C_6$ is $Cr_{21}Mo_2C_6$. It is also possible for small amounts of nickel, cobalt or iron to substitute for chromium.

The M_6C carbides have a complex cubic structure and form at higher temperature (815-980°C), than $M_{23}C_6$. They are similar carbide to $M_{23}C_6$ but are formed when the molybdenum and/or tungsten content is more than 8 at%. The typical formula for M_6C is $(Ni, Cr)_3Mo_3C$. M_6C carbides are more important as grain-boundary precipitates for controlling grain size during the processing of wrought alloys at high temperature.

(iv) Gamma double prime (γ''): γ'' is a BCT coherent precipitate of composition $Ni_3(Nb, Al, Ti)$. In the absence of iron, or at temperature (740-1000°C) and exposure time more than 50 hours, this phase gets transformed to an orthorhombic precipitate of the same $Ni_3(Nb, Al, Ti)$ composition known as delta, δ -phase. The δ -phase is invariably incoherent and does not confer strength when present in large quantities. However, small amount of δ -phase can be used to control and refine grain size, resulting in improved tensile properties, fatigue resistance, and creep rupture ductility. A careful heat treatment is required to ensure precipitation of γ'' -phase instead of δ -phase.

During heat treatment, or more commonly during long hours of service conditions, undesirable phases can form if the composition has not been carefully controlled. These precipitates are known as topologically closed-packed (TCP) phases, they tie up γ and γ' strengthening elements in a non-useful form. These TCP phases are composed of close-packed layers of atoms parallel to $\{111\}$ planes of the γ matrix. They are usually harmful to mechanical properties and appear as long plates or needles in the microstructure. These TCP phases are

often nucleated near or on the grain-boundary carbides. The nickel alloys containing a high level of BCC transition metals such as niobium, chromium, molybdenum and tungsten etc, are most susceptible to TCP phase precipitation. Nickel alloys are especially prone to the formation of TCP phase such as σ and μ -phase. The typical chemical formula for σ is $(Cr, Mo)_x(Ni, Co)_y$, where x and y can vary from 1 to 7. The crystal structure of σ is very similar to $M_{23}C_6$. The brittleness and plate-like structure of σ -phase adversely affects the mechanical properties such as tensile ductility, impact toughness, corrosion resistance and creep-rupture properties. This leads to a decrease in high temperature strength and finally ends in premature fracture. The high temperature fracture occurs mainly along the σ platelets rather than along the normal intergranular path, resulting in a sharp reduction of creep rupture life. The other TCP phase is μ -phase, belongs to a rhombohedral lattice with parameters $a = 0.476$ nm, $c = 2.56$ nm in a hexagonal system (Zhu & Ye, 1990 and Tawancy, 1996). The μ phase has the same crystal structure and compositions as M_6C . A general chemical formula for μ -phase is $(Co, Fe)_7(Mo, W)_6$. Nickel can substitute for part of iron or the cobalt. Thus, TCP phases act as crack initiators due to their brittle nature (Davis, 1999 and Sims et al, 1987).

Development of Strength: A summary

The major features of achieving useful elevated temperature rupture strength in nickel base alloys are through structure-property relationships which can be summarised as follows (Decker, 1969).

1. Solid-solution strengthen γ and γ' .
2. Increase volume percent γ' .
3. Increase stacking fault energy of γ' .
4. Dislocation interaction with γ' .
5. Decrease ripening rate.
6. Minimise formation of TCP phases (η -, δ -, μ -phases etc, if any).
7. Control carbides to prevent denuded zones.
8. Control carbides and grain boundary γ' to enhance rupture strength.
9. Control component-thickness-to-grain-size ratio.

1.1.3 Multi-component Ni-base Superalloys

Nickel base superalloys are multi-component system, with more than ten alloying elements in the superalloy. The composition of the alloy was based on Ni-Cr-Co-Mo-Al-Ti-Fe-Nb-W elements to get the metastable equilibrium phases at a range of temperatures. Ni-base superalloys are primarily based on the Ni-Cr binary phase system. Chromium in the range of 20-23 wt. % in nickel (balance wt. %) imparts solid-solution strengthening, oxidation and hot corrosion resistance. *Figure 1.1.3.1* shows the Ni-Cr binary phase diagram. The weight percent of chromium in Ni-base alloys maintain the FCC crystal structure up to 1400°C. A bar (shown in *Figure 1.1.3.1*) at 20-23 wt % tells that the FCC structure of Ni in Ni-Cr binary alloy remain stable until temperature of 1400°C. Carbide precipitation in Ni-base alloy is an important strengthening mechanism; and chromium plays a strong role in the formation of carbides of varied chromium-carbon ratio. Therefore, chromium is the key role player in such alloys system. *Figure 1.1.3.1* shows that at above 30 wt. % of chromium, two solid solutions - face-centered cubic (FCC) nickel and body-centered cubic (BCC) chromium are formed, which is undesirable for the high temperature stability of the alloy.

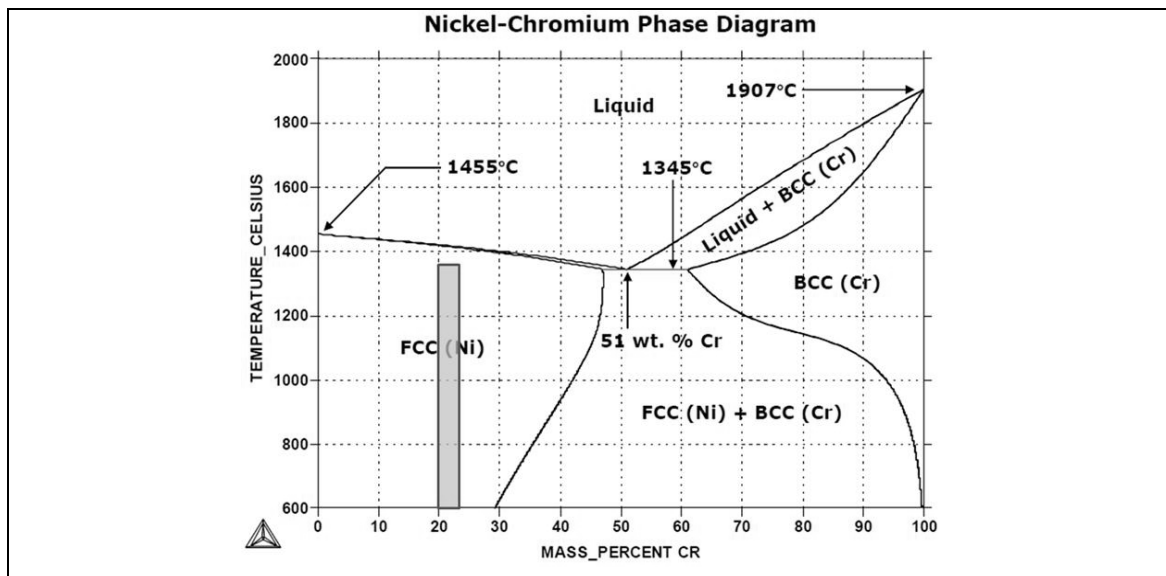


Figure 1.1.3.1: The phase diagram of Ni-Cr binary system shows equilibrium phases at different mass% of chromium and temperature (calculated with Thermo-calc). The chromium content of 20-23% in Ni justify the FCC structure of Ni as the matrix in nickel base superalloys (Calphad.com, 2006).

Therefore, addition of chromium up to 30 wt. % is required to get single austenitic FCC phase and this helps to maintain face-centered-cubic (FCC) nickel matrix in the alloy for extreme exposure temperature (*Figure 1.1.3.1*).

Ni_3Al (γ') is the one of the primary strengthening phases in solid-solution strengthened and precipitation-strengthened alloys. *Figure 1.1.3.2* shows the Ni-Al binary phase diagram.

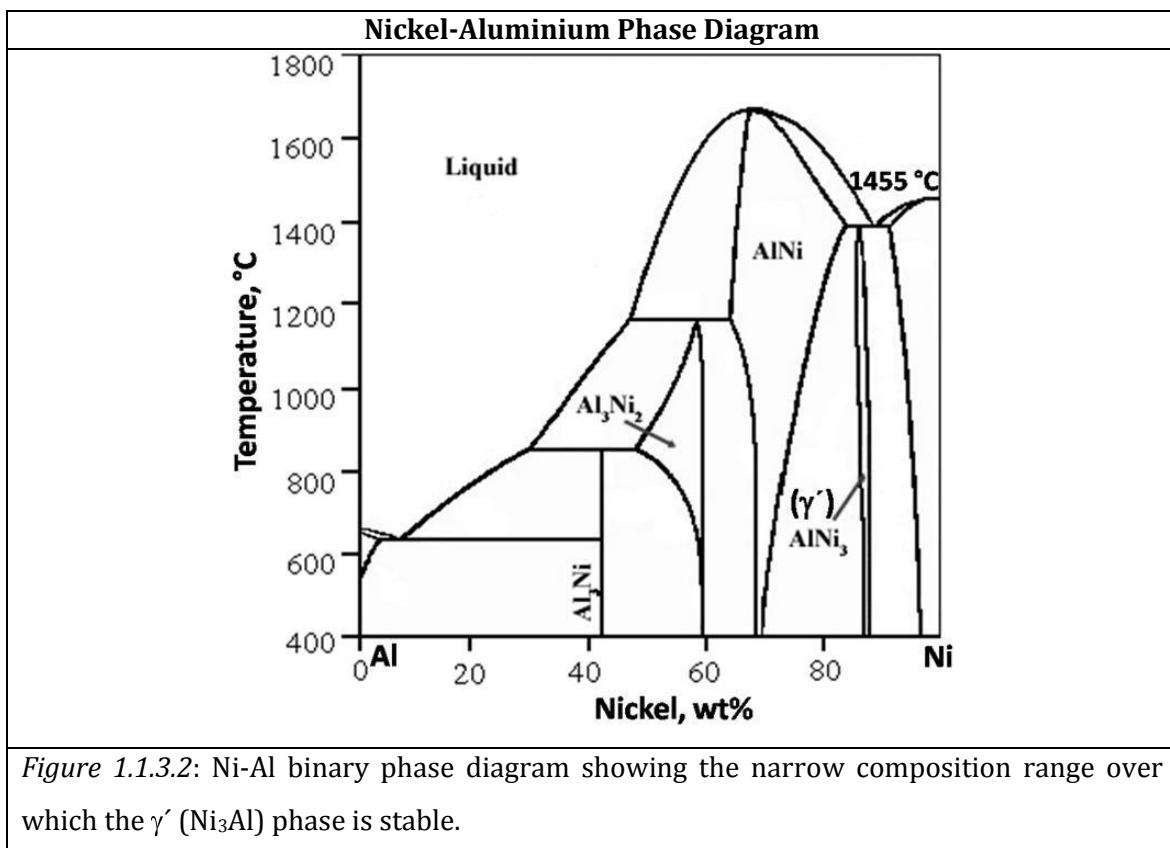


Figure 1.1.3.2 shows that γ' (Ni_3Al) phase (crystal structure: FCC/ $L1_2$) exists over a narrow composition range, at high wt% percent of Ni. The γ' (Ni_3Al) phase is required in nickel base alloys for high strength at high temperature.

A schematic isothermal ternary section of elements with nickel and aluminum of *Figure 1.1.3.3* shows the substitution of elements partitioning in γ' . Cobalt, with its horizontal phase field, substitutes for nickel. Titanium, would substitute for aluminum positions in the ordered structure of Ni_3Al , as demonstrated by a phase running diagonally from Ni_3Al to $\text{Ni}_3(\text{Al}, \text{Ti})$.

Molybdenum, chromium, and iron would substitute for both nickel and aluminum since their fields are intermediate between the above two extremes.

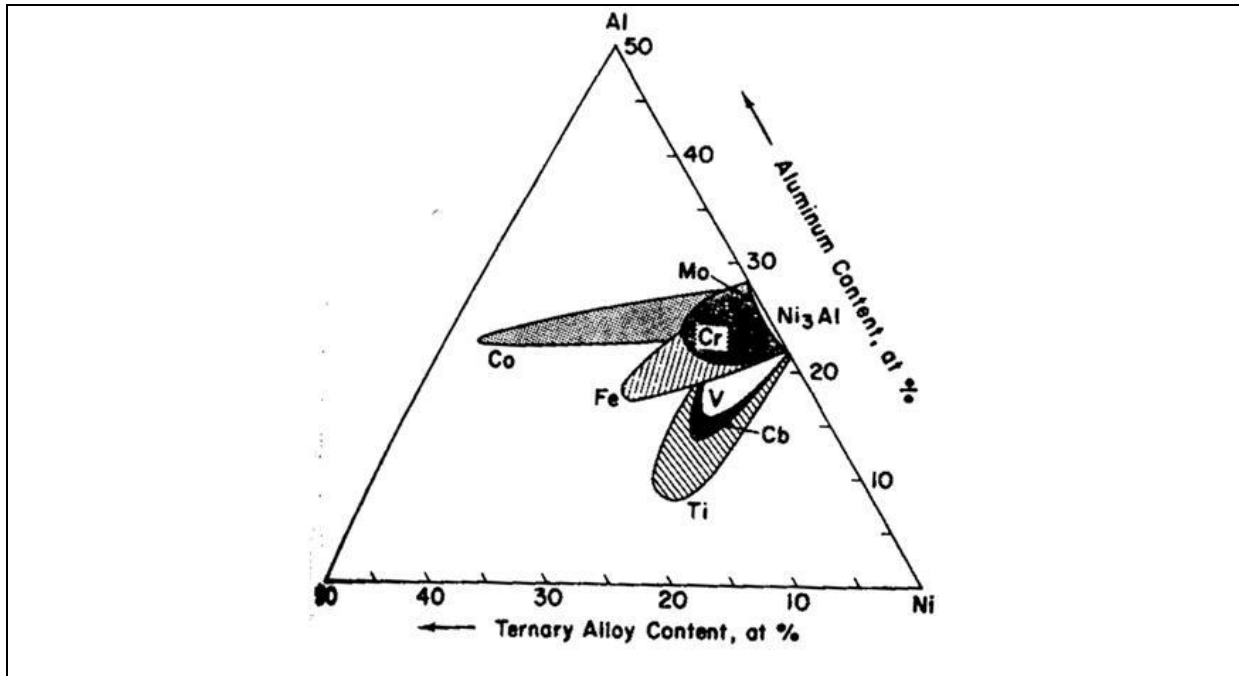


Figure 1.1.3.3: Schematic presentation of Ni_3Al solid solution field at approximately 1100°C for various alloying elements (Sims et al, 1987).

Figure 1.1.3.4 shows Ni-Co-Mo ternary phase diagram at 1200°C . The structural phases found in this ternary system are shown in Table 1.1.3.1.

Phase	Composition	Structural phases				
		Pearson's symbol	Structure-bericht designation	Space group	Type	Lattice parameter (\AA)
γ	Ni-Co-Mo	cI4	A1	$\text{Fm}\bar{3}\text{m}$		
μ	Co_7Mo_6	hR13	D8 ₅	$\text{R}\bar{3}\text{m}$	Fe_7W_6	a=4.76 c=25.02
δ	MoNi	oP56	-	$\text{P}2_12_12_1$	$\delta(\text{Mo, Ni})$	a=b=9.11 c=8.85

Nickel-Cobalt-Molybdenum Phase Diagram

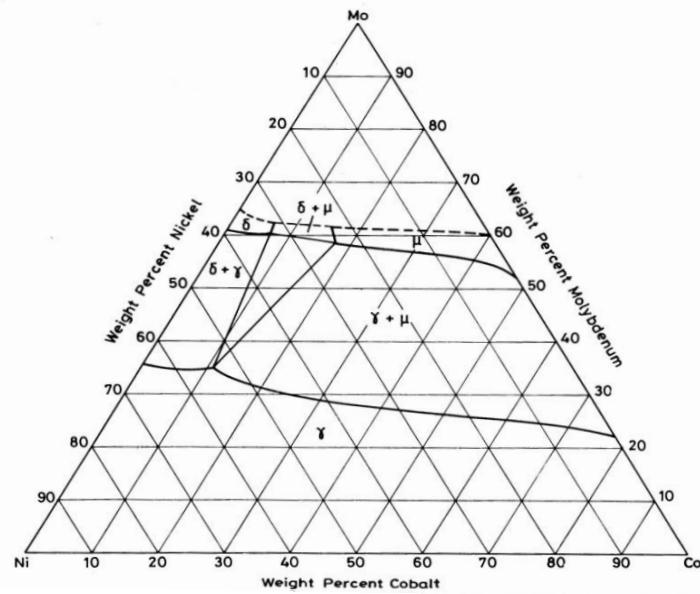


Figure 1.1.3.4: Ni-Co-Mo ternary phase diagram showing the isothermal section at 1200°C.

Figure 1.1.3.5 and Figure 1.1.3.6 show Ni-Co-Cr and Ni-Cr-Mo ternary phase diagrams at 1200°C. The phases present in the alloy at different compositions are shown in ternary diagrams.

Nickel-Cobalt-Chromium Phase Diagram

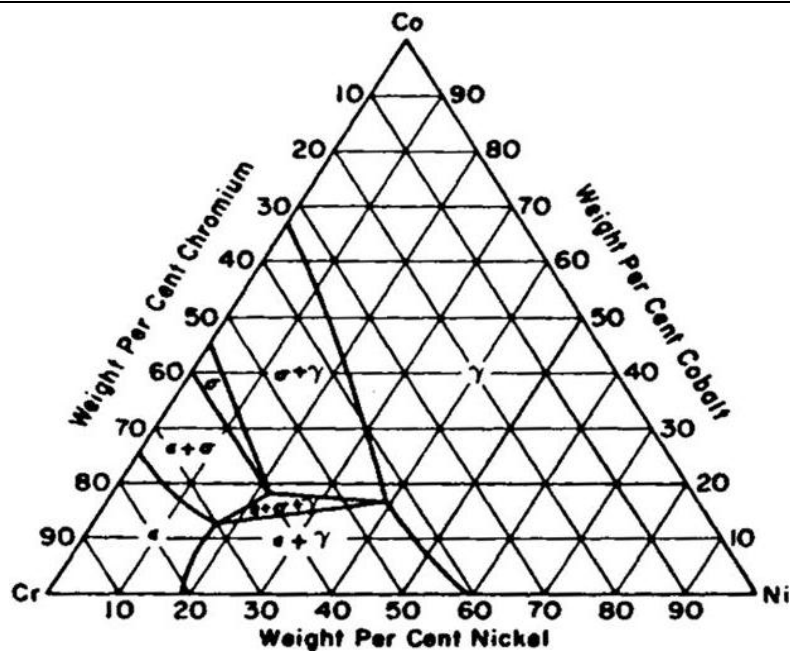


Figure 1.1.3.5: Ni-Co-Cr ternary phase diagram shows phases present at isothermal section of 1200°C (Gupta, 1991).

Nickel-Chromium-Cobalt-Molybdenum Phase Diagram

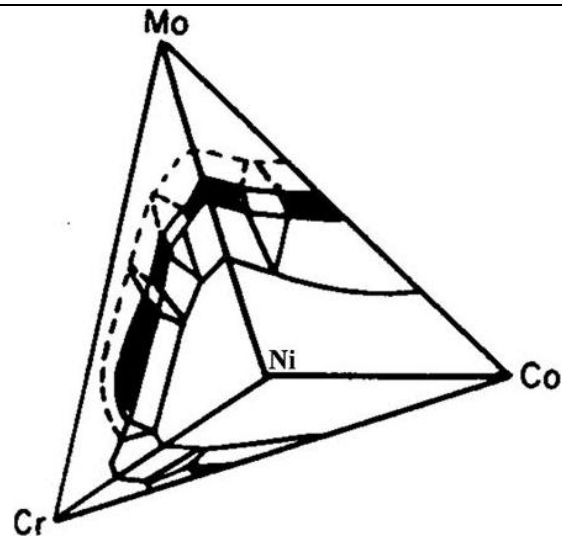


Figure 1.1.3.7: Ni-Cr-Co-Mo quaternary phase diagram showing the isothermal section at 1200°C (Sims et al, 1987).

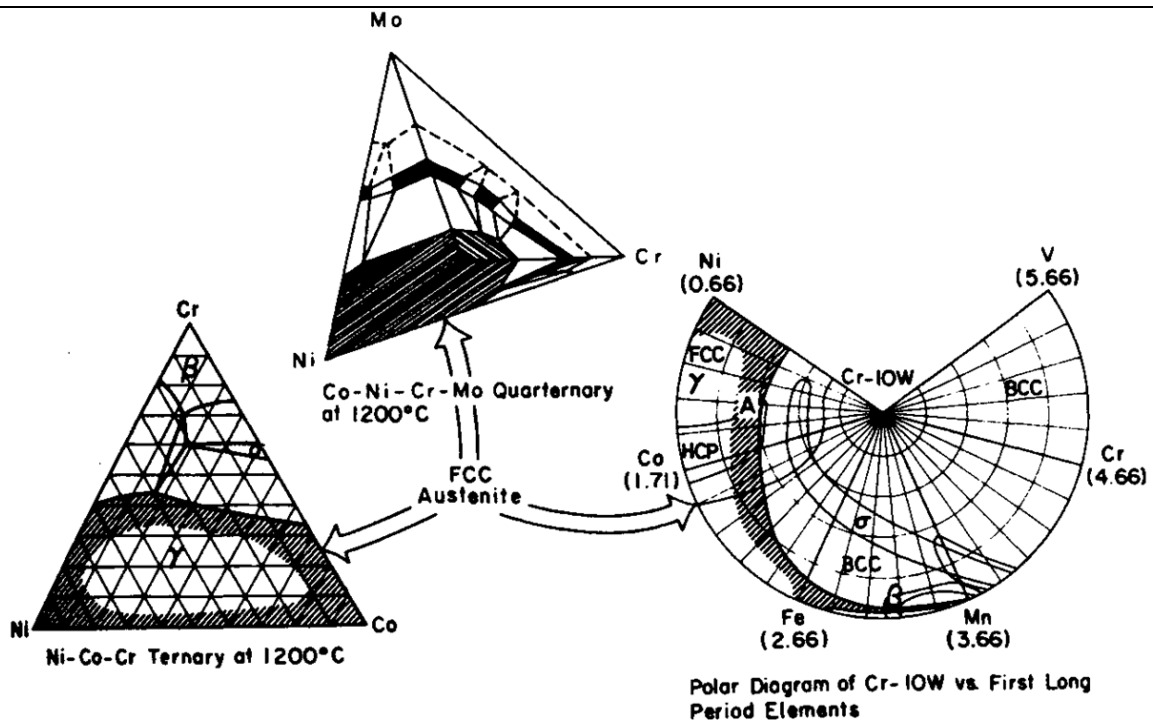


Figure 1.1.3.8: Phase diagram illustrating the FCC γ field; basis of austenitic superalloys (Sims et al, 1987).

1.1.4 Creep-rupture Mechanism

The nucleation and growth of cavities during the service exposed condition is an important phenomenon in deciding the creep rupture mechanism. The formation of cavities

typically occurs at the grain boundaries or near the semi-coherent precipitates during the creep deformation process. The nucleated micro-cavities at grain boundaries or near to the precipitates coalesce and eventually lead to rupture. The applied stress, temperature, composition, modes of creep deformation and environment play major roles in the nucleation and growth of cavities at grain boundaries under creep deformation condition. A schematic creep curve is shown in *Figure 1.1.4.1*. The primary or transient creep, secondary or steady-state creep and tertiary creep are the characteristics of this typical creep curve (*Figure 1.1.4.1*). During primary creep up to t_1 (shown in *Figure 1.1.4.1*), creep rate decreases with time, however it remains constant during secondary creep between t_1 and t_2 . Beyond t_2 the creep rate increases with time until the rupture time t_r is reached. The portion of the creep curve between t_2 and t_r is referred to as 'tertiary creep'. The inception of tertiary creep is attributed to many factors such as increasing stress during necking or void formation, inter-crystalline fracture, recrystallization, precipitation of one or more phases and nucleation of intergranular cracks. The secondary creep rate ($\dot{\epsilon}_s$) is expressed as

$$\dot{\epsilon}_s = (\epsilon_4 - \epsilon_1) / t_r \quad (1.1.4.1)$$

If the quantity $(\epsilon_4 - \epsilon_1)$ remains constant with stress and temperature then t_r is inversely proportional to the secondary or minimum creep rate. In other way,

$$\dot{\epsilon}_s = (\epsilon_3 - \epsilon_2) / (t_2 - t_1) = (\epsilon_3 - \epsilon_1) / t_2 \quad (1.1.4.2)$$

This relationship is valid in most cases for lower temperature range but as temperature increases, deviation from linearity is observed.

This might be due to premature intergranular failure induced by grain boundary segregation of foreign particles, formation of brittle films at grain boundaries or occurrence of other embrittling effects (Guard, 1961).

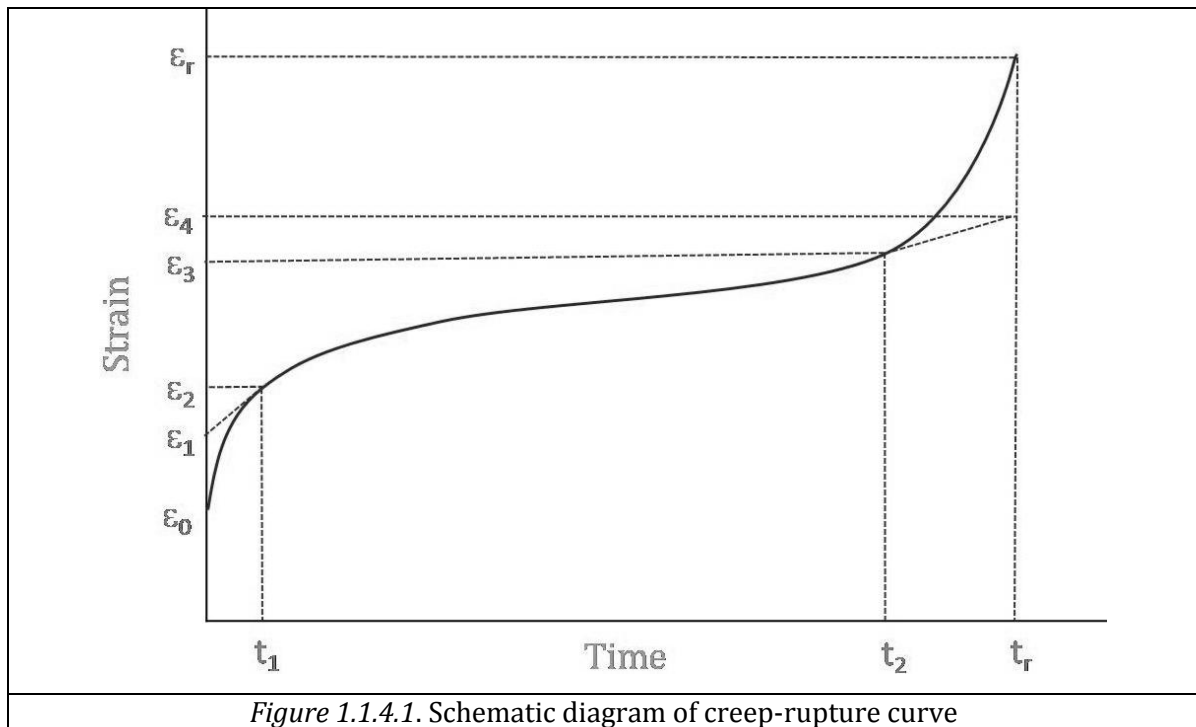


Figure 1.1.4.1. Schematic diagram of creep-rupture curve

The creep rupture strength in Ni-base alloys is sensitive to the carbon, nitrogen, tungsten and silicon. Grain-boundary precipitation is dependent upon the residual non metals in the matrix and has an important effect on inception of tertiary creep and eventually on creep rupture strength. The continuous grain-boundary precipitates and films are detrimental to creep rupture life, however discrete precipitates favour the creep rupture life. Grain structure is also an important microstructural feature that affects both creep and creep rupture strength. The modes of creep fractures found in alloys are; (i) trans-crystalline or transgranular type (ii) inter-crystalline or intergranular type. In some conditions, both types of fractures are observed in creep ruptured samples. In general, high strain rate at low temperature favours transgranular rupture and low strain rate at high temperature leads to intergranular rupture. However, it is difficult to predict strain rate or temperature at which rupture characteristics transition from intergranular to transgranular or vice versa. In addition to temperature and strain rate the change from one type of fracture mode to the other typically depends on one or more of composition, microstructure, grain size and grain-boundary sliding. Intergranular fracture is dependent upon intergranular voids formation and their propagation. This mode of fracture can be delayed by delaying the intergranular voids formation. If grain boundary migration is the

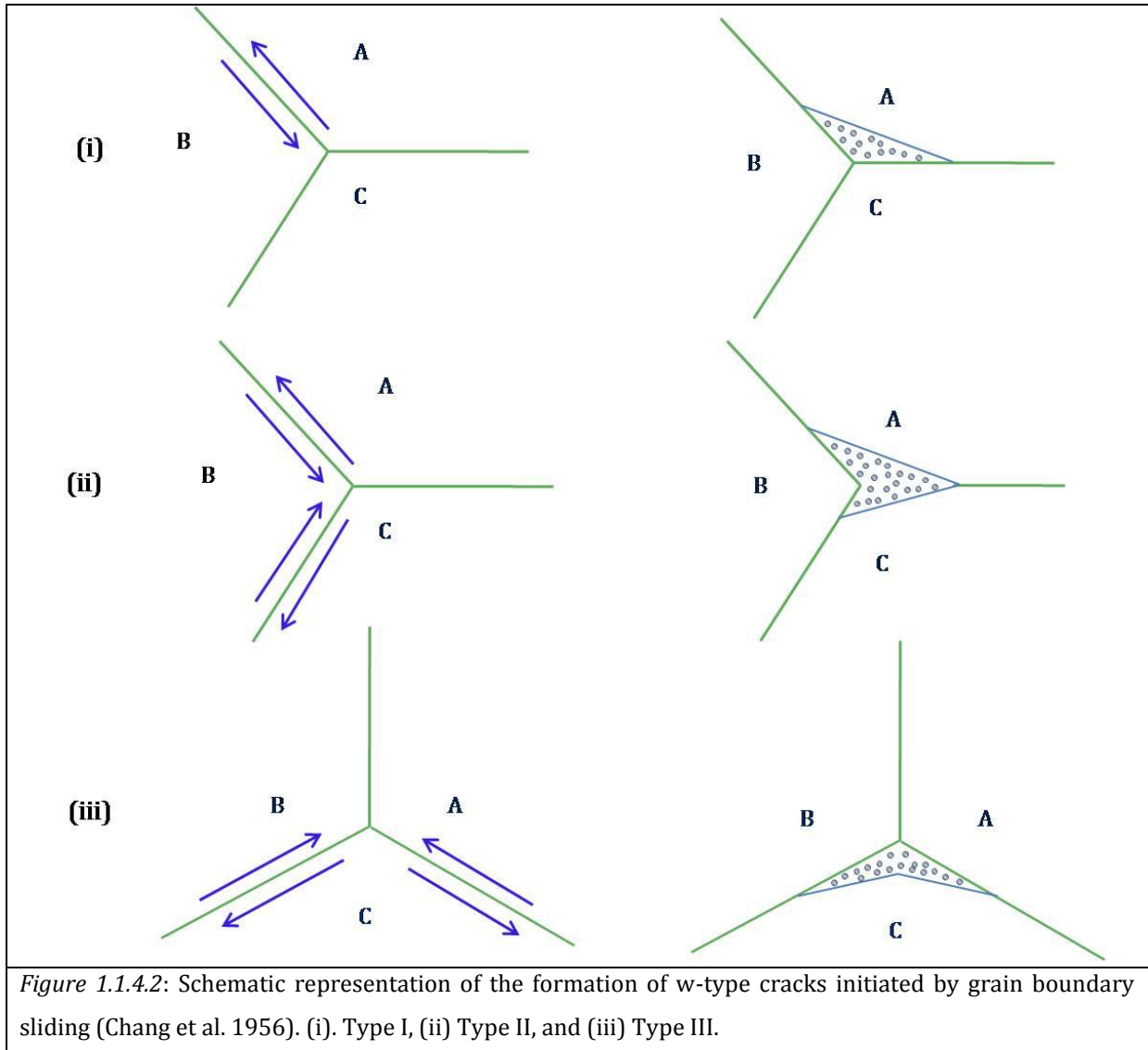
creep deformation mechanism active in the alloy, then it prevents the intergranular void formation. The intergranular void formation is associated with crack formation at triple points and at high temperature. Grain boundary migration and re-crystallization are generally observed at low to intermediate temperature range (400-600°C). However, grain-boundary void-formation plays a more prominent role during high temperature creep fracture (>600°C). Intergranular creep fractures are also identified microstructurally through wedge-type cracks and round or elliptically-shaped cracks.

Wedge-Type Cracks: These cracks, often called 'w-type' cracks, usually originated at triple points where three grains join together and they grow along the grain boundaries. These cracks propagate primarily along the grain boundaries which are normal to the applied stress, although propagation along boundaries oblique to the direction of loading (Garofalo, 1960). A number of configurations of w-type cracks have been observed in alloys and are summarized in *Figure 1.1.4.2*. Type (I) and (III) are lead to rectangular shaped voids after crack has propagated across the entire length of the boundary between grains 'A' and 'C'. Wedge-type fractures are generally observed at the lower creep temperatures, and for any other creep temperature with high stress condition. They are the result of the linkage of cavities at triple points.

Elliptically-shaped or Round Cavities: These cavities are r-type cavities. They are generally round or elliptical in shape and increase in number and size with creep deformation. The change is from w-type to r-type or with both types observed at intermediate stresses and temperatures. The total rupture occurs when the density of voids and their diameters increase to a critical limit, producing continuous cracks along the grain boundaries. This type of cavity is found primarily at grain boundaries normal to applied load.

The high stress and low temperature promote the formation of w-type cracks and low stresses and high temperature lead to r-type cavities. At intermediate stress, both w-type and r-type cavities can be observed. Intergranular fracture can be observed in the presence of grain-boundary sliding and in the absence of grain-boundary migration, phase change, or re-crystallization. The schematic representation of w-type cracks in *Figure 1.1.4.2* indicates that

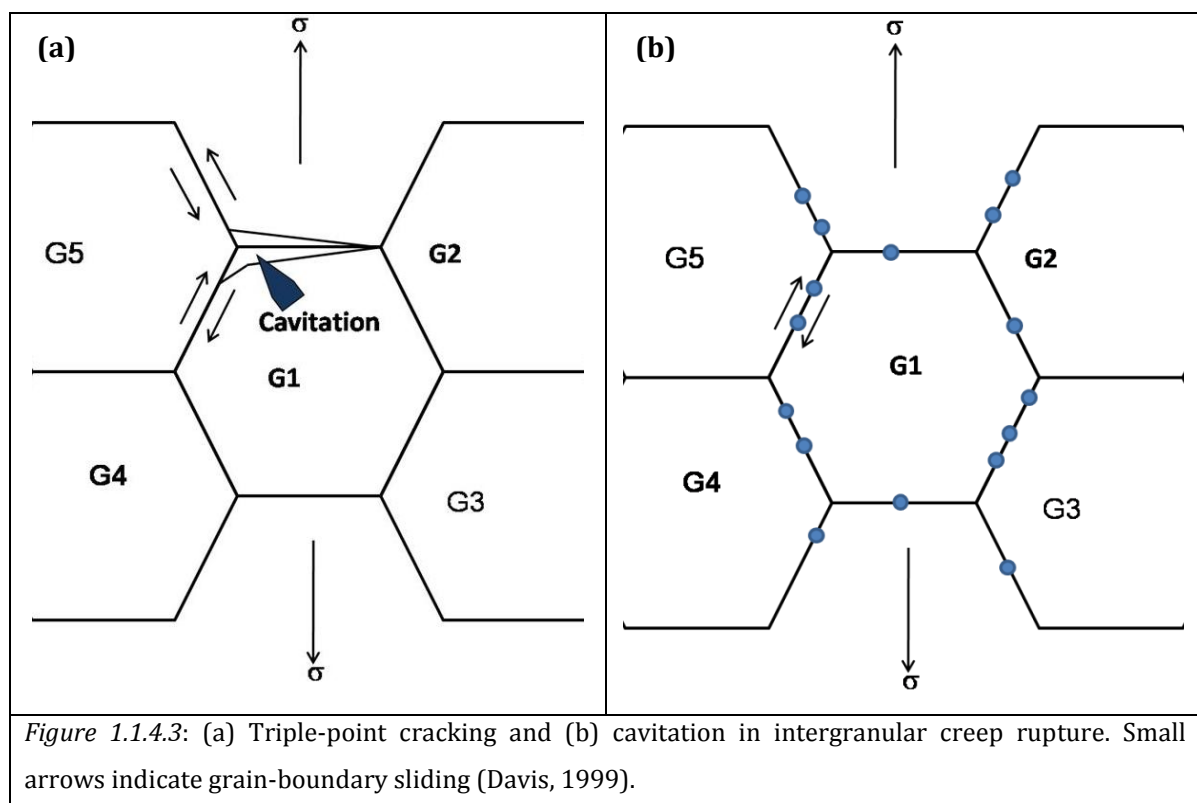
initiation primarily depends on the grain-boundary sliding. Macroscopically it is observed that intergranular rupture is dependent on the relative shear strength of matrix and grain boundary. The shear strength of the matrix can be increased by ageing without a relative increase in the shear strength of the grain boundaries, which makes it susceptible for intergranular fracture and brittleness. The high shear strength value for matrix makes the deformation primarily by grain-boundary sliding, which leads to intergranular fracture (Garofalo et al. 1961).



In summary, intergranular creep ruptures occur by the fracture processes of (a) triple-point cracking and/or (ii) grain-boundary cavitation. The temperature and strain rate decide which type of fracture process will dominate. The high strain rates at intermediate

temperatures promote the formation of triple-point cracks, known as wedge cracks (*Figure 1.1.4.2 & Figure 1.1.4.3 a*).

As a result of applied tensile stress grain boundary sliding can produce sufficient stress concentration at grain-boundary triple points to initiate and propagate wedge cracks. Some cracks can also nucleate in the grain boundary at the interacting locations of primary and secondary slip steps. Any exposed-service environment that lowers the grain-boundary cohesion also promotes the cracking. As sliding proceeds, grain boundary cracks propagate and join to form intergranular fracture. At high temperatures and low strain rates (long rupture lifetimes), grain-boundary sliding favours cavity formation (*Figure 1.1.4.3 b*) at grain boundaries or at irregularities such as second-phase inclusion particles.



The grain-boundary cavities are the result of a diffusion-controlled process. As deformation continues, the cavities join to form an intergranular fracture. Transgranular failures are favoured at high strain rates/stresses and relatively low temperatures (outcome as short rupture lifetime).

1.1.5 Alloy Stability & Microstructural Degradation

Alloy stability at high temperature service conditions depends principally on microstructural variables such as the amount of precipitate (γ' -phase) and its morphology, grain size and shape, and carbide distribution. Nickel base superalloys consist of a FCC γ' phase dispersed in a γ -matrix, and the strength increases with increasing γ' volume fraction. The lowest volume fractions of γ' are found in first-generation nickel base superalloys, where the volume fraction is generally less than 20 vol%. The γ' is commonly spheroidal in lower volume fraction γ' alloys but often cuboidal in higher volume fraction nickel base superalloys. The inherent strength capability of such superalloys is controlled by the morphology of intragranular distribution of carbide-phase and the distribution of carbide phases at the grain boundaries. Optimization of the γ' volume fraction and its morphology in conjunction with dispersion of discrete globular carbides along the grain boundaries, allows satisfactory elevated temperature mechanical properties to be achieved. The strength of superalloys is very dependent on grain size. Control of grain size is vital for the alloy's stability. A balance must be made between excessively fine grains, which decrease creep and rupture strength, and excessively large grains, which lower tensile strength and fatigue properties (but conversely have good rupture strength). Thus, high temperature nickel base superalloys are a complex chemical and crystallographic composite consisting of an austenitic matrix, and a variety of precipitated phases such as carbides and intermetallic compounds belonging to the geometrically closed-packed (GCP) and/or topologically closed-packed (TCP) type structures. They are not stable at service temperatures since a dynamic environment involving stress, temperature, time and surface-atmosphere interactions is experienced. The inter-diffusion of elements between phases, along grain boundaries or to the surface promotes various solid-state reactions that constantly alter compositional relationships and strongly influence phase stability. These effects all consequently contribute to failure by reducing strength and/or ductility. The structural changes or metallurgical instabilities have influence on stress-rupture

properties. Instabilities usually are associated with ageing (phase precipitation), overaging (phase coalescence and coarsening), phase decomposition (generally involving carbides, borides and nitrides), intermetallic phase precipitation, order-disorder transition, internal oxidation, and stress corrosion. A typical instability problem with the γ' nickel base superalloys involves intermetallic phase precipitation. Topologically close packed (TCP) phases such as σ , μ and Laves phases form at elevated temperatures, and generally have a deteriorating effect on stress-rupture properties (Davis, 1999; Sims et al, 1987).

If the alloys are exposed for prolonged times at high temperatures that exceed about 650°C, at high stress and in aggressive environment, the elevated temperature mechanical properties of the alloys degrade owing to changes that occur in their microstructures. This effect is attributed to the coarsening of γ' precipitates, breakdown of primary carbides and formation of secondary carbides, formation of TCP phases, carbide transitions. The coarsening of γ' precipitates reduce the creep strength with the exposure time but generally are not as detrimental as the formation of TCP phases. Changes in the carbide phases also adversely affect strength although initially there may be increase in strength as additional carbides precipitate. TCP phases enhance the strength but also reduce ductility. Some high temperature phases that evolve during long term exposure are discussed below.

❖ ***Topologically close-packed (TCP)-type phases***, are plate-like or needle-like phases such as σ , μ and Laves. These undesirable phases can form for some specific compositions, under certain conditions. They can either form during heat treatment, or more commonly, during service. These precipitates are composed of close-packed layers of atoms parallel to $\{111\}$ planes of the γ matrix. The phases are harmful, and often nucleate on grain boundary carbides. Nickel alloys are especially prone to the formation of σ and μ . The formula for σ , is $(\text{Fe}, \text{Mo})_x(\text{Ni}, \text{Co})_y$, where x and y vary from 1 to 7. Alloys containing a high level of body-centered cubic (bcc) transition metals (tantalum, niobium, chromium, tungsten, and molybdenum) are most susceptible to TCP formation. The σ hardness and its plate-like morphology cause

premature cracking, leading to low-temperature cracking, although the yield strength is unaffected. The formation of σ phase depletes refractory metals from the γ matrix, causing a loss of strength in the matrix. Also, high-temperature fracture can occur along σ plates rather than along the normal intergranular path, which results in a sharply reduced rupture life. Plate-like μ can also form at similar conditions. A general formula for μ is $(\text{Fe, Co})_7(\text{Mo, W})_6$. Nickel can substitute for part of the iron or the cobalt. Laves phase has MgZn_2 hexagonal crystal structure with a composition of the AB_2 type. This is most likely to be observed in iron-nickel base alloys as coarse intergranular particles. Silicon and niobium promote formation of Laves phase in Inconel 718. Excessive amounts will impair room-temperature tensile ductility and creep properties (Sims et al, 1987).

❖ **Eta (η) phase**, has a hexagonal $D0_{24}$ crystal structure with a Ni_3Ti composition. Eta can form at long high temperature exposures, especially in alloys with high titanium/aluminium ratios. Eta phase has no solubility for other elements. Its growth rate is more rapid than γ' precipitates, although it nucleates slowly. Two forms of η are found in the nickel base alloys. The first develops at grain boundaries as a cellular constituent similar to pearlite, with alternate lamellae of γ and η ; the second develops intragranularly as platelets with a Widmanstätten pattern. The cellular form is detrimental to notched stress-rupture strength and creep ductility, and the Widmanstätten pattern impairs stress-rupture strength but not ductility (Sims et al, 1987).

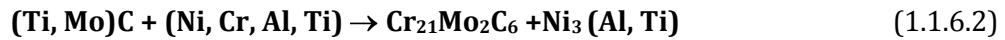
1.1.6 Carbide Reactions

MC carbides are a major source of carbon in most nickel–base superalloys below 980°C. However, MC decomposes slowly during heat treatment and service, releasing carbon for several important reactions.

The principal carbide reaction in many alloys is believed to be the formation of M_{23}C_6 , by the following reaction:



Or



Both above reactions (1.1.6.1) and (1.1.6.2) occur in the temperature range from 750-1000°C. Both reactions are most beneficial, since carbides and γ' are important for deciding strength of the alloys. M_6C can form in a similar manner,



Or



Further, M_6C and M_{23}C_6 also interact with each other and forming one from the other (Ross and Sims, 1987), depending on the alloy composition.



Or



The long-term exposure causes conversion M_6C to M_{23}C_6 or vice-versa, and is controlled by the type of refractory metal atoms present in the alloy. These reactions yield the lower carbides in various locations, but typically at grain boundaries. Most beneficial reaction for high creep resistance applications, one that is controlled in many heat treatments, is that shown in *Eq. 1.1.6.1*. Both the blocky carbides and the γ' produced are important in that they may inhibit grain-boundary sliding. In many cases, the γ' generated by this reaction coats the carbides, and the grain boundary becomes a relatively ductile, creep-resistant region (Ross & Sims, 1987; Decker, 1969; Davis, 1999).

1.1.7 Inter- & Intragranular Precipitates

This section discusses the precipitation of phases inter- and intragranularly and the influence of these precipitates on the creep properties of Ni-based superalloys. Grain-boundary precipitations have pronounced effect on tertiary creep and creep-rupture life. As

chromium, molybdenum, cobalt, titanium along with carbon are important alloying elements in nickel base superalloys, $M_{23}C_6$ ($M = Cr + Mo$) and $M(C, N)$ ($M = Ti$) are the primary precipitated phase. The chromium rich carbides $M_{23}C_6$ and titanium rich carbo-nitrides (identified cyano-nitrides in early literature) $M(C, N)$ are characterized as grain boundary precipitates. $M(C, N)$ type cyano-nitrides have been also observed within the grains. Their precipitation location, morphological evolution (shape and size), composition and fractions are critical in deciding the creep rupture properties and controlling the fracture behaviour. A large number of researchers found that the grain boundary precipitate $M_{23}C_6$ carbide morphology and its distribution play an important role in optimizing the creep rupture properties. At higher temperature ($>650^{\circ}C$), the grain boundaries are decorated with $M_{23}C_6$ but at lower temperature the precipitates are also found in grain interiors. Although the grain boundary carbides do not increase the strength of the matrix, they play an important role in deciding the creep fracture mechanism. The evolution of these carbides is part of the microstructural changes that occur and consequently affects elevated temperature mechanical properties (Mankins et al. 1974; Kimball et al 1976). The grain boundary carbide increases the creep strength and restricts grain growth at elevated temperature, up to $1150^{\circ}C$. (Frag and Hamdy, 1976; Shang-Slaiang HSU, 1993). Titanium carbides and titanium cyano-nitrides, $M(C, N)$ phases are also found inter- and intragranularly and remain unchanged by any heat-treatment process and take an important part in strengthening of the matrix. Mankins et al (1974) studied the effect of long term (10,000 h) exposure to temperature up to $1093^{\circ}C$ on microstructure and phase stability of alloy 617. The discontinuous grain boundary precipitate $M_{23}C_6$ carbides are coarse, discrete and effectively strengthen the required high temperature properties. The individually distinct nature of the carbides effectively pinned the grain boundaries and inhibited grain-boundary sliding. Betteridge (1959) also observed that $M_{23}C_6$ carbides are the major precipitated phase at grain boundaries in a similar alloy. Creep-rupture properties (longer life and longer elongation) were observed to be superior when $M_{23}C_6$ carbides precipitated at grain boundaries as well as within the matrix. The discontinuous form of grain boundary precipitates was found in parallel

orientation within the grains. Lewis and Hattersley (1965) have reported that intragranular $M_{23}C_6$ carbides precipitate in austenitic steel, and observed that nucleation occurred on the dislocations. An extensive literature review has shown that $M_{23}C_6$ carbides first precipitated on grain boundaries and later on twin boundaries followed by intragranular precipitation after continued exposure (Beckitt and Clark 1967; Singhal, and Martin 1967; Takahashi et al. 1978). Therefore the precipitation characteristics of chromium carbides on grain boundaries (of different types) play an important role in deciding mechanical behaviour of the alloy in various environments. Bruemmer and Henager Jr. (1986) have reported that intergranular carbides promote crack tip blunting, decrease the crack tip stress state, and therefore, increase the resistance to crack nucleation and propagation. Intergranular chromium carbides were significantly developed by ageing treatment on most of the grain boundaries except on special boundaries (coherent twin boundaries). However, on continued exposure, twins strongly affected the precipitation behaviour of the intergranular chromium carbides, owing to changes in orientation as the twin boundary impinges on a grain boundary. Bowman et al. (1972) reported that Cr-rich $M_{23}C_6$ has a face-centered cubic (FCC) structure, with a lattice constant of 10.65 Å. The Cr-rich $M_{23}C_6$ has a cube-on-cube orientation relationship as $\{100\}_\gamma \parallel \{100\} M_{23}C_6$, $\langle 100 \rangle_\gamma \parallel \langle 100 \rangle M_{23}C_6$ with austenitic FCC grain.

1.1.8 Effect of Precipitates on Dislocations

The dislocation sub-structure is affected to a great extent by closely spaced particles within the matrix of alloy. If the spacing between particles is sufficiently small, sub grains are not formed. Dislocations near to the particles form clusters or tangles, and decrease the mean free path for gliding dislocations (Garofalo et al. 1961). The precipitated particles and tangles that form between them inhibit dislocation motion and promote creep strengthening. Carbides exert a profound effect on properties by their precipitation on grain boundaries. A series of discrete globular $M_{23}C_6$ carbides were found to optimize creep-rupture life by preventing grain-boundary sliding in creep rupture while simultaneously providing

sufficient ductility in the surrounding grain for stress relaxation to occur without premature failure. At the extreme, when no grain-boundary carbide precipitate is present, premature failure will also occur because grain-boundary movement is essentially unrestricted, leading to subsequent cracking at grain-boundary triple points.

1.1.9. Role of Grain Boundaries during Creep

The grain boundaries play different roles during creep deformation above and below $0.3T_m$. Below about $0.3T_m$, deformation occurs almost entirely intragranularly and the presence of grain boundaries leads to a strengthening effect. In polycrystalline material, it is often found that the yield strength increases as the grain diameter decreases, according to the Hall-Petch relationship (Hall, 1951; Petch, 1953)

$$\sigma_y = \sigma_o + \bar{k} / \sqrt{d} \quad (1.1.9.1)$$

where σ_y is the yield strength, σ_o is lattice friction parameter dependent on composition, strain rate and temperature, k is also a parameter dependent up on composition, temperature and strain rate, and d is the grain diameter.

The effect of grain size on yield strength reduces as the temperature is increased and above $0.5T_m$ it becomes negligible. But grain size does affect creep even at temperatures where the yield strength is nearly independent of grain size. At low constant temperature and constant steady state creep rate conditions grain boundaries provide a strengthening effect, but on decrease in grain size (from a critical value), grain boundaries reduce creep resistance. This is due to grain-boundary mobility and generation of dislocations at grain boundaries. In addition to mobility (migration), grain boundaries also exhibit sliding, which is observed as rotation or translation of one entire grain with respect to adjacent grains. Above $0.3T_m$, grain boundary sliding becomes more prominent and grain boundaries provide less resistance to deformation and rupture. Grain boundary sliding occurs on the boundaries randomly oriented with respect to specimen axis. It has been associated in polycrystalline materials with recovery process involving sub-grain formation and strain-induced migration. However, on the atomic scale,

grain-boundary migration involves diffusion of atoms across the boundary. Thus at high temperature, grain boundaries emit dislocations from ledges during primary and secondary creep. Many evidences indicate a close relationship between grain-boundary sliding and bulk creep behaviour (Zener, 1948; Garofalo, 1960).

The initial sliding occurs in early stages of creep and occurs in the immediate vicinity of boundary region. As creep continues, sliding gradually takes a zone of finite width. The an-elastic effects associated with grain-boundary sliding at low stress were discussed by Zener (1948). It was proposed that during sliding, grain boundaries behave like viscous flow. On the onset of sliding, elastic distortions (non-uniform) originating from triple point grain junctures are produced in adjacent grains that lead to sub-grain or cell formation (as shown in *Figure 1.1.9.1*).

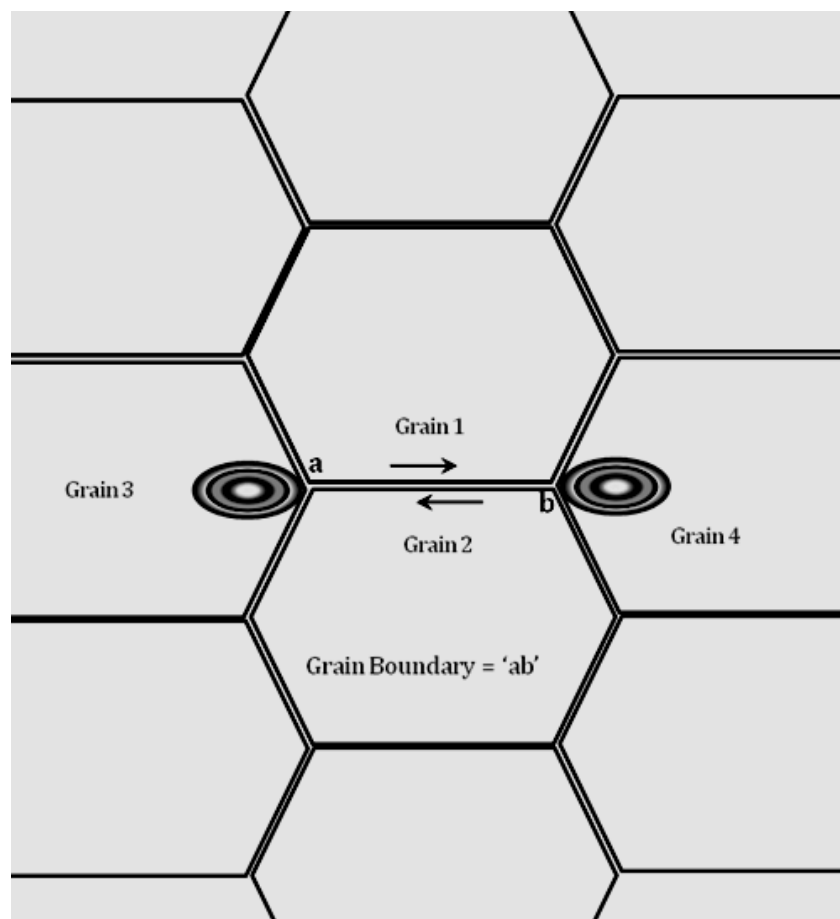


Figure 1.1.9.1: Schematic diagram of an-elastic grain boundary sliding in adjacent grains.

On development of a constant shear stress, grain 1 slides over grain 2, along the grain boundary a-b in a viscous manner. Elastic distortions are produced in grain 3 and 4. The elastic distortion however, develops a back stress which increases as sliding continues. The back stress increases to the level of the applied stress and sliding stops. Since all areas of the boundary do not behave in a similar way. Such grain boundary migration leads to the development of serrations at grain boundaries (wavy structure).

These serrations are associated with sub-grain formation near grain boundaries and the wavelength of these serrations is of the order of the sub-grain diameter. The high cohesion between grain boundary particle and matrix are beneficial for high temperature strength in Ni-base alloys.

1.2 Objective of the Thesis

As a part of UK Government's Technology Strategy Board's DTI project (No: TP/5MAT/6/I/H0101B) entitled 'Improved Modelling of Material Properties for Higher Efficiency Power Plant' the microstructure of three alloys Inconel 617 & 625 and Nimonic 263 from nickel base superalloys family, have been evaluated. The objective of this study has been to concentrate on the details of microstructural characterisation of these materials that have been creep-exposed to different conditions of stresses, time and temperatures. The creep-exposed conditions are relevant to future generation power plants. Evolution of the microstructural changes in these alloys under typical service conditions is fundamental to predicting the long term elevated temperature creep properties. The evolved microstructure of the exposed alloys has been compared with the microstructure of the 'as-received' alloy. Precipitate evolution and morphology in all creep-exposed alloys has been studied with scanning and transmission electron microscopy. The detailed understanding of mechanisms of microstructural evolution that significantly lead to strengthening or weakening over phase precipitation in the microstructure, was conducted using light microscopy, scanning electron microscopy (SEM), energy dispersive X-ray analysis (EDAX), electron backscattered diffraction

(EBSD) patterns in SEM and transmission electron microscopy (TEM). The evolution of mechanical properties has been investigated using hardness testing. Finally, the creep failure mechanism of the failed sample has been investigated by observation of the fracture surfaces and cross-sections through the fracture by scanning electron and optical microscopy respectively. The results from this study have been used to inform and validate microstructural models developed by other partners in the larger project.

1.3 Structure of the Thesis

In this introductory chapter (chapter one) the importance of nickel base superalloys relevant to the high temperature requirement for future generation power plants has been discussed. The concepts of phase evolution and high strength of solid solution have been discussed in relation to binary, ternary and quaternary phase diagrams. Creep-rupture mechanisms, microstructural evolutions/degradations, phase-precipitation and role of grain boundaries during creep have been discussed for high temperature materials. In chapter 2, a detailed literature review of Inconel 617, 625 and Nimonic 263 alloys is presented. The experimental materials and procedures including various characterisation techniques are detailed in chapter 3. Chapters 4, 5 and 6 deal with the results of microstructural evolution of the Inconel 617, Inconel 625 and Nimonic 263 alloys. Light microscopy, SEM, TEM and AFM analysis are presented with characteristic micrographs. Discussion of the results is given in chapter 7. In chapter 8 conclusions are outlined. Finally, chapter 9 closes with suggestions for future work.

References

- Betteridge, W. and Shaw, S.W.S. (1987). Development of superalloys, *Material Science and Technology*, 3, 682-694.
- Betteridge, W. (1959). *The Nimonic Alloys*, Edward Arnold Ltd. London 66-117.
- Beckitt, F.R and Clark, B.R. (1967). The shape and mechanism of formation of $M_{23}C_6$ carbide in austenite, *Acta Metallurgica* 15 (1), 113-129.
- Bruemmer, S.M. and Henager Jr., C.H. (1986) High voltage electron microscopy observations of microdeformation in alloy 600 tubing *Scripta Metallurgica*, 20 (6), 909-914.
- Bowman, A.L., Arnold, G.P., Storms, E.K. and Nereson, N.G. (1972) *The crystal Calculation of Phase Diagrams using the CALPHAD Method* (2006). <http://www.calphad.com/nickel-chromium.html> (Retrieved on 3rd March 2010).
- Davis, J.R. (Ed.) (1999). *ASM Specialty Handbook: Heat Resistant Materials*, ASM International.
- Decker, R.F. (1969). *Strengthening Mechanisms in Nickel base Superalloys*, climax Molybdenum Company symposium, Zurich, May 5-6, 1969.
- Farag, M.M. and Hamdy, M.M. (1976). Behaviour of Nickel base High Temperature Alloy Under Hot-Working Conditions. *Metallurgical Transactions A* 7(2) 221-228.
- Garofalo, F. (1960). *J. Basic Eng.*, 82, 867.
- Garofalo, F., Whitmore, R. W., Domis, W. F., and Von Gemmingen, F. (1961). *Trans. AIME*, 221, 310.
- Green, K.A., Pollock, Harada T.M. et al. (Eds.). (2004). *Superalloys 2004*, Proceedings of the Tenth International Symposium on the Superalloys (Warrendale, PA: The Minerals, Metals and Materials society (TMS), 2004).
- Gupta, K.P. (1991). *Phase Diagram of Ternary Nickel Alloys, Part 2, Ternary Systems Containing Co-Ni-X, Mn-Ni-X, Mo-Ni-X, Nb-Ni-X, Ni-Ta-X, Ni-Ti-X and Ni-V-X*. Indian Institute of Metals, Calcutta.
- Hall, E.O. (1951). *Proc. Phys. Soc.*, 64B, 747.

- Kimball, O. F., Lai G. Y. and Reynolds G. H. (1976) Effects of thermal aging on the microstructure and mechanical properties of a commercial Ni-Cr-Co-Mo alloy (Inconel 617) *Metallurgical Transactions A*, 7 (12) 1951-1952.
- Lewis, M.H. and Hattersley, B. (1965) Precipitation of $M_{23}C_6$ in austenitic steels. *Acta Metallurgica*, 13 (11), 1159-1168.
- Mankins, W.L., Hosier, J.C and Bassford, T.H. (1974). Microstructure and phase stability of Inconel alloy 617. *Metallurgical Transactions* 1974; 5 (12): 2579-2590.
- Meetham, G.W. (1986) *High Temperature Alloys for Gas Turbines and Other Applications*, (Eds. W. Betz, R. Brunetaud, D. Coutouradis, H. Fischmeister, T.B. Gibbons, I. Kvernes, Y. Lindblom, J.B. Marriott, D.B. Meadowcroft), D. Reidel Publishing Company, Dordrecht, Holland, 1-18.
- Petch, N.J. (1953). *J. Iron and Steel Inst.*, 173, 25.
- Reed, R.C. (2007). *Proceedings of the Seventh International Charles Parsons Turbine Conference on 'Power Generation in an Era of Climate Change'*, (Eds. A Strang, W.M. Banks, G.M. McColvin, J.E. Oakey, R.W. Vanstone), University of Strathclyde, Glasgow, 11-13th September, Institute of Materials, London 2007; 89-97.
- Ross, E.W. and Sims, C.T., (1987). *Nickel base alloys, Superalloys II*, Sims, C.T., Stoloff, N.S. and Hagel, W.C. (Eds.), John Wiley & Sons, 97-135.
- Shang-Slaiang HSU (1993). Time-Dependent Crack Growth in a Heat-Resistant Alloy Inconel 617. *Journal of Nuclear Science and Technology*, 30, 4,302-313.
- Sims, C.T., Stoloff, N.S. and Hagel, W.C. (Eds.) (1987) *Superalloys II: High-Temperature Materials for Aerospace and Industrial Power*, New York: John Wiley and Sons.
- Singhal, L.K. and Martin, J.W. (1967). The growth of $M_{23}C_6$ carbide on incoherent twin boundaries in austenite, *Acta Metallurgica* 15 (10) 1603-1610.
- Takahashi, T., Fujiwara, J., Matsushima T., Kiyokawa, M., Morimoto, I. and Watanabe, T. (1978). Analysis of precipitated phase in heat treated INCONEL alloy 617, *Transactions ISIJ* 18 221-224.
- Tancret, F. Bhadeshia, H.K.D.H. and MacKay, D.J.C. (2003) *Materials Science and Technology*, March 19, 283-290.

Tawancy, H. M. (1996). *J. Mater. Sci.*, 31, 3929.

Viswanathan, R., Henry, J. F., Tanzosh, J., Stanko, G., Shingledecker, J., Vitalis, B. and Purgert, R. (2005). U.S. Program on Materials Technology for Ultra-Supercritical Coal Power Plants. *Journal of Materials Engineering and Performance*, 14(3), 281-292.

Zener, C. (1948). *Elasticity and Anelasticity*. Chicago: University of Chicago Press.

Zhao, S. Xie, X. Smith, G. D. and Patel, S. J. (2003). Microstructural stability and mechanical properties of a new nickel based superalloy *Materials. Science and Engineering: A*, 355, 96-105.

Zhu, J. And Ye, H.Q. (1990). On the microstructure and its diffraction anomaly of the μ phase in superalloys, *Scripta Metallurgica et Materialia*, 24 (10) 1861-1866.

In this chapter, a review is presented on Inconel 617, 625 and Nimonic 263 alloys. Their room and high temperature mechanical properties are discussed and correlated with the microstructural evolutions (precipitate morphology and distribution, grain shape and size, and carbide distribution), that occur during heat-treatment, ageing and exposed conditions; relevant to service conditions that exist in power generation plants. A major emphasis has been placed on microstructural evolution in creep and thermally exposed alloys. The literature of high temperature creep-rupture properties, thermal ageing and creep-exposed microstructures with respect to composition of the alloys has been reviewed. The topics covered include microstructural evolution, precipitation, hardness, creep-rupture properties, fracture mechanisms and mechanical properties such as toughness, fatigue and crack growth.

2.1 Background

The scientific understanding, of microstructural evolution during creep and thermal ageing in Inconel and Nimonic alloys has made impressive progress in the last four decades, in correlating the microstructures with their mechanical properties. In the last few years, materials for future generation power plant applications have received a greater attention among researchers and plant operators. This is due to the fact that nickel base superalloys are capable of withstanding longer design lives, under severer conditions than iron based alloys. For specific applications, in which temperature, stress and environmental effects are of prime concern, such as components of steam boilers and turbines, heat exchangers, HP/IP valve chest, rotor forgings, blades, pipes, superheat tubes, headers, hot gas ducting, bolting etc, nickel based alloys are being investigated. However, in most of these alloys, a range of properties is required e.g. mechanical strength at elevated temperature, metallurgical stability, creep-rupture strength for long term operation, and excellent corrosion and oxidation resistance in aggressive

operating environments. These alloys respond to heat treatment, and therefore exposure to high temperature, with or without stress, can cause microstructural changes that affect the properties. The higher the exposure temperature, the faster would be the structural degradation. To understand the response of Inconel 617, 625 and Nimonic 263 alloy to long-term creep exposure conditions, the available literature on these alloys, has been reviewed. The topics considered mainly include microstructural changes, precipitation hardness, tensile properties, creep-rupture, and fracture mechanisms.

2.1.1 Research Activities on Inconel 617 Alloys

Inconel alloy 617 is a nickel-based superalloy that has been developed for high strength, high temperature applications. Alloy 617 was first introduced by Hosier and Tillack (1972) as a solid-solution strengthened alloy with good high temperature mechanical properties. This alloy is widely used for service involving high stress at temperature in excess of 700°C, because of its capability to withstand severely hostile operating environment without compromising its high temperature properties. Alloy 617 is nickel-chromium-cobalt-molybdenum solid-solution strengthened alloy commercially known as Inconel[®] 617 alloy (registered trademark by INCO family of companies). After the introduction of Inconel 617 alloy in 1972 (Hosier and Tillack, 1972), many research programs were actively conducted on the material for its applicability to high temperature service conditions and its microstructural changes after extended exposure to high temperatures and high stresses.

Inconel alloy 617 (IN617) is a stable austenitic solid-solution alloy. The high temperature capability of IN617 arises from good mechanical strength at elevated temperature, long term metallurgical stability, good creep rupture strength for long term operation, and excellent corrosion and oxidation resistance in aggressive operating environments [Cummins and Given 1992; Tawancy, 1990].

Mankins et al. (1974) have studied extensively on creep exposed Inconel alloy 617 in the temperature range of 649 – 1093°C for durations 215 to 10,330 hours under stress range from 7 to 241 MPa. The reported work was on strengthening mechanism by phase identification and correlation of microstructures with mechanical properties. All creep specimens were from hot-rolled bar, and were given solution treatment at 1177°C/1h, before being creep tested (all creep tests were discontinued before rupture). Samples were exposed from 215 h/7 MPa at 1093°C to beyond 10,000 h/69 MPa at 760°C. The precipitated phases evolved during creep exposure were extracted from the samples through extraction replica techniques. These extracted phases were quantified by X-ray diffraction and X-ray fluorescence. A modified computer model, PHACOMP analysis was performed to predict the amount and lattice parameter of intermetallic secondary phase, gamma prime (γ'). Gamma prime was predicted at < 1 volume%, having lattice parameter (a_0) of 3.55052 Å, with solvus temperature in between 760°C to 816°C. Room temperature tensile, impact tests, Charpy V-notch, and hardness, were performed on the exposed samples to study the ageing effects on mechanical properties (yield strength, ultimate tensile strength, ductility, toughness etc). The major phase found in the alloy after such exposure was identified as $M_{23}C_6$ carbides intragranularly distributed in all the samples. $M_{23}C_6$ precipitates intragranularly during the initial stage of treatment, after continued exposure, the additional discrete $M_{23}C_6$ carbides are precipitated in the grain boundaries, along twin boundaries, and around the polyhedral particles of TiN. Another rare phase that has been found was $\{(Cr, Mo) (C, N)\}$ without any topological close-packed phases such as sigma, mu, and chi. Gamma prime was not observed to be prone to overaging or transformation to any morphologically deleterious phase after long term exposure. Molybdenum and cobalt play an important part in retarding gamma prime overaging. The work by Mankins et al. on Alloy 617 led to a good understanding of the high temperature mechanical properties of IN617 and it became a strong candidate for structural components in high temperature design applications. Other properties like oxidation and corrosion resistance, fatigue strength and environmental effect at high temperature on the alloy's performance was reported in 1980s-1990s (Kirchhöfer

et al. 1984; Bruch et al. 1984; Schneider et al. 1984; Ennis et al. 1984; Srivastava et al. 1990; Lai, 1993; Meyer-Olbersleben et al. 1999; Coade et al. 2002).

Hosoi and Abe (1975) have investigated creep rupture properties of Inconel 617 in helium and vacuum at 1000°C under a stress of 34 MPa. Creep rupture properties in air were always greater than in helium and high vacuum. The low oxygen content in helium (99.9% He) causes a remarkable decrease of the creep rupture time and a similar effect of oxygen is also found in the controlled pressure of air. The effect of oxygen on the creep rupture properties is attributable to surface decarburization and oxidation attack, which tends to decrease the high temperature strength.

Kimball et al. (1976) reported the effect of thermal ageing on the microstructural and mechanical properties of Inconel 617. Their investigation was to examine the microstructural and mechanical properties changes which occurred during ageing in the absence of an applied stress for temperatures in the range 593 to 816°C for times up to 8000 h. The material was solution annealed at 1177°C/air cooled before the ageing process. Hardness, Charpy V-notch tests, toughness etc were studied for the aged samples. Age-hardening was observed for all temperatures, however softening was observed after long time ageing at 760°C. This temperature was identified by Mankins et al. (1974) as the temperature at which solutioning of γ' particles occurs. The microstructure was characterized by a discontinuous grain boundary network of carbides and the presence of numerous carbides stringers. A number of discrete carbide particles are also present in intragranular regions. These carbides were identified as being of $M_{23}C_6$ type where M is Cr and/or Mo. After ageing for 1000 h the grain boundary carbide network was seen to be nearly continuous and in many areas the large grain boundary carbides were surrounded by numerous fine carbide particles. These fine particles were also of $M_{23}C_6$ type. No significant changes occurred in the intragranular carbides. After ageing for 8000 h the grain boundary carbide network was observed to be continuous throughout the specimen. The grain boundary carbides were further observed to be somewhat increased in size compared to the solution annealed material. Also no fine carbides were observed in the vicinity of the

grain boundary carbides. The individual carbide particles present in the carbide stringers and isolated intragranular carbides appeared to have increased slightly in average size ($<1\mu\text{m}$) over that of the solution annealed materials (Kimball et al, 1976).

Kihara et al. (1980) reported that for creep exposed Inconel 617 alloys at $1000^\circ\text{C}/25\text{MPa}$, the major observed phases were M_{23}C_6 and M_6C types of carbides. They were precipitated both in grain boundaries and as intragranular particles. It was reported earlier (Hosoi and Abe, 1975) that creep strength of this alloy at 1000°C in He atmosphere is remarkably reduced by decarburization. Therefore, carbides are associated with the creep strength of this alloy (Mankins et al. 1974). Grain boundary migration is an important mechanism during creep at 1000°C , however grain boundary carbides act to suppress grain boundary migration, and this significantly affects the recovery mechanism. All samples before creep tests were subjected to a solution and ageing treatment. Solutionization was conducted to increase the grain size and to dissolve all carbides. Ageing treatments to all solution treated samples were conducted to eliminate the precipitation of carbides during creep. After this treatment fine intragranular carbides (metastable) were quickly precipitated as massive and stable grain boundary carbides. BSE micrographs showed that M_{23}C_6 carbides were dark and small in size and had high chromium rich and low molybdenum contents. However, M_6C types of carbides were bright due to high molybdenum and low chromium content, and of massive size. The M_6C type carbides were localized mainly on the grain boundaries and near to the M_{23}C_6 type carbides. It was concluded in the report that fine intragranular carbides contribute to a lower creep rate only in the transient state (negative transient curve) by impeding dislocation movement, however they did not give lower creep rate in the steady state region. This was owing to a decrease in the discrete number of carbides to a significantly low value, which then increase the ability of dislocations to move through the microstructure, prior to the onset of the steady state creep. Therefore, the main contribution to creep strength in the steady state region is due to interstitial atoms of carbon/or grain boundary carbides. Grain size also influences the creep rupture life. The creep-rupture life for smaller grain size samples were remarkably

decreased by the finer grain size. In relation to microstructural changes during creep Kihara et al. (1980) made very concise and clear understanding on migration of grain boundary & their carbides and voids formation & creep deformation mechanism during tertiary creep. The wavy grain boundaries are attributed to grain boundary migration which occurred during the creep deformation. Grain boundary migration was independent of applied stress direction and observed at all grain boundaries. A list of intermetallic compounds, carbides and nitrides that are precipitated in Inconel alloys is given in Table 2.1.1.1.

Table 2.1.1.1 Constituent phases observed in Inconel alloys, which are present in IN617.

Phase	Crystal structure	Lattice parameter, Å	Formula
γ'	fcc (ordered $L1_2$)	3.561 for pure Ni_3Al to 3.568 for $Ni_3(Al_{0.5}Ti_{0.5})$	$Ni_3Al, Ni_3(Al, Ti)$
η	hcp ($D0_{24}$)	$a_0 = 5.093, c_0 = 8.276$	Ni_3Ti (no solubility of other elements)
γ''	bct (ordered $D0_{22}$)	$a_0 = 3.624, c_0 = 7.406$	Ni_3Nb
MC	Cubic	4.3 – 4.7	TiC, NbC
$M_{23}C_6$	fcc	10.50 – 10.70 (varies with composition)	$Cr_{23}C_6, (Cr, Fe, W, Mo)_{23}C_6$
M_6C	fcc	10.85-11.75	$Fe_3Mo_3C, Fe_3W_3C, Fe_4W_2C, Fe_3Nb_3C, Nb_3Co_3C$
M_7C_3	hcp	$a_0 = 13.98, c_0 = 4.523$	Cr_7C_3
MN	Cubic	4.240	TiN
μ	Rhombohedral	$a_0 = 4.75, c_0 = 25.77$	$(Fe,Co)_7(Mo,W)_6$

The carbide precipitation phenomenon does not preferentially occur on tensile boundaries but from the migration of carbides from compressive boundaries to tensile

boundaries. Carbides on the tensile boundaries grew rapidly and those on the compressive boundaries disappeared. The migration of carbides is as a sequence containing dissolution of carbides at the compressive boundary, diffusion of carbide forming atoms from compressive to tensile boundary region and re-precipitation of carbides on the tensile boundary.

The research effort on this alloy for gas-cooled reactors was vigorous in 1980s, and in 1984, an entire issue of Nuclear Technology, Special issues on high-temperature gas-cooled reactor materials, was devoted to review the progress (Nuclear technology, 1984).

Kirchhöfer et al. (1984) developed a time-temperature precipitation (TTT for time-temperature transformation) diagram for Alloy 617. Two solution-treated alloys at 1200°C followed by a water quench were examined. The ageing temperatures ranged from 500°C to 1000°C for times from 0.5 h to 1000 h. Additional samples aged for longer times to 10,000–30,000 h at 900°C. Precipitate characterization methods included optical metallography, scanning electron microscopy, transmission electron microscopy, energy dispersive X-ray analysis, and X-ray diffraction of extracted residues. Vickers diamond hardness values (HV_s) were also reported for ageing times of 300–1000 h. The precipitation of primary M₆C, Ti(C, N) and small amount of γ' was reported. Bruch et al. (1984) aged a tubing product at temperatures from 700°C to 1000°C for times up to 30,000 h. Schneider et al. (1984) included ageing effects in their examination of the creep behaviour of Alloy 617. They performed testing at 850°C and 950°C for times of up to 10,000 h. Samples aged 175 h, 500 h, 3100 h, and 8700 h were tested at 950°C and 44 MPa. Ennis et al. (1984) also reported their observation of some ageing effects in Alloy 617 during the course of the study of helium and carburization effects on the creep behaviour, tensile properties, and toughness. Their ageing treatments were performed for 2000 h at 850°C. Several papers were published on Alloy 617 for turbine applications in the 1990s (Srivastava et al. 1990; Lai, 1993; Meyer-Olbersleben et al. 1999; Coade et al. 2002). The temperatures of concern were in the range of 760–982°C and loadings included creep, low-cycle fatigue, and thermal fatigue. The microstructural studies and ageing effects were briefly discussed in these papers. Research activities on high-nickel alloys for use in ultra-supercritical steam boiler

technology for boiler tubing, headers, and piping have increased interest in 1990s. Alloy 617 became a potential candidate material for the manufacture of boiler components that operate at 750°C (Starr & Shibli, 2000; Swindeman et al. 2004; Viswanathan et al. 2002).

IN617 is one of the acknowledged candidate materials widely used in high temperature service (600–800°C) component applications for future generations of power plants when the steam inlet temperatures exceeds 750°C. The current working steam temperatures of most efficient power plants are now in the range of 600°C-650°C with steam pressures of 30 MPa and it is expected that temperatures will rise up to 700°C and above to obtain the necessary high thermal efficiencies (Meetham, 1986; Vanstone, 2000; Viswanathan et al., 2005; Viswanathan et al 2005; Amorelli, 2007). In order to meet the material requirements, selection was based on long-term creep rupture properties (longer creep life & creep resistance), microstructural stability, structural stability, fatigue resistance, fracture toughness, corrosion & oxidation resistance and fabricability (Nickel et al., 1984). Alloy 617 was therefore chosen for investigation for the critical components used in steam turbine technology (Meetham, 1986; Tancret and Bhadeshia, 2003).

In a European project, Allen et al. (2004) examined solution-annealed base metal and service-aged Alloy 617 and its weldment from a gas turbine combustion system with 25,000 operating hours. The microstructures of the aged base metal, the HV of the aged base, the weld, the outside and inside wall metals, etc., were studied. Shingledecker et al. (2004) continued the research on Alloy 617 for boiler application and constructed hardness versus time curves for a broad range of temperatures and times. Microstructural studies were conducted by Wu et al. (2008) to examine the ageing response of IN617, as a part of USC Steam Boiler Consortium project. Prolonged ageing conditions for the precipitate study ranged up to 65,000 hours at a series of temperatures from 482°C to 871°C. Hardness was also measured for various ageing conditions. Solid solution strengthened IN617 alloys are attributed with exceptional creep life and rupture strength at temperatures up to 800°C, due to solid solution strengthening of matrix by the molybdenum and cobalt additions and precipitation strengthening by intermetallic

precipitate (gamma prime), carbides precipitation etc. It has an excellent combination of high strength and oxidation resistance, particularly at temperatures over 980°C (Huntington Alloy, 1972; Hosier and Tillack, 1972; Mankins et al., 1974; Nickel et al., 1982; Bassford and Hosier, 1984). The high nickel and chromium contents make the alloy resistant to both reducing and oxidizing media. The aluminium, in conjunction with the chromium, provides high-temperature oxidation and decarburization resistance. The high chromium promotes the formation of chromium oxide as a protective oxide under adequately oxidizing conditions. Cr and Mo are carbide formers that act to improve the creep resistance. These carbides, especially at grain boundaries, play an important role in deciding long term creep rupture strength of the alloy 617. However, an excess loss of chromium from the matrix reduces the effectiveness of solid-solution strengthening. It also leads to dissolution of chromium carbides from the chromium-depleted zone as the chromium activity decreases (Ennis et al. 1993). In addition, Mo and Co enhance the strength. The presence of 1 wt% aluminium in the matrix enhances the oxidation resistance and improves the strength of the matrix by precipitating coherent phase during ageing $\text{Ni}_3(\text{Ti, Al})$ type intermetallic compound (γ'). It increases the strength and creep resistance at higher temperatures. However, the major role of aluminium and chromium additions is to improve the oxidation and carburization resistance at high temperatures. The solute element, titanium, promotes the formation of thin protective aluminium oxide surface scales, if titanium/aluminium (Ti/Al) ratios near to unity. In Alloy IN617, Ti/Al ratio is 0.63 and forms protective surface scale, whereas the alloys have lower Ti/Al ratios form semi protective aluminium-oxide scales such as Alloy IN713C, Ti/Al = 0.4. Some alloys that contain aluminium but no titanium such as alloy M21 form un-protective surface scales. (Mankins et al., 1974; Kimball et al., 1976; Takahashi et al., 1978; Hosoi and Abe, 1975; Kihara et al. 1980; Johnson et al., 1984). The alloy is considered superior to Inconel 625 since it does not form any embrittling TCP phases such as σ , μ , and χ in the temperature range 649°C to 1093°C for durations below 10,330 hours (Mankins et al., 1974). The primary precipitated phases present in the microstructure are titanium nitride, titanium carbides (or solution of those two compounds

commonly called cyano-nitrides), and chromium carbides. These nitrides and cyano-nitrides are stable at all temperatures below the melting point and are unaffected by heat treatment. Strengthening behaviors are also derived from these precipitates. These precipitates are precipitated both in grain boundaries and as intragranular particles.

The mechanical performance of the alloy degrades during service under stress, temperature and in aggressive environments, owing to changes in the microstructure. At temperatures in excess of 650°C, under application of stress, the alloying elements start to interact with the environments and precipitate out in the matrix, causing de-alloying of matrix. Such evolution of the microstructure usually results in degradation of properties especially creep-rupture strength and creep life. This degradation in performance leads to creep deformation and ultimately to fracture. Therefore, this study is preliminary focused on the mechanistic understanding between creep deformation mechanisms and microstructural evolution that arise during long-term creep exposure.

Creep resistance to failure is one of the primary considered materials properties for components used for high temperature applications in potentially aggressive environments. Time dependent slow plastic deformation under the application of constant load till failure is studied in creep behaviour of materials. Creep damage and failure is associated with permanent change in shape of the material during tertiary creep and quantified by the nucleation, growth, distribution and coalescence of microscopic internal cavities and voids.

The identified phases in Inconel 617 by researchers after different thermal ageing and creep exposure conditions from a range of temperature of 482 – 1050°C are shown in Table I. The primary phases present in IN617 are γ' , $M_{23}C_6$, Ti(C, N) and M_6C .

Table I: Identified phases in IN617 reported by other researchers (continued)

Phases	Temp (°C)	Tests	Amount	Researchers
M₂₃C₆ [M= Cr + Mo]; Cr₂₁Mo₂C₆	649-1093	Creep tested in Air	Very abundant	Mankins et al.
	593-816	Aged	-	Kimball et al.
	700-800	Creep tested	-	Gariboldi et al.
	1000	Aged	-	Takahashi et al.
	1000	Creep Tested	-	Kihara et al.
	482-871	Aged (He atmosphere)	High volume fraction at 871°C	Wu et al.
	500-1050	Aged	-	Kirchhöfer et al.
Ti (C,N)	1000	Aged	-	Takahashi et al.
	500-1050	Aged	-	Kirchhöfer et al.
TiN	649-1093	Creep tested in Air	Rare	Mankins et al.
Cr Mo (C, N)	649-1093	Creep tested in Air	Very Rare	Mankins et al.
MC [M=Ti, Mo]	482-871	Aged in Helium atmosphere	-	Wu et al.
MC [M= Cr, Mo]	700-800	Creep tested	Rare	Gariboldi et al.
γ	649-760	Creep tested in Air	0.6%	Mankins et al.
	593-816	Aged	Very small	Kimball et al.
	700-800	Creep tested	-	Gariboldi et al.
	1000	Aged	-	Takahashi et al.
	500-1050	Aged	Very small	Kirchhöfer et al.
	482-871	Aged in Helium atmosphere	593°C – 5% Volume fraction (V.F.), 704°C – 2% V.F., 871°C – very low V.F.	Wu et al.

Table I: Identified phases in IN617 reported by other researchers

η - M_6C ; Mo_3Cr_2 (Ni, Co)C	1000	Aged	-	Takahashi et al.
	1000	Creep Tested	-	Kihara et al.
	482-871	Aged in Helium atmosphere	Very low volume fraction at low temperature	Wu et al.
	500-1050	Aged		Kirchhöfer et al.
Ni_2 (Cr, Mo)	482-871	Aged in Helium atmosphere	Absent at high temperature	Wu et al.
δ - Ni_3Mo	Only at 700	Creep tested	-	Gariboldi et al.
$M_{12}C$	500-1050	Aged	-	Kirchhöfer et al.

2.1.2 Research Activities on Inconel Alloy 625

Inconel alloy 625 is a nickel based superalloy solid-solution strengthened mainly by the additions of carbon, chromium, molybdenum, and niobium. This alloy is developed for application at temperatures below 700°C. It has been used extensively in the petrochemical and aerospace industries and in many marine applications. The alloy possesses high strength and toughness at elevated temperature, excellent corrosion and creep resistant properties, with excellent fatigue strength and fabrication characteristics as one of the age-hardened nickel based superalloys. The alloy is a solid solution hardened, but extra hardening appeared in the alloy due to precipitation of intermetallic ordered phases and carbides (Eiselstein and Tillack, 1991). Several ordered phases are formed in this alloy as a function of temperature and duration of ageing. Among the observed ordered phases, Ni_2 (Cr, Mo) and γ'' phases are formed on ageing below 600°C. Precipitation hardening in this alloy at elevated temperatures (600–700°C) is mainly derived from the metastable phase γ'' [Ni_3 (Nb, Al, Ti)]. It has ordered body-centered tetragonal DO_{22} crystal structure. The precipitates of γ'' are generally small in size (~10 to 20 nm) and coherent with the matrix. Coherency strain plays an important role in strengthening the alloy. It also influences the coarsening behaviour of precipitates and the long

term behaviour of the microstructure and mechanical properties at elevated temperature (Collier et al. 1988). The metastable γ'' phase gets transformed to the equilibrium orthorhombic δ -phase $[\text{Ni}_3(\text{Nb}, \text{Mo})]$ upon prolonged ageing. M_{23}C_6 (M is rich in Cr), M_6C and MC (M is rich in Ni, Nb & Mo) carbides get precipitated in the range of 760-980°C. The primary MC carbide has shown their presence in solution annealed condition and has been reported to decompose into M_{23}C_6 and M_6C on prolonged exposure at elevated temperatures (Shankar et al. 2001). The orthorhombic phase deteriorates the alloy tensile, creep ductility and toughness properties

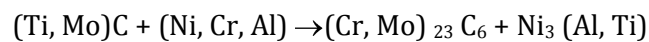
Inconel Alloy 625, nickel-based superalloy is extensively used under aggressive environment of high stress, high temperature and corrosive atmosphere. The material shows a good combination of yield strength, tensile strength, creep strength, excellent fabricability, weldability and good resistance to high temperature corrosion and oxidation on prolonged exposure to aggressive environments (Rai et al., 2004). It is a nickel-chromium-molybdenum alloy with an addition of niobium that acts with the molybdenum to strengthen the alloy's matrix.

The outstanding strength and toughness of Inconel 625 in the temperature range cryogenic to 1093°C are derived primarily from the solid solution strengthening effects of the transition metals, niobium and molybdenum, in a nickel-chromium matrix. Nickel and chromium provide resistance to oxidizing environment, while nickel and molybdenum provide resistance to non-oxidizing environment. Pitting and crevice corrosion are prevented by molybdenum. Niobium resists scaling and oxidation at high temperatures. Some typical applications for Inconel 625 are heat shields, furnace hardware, gas turbine engine ducting, combustion liners and spray bars, chemical plant hardware and special seawater applications (Paul et al., 2007).

Eiselstein & Tillack (1991) studied intermetallics phases and carbides precipitation in Inconel alloy 625 on ageing in the range of 550 – 750°C. Alloy 625 shows secondary precipitation hardening at temperatures above 650°C. The precipitates observed in this alloy

are metastable γ'' phase $[\text{Ni}_3 (\text{Nb}, \text{Al}, \text{Ti})]$ having ordered BCT DO_{22} structure and $\text{Ni}_2 (\text{Cr}, \text{Mo})$ phase having an orthorhombic, Pt_2Mo type structure. The metastable γ'' phase is transformed from orthorhombic δ to phase $[\text{Ni}_3 (\text{Nb}, \text{Mo})]$ upon prolonged ageing (Brown & Muzyka, 1987; Shankar et al., 2001; Sundararaman et al., 1999). Sundararaman et al. (1999) also discussed different variants of $\text{Ni}_2 (\text{Cr}, \text{Mo})$ precipitates; usually in the austenite grains. These particles exhibited a snowflake-like morphology and were uniformly distributed in the matrix. Apart from the intermetallic phases, the precipitation of a M_6C type carbide phase within the matrix and the formation of near continuous films, comprising discrete $\text{M}_6\text{C}/\text{M}_{23}\text{C}_6$ carbide particles, at the austenite grain boundaries have been observed in the alloy after prolonged service. Delta (δ) phase has also been found to form directly from the supersaturated solid solution on ageing at higher temperatures.

Xuebing et al. (1998) investigated in detail the microstructural features of Ni-based superalloys used in gas turbines and its high temperature properties were attributed to the high volume fraction of the gamma-prime (γ') phase. The gamma-prime (γ') precipitate has a slight mismatch with the matrix but can block the movement of dislocations, resulting in a high creep resistance. They concluded that the degeneration of MC to M_{23}C_6 was facilitated by the formation of the gamma-prime (γ') phase. This can be described by the following reaction:



M_{23}C_6 type carbides play a more important role in strengthening the grain boundary than MC carbides because of the finer grain size of the M_{23}C_6 carbides.

Kumar et al. (2002) have reported about the change in properties of prolonged (about 60 000 h) exposure in Inconel 625 to a temperature close to 600°C and reported a substantial decrease in ductility and toughness of the alloy due to heavy intragranular and intergranular precipitation. In this work the authors demonstrated the influence of various precipitates, such as intermetallics γ'' , $\text{Ni}_2 (\text{Cr}, \text{Mo})$ and δ - phases, and grain-boundary carbides, and correlated the

results with yield strength. The changes in microstructure, due to precipitation of second phase precipitate led to a decrease in room temperature tensile properties.

The excellent oxidation resistance of Inconel 625 alloy has reported by Fujikawa et al. (2007). Inconel 625 alloy showed better oxidation resistance to other Ni-based crystalline superalloys and the oxide scale of Inconel 625 alloy is very thin and mainly comprised of Cr_2O_3 . Microstructural evolution in alloy 625 during creep deformation was investigated by Mathew et al. (2007), in the temperature range of 650°C to 875°C for duration from 30 to 31,800 h. Microstructural changes were observed under different test conditions with precipitation of intermetallics γ'' and δ phases in the austenitic matrix. The observed phase γ'' was at 700°C and δ phase at above 700°C. A continuous decoration of MC type carbides was also observed on the grain boundaries. The carbides precipitated at grain boundaries play an important role in the strengthening of grain boundaries at elevated temperatures (Fernandez et al., 1978; Bae et al. 2001).

The service-exposed alloy 625 at 600°C for 60,000 h showed higher strength and lower ductility compared to the virgin material in the solution annealed state. Precipitation of intermetallic γ'' and $\text{Ni}_2(\text{Cr}, \text{Mo})$ phases and inter- and intragranular carbides were found to be responsible for higher strength of the service-exposed alloy. On subjecting the service-exposed alloy to subsequent thermal ageing treatments at 650°C and 850°C (above the service temperature of the exposed alloy) dissolution of the intermetallic phases occurred that in turn increased the ductility of the alloy. Post-service ageing of the alloy at 650°C for short durations resulted in the dissolution of the $\text{Ni}_2(\text{Cr}, \text{Mo})$ phase. The dissolution of the $\text{Ni}_2(\text{Cr}, \text{Mo})$ phase exhibited significant influence upon yield strength (YS) but a negligible effect on ductility. Prolonged ageing of the alloy for 500 h at 650°C resulted in the precipitation of intermetallic δ phase. Post-service ageing of the alloy at 850°C promoted the dissolution of both $\text{Ni}_2(\text{Cr}, \text{Mo})$ and γ'' formed during service. Longer duration ageing at the same temperature led to the precipitation of δ phase with an associated increase in strength and loss in ductility. Re-resolution

annealing of the service-exposed alloy at 1150°C caused dissolution of the strengthening phases. When the re-solution annealed alloy was subjected to prolonged exposure at 650°C, the yield stress was found to increase rapidly with ageing time with significant loss in ductility due to the precipitation of γ'' (Shankar et al., 2001).

Yang et al. (2006) studied the morphology, location and stability of MC, M_6C and $M_{23}C_6$ carbides in thermally exposed polycrystalline Ni-based superalloy and it was reported that MC carbide is stable from 850 to 950°C; M_6C carbide was stable above 1000°C; $M_{23}C_6$ carbide appeared in the 950–1000°C temperature range.

Angeliu et al. (1990) reported that the thermodynamic analysis of the carbide stability indicates that factors, such as favourable orientation relationships, play an important role in controlling the precipitation of $Cr_{23}C_6$ in nickel-based superalloys.

The tensile creep behaviour of alloy 625 was investigated by Rodriguez et al. (2003). The dominant strengthening contribution comes from grain size refinement. Solid solution strengthening plays a secondary role. The analysis of creep curves over the temperature range 538–650°C revealed two distinct regions of creep behaviour. At lower stress levels the creep characteristics were consistent with a structure controlled creep process. At higher stress levels the creep characteristics were consistent with mobility-controlled deformation where creep was controlled by the viscous glide of dislocations. The species thought to be responsible for viscous glide is niobium (Nb). The apparent activation energies determined for creep in both the low stress region and high stress region exceed by a considerable amount the values for lattice self-diffusion of Ni. In addition, normalization of the creep data using Young's modulus for Inconel 625 to compensate the stress and the activation energy for self-diffusion of Ni to compensate the strain rate fails to collapse the data onto a single slope. These phenomena are explained in terms of the simultaneous deformation of second phase particles along with the austenitic γ matrix during creep. The second phase most likely to be deforming along with the austenitic γ matrix is the equilibrium delta (δ) phase.

2.1.3 Research Activities on Nimonic Alloy 263

Nimonic 263 is a wrought Ni-based super alloy, which has found wide applications in gas turbines for power plants, aircraft and aero-engines, because of its attractive creep strength and good oxidation resistance. It is a precipitation-hardening creep-resistant nickel-chromium-cobalt-molybdenum alloy developed and introduced by Rolls-Royce in 1960.

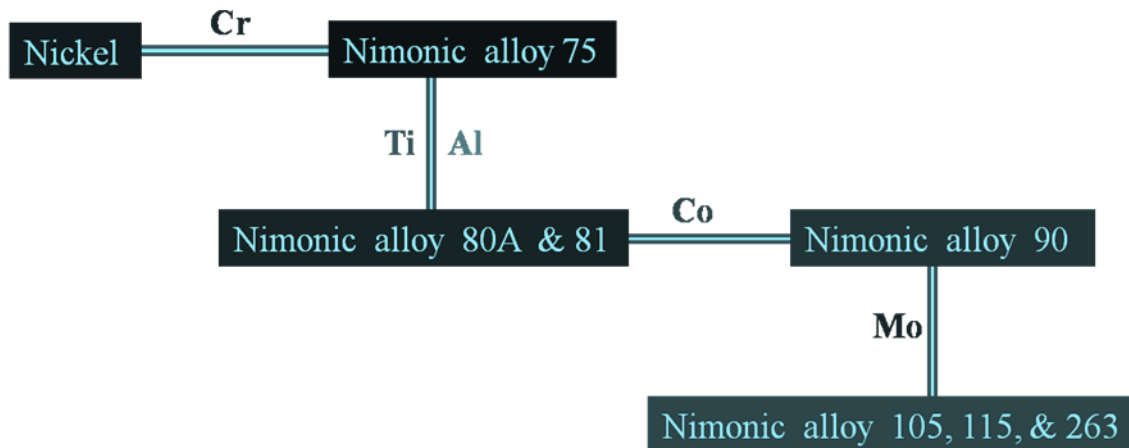


Figure 2.1.3.1: Nickel-base superalloy NIMONIC tree.

It is primarily used for applications where welding is important. This alloy shows excellent weld ductility and fabrication characteristics as of Nimonic 75, as well as excellent creep-rupture strength as of Nimonic 80A (Stubbs, 1974; Brown and Muzyka, 1987). Figure 2.1.3.1 shows the development tree of Nimonic alloys. Polycrystalline Nimonic 263 is an important age-hardened alloy, mainly strengthened by γ' precipitation from the addition of aluminium and titanium, and by carbides. Some strengthening is also achieved by solid-solution hardening from chromium, cobalt and molybdenum. The nature and morphology of the γ' phase $\text{Ni}_3(\text{Al}, \text{Ti})$ are of primary importance during age-hardening in obtaining optimum high temperature properties. Compositionally, the aluminium and titanium contents and their ratio are very important, as is heat treatment. On increasing the aluminium/titanium ratio, high temperature properties improve. Figure 2.1.3.2 shows precipitation-strengthened alloys (Nimonic series) have considerably higher strength values than solid-solution strengthened alloys. The addition of cobalt also increases the solubility of γ' above 1100°C , thus facilitating hot working despite the

high aluminium and titanium contents. In the fully heat-treated condition, the microstructure shows fine discontinuous precipitates of carbides ($M_{23}C_6$) at the grain boundaries. After solution and ageing heat-treatment the hardness is around 275H_V.

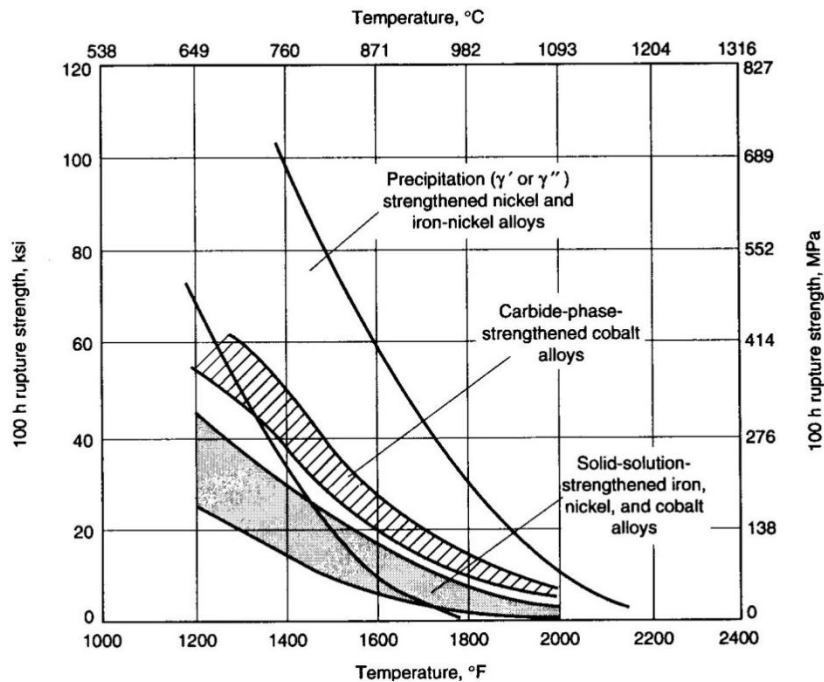


Figure 2.1.3.2: Stress-rupture characteristics of wrought superalloys (Davis, Ed. Heat-Resistant Materials, 1999)

The high temperature performance of the complex alloy is improved by the fine dispersion of second-phase particles within the grains. These particles primarily provide (1) impedance to dislocation motion/glide, which increases strain hardening of the alloy; (2) restriction to recovery by imbedding the dislocation networks formed during strain hardening. Smaller particles do not present significant obstacles to dislocation motion and dislocations may readily loop around the largely spaced precipitates. The high temperature properties are optimized by controlling the magnitude of precipitates size and their spacing.

Most of the nickel base superalloys are precipitation-hardened by the presence of intermetallic precipitates, having geometrically closed packed (GCP) cubic structures, coherent with the Ni-rich austenitic matrix. Nimonic alloys are categorized as precipitation-hardened

nickel-based superalloys. Nimonic® is a trademark of the Special Metals Corporation group of companies. Nickel, the base metal, has fairly high melting point and has the additional advantage of face-centered-cubic structure. Sufficient chromium is added to nickel to provide oxidation resistance without destroying the face-centered-cubic structure. The first alloy was Nimonic 75, essentially 80/20 Ni/Cr +Ti with additions of titanium (0.4 wt. %) and carbon (0.12 wt. %) for precipitation hardening. It was then found that a more effective precipitation hardening agent was one based on f.c.c. phase Ni_3Al , in which titanium can replace some of the aluminium to give $\text{Ni}_3(\text{Ti}, \text{Al})$, termed as gamma-prime, γ' . The first of the turbine blade materials to be strengthened with γ' was Nimonic 80A & 81 alloys, with varying Ti/Al ratios. Further improvements were then made by adding cobalt to lower the stacking fault energy of nickel. With addition of cobalt up to ~ 21%, Nimonic 90, was developed as a better heat and corrosion resisting alloy. The addition of molybdenum and cobalt also provided solid solution strengthening. Nimonics 105 & 115 alloys were the next alloys in this category with Ti/Al ratios of up to ≤ 0.8 . The presence of the γ' -precipitates decreased the rate of coarsening obtained by decreasing the lattice mismatch between precipitates and matrix. This has a substantial influence on the high temperature mechanical, and creep-rupture properties. The workability of these alloys was low and interest focused on the development and processing of alloys, with optimum chemical compositions, which can show superior high temperature properties, fatigue, creep-fatigue interactions, and better oxidation and corrosion resistance (Crane et al, 1997).

Nimonic alloy 263, an air melted nickel-base alloy, was developed by Rolls-Royce Ltd., in 1971 to provide improved ductility, weldability and fabricability over Nimonic alloy 80A. Nimonic 263 primarily intended as a material having the weld ductility and fabrication characteristics of Nimonic 75 combined with the creep-rupture strength of Nimonic 80A (Stubbs, 1974; Brown and Muzyka, 1987). Nimonic 263 shows improved high-temperature strength (up to 900°C) and excellent mechanical properties (Special metals, 2010). Nimonic 263 was designed primarily for use in the stationary components of gas turbines like the

combustion chamber, casing, liner, exhaust ducting, bearing housing and others. These components are fabricated from plate/sheet forms of the alloy. The formability and weldability of the alloy are an important factor for the fabrication of these components. Controlled precipitation of the intergranular γ' phase greatly enhances the strength of the Nimonic 263. This alloy differs from Inconel 617 & 625 alloys on elemental composition and heat treatment processes. The controlled heat treatment process in this alloy gave high strength and good creep properties for applications.

The precipitation of γ' -phase is the primary strengthening phase in Nimonic alloy 263 and its properties are strongly dependent upon the morphology and distributions of the γ' precipitates. The γ' -precipitates are ordered and coherent, with a long-range ordered Cu_3Au structure, which is also called L_{12} structure and show distinct cube-to-cube orientation relationship with Ni-rich austenitic matrix (γ). It has an ordered face-centered cubic structure below 1150°C , as shown in (Figure 2.1.3.1)

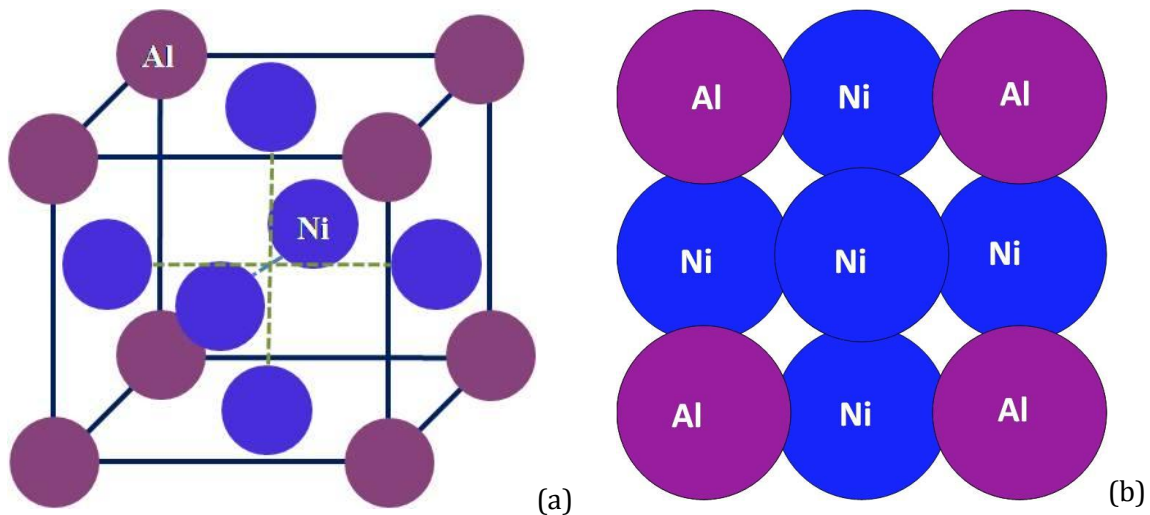


Figure 2.1.3.1: Ni_3Al phase (γ') responsible for age-hardening in Ni-based superalloys. (a) Primitive ordered L_{12} crystal structure, (b) Stoichiometric arrangement of Ni and Al atoms. The unit cell density is 0.37.

The coherency of γ/γ' interface is due to the very small lattice misfit between their lattice parameters. The excellent properties of the alloys are found to depend critically on the coherency of the γ/γ' interface. The orientation relationship can be described by

$$\{100\}_{\gamma} // \{100\}_{\gamma'} \& \langle 010 \rangle_{\gamma} // \langle 010 \rangle_{\gamma'}$$

, which is referred as the cube-to-cube orientation relationship.

The polycrystalline Nimonic alloy 263 is also solid solution-strengthened by chromium, cobalt and molybdenum. The fine precipitates at the grain boundaries are important in controlling creep rupture ductility. Carbides and borides play an important role in improving the high temperature creep-rupture properties in these alloys. If no carbides are present, grain boundary sliding causes premature failure. The optimum conditions are provided by discrete globular particles. The presence of carbon and boron cause the formation of these phases. The improved properties are primarily due to the preferred location of carbides and borides at the γ -grain boundaries, which improves the rupture strength by inhibition of grain-boundary sliding. Therefore, carbon and boron are often referred to as grain-boundary strengtheners. The important carbides phases reported are MC, $M_{23}C_6$ and M_6C , which are rich in Ti, Cr, and Mo respectively. When grain boundaries of misorientation equal to 10° were introduced, carbon and boron concentrations of 0.09 and 0.01 wt%, respectively, were sufficient to improve the rupture life from 10h to 100h. The effect was attributed to small, distinct, coherent and closely spaced $M_{23}C_6$ carbides precipitating on the grain boundaries.

Gibbons and Hopkins (Gibbons and Hopkins, 1984) have found that γ' strengthening effect was most dominant when the grain size was large. This effect occurs because the prominent form of creep damage in polycrystalline nickel-based alloy is creep cavitation at the γ -grain boundaries, this become less effective as the grain size increases.

Excessive quantities of Cr, Mo and W promote the precipitation of intermetallic phases which are rich in these elements. The resulting phases are known as topologically closed-packed

(TCP), have complex crystal structure and general chemical formulae A_xB_y , where A and B are transition metals. The important TCP phases are σ , μ , and P-phases. The μ phase is based upon the stoichiometry A_6B_7 and has rhombohedral crystal structure containing 13 atoms per unit cell, for example Mo_6Co_7 . The σ -phase is based upon the stoichiometry A_2B and has a tetragonal structure containing 30 atoms, for example $Cr_{61}Co_{39}$. The P-phase has an orthorhombic unit cell, containing 56 atoms, for example $Cr_{18}Mo_{42}Ni_{40}$ (Reed, 2006).

Zhao et al (2001) have investigated precipitation behaviour in Nimonic 263. The major precipitates at temperatures below 900°C were gamma-prime (γ') and eta (η -Ni₃Ti). They reported that eta phase precipitated at the expense of the gamma-prime (γ') phase after prolonged annealing. The eta (η) precipitates had a thin-plate morphology and formed a regular Widmanstätten pattern. Both phases had a fixed orientation relationship with the FCC matrix. Very fine particles of $M_{23}C_6$ also precipitated intragranularly, and they had a cube-on-cube orientation relationship (OR) within the FCC matrix. Intragranular precipitation of very fine cylindrical MC carbide was also observed. Grain-boundary (GB) precipitates were mostly $M_{23}C_6$, with a small fraction of MC.

The deterioration of the creep performance of Nimonic 263 at high temperature was reviewed by Srinivas et al. (1995). The effect of degradation on creep properties in the air exposed alloy at 780°C in the stress range of 160-275 MPa was discussed in terms of the outer layer of intergranular oxide and the depletion of gamma prime (γ'). The presence of intergranular oxide and the γ' denuded region led to a creep weakening effect, resulting in an enhanced creep rate and poor creep life. Higher creep rates in air-exposed specimens of Nimonic 263 provided evidence that the formation of CO gas bubbles occurred along the grain boundaries during exposure to air. The presence of CO gas bubbles acted as cavity nuclei during creep. Growth and inter linkage of cavities led to failure and hence poor creep ductility. Extensive cavitation was also observed in the Nimonic 263 alloy.

Polycrystalline Nimonic 263 is strengthened by gamma prime (γ') particles with a spherical shape and size of around 20 nm. The creep rate dependence on dislocation flux as a function of the gamma prime (γ') volume fraction with temperature has been studied by Manonukul et al., (2002) who described the creep of Nimonic 263 in the temperature range between 700 and 950 °C, above and below the gamma prime (γ') solvus temperature respectively. They found that below the solvus temperature of γ' (925°C) the material undergoes creep at a rate which is determined by precipitate cutting, or by dislocation bowing at pinning occurring at either the γ' precipitate particles, or within the dislocation network. Precipitate coarsening contributes significantly to the creep rate if bowing at precipitate particles is rate-controlling. Particle coarsening has been quantified and embodied in the model. Above the γ' solvus, the separation of pinning distance is defined by the dislocation network.

Several authors have proposed that for Ni-based superalloys containing high volume fractions of γ' , particle-coarsening causes a progressive increase in creep rate (i.e. a long period of tertiary creep) due to a steady decline in σ_0 . It has been shown that coarsening of gamma prime (γ') is unable to account for tertiary creep in these alloys. The extent of acceleration of strain rate and that tertiary creep is produced by at least two competing strain-softening damage micromechanisms. One is fracture damage—cavitation and cracking—while the other is suggested as being caused by the accumulation of dislocations (Dyson and McLean, 1983).

It was reported (Manonukul et al. 2005) that after standard heat treatment, Nimonic 263 material has a mean grain size of 104 μ m, 9.5% volume fraction of γ' with an average precipitate size of 22 nm, and almost continuous precipitation of $M_{23}C_6$ carbide at grain boundaries. The precipitation solvus temperature is approximately 925°C. Creep deformation becomes significant once the temperature has exceeded about 600 °C. In standard creep tests at temperatures below the precipitation solvus, particle (γ') cutting, dislocation bowing and climbing have been observed (Manonukul et al., 2002), dependent on the size of the γ' precipitate (Zhang and Knowles, 2002; Zhang et al., 2001; Sundararajan, 1985). During

isothermal creep tests, the volume fraction of precipitate remains constant but the precipitates coarsen. The rate of coarsening has been found to be independent of applied stress (Stevens and Flewitt, 1979). As the precipitate coarsens, eventually the critical particle size is achieved and exceeded, and dislocation (Orowan) bowing takes over and climb occurs as the rate-controlling deformation mechanism. Cavitation occurs at grain boundaries during creep, but other microstructural evolutions such as precipitation, precipitate coarsening, generation & multiplication of mobile dislocations are also observed.

Summary:

Inconel 617, 625 and Nimonic 263 alloys are used for high temperature applications as high temperature components in steam boilers, discussed in Table II.

Table II: Properties and Applications of IN617, IN625 & Nimonic 263

	Inconel 617	Inconel 625	Nimonic 263
Properties	Good corrosion resistance, Exceptional combination of metallurgical stability, strength, and oxidation resistance at high temperatures.	High strength, creep and excellent corrosion (pitting and crevice) resistant, very good fabricability, high corrosion-fatigue strength, resistive to stress-corrosion cracking	Attractive creep strength, oxidation and corrosion resistance along with good formability and high-temperature ductility
Applications	HP/IP valve chest, rotor forgings, blades, pipes, tubes, headers, and superheater tubes in steam boilers	Thinner-walled vessels or tubing, reaction vessels, distillation column, heat-exchangers, transferring piping, valves, gas coolers, cladding on ferritic steel tubes in steam boilers	Superheater tubes, outlet headers, steam lines, hot gas ducting (transition piece) and bolting in steam boilers

References

- Allen, D., Keustermans, J.-P., Gijbels, S., and Bicego, V., (2004). "Creep Rupture and Ductility of As-Manufactured and Service-Aged Nickel Alloy IN617 Materials and Welds," *Mater. High. Temp.*, 21(1), 55–60.
- Amorelli, A. and Howes, G. (2007). Impact of low carbon fuels on gas turbines design, *Proceedings of the Seventh International Charles Parson's Turbine Conference, Power Generation in an Era of Climate Change*, (Eds. A. Strang, W. M. Banks, G. M. McColvin, J. E. Oakey and R. W. Vanstone) Institute of Materials, London 2007, 9-12.
- Angeliu, T.M. and Was, G.S. (1990). Behavior of grain boundary chemistry and precipitates upon thermal treatment of controlled purity alloy 690, *Metallurgical and Materials Transactions A*, 21(8), 2097-2107.
- Bae, J.S., Lee, J.H., Kim, S.S. and Jo, C.Y. (2001). Formation of MC- γ/γ' eutectic fibers and their effect on stress rupture behavior in D/S Mar-M247LC superalloy, *Scripta Materialia*, 45(5), 503-508.
- Bassford, T.H. and Hosier, J. C. (1983). Production and welding technology of some high temperature nickel alloys in relation to their properties, *Nuclear Technology*. 1984, 66(1), 35-43.
- Beckitt, F.R and Clark, B.R. (1967). The shape and mechanism of formation of $M_{23}C_6$ carbide in austenite, *Acta Metallurgica* 15 (1), 113-129.
- Betteridge, W. (1959). *The Nimonic Alloys*, Edward Arnold Ltd. London 66-117.
- Bowman, A.L., Arnold, G.P., Storms, E.K. and Nereson, N.G. (1972) The crystal structure of $Cr_{23}C_6$, *Acta Crystallographica*, B, 28 (10) 3102-3103.
- Brown, E.E and Muzyka, D.R. (1987). (Eds. C.T. Sims and W.C. Hagel), *The Superalloys II*, Wiley, New York.
- Bruemmer, S.M. and Henager Jr., C.H. (1986) High voltage electron microscopy observations of microdeformation in alloy 600 tubing *Scripta Metallurgica*, 20 (6), 909-914.

- Bruch, U., Schumacher, D., Ennis, P., and Heesen, E., 1984, "Tensile and Impact Properties of Candidate Alloys for High-Temperature Gas-Cooled Reactor Applications," *Nuclear Technology*, 66 (2), pp. 357–362.
- Chang, H. C. and Grant, N. J. (1956). *Trans. AIME*, 206, 544.
- Collier, J.P., Selius, A.O., Tien, J.K. (1988). in: Reichman S (Ed.), *Superalloys*, Warrendale, PA: TMS; 1988, pp 43-52.
- Cummins, A.B. and Given, I.A. (1992). *SME Mining Engineering Handbook: Vol.1, 2nd edition* (H.L. Hartman, Ed.), Society for Mining, Metallurgy, and Exploration (Publisher), 1992.
- Coade, R., and Tunjic, M., (2002). Failure of an Inconel 617 Gas Turbine Liner, *Proceedings of the Seventh Conference on Operating Pressure Equipment*, Institute of Materials Engineering Ltd., Melbourne, Victoria, April 2–4, 2003, Vol. 7.
- Crane, F. A. A., Charles, J. A., Furness, Justin. (1997). *Selection and Use of Engineering Materials*, Third Edition, Butterworth-Heinemann Publication.
- Davis, J.R. (Ed.) (1999). *ASM Specialty Handbook: Heat Resistant Materials*, ASM International®, Material Park, OH 44073-0002.
- Davies P. and Randle V. (2001). Grain boundary engineering and the role of the interfacial plane, *Materials Science and Technology*, 2001, 17 (6), 615-626.
- Dyson, B.F. and McLean, M. (1983). Particle-coarsening, σ_0 and tertiary creep, *Acta Metallurgica*, 31(1), 17-27.
- Eiselstein, H.L. and Tillack, D.J. (1991). (Ed. Loria E.A.) *Superalloy 718, 625 and various derivatives*. TMS, Warrendale, PA, 1-14.
- Ennis, P. J., Mohr, K. P., and Schuster, H., (1984). "Effect of Carburizing Service Environments on the Mechanical Properties of High-Temperature Alloys," *Nuclear Technology*, 66(2), 363–368.
- Ennis, P.J., Quadakkers, W.J., Schuster, H. (1993). The effect of selective oxidation of chromium on the creep strength of alloy 617, *Journal de Physique. IV France* (3) C9-979-C9-986. 1993.
- Farag, M.M. and Hamdy, M.M. (1976) Behaviour of Nickel-Base High Temperature Alloy Under Hot-Working Conditions. *Metallurgical Transactions A* 7(2) 221-228.

- Fernandez, R., Lecomte, J.C. and Kattamis, T.Z. (1978). Effect of solidification parameters on the growth geometry of MC carbide in IN-100 dendritic monocrystals, *Metallurgical Transactions A: Physical Metallurgy and Materials Science*, 9A (10), 1381-1386.
- Fujikawa, H., Murakumo, T., Newcomb, S.B. and Harada, H. (2007) (Eds. Cermak, J. & Stloukal, I.) Steam oxidation behavior of Ni-based single crystalline superalloy for the advanced gas turbine, *Diffusion and Thermodynamics of Materials 263*, Trans Tech Publications Ltd, Switzerland, 111-116.
- Guard, R. W. (1961). *Mechanical Behavior of Materials at elevated Temperatures*. J. E. Dorn (ed.), New York: McGraw-Hill.
- Gibbons, T.B. and Hopkins, B.E. (1984). Creep behaviour and microstructures of Ni-Cr base alloys. *Metal Science* 18 (5), p. 273-280.
- Hosoi, Y., and Abe, S. (1975). The Effect of Helium Environment on Creep Rupture Properties of Inconel 617 at 1000°C, *Metallurgical Transactions A*, 6(6), 1171–1178.
- Huntington Alloys: Inconel Alloy 617, (1972). Huntington Alloys, Inc., Huntington, West Virginia.
- Johnson, W. R, Thompson, L.D. and Lechtenberg, T. A. (1984). Design of wrought nickel-base alloys for advanced high-temperature gas-cooled reactor applications. *Nuclear Technology*. 1984, 66(1), 88-102.
- Kihara, S., Newkirk, John B., Ohtomo, A., Saiga, Y. (1980). Morphological changes of carbides during creep and their effects on the creep properties of Inconel 617 at 1000°C *Metallurgical Transactions A*, 11(6) 1019-1031.
- Kimball, O. F., Lai G. Y. and Reynolds G. H. (1976) Effects of thermal ageing on the microstructure and mechanical properties of a commercial Ni-Cr-Co-Mo alloy (Inconel 617) *Metallurgical Transactions A*, 7 (12) 1951-1952.
- Kirchhöfer, H., Schubert, F., and Nickel, H., (1984). Precipitation Behavior of Ni-Cr-22Fe-18Mo (Hastelloy X) and Ni-Cr-2Co-12Mo (Inconel 617) After Isothermal Ageing, *Nuclear Technology*, 66 (1), 139–148.

- Kumar, A., Shankar, V., Jayakumar, T., Rao, K.B.S. and Raj, B. (2002). Correlation of microstructure and mechanical properties with ultrasonic velocity in the Ni-based superalloy Inconel 625, *Philosophical Magazine A*, 82 (13), 2529-2545.
- Lai, G. Y., (1993). Nitridation of Several Combustor Alloys in a Simulated Gas Turbine Combustion Environment, *Proceedings of the ASM 1993 Materials Congress Materials Week '93*, Pittsburgh, PA, Oct. 17-21, 113-121.
- Lewis, M.H. and Hattersley, B. (1965) Precipitation of $M_{23}C_6$ in austenitic steels. *Acta Metallurgica*, 13 (11), 1159-1168.
- Mankins, W.L., Hosier, J.C and Bassford, T.H. (1974). Microstructure and phase stability of Inconel alloy 617. *Metallurgical Transactions* 1974; 5 (12): 2579-2590.
- Murr, L. E. (1975). *Interfacial phenomena in metals and alloys*, Reading, MA, Addison and Wesley. Pub. Co.
- Manonukul, A., Dunne, F.P.E., Knowles, D. (2002). Physically-based model for creep in nickel-base superalloy C263 both above and below the gamma solvus, *Acta Materialia*, 50, 2971-2931.
- Manonukul, A., Dunne, F.P.E., Knowles, D. and Williams, S. (2005). Multiaxial creep and cyclic plasticity in nickel-base superalloy C263, *International Journal of Plasticity*, 21 (1), 1-20.
- Mathew, M.D., Parameswaran, P. and Rao, K.B.S. (2007). Microstructural changes in alloy 625 during high temperature creep, *Materials Characterization*.
- Meetham, G.W. (1986). *High Temp Alloys for Gas Turbines and Other Applications*, (Eds. Betz, et al.) Publisher: Reidel, Dordrecht, Holland, 1986.
- Meyer-Olbersleben, F., Kasik, N., Ilschner, B., and Rezai-Aria, F., (1999). The Thermal Fatigue Behavior of Combustor Alloys IN 617 and HAYNES 230 Before and After Welding, *Metall. Mater. Trans. A*, 30A, 981-989.
- Nuclear technology*, 1984, July, 66 (1-3).
- Nickel, H., Ennis, P. J., Schubert, F. and Schuster, H. (1982). Qualification of metallic materials for application in advanced high-temperature gas-cooled reactors, *Nuclear Technology*. 1982, 58, 90.

- Nickel, H., Kondo, T. and Rittenhouse, P. L. (1984). Status of metallic materials development for application in advanced high-temperature gas-cooled reactors. *Nuclear Technology*. 1984, 66(1), 12-22.
- Paul, C.P., Ganesh, P., Mishra, S.K., Bhargava, P., Negi, J. and Nath, A.K. (2007). Investigating laser rapid manufacturing for Inconel-625 components, *Optics & Laser Technology*, 39(4), 800-805.
- Rai, S.K., Kumar, A., Shankar, V., Jayakumar, T., Rao, K.B.S., Raj, B. (2004). Characterization of microstructures in Inconel 625 using X-ray diffraction peak broadening and lattice parameter measurements, *Scripta Materialia*, 51, 59-63.
- Reed, R.C. (2006). *The Superalloys: Fundamentals and Applications*, Cambridge University Press.
- Rodriguez, R., Hayes, W.R. Berbon, P. B. and Lavernia, E. J. (2003). Tensile and creep behavior of cryomilled Inco 625, *Acta Materialia*, 51 (4), 911-929.
- Ross, E.W. and Sims, C.T., (1987). Nickel-base alloys, *Superalloys II*, Sims, C.T., Stoloff, N.S. and Hagel, W.C. (Eds.), John Wiley & Sons, 97-135.
- Shang-Slaiang HSU Time-Dependent Crack Growth in a Heat-Resistant Alloy Inconel 617. *Journal of Nuclear Science and Technology*, 30, 4(1993) 302-313.
- Singhal, L.K. and Martin, J.W. (1967). The growth of $M_{23}C_6$ carbide on incoherent twin boundaries in austenite, *Acta Metallurgica* 15 (10), 1603–1610.
- Stubbs, G.B. (1974) *Physical Properties, The Nimonic Alloys and Other Nickel-Base High-Temperature Alloys*, (Eds. W. Betteridge and J. Heslop) Edward Arnold Ltd., London.
- Schneider, K., Hartnagel, W., Schepp, P., and Ilschner, B., (1984). "Creep Behavior of Materials for High-Temperature Reactor Application," *Nuclear Technology*, 66 (2), 289–295.
- Shankar, V., Rao, K.B.S. and Mannan, S.L. (2001) Microstructure and mechanical properties of Inconel 625 Superalloy, *Journal of Nuclear Materials*, 288 (2-3), 222-232.
- Shingledecker, J. P., Swindeman, R. W., and Vasudevan, V. K., (2004). "Creep Strength of High Temperature Alloys for Ultrasupercritical Steam Boilers," *Fourth International Conferences on*

Advances in Materials Technology for Fossil Power Plants, Hilton Oceanfront Resort, Hilton Head Island, SC, Oct. 25–28.

Special Metals Corporation Products, NIMONIC® alloy 263, www.specialmetals.com/products (Retrieved March 16, 2010).

Srinivas, S., Pandey, M.C. and Taplin, D.M.R. (1995) Air-environment-creep interaction in a nickel base superalloy, *Engineering Failure Analysis*, 2(3), 191-196.

Srivastava, S. K., and Klarstrom, D. L., (1990). The LCF Behavior of Several Solid Solution Strengthened Alloys Used for Gas Turbine Engines, The Gas Turbine and Aeroengine Congress and Exposition, Brussels, Belgium, Jun. 11–14, Paper No. 90-GT-80.

Starr, F., and Shibli, I. A., (2000). Fundamental Issues in the Development of Austenitic and Nickel Based Alloys for Advanced Supercritical Steam and High Temperature Indirect Fired Gas turbine Systems, Parsons Advanced Materials for 21st Century Turbines and Power Plant, IOM Communications, London, 459–471.

Stubbs, G.B. (1974) Physical Properties, The Nimonic Alloys and Other Nickel-Base High-Temperature Alloys, (Eds. W. Betteridge and J. Heslop) Edward Arnold Ltd., London.

Sundararaman, M., Kumar, L., Prasad, E.G., Mukhopadhyay, P. and Banerjee, S. (1999). Precipitation of an intermetallic phase with Pt₂Mo-type structure in alloy 625, *Metallurgical and Materials Transactions A: Physical Metallurgy and Materials Science*, 30 (1), 41-52.

Swindeman, R. W., Shingledecker, J. P., Klueh, R. L., Wright, I. G., and Maziasz, P. J., (2004). Boiler Materials for Ultra Supercritical Coal Power Plants Task 2: An Assessment of Candidate Materials–A Review of Literature Part I: Overview and Recommendations, National Energy Technology Laboratory, Report No. NETL/DOE, USC T-7.

Stevens, R.A. and Flewitt, P.E., (1979). The effects of γ' precipitate coarsening during isothermal ageing and creep of the nickel-base superalloy IN-738, *Materials Science and Engineering*. 37(3), 237-247.

Sundararajan, G. (1985). Effect of cavitation and microstructural damage on the intergranular creep fracture of nickel-base superalloys. *Materials Science and Engineering* 74 (1), 55–73.

Tancret, F. and Bhadeshia, H.K.D.H. (2003). An affordable creep-resistant nickel-base alloy for power plant, Proceedings of the 6th International Charles Parsons Turbine Conference, Engineering Issues in Turbine Machinery, Power Plant and Renewables, (Eds. A. Strang, R. D. Conroy, W. M. Banks, M. Blackler, J. Leggett, G. M. McColvin, S. Simpson, M. Smith, F. Starr and R. W. Vanstone) Institute of Materials, London 2003; 525-535.

Tawancy, H.M., Allam, I. M. and Abbas, N. M. (1990). Effect of Ni₃Nb precipitation on the corrosion resistance of Inconel alloy 625, Journal of Materials Science Letters 1990; 9: 343-347.

Takahashi, T., Fujiwara, J., Matsushima T., Kiyokawa, M., Morimoto, I. and Watanabe, T. (1978). Analysis of precipitated phase in heat treated INCONEL alloy 617, Transactions ISIJ **18** 221–224.

Viswanathan, R., Purgert, R., and Rao, U., (2002). Materials for Ultra-Supercritical Coal-Fired Power Plant Boilers, Materials for Advanced Power Engineering 2002, Forschungszentrum Julich GmbH, September 2002, 1109–1129.

Viswanathan, R., Gandy, D., Coleman, K. (Editors). (2005). Advances in Materials Technology for Fossil Power Plants (Proceedings of the Fourth International Conference, EPRI). ASM International, Jan 2005.

Vanstone, R.W. (2000). Advanced (700°C) pulverised fuel power plant, Proceedings of the Fifth International Charles Parsons Turbine Conference, Advanced Materials for 21st Century Turbines and Power Plant, (Eds. A. Strang, W. M. Banks, R. D. Conroy, G. M. McColvin, J. C. Neal and S. Simpson) Institute of Materials, London 2000; 91-97.

Viswanathan, R., Henry, J.F., Tanzosh, J., Stanko, G., Shingledecker, J., Vitalis, B. and Purgert, R. (2005) U.S. program on materials technology for ultra-supercritical coal power plants, J. Mater. Eng. Perform. 14 (3) 2005, 281–292.

Wu, Q., Song, H., Swindeman, R.W., Shingledecker, J.P. and Vasudevan, V.K, Microstructure of long-term aged Alloy 617 Ni-base superalloy, Metall. & Mater. Trans. A. 2008; 39: 2569-2585

Yang, J., Zheng, Q., Sun, X., Guan, H. and Hu, Z. (2006). Relative stability of carbides and their effects on the properties of K465 superalloy, Material science and Engineering: A, 429 (1-2), 341-347.

Zhao, J.C., Ravikumar, V. and Beltran, A.M. (2001). Phase Precipitation and Phase Stability in Nimonic 263, *Metallurgical and Materials Transactions A*, 32(6), 1271-1282.

Zhang, Y.H., Chen, Q.Z. and Knowles, D.M. (2001). Mechanism of dislocation shearing of γ' in a fine-precipitate strengthened superalloy. *Materials Science and Technology*, 17 (12), 1551-1555.

Zhang, Y.H. and Knowles, D.M. (2002). Prestraining effect on creep behaviour of nickel base C263 superalloy. *Materials Science and Technology*. 18 (8), 917-923.

Chapter 3 Materials & Experimental Procedures

This chapter gives details about materials investigated in this thesis, their nominal chemical compositions, heat-treatments and the experimental techniques employed to evaluate the materials. The first part describes the materials, their composition and the heat-treatment process for the solid-solution strengthened alloys, Inconel 617 and 625. The later part discusses the precipitation-strengthened (age-hardenable) alloy, Nimonic 263. Solid-solution strengthened alloys are generally distinguishable from precipitation-strengthened (age-hardenable) alloys by their relatively low content of precipitate-forming elements such as aluminium, titanium, or niobium. The heat-treatment procedure for high-temperature alloys include stress relieving, annealing, solution treating and quenching.

Solution Treating: The first step in heat-treatment is usually solution treatment, whereas stress relieving and annealing is conducted simultaneously after cold forming process to promote adequate formability of the material being deformed. The solution-treatment temperature will depend on the properties desired. Basically, a higher temperature is required for optimum creep-rupture properties. Higher solution-treatment temperatures will result in some grain growth and more extensive dissolution of carbides. The principle objective is to put hardening phases into solution and dissolve some carbide.

Quenching: The purpose of quenching after solution treating is to maintain at room temperature the supersaturated solid solution obtained during solution treating. Quenching permits a finer age-hardening precipitates size.

Ageing Treatments: Ageing heat-treatments are used to harden the alloys, through the precipitation of intermetallic phase from the supersaturated matrix. After ageing, the resulting microstructure of wrought alloys (forged) consists of large grains that contain the principal ageing intermetallic phases such as γ' , η and γ'' and localized precipitation of

carbides ($M_{23}C_6$, MC, M_6C , and M_7C_3), nitrides (MN), carbo-nitrides (MCN), and borides (M_3B_2) as well as δ phase (Davis, 1999).

3.1 Inconel 617 Alloy

The complete nominal chemical composition of the 'as received' IN617 is given in *Table 3.1.1*. A standard creep rupture specimen was prepared from a solution-annealed forged rod of IN617. The solution-annealed forged rods (1100°C/3 Hrs/WQ) were given a heat-treatment (670°C/ 10 Hrs/AC) which usually precipitates primary carbides only on grain boundaries (*Figure 3.1.1*). Creep-test specimens were then machined from the rods. The creep rupture tests were conducted at 650 and 700°C under an applied intermediate stress in air by ALSTOM Power Ltd. Rugby, UK. The creep tests were continued until fracture occurred.

Elements	Ni	Cr	Mo	Co	Al	Ti	Fe	C	Si	W
Wt %	Bal.	22.8	9.0	11.9	1.15	0.48	0.35	0.06	0.05	0.02
Elements	Mn	Cu	Zr	P	V	N	Nb	S	B	
Wt %	0.02	0.013	0.005	0.005	0.005	0.004	0.003	0.001	0.0002	

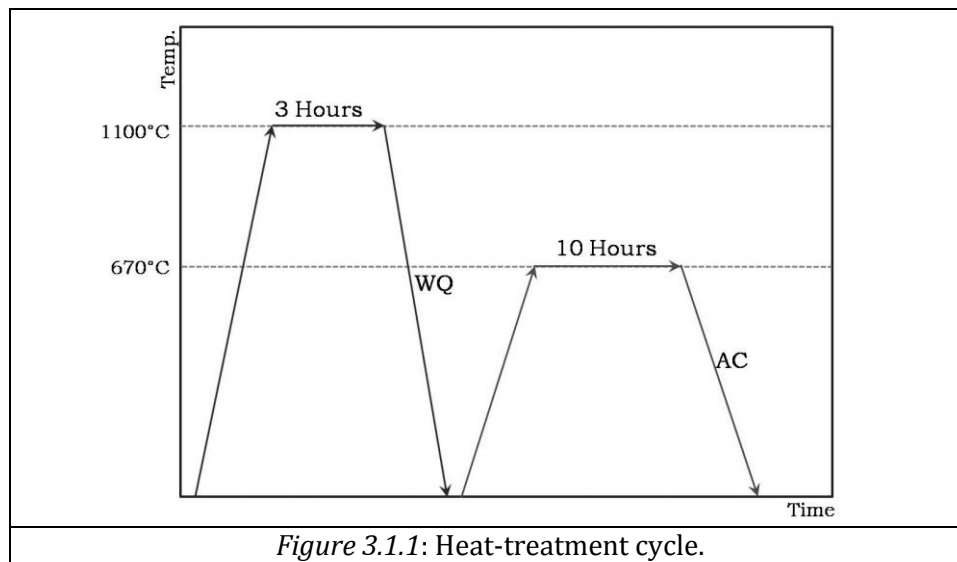


Figure 3.1.1: Heat-treatment cycle.

The solution exposure dissolves all phases except MC carbides, and γ' precipitates nucleate during cooling (quenching) from the solution temperature. During ageing, the γ' volume

fraction increases. Grain boundary $M_{23}C_6$ increases stress-rupture life as long as it is not a continuous carbides film on grain boundary, which markedly decreases rupture ductility.

The creep test conditions and durations to failure along with their corresponding reduction in area after testing of the samples investigated in this study are shown in *Table 3.1.2*.

Table 3.1.2: Creep-test conditions (IN 617)

Alloy	Specimen ID	Temp.	Stress ^ψ (MPa) (Estimated)	Duration* (h)	RA%
IN617 (Solution-annealed condition) Forged	1 (T0154)	700°C	145	32,000	-
	2 (T0151)	700°C	200	4,000	45.1
	3 (T0008)	650°C	275	45,000	16.9
	4 (T0003)	650°C	350	574	17.6
ψ Estimated stress values are reported from life times creep-rupture data of Inconel 617 alloy. (Ennis et al. 2007; Chandra et al. 2005)					
* All creep tests were continued till rupture. - %RA was not measured for T0154.					

3.2 Inconel 625 Alloy

The complete nominal chemical composition of 'as received' IN625 is given in Table 3.2.1. A standard creep rupture specimen was prepared from a solution-annealed forged rod of IN625. The solution-annealed forged rods (1100°C/3 Hrs/WQ) were given a heat-treatment (670°C/ 10 Hrs/AC) which usually precipitates primary carbides only on grain boundaries (Fig. 1). Creep-test specimens were then machined from the rods. The creep rupture test was conducted at 650°C under an applied intermediate stress in air by ALSTOM Power Ltd. Rugby, UK. The creep tests were continued until fracture occurred.

Element	Ni	Cr	Mo	Nb	Fe	Ti	Al	C	Si	W
Wt %	Bal.	21.9	9.1	3.7	2.17	0.2	0.19	0.03	0.02	0.03
Element	Co	Zr	Mn	V	Cu	N	P	S	B	
Wt %	0.02	0.01	0.01	0.01	0.012	0.006	0.002	0.001	0.004	

The creep test conditions and durations to failure along with their corresponding reduction in area after testing of the samples investigated in this study are shown in *Table 3.2.2*.

Table 3.2.2: Creep-test conditions (IN625)

Alloy	Specimen ID	Temp.	Stress (MPa)	Duration* (h)	RA%
IN625 (Solution-annealed condition) Forged	1 (S9976)	650°C	High	1,000	12.7
	2 (S9980)	650°C	Intermediate	33,000	21.8

*All creep tests were continued till rupture. %RA was measured from the ruptured samples

3.3 Nimonic Alloy 263

The complete nominal chemical composition of 'as received' Nimonic 263 alloy is given in *Table 3.3.1*.

Table 3.3.1: Chemical composition of Nimonic 263 Alloy (in weight %)										
Elements	Ni	Cr	Mo	Co	Al	Ti	Mn	C	Si	W
Wt %	Bal.	20.02	5.85	19.6	0.49	2.2	0.35	0.055	0.13	0.05
Elements	Nb	Cu	P	S	Sn		B		Zr	
Wt %	0.03	0.02	0.005	0.00	4.9 (ppm)		10.0 (ppm)		1.0 (ppm)	

The standard pre-heat treatment normally given to Nimonic alloy 263 is two-stage heat-treatments, that is, solution treatment at 1150°C for 2 hours followed by WQ and precipitation hardening (ageing) for 8 hours at 800°C followed by AC, prior to service. The objective of the solutionization is to dissolve the precipitates, present in the matrix, as carbides, prior to their controlled precipitation of γ' and discrete carbides, during precipitation hardening (ageing). Precipitation hardening is related to high temperature mechanical properties, and it depends upon the controlled precipitation of hardening particles, γ' . The precipitation response of γ' is dependent on the ageing temperature and time. Doosan Babcock conducted stress-rupture tests thereafter at 725°C and 775°C for the durations to failure (645 hours to 16,172 hours at 200 MPa to 286 MPa of applied tensile

stresses), as detailed in *Tables 3.3.2* and *3.3.3*. The creep fractured samples were supplied to the University of Leicester for microstructural studies.

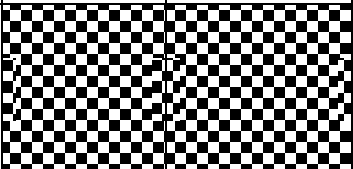
Specimens		Hardening		Macrostructures
		Temp. (°C)	Duration (h)	
N0		800	8	 Nimonic 263 N0 8hrs 800°C
Parent Pipe		800	4	 Specimen ID Parent As Hardened
Welded Pipe		800	4	 Specimen ID Weld As Hardened
Parent	Hardened	800	4	 Specimen ID Parent As Hardened
	Aged	725	3000	
Weld	Hardened	800	4	 Specimen ID Weld As Hardened
	Aged	725	3000	
Parent (Solution-treated)				 Specimen ID Parent Wedge of Pipe

Table 3.3.2: Macrostructures and ageing conditions of precipitation hardened (age-hardened) specimens of Nimonic 263 alloy from 16mm diameter bar (Parent and Welded Pipe).

Specimens	Temp. (°C)	Stress (MPa)	Time to Rupture (h)	Hardening		Macrostructures
				Temp. (°C)	Duration (h)	
N1	725	200	16,172	800	8	 Specimen ID Parent N1
N2		230	7089	800	8	 Specimen ID N2

SR1	725	286	1828	800	4	 Specimen ID SR1
SR3		286	1814	800	8	 Specimen ID SR3
SR4		250	3529	800	8	 Specimen ID SR4
263-P3		286	1833	800	24	 Specimen ID 263-P3
X-Weld 263-W1		265	2376	800	4	 Specimen ID X-Weld 263-W1
X-Weld 263-W2		265	1988	800	8	 Specimen ID X-Weld 263-W2
Specimens		Temp. (°C)	Stress (MPa)	Time to Rupture (h)	Hardening	
				Temp. (°C)	Duration (h)	
N3	775	200	1232	800	8	 Specimen ID N3
N4		230	645	800	8	 Specimen ID N4

Table 3.3.3: Macrostructures and tests conditions of creep-ruptured specimens of Nimonic 263.

3.4 Specimen Preparation Techniques

Metallographic studies were conducted on the load free and load-bearing regions of all samples (head regions and gauge length, respectively) using optical microscopy (OM), scanning electron microscopy (FEGSEM), Electron backscattered diffraction (EBSD) in FEGSEM, and transmission electron microscopy (TEM) techniques in order to characterize the microstructure. Scanning electron microscopy (SEM) and transmission electron microscopy (TEM) were performed with a FEI Sirion 200 field emission gun scanning electron microscope

(FEGSEM), Philips XL 30 ESEM and Jeol JEM-2100, LaB₆ TEM. The SEM was performed on mechanically polished and unetched metallographic specimens.

3.4.1 Specimen preparation for light microscopy

Metallographic specimens were prepared from the head and gauge length of each failed creep specimens. Specimens were mounted in phenolic resin. The mirror polished surface was achieved by grinding with SiC abrasive paper of 1200 grit, then by polishing using 9 to 3 μ m diamond slurry, and finally polished using colloidal silica (0.05 μ m), and then etched with glyceresia (etchant for Inconel 617 and 625) which is a mixture of hydrochloric acid, glycerol and nitric acid in a 3:2:1 ratio. A mixture of 2 gm CuCl₂, 40 ml HCl and 40-80 ml ethanol, called Kallings reagent (or Fry's reagent), as an etchant, was used for Nimonic 263 alloy. The etchant mixture was swabbed on the polished surface for 30-40 seconds. After etching, all samples were examined by reflected light microscope.

3.4.2 Specimen preparation for scanning electron microscopy (FEGSEM)

To observe the specimens in the FEGSEM, mirror polished specimens were prepared from the head and gauge length of the failed creep specimens. Specimens were mounted in phenolic resin. The mirror polished surface was achieved by grinding with SiC abrasive paper of 1200 grit, then by polishing using 9 to 1 μ m diamond slurry, and finally polished using colloidal silica (0.05 μ m). The final polishing is to remove all scratches from the surface. After mirror polishing, FEGSEM was performed on unetched specimens. The SEM images were acquired at 20kV with either secondary electron (SE) or the backscattered electron (BSE) detector. Phase identification, and quantification (Spirit) of major elements (for Z > 10) present in phases observed in the SEM was accomplished with energy dispersive X-ray spectrometry (EDS).

3.4.3 Specimen preparation for Electron backscattered diffraction (EBSD)

Specimens for Electron backscattered diffraction (EBSD) orientation investigations were prepared with an additional step of polishing on $\frac{1}{4}$ μm diamond slurry prior to polishing with colloidal silica. EBSD orientation images were obtained using an HKL Channel 5 EBSD system attached to a FEI Sirion 200 field emission gun scanning electron microscope. The accelerating voltage used was 20kV. A step size of $4.3\mu\text{m}$ was used. Full automatic indexing of the microstructure was obtained using proprietary software: Flamenco was used for image acquisition and indexing and Tango was used for orientation maps. Indexing was performed using an FCC nickel structure with a lattice parameter $a = 0.352$ nm. Typical indexing rates were 97-98%.

3.4.4 Specimen preparation for transmission electron microscopy (TEM)

3.4.4.1 Thin foil preparation

3mm thin foils of specimens were mechanically thinned using a Gatan Model 623 Disk Grinder, to 40-60 μm thickness. Specimens from the gauge length of the creep tested samples were prepared for transmission electron microscopy. Final electro-polishing perforation was performed with twin-jet electro polishing (Model: 120; Fischione Instrument, USA) using an electro-polishing mixture of perchloric acid (HClO_4) and methanol (MeOH) in 1:4 ratios at 14 V and -22°C . a JEOL JEM-2100, LaB_6 electron source transmission electron microscope (TEM) with an operating voltage of 200 kV was used to observe the microstructure of the as-received and creep-exposed samples and to analyze the crystal structures of the precipitates.

3.4.2.1 Carbon-replica preparation

- i. The sample was prepared using standard metallographic techniques for general optical or SEM observations. For extraction replicas, the polished specimens were lightly etched to reveal the microstructure.
- ii. This first etching step used Kallings etchant (a), 10% oxalic acid or a γ' etchant (b), depending on the phase to be studied.

(a). Kallings modified reagent - 40 ml distilled water + 480 ml HCl + 48 gm of CuCl₂

(b). γ' etchant - a mixture of 12ml H₃PO₄ + 40ml HNO₃ + 48ml H₂SO₄ for 6V at 5-6 seconds
- iii. After etching, the area of interest was observed under a low magnification microscope and the remaining area was carefully covered by a masking tape.
- iv. A thin carbon film was then deposited on the specimen.
- v. After coating, the masking tape was removed and the remaining coating was scored into approximately 3mm² areas. This allowed the electrolyte to penetrate beneath the coating and help in removing it during the final stage.
- vi. After scoring, the specimen was electrolytically re-etched, either in the same solution used for initial etching or with a solution of 10 ml HCl and 1 g tartaric acid in 90 ml methanol at 4 V.
- vii. Once etched, the specimens were carefully lowered, at a shallow angle into a beaker filled with distilled water to detach the carbon replica.
- viii. These replicas were then be collected on to 200 mesh copper grids and dried before TEM examination.

3.5 Characterisation of alloys

The exposed alloys were characterised through X-ray diffraction on bulk samples, carbides extracts, from 10% Br₂ dissolution techniques and gamma prime extracts from electrolytic dissolution in 10% phosphoric acid.

3.5.1 X-ray diffractometry (XRD) and peaks separation

X-ray diffractometry (XRD) was performed using a Philips PW 1716 diffractometer with $\text{CuK}\alpha_1$ radiation ($\lambda=1.54\text{\AA}$) in the angular range of $2^\circ \leq 2\theta \leq 125^\circ$, $\Delta 2\theta = 0.0096^\circ$, $t = 0.5$ s/step, to characterize the phases present in the creep failed sample. Some potential precipitate peaks overlap with the austenitic γ -matrix peaks and thus PeakFit® (PeakFit® 4.12, 2003; Mukherji, et al. 2003) software was used to separate the peaks.

3.5.2 Extraction techniques for x-ray diffraction (XRD)

Typical solutions and techniques used for the extraction of phases for identification by XRD technique are as follows:

- (i) Extraction of carbides and certain intermetallics: 3gram of sample chippings were dissolved in 10% bromine in ethanol for 24 hours. The supernatant liquid was centrifuged at 15000 rpm for 30 minutes at 4°C to separate the residue. Then the residue was washed with water and dried for XRD.
- (ii) Gamma prime, eta phase, and M (C, N): 5gram extracts of bulk sample was electrolytically dissolved in 10% phosphoric acid in water at a current density of $10\text{A}/\text{dm}^2$ (current ~ 0.5 mA). The time of extraction was 5-8 hours. The residue was filtered and dried for XRD.

3.5.3 Mechanical property i.e bulk hardness determination

Hardness is an extrinsic material property that enables it to resist plastic deformation, bending, scratching, abrasion or cutting Vickers hardness tests were conducted using a Vickers hardness testing machine, Hardness Control Services Ltd. Make, with a 20kgf load on ground and polished longitudinal cross-section of the creep fractured specimens. The hardness measurements were conducted on the head and gauge length of creep ruptured specimens. The average hardness value along the length of the specimen was average of three hardness values at intervals of 2mm.

3.5.4 Average grain size measurement

Linear Intercept Method is used for the measurement of average grain size on optical and secondary electron images. Linear intercept length is the average length of a line segment that crosses the grains. It is proportional to the equivalent diameter of a spherical grain (grain size). The mean linear intercept length (L) is determined by laying a number of randomly placed test lines on the image and counting the number of times that grains or grain boundaries are intercepted. Mathematically, it is defined as: $L = \left(\frac{L\tau}{PM} \right)$, where $L\tau$, is the total length of the test lines, P , is the total number of grains or grains boundary intersections and M is the magnification.

3.6 Estimation of area fraction of precipitates

The area fractions of individual precipitates were determined on back-scattered scanning electron (BSE) micrographs. These micrographs were from magnification 5000 to 10,000. The high range of magnifications was used to resolve the precipitate shape and size. The representative area fractions of precipitates are the average of individual area fractions of precipitates in 20 BSE micrographs. ImageJ software was used to analyse the BSE micrographs to get area fractions of different precipitates. *Figure 3.6.1* shows the (a) BSE micrograph of sample T0151 (700°C/4000 H) (b) analysis of ImageJ software to get the area of the precipitates. The systematic steps were (i) setting of exact scale, as global for the area measurement from the micrograph's micron bar, (ii) selection of precipitate of interest from the tool (use of 'Freehand selection'), (iii) outline the selected precipitate, (iv) fill the precipitate and finally (iv) analyse the filled precipitate for its area. The standard errors in the area measurement were in the range from 0.1% to 3.4%.

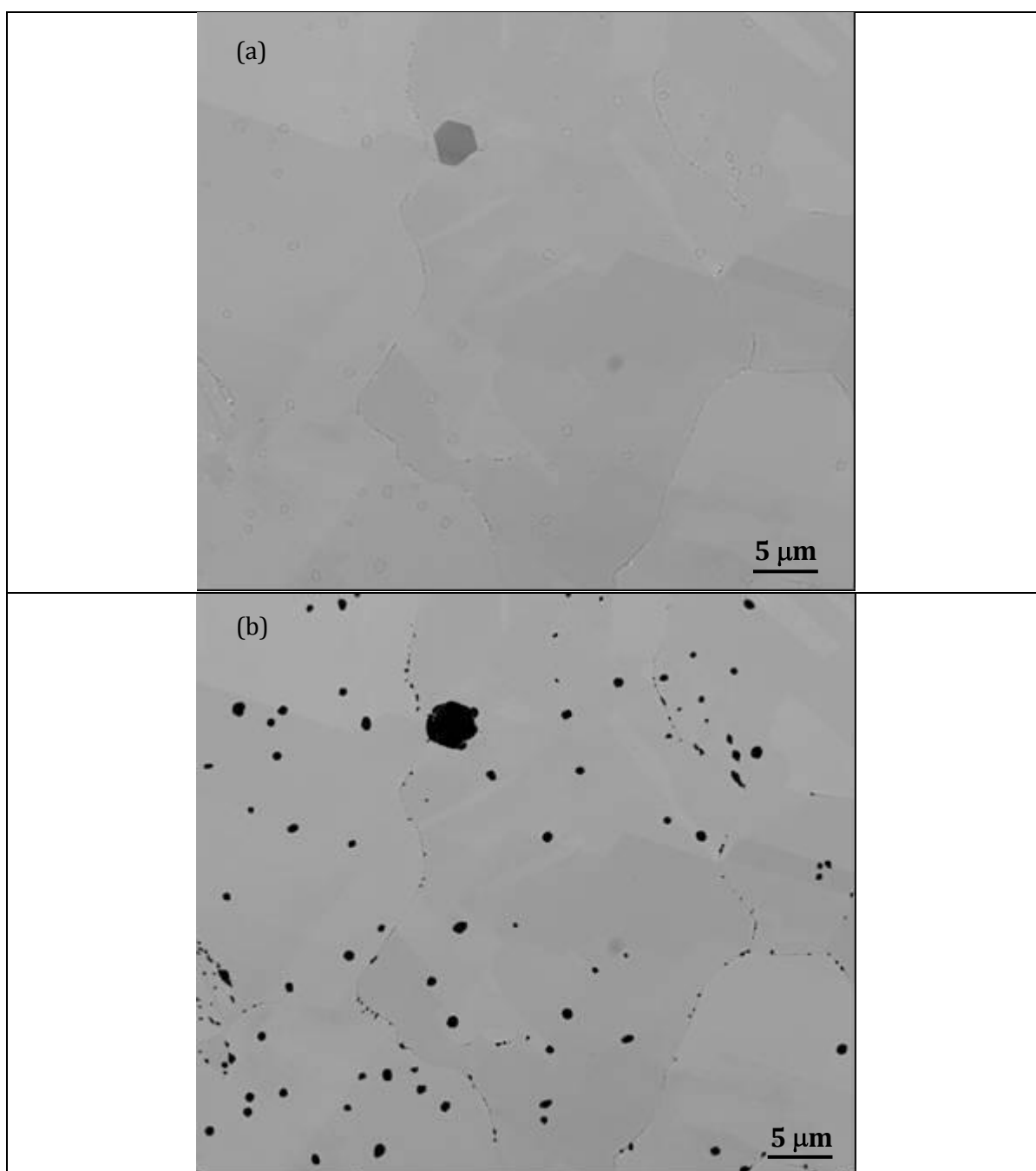
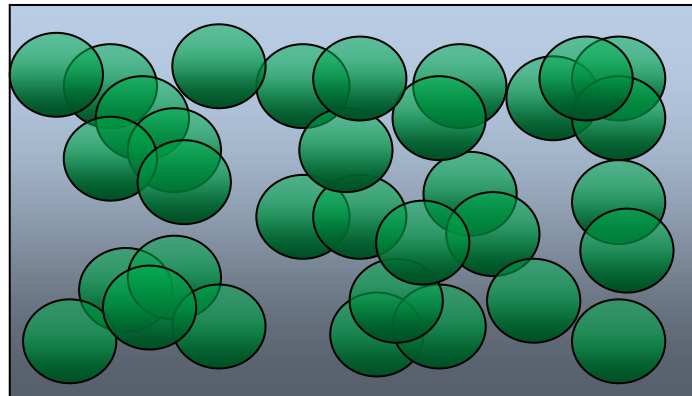


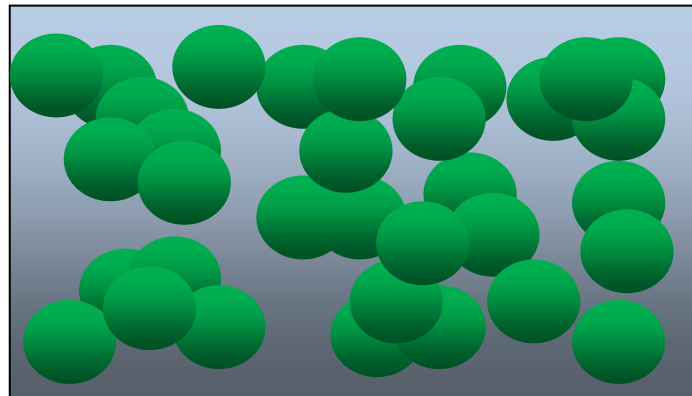
Figure 3.6.1: Illustration of application of ImageJ on BSE micrograph of sample T0151 to get the area of the precipitates. (a) Micrograph shows the precipitates of Ti rich (dark), Cr rich (gray) and a very fine precipitates of Mo rich (white). (b) Micrograph shows area dimension on the respective precipitates using ImageJ software.

3.7 Estimation of volume fraction of precipitates from TEM Images

The volume fraction of precipitates from TEM images are estimated as follows. The TEM image of gamma prime particles gives the superimposed view through a cross-section of material of a number of particles at different depths, as in Figure 3.7.1a. The resulting observed area fraction (Figure 3.7.1b) is not the same as the volume fraction of the particles as particles are imaged through the entire thickness, not just on the top surface. Also, for the high particle densities we are observing, the effect of particle overlap is very significant.



(a)



(b)

Figure 3.7.1: Spherical particles observed in a thin film via TEM. (a) The particles are at different positions through the thickness of the film and hence appear to overlap in a TEM image. (b) The actual area of particles observed in the TEM image.

The effect of overlap can be taken into consideration in the following way. The different visualisations of the images in Figures 3.7.1a and 3.7.1b are very similar to those for a

partially complete 3D phase transformation. The classic Avrami-Mehl equation relates the difference in the actual volume fraction transformed, V_f , to the so-called “extended volume fraction”, V_{ext} , by

$$V_f = 1 - \exp(-V_{ext}) \quad (3.7.1)$$

where the extended volume is the volume of particles in the absence of particle impingement (i.e the particles touching). For small volume fractions the likelihood of impingement is small and the two volume fractions are the approximately the same.

Equation (3.7.1) is widely used throughout the work. In this case (3.7.1) can be written as

$$A_f = 1 - \exp(-A_{ext}) \quad (3.7.2)$$

This applies to the 2D images of particles that we see in the TEM images.

If there are N particles in a film of total area A_0 and thickness h then the total extended area fraction (area fraction in the absence of impingement/overlap) of the particles is

$$A_{ext} = \frac{N\pi R^2}{A_0} \quad (3.7.3)$$

The extended volume fraction of the particles in the film is simply

$$V_{ext} = \frac{4N\pi R^3}{3A_0h} = \frac{4R}{3h} A_{ext} \quad (3.7.4)$$

From (3.7.1) and (3.7.2) we can express the actual volume fraction, V_f , in terms of the observed area fraction (in the TEM image), A_f , such that

$$-\ln(1 - V_f) = -\frac{4R}{3h} \ln(1 - A_f) \quad (3.7.5)$$

or, finally

$$V_f = 1 - (1 - A_f)^{\frac{4R}{3h}} \quad (3.7.6)$$

Note that this necessarily assumes that $h \gg R$, i.e. the particles are smaller than the film thickness (which is the case here).

Summary:

Table I shows the chemical composition of tested alloy.

Table I: Chemical composition of alloys

	IN617	IN625	Nimonic 263
Elements	Weight %	Weight %	Weight %
Ni	Bal.	Bal.	Bal.
Cr	22.8	21.9	20.02
Mo	9.0	9.10	5.85
Co	11.9	0.02	19.6
Al	1.15	0.19	0.49
Ti	0.48	0.20	2.23
Fe	0.35	2.17	0.00
C	0.06	0.03	0.055
Si	0.05	0.02	0.13
W	0.02	0.03	0.05
Mn	0.02	0.01	0.35
Cu	0.013	0.012	0.02
Zr	0.005	0.01	1(ppm)
P	0.005	0.002	0.005
V	0.005	0.01	0.00
N	0.004	0.006	0.00
Nb	0.003	3.70	0.03
S	0.001	0.001	0.001
B	0.0002	0.004	10 (ppm)
Sn	0.00	0.00	4.9 (ppm)

References

D. Mukherji, R. Gilles, B. Barbier, D. Del. Gemovese, B. Hasse, P. Strunz, T. Wroblewski, H. Fuess, J. Rösler: *Scripta Materialia*, 2003, 48, 333-339.

Ennis, P.J. and Quadakkers, W.J. (2007). Mechanical properties and high temperature corrosion resistance of Alloy 617 at 700 – 1000 °C, *Proceedings of the Seventh International Charles Parsons Turbine Conference, Power Generation in an Era of Climate Change*, (Eds. A. Strang, W. M. Banks, G. M. McColvin, J. E. Oakey and R. W. Vanstone) Institute of Materials, London, 509-518.

PeakFit® 4.12, SeaSolve Software Inc. 1999-2003 (Retrieved on 30th March, 2009).

Sharad Chandra, R. Cotgrove, S. R. Holdsworth, M. Schwienheer, and M. W. Spindler, *Creep Rupture Data Assessment of Alloy 617. Proceedings Creep & Fracture in High Temperature Components – design & Life Assessment Issues* (Eds. I. A. Shibli, S. R. Holdsworth, G. Merckling). ECCC Creep Conference, September 12-14, 2005, London, UK, Lancaster, PA: DEStech Publications, 178-188, (2005).

Inconel 617 alloy is well known for excellent creep properties at high temperature. The microstructure consists of γ' precipitates, primary carbides ($M_{23}C_6$) and occasional TiN particles dispersed in a single-phase austenitic matrix. Owing to high temperature exposure and the creep deformation processes that occur in-service, evolution of the microstructure occurs. This chapter discusses the influence of creep deformation at an operating condition of 650 to 700°C for 574 to 45,000Hrs, with emphasis on the morphology and distribution of carbide/nitride or any other phase precipitation.

4.1 'As-received'

4.1.1 Grain Morphology

The grain structure and its morphology is one of the important structural factors which controls the high temperature creep and fracture behaviour of nickel base superalloys. Therefore, it is vital to control its size to avoid excessively fine grains, which decrease creep and rupture strength and excessively large grains, which lower tensile strength. An optimal structural state in this type of alloys may be achieved by way of single or multi-stage heat treatments. In this section metallographic observation of the grain structure and its morphology for the 'as-received' sample of Inconel 617 (IN617) alloy are discussed.

The 'as-received' sample is in solution-annealed condition (heat-treated at 670°C/ 10 Hrs/ AC after solutionization for 1100°C/3 Hrs/WQ). The optical microstructure of the 'as-received' Inconel 617 sample is shown in *Figure 4.1.1*. The 'as-received' sample shows an equiaxed austenitic γ -grain structure with an average size of 120 μ m. This coarse grain structure in the solution-annealed condition is the prerequisite for high creep rupture strength. The grain orientation has been shown to be random (Krishna et al. 2009). Annealing twins and twinning boundaries are observed in a number of grains. Twins have faceted

appearance and are broad, whereas twin boundaries have flat and straighter sides. Twins can be observed in *Figure 4.1.1*, and they have shown special orientation relationship with grains and grain boundaries. Twin boundaries are as readily visible as grain boundaries, since the etchant etched both at about the same rate, indicating they are high-energy boundaries. They are oriented in particular direction inside the grains and formed at the grain boundaries. The observed annealing twins are of type edge (a), incomplete (b), or complete (c) (*Figure 4.1.1*). A summary of the morphology of grains and grain boundary is listed in *Table 4.1.1*.

As-received IN617	Grain Morphology			ASTM grain size No.	Grain- boundary morphology
	Grain-size range (μm)	Avg. grain size (μm)	Grain shape		
	70 to 440	120	Equiaxed	5-6	Flat & Zigzag

Twin boundaries and twin-limited microstructures are important in evolutions of structure and in determining the bulk properties of the polycrystalline material. They also make materials resistant to intergranular degradation (Murr, 1975; Davies and Randle, 2001). The Vickers hardness value for the 'as received' sample was found to $186.6 \pm 5 \text{ Hv}/20$.

The intergranularly distributed precipitates are supposed to strengthen the alloy at high temperatures. Solutionization and ageing heat treatments were used to dissolve the intragranular precipitates (mainly carbides) and to enhance localized precipitation of fine carbides intergranularly. *Figure 4.1.1* shows that there is fine precipitation of intragranular precipitates observed in the optical micrograph. In some regions of the microstructure, intragranular precipitates were observed; which indicates that the ageing heat treatment duration was not sufficient to dissolve all the primary precipitates.

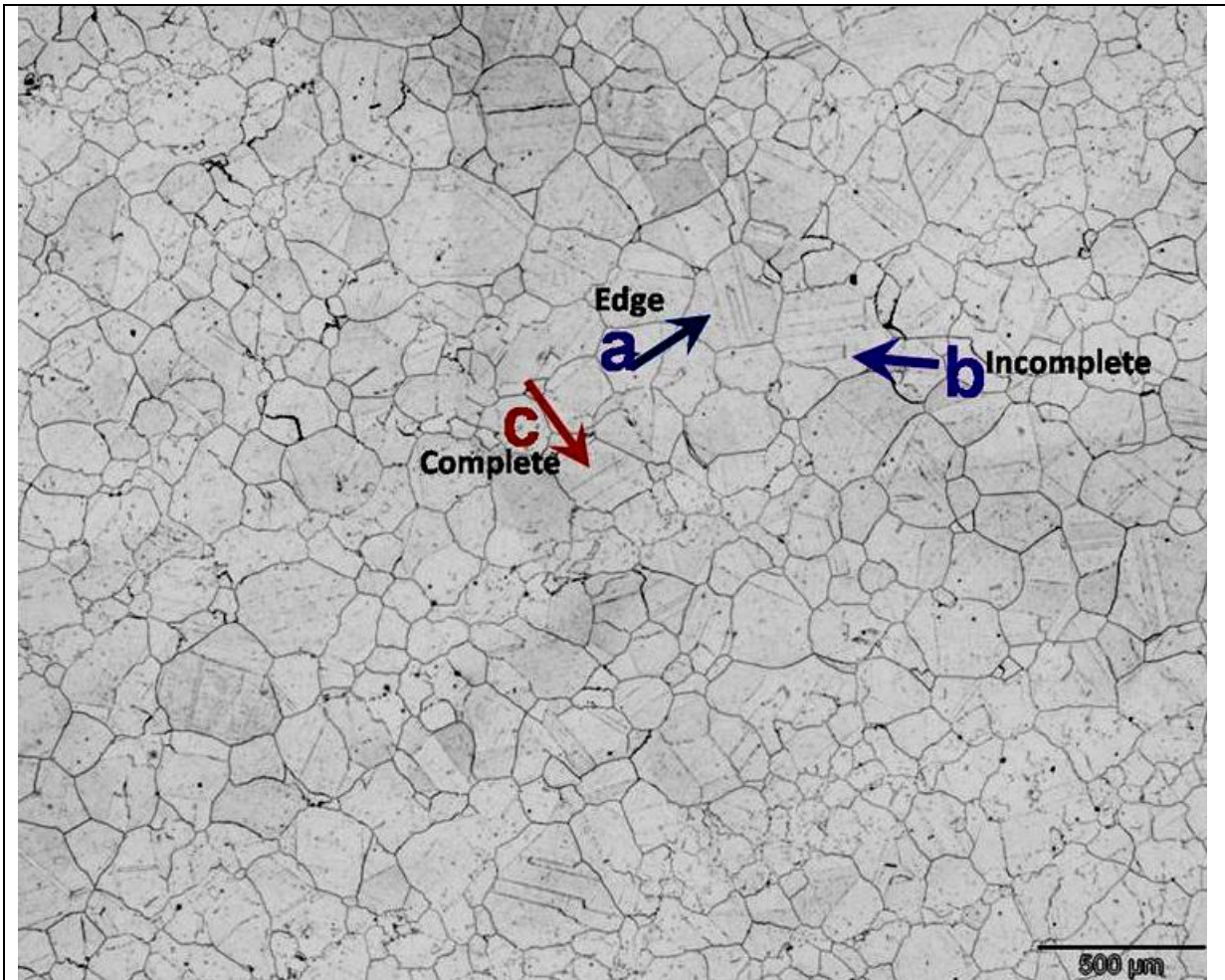
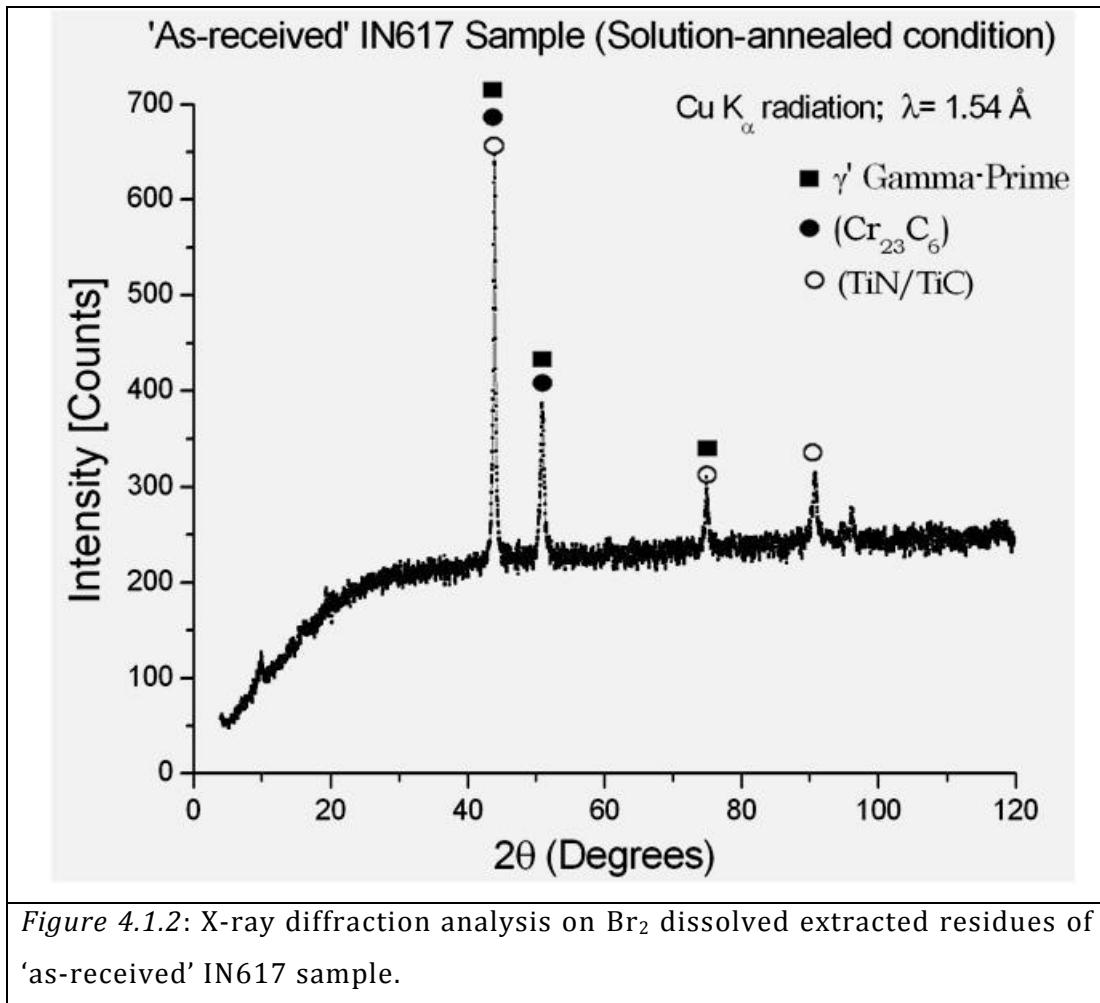


Figure 4.1.1: Optical micrograph of 'as-received' (solution-annealed) IN617 shows the grain structure, fine intra- and intergranular precipitates (dark points) and annealing twins (arrowed). The annealing twins are of edge, incomplete and complete types, as shown in micrograph.

4.1.2 Phase Identification

The exact nature of the precipitates was identified through X-ray powder diffraction analysis on electrolytic and Br₂ dissolved extracted residues of carbides, nitrides and intermetallics. Both techniques registered similar types of peaks in X-ray pattern. The resultant X-ray pattern was analysed by comparing experimental diffraction data with standard (JCPDS) diffraction data. It was observed that some potential precipitate peaks overlapped with the austenitic γ -matrix peaks.

PeakFit® software was used to separate the peaks. X-ray diffraction pattern analysis of the 'as-received' sample is shown in *Figure 4.1.2*.



The phases are identified as γ'-gamma prime, Cr₂₃C₆ and TiN/TiC by analysis of the XRD traces. The term M₂₃C₆ is a more general notation for Cr₂₃C₆, as often elements such as Ni, Mo, and Co, are found to substitute partially for chromium. M₂₃C₆ is referred to in many places of this work in place of the Cr-rich precipitate Cr₂₃C₆.

The nature of phases and their identification were further accomplished by the EDX measurements in transmission electron microscopy (TEM) and the analysis of selected area electron diffraction (SAED) patterns, discussed later in this chapter.

4.1.3 Precipitate Morphology and its Location

The role of precipitate morphology and its precipitation influences the creep-rupture behaviour of high temperature nickel base alloys. In this section precipitate morphology and their locations are discussed, for the solution-annealed 'as-received' sample. A backscattered electron (BSE) SEM micrograph in *Figure 4.1.3* shows the precipitates in the 'as-received' sample.

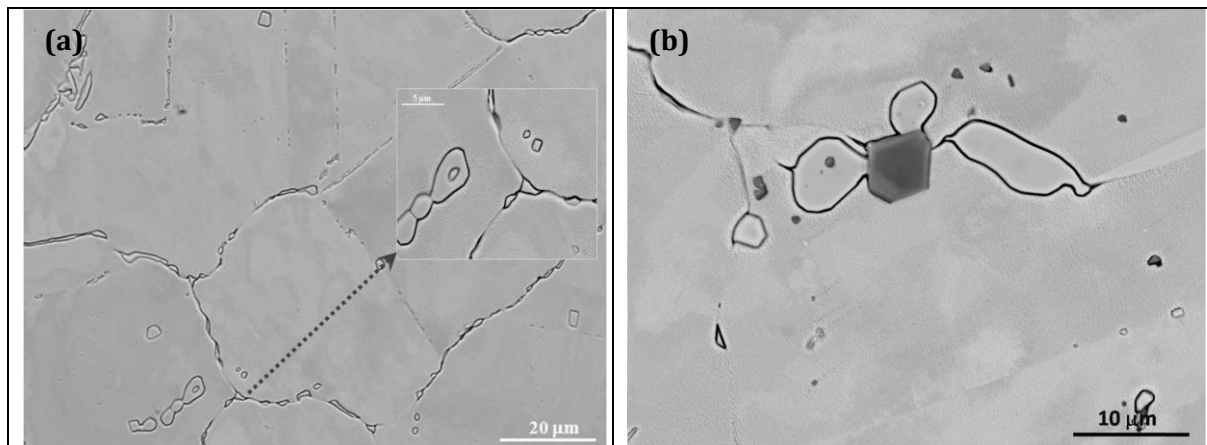


Figure 4.1.3: Scanning electron micrographs of 'as-received' IN617. In (a) Inset micrograph is magnified image of triple point at where Cr-rich precipitate is situated (arrowed) and (b) Ti-rich precipitates found randomly in the matrix.

The atomic number (or Z) contrast mechanism that produces BSE images shows that some precipitates have a higher average Z than the austenite grains, whereas some, appearing dark in the image, have a lower average Z than the austenite. EDX spectra acquired from these precipitates indicated the high- Z and low- Z phases were enriched in Cr and Ti, respectively. These therefore, appear as $M_{23}C_6$ -type Cr enriched phase and an $M(C, N)$ -type Ti enriched phase. In the SEM, EDX spectra were measured from these precipitates and quantified for elemental analysis using a standardless approximation. These precipitates were found both intra- and intergranularly in the specimen. Their morphology varied from a regular to a totally irregular morphology. They are the primary precipitates, and beneficial to creep properties. The typical elemental composition of these precipitates was measured by EDX, is shown in *Table 4.1.3.1*.

$M_{23}C_6$	Cr-30.6Mo-12.3Ni-4.4Co-7.2Ti
Ti (C,N)	Ti-1.8Cr

The precipitation strengthening phase in the austenitic gamma (γ) matrix was ordered intermetallic gamma prime (γ') precipitates. Their morphology and locations were identified using transmission electron microscopy, and are discussed in the next section. The shape and size of the coherent precipitates of γ' were identified as spherical, and varied from 10nm to 15nm. The size of Cr-enriched ($M_{23}C_6$) precipitates varied in size from less than 1 μ m to 6 μ m. The size of the Ti-enriched precipitate varied from 2 μ m to 10 μ m. The precipitate morphology and their locations and area fractions, in the 'as-received' specimen after solution-annealed are listed in Table 4.1.3.2. The area fraction was estimated as discussed in section 3.6. The precipitates size shown here is the average of the size measured on more than 50 BSE micrographs and 20 TEM micrographs. The average standard error in the measurement was in range from 1.1 to 1.5%.

Specimen ID	Precipitate location	Precipitates Morphology			
		Phases	Size	Shape	Area fraction (%)
As-received	throughout the matrix	γ' - Ni ₃ (Ti, Al)	10-25nm	Spherical	8
	Intra- and inter-granularly, twin boundary	Ti (C,N)	<1-10 μ m	regular to totally irregular geometry	0.3
		$M_{23}C_6$	<1-6 μ m		1.4

Precipitates of size less than 1 μ m were situated intergranularly and some larger particles were observed within the grains. The blocky particles of Ti-enriched phase, of M(C, N) type carbo-nitrides were randomly distributed in the matrix and at twin boundaries. XRD analysis confirmed that the precipitates of Cr-rich and Ti-rich are $M_{23}C_6$ carbides and Ti (C, N) respectively. Carbides were present in the matrix and at the grain boundaries. A discrete carbides network along the grain boundaries was observed in Figure 4.1.3. Energy dispersive X-

ray microanalysis (EDX) showed that the grain boundary precipitates were mostly rich in chromium. The blocky particles M(C, N), were mainly composed of titanium.

Precipitates at prior austenitic grain boundaries play an important role in metallurgical stabilization of the microstructure during creep and thermal exposure. They also act as barriers for moving dislocations as do grain boundaries. The effectiveness of precipitates in hindering the movement of dislocations is dependent on the morphology, size, volume fraction and orientation with the direction of dislocation motion. Precipitate morphology, fraction and location depend upon the creep exposure temperature, strain and creep duration.

4.1.4 Transmission Electron Microscopy (TEM) Observations

The microstructure of the as-received IN617 sample has been analysed using analytical transmission electron microscopy and the results are presented in this section. The precipitates of different phases shown in *Figure 4.1.3* are further identified using selected area electron diffraction patterns and energy dispersive X-ray spectrometry (EDX), in TEM. The microstructure of the 'as-received' sample consists of a γ -austenitic matrix with coherent precipitates of γ' , and semi coherent dominant precipitates of $M_{23}C_6$ (M = Cr, Mo, Co) and Ti (C, N), with arrays of dislocations. These precipitates were mainly located at austenitic grain boundaries and sub-grain boundaries and also appeared randomly within the matrix. The morphological geometries of these precipitates are discussed in the following subsections. A typical precipitate-dislocation interaction and symmetric precipitates are shown in *Figure 4.1.4*.

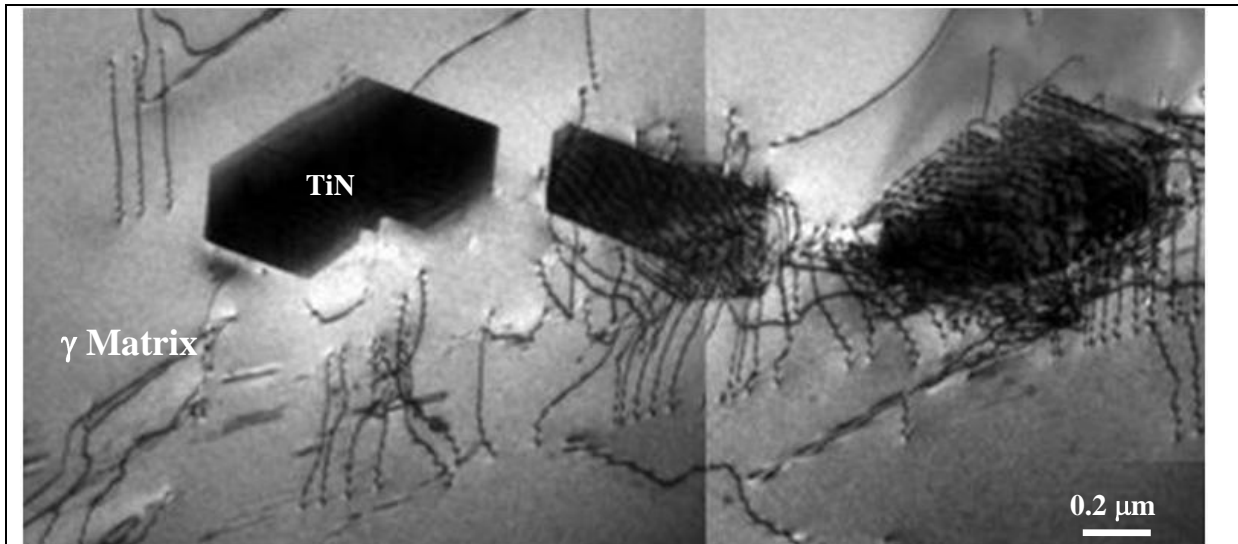
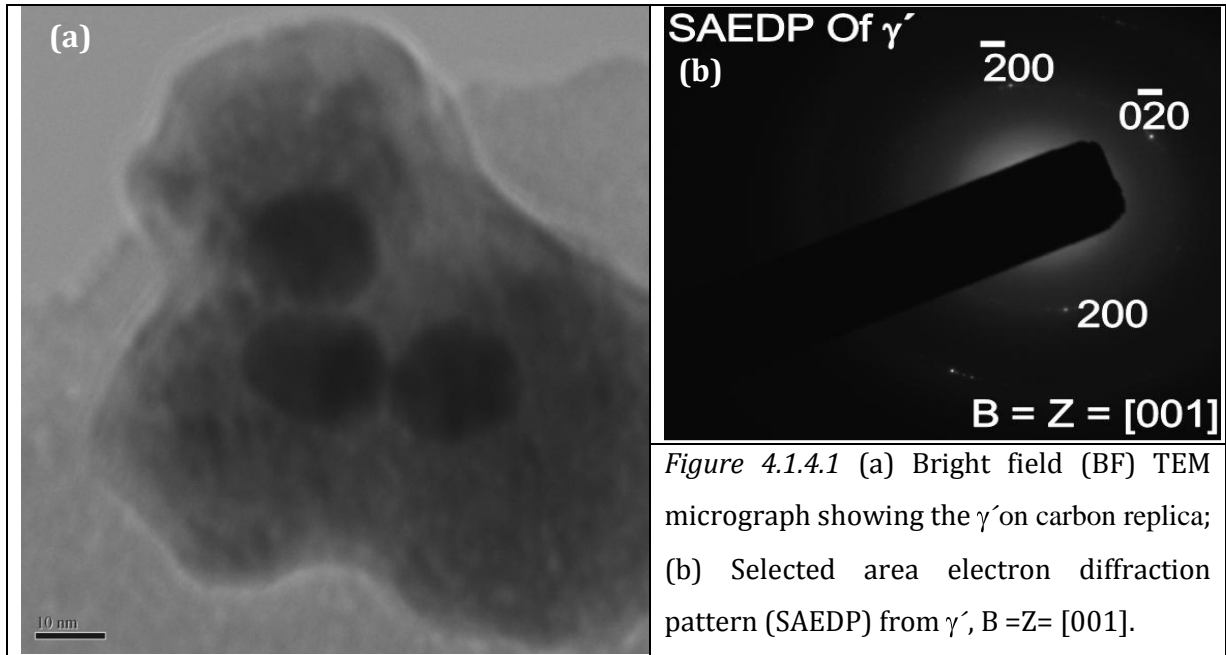


Figure 4.1.4. Montage of BF-TEM micrographs of solution-annealed as-received IN617 alloy illustrating the dislocation structure, precipitate particles and dislocation-particle interactions in the solid solution strengthened austenitic γ - matrix.

4.1.4.1 Gamma Prime

Gamma prime (γ') is a strongly ordered intermetallic, stable up to its melting point and having a cubic-primitive centre crystal structure ($L1_2$). The γ' precipitate coherent interfaces were in a cube-to-cube orientation relationship with the γ -matrix as $111_{\{\text{matrix-}\gamma\}} \parallel 111_{\{\gamma'\}}$. TEM micrographs showed that the matrix was found to consist of face centered cubic austenitic - γ , and a fine distribution of hardening phase - γ' . It was difficult to resolve the gamma prime in thin foil; however the carbon replica technique would be able to extract some of the fine γ' precipitates. *Figure 4.1.4.1* shows TEM micrograph of fine γ' precipitates and the selected area diffraction pattern acquired from these precipitates. The reflections from γ' and indexed pattern are shown in *Figure 4.1.4.1b*. The beam direction was along $B = [001]$.



XRD spectra were used to find the lattice parameter (a_0) of fine distribution of γ' precipitates as $a_0 = 0.36$ nm. Its typical cube-on-cube crystallographic relationship with austenitic γ matrix provides precipitation hardening at high temperature creep exposure.

4.1.4.1 (a) Volume fraction of Gamma Prime

The method for volume fraction estimation of gamma prime precipitates is discussed in previous section 3.7. The thickness (h) of carbon film was measured from the AFM and found in range of 18-24nm. The estimation was conducted on 20 TEM images and the estimated typical value is shown in *Table 4.1.4.1*.

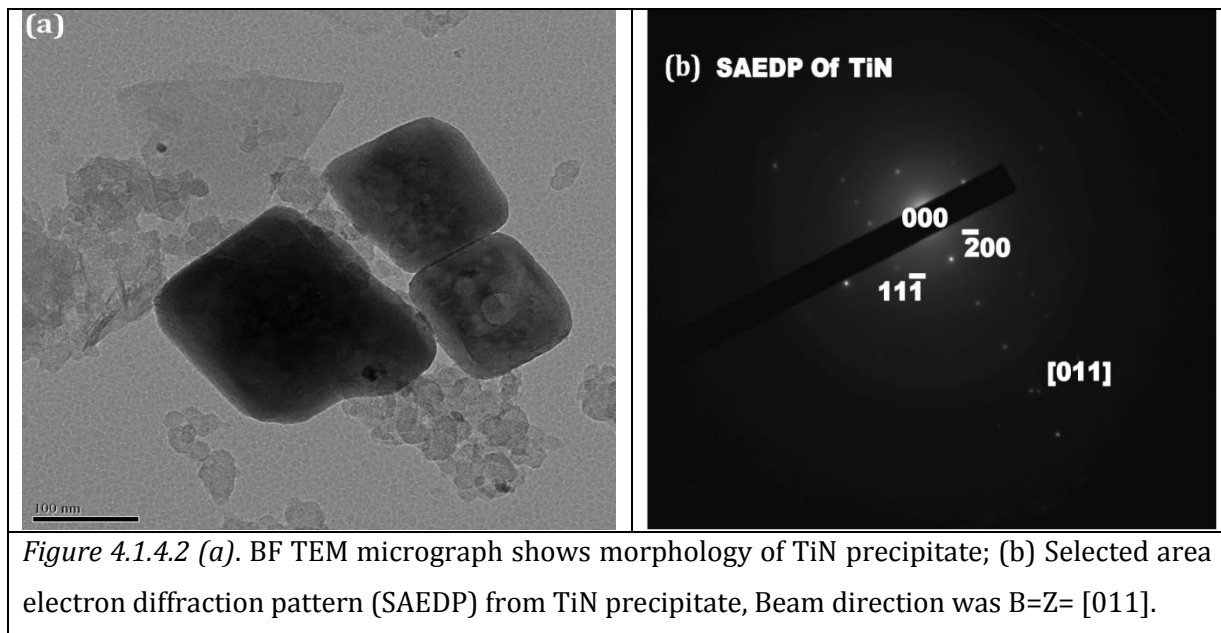
Table 4.1.4.1: Estimated values of volume fraction in as-received Inconel 617

Diameter (2R, nm)	$A_{ext} = \frac{N\pi R^2}{A_0}$	A_0 (nm ²)	$A_f = 1 - \exp(-A_{ext})$	$V_f = 1 - (1 - A_f)^{\frac{4R}{3h}}$
20	0.155	8100	0.145	0.079

The volume fraction of gamma prime in this specimen was estimated approximately 8%. The error in the measurement was 1.3%.

4.1.4.2 TiN

Ti-enriched precipitates in the 'as-received' sample, (noted in *Figure 4.1.3*), were examined in the TEM. *Figure 4.1.4.2* shows a bright field (BF) transmission electron micrograph of Ti-enriched precipitates, in the solution-annealed 'as-received' Inconel 617 sample.

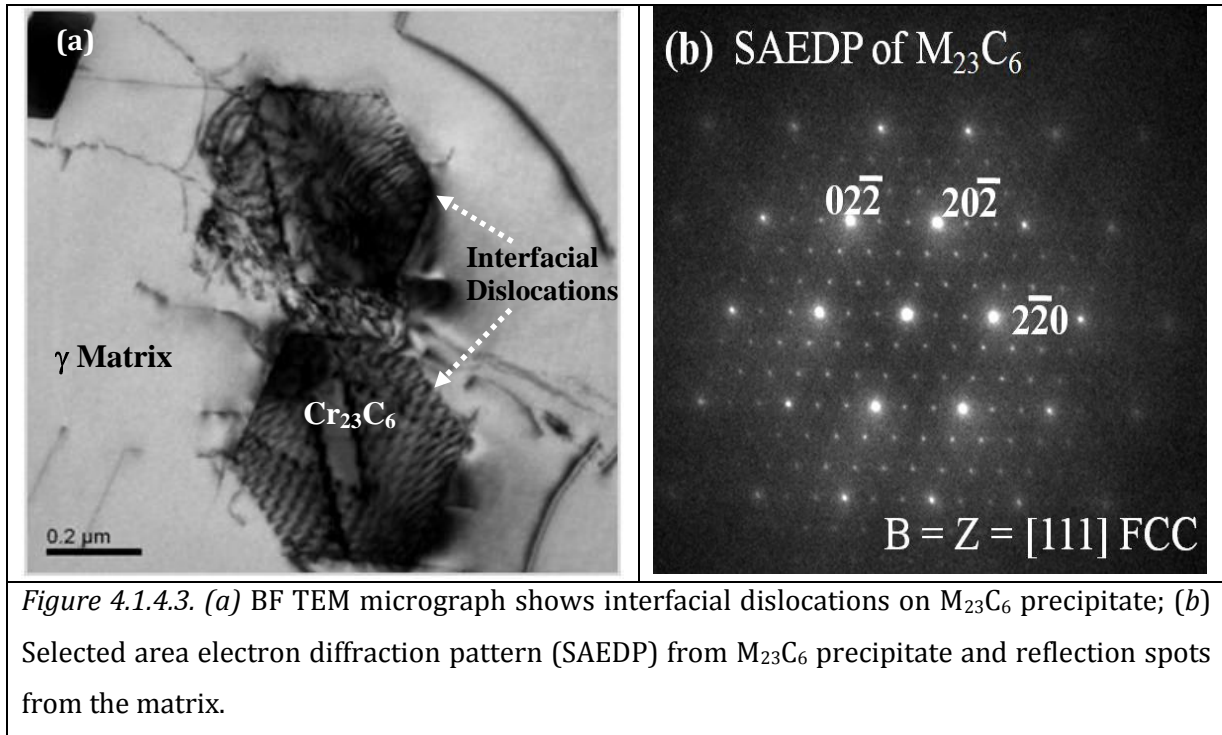


Selected area electron diffraction pattern (SAEDP) identified these precipitates as TiN. The beam direction and zone axis were along the [011] direction. An indexed selected area diffraction pattern acquired from the TiN precipitate is shown in *Figure 4.1.4.2b*.

4.1.4.3 $M_{23}C_6$

$M_{23}C_6$ precipitates have a complex FCC structure. They form during heat-treatment from the degradation of M(C, N) carbo-nitrides and reaction of chromium with soluble residual carbon in the alloy matrix. The precipitates of $M_{23}C_6$ are shown in *Figure 4.1.4.3*. They usually occur at grain boundaries, along twin bands and boundaries, at twin ends and occasionally occur in the grain interior. The approximate composition of $M_{23}C_6$ precipitate has Cr-5.9Co-26.1Ni-14.7Mo (wt%). The discrete particles of $M_{23}C_6$ influence the high temperature properties of the alloy through the inhibition of grain-boundary sliding. Interfacial dislocations can also be observed in the micrograph (*Figure 4.1.4.3*). Interfacial dislocations are lying on

semi-incoherent precipitates forming an interface-inter-phase boundary (*Figure 4.1.4.3a*). The SAEDP shows the orientation relationship between the Cr_{23}C_6 and the austenitic γ phase, since the crystallographic close packed directions are parallel (*Figure 4.1.4.3b*).



Electron diffraction patterns obtained from the grain boundary precipitates show that they are M_{23}C_6 (rich in Cr, *Figure 4.1.4.3b*) having lattice parameter $a_0 = 10.6 \text{ \AA}$.

4.1.4.4 Quantitative Measurements of Dislocation density

The dislocation structure observed in thin foil samples was approximately representative of the bulk material. Great care and extra precautions have been taken during the handling and thinning of foils, to minimize dislocations introduced during the thinning. The measurement of dislocation density was based on twenty micrographs, using $\langle 001 \rangle$ orientation from different areas of the foil, taken at different magnifications from 7,000 to 12,000. These magnifications were high enough to resolve the individual dislocations. The arrays of dislocations and piling-up of dislocations near to grain boundary and around precipitates can be seen in *Figure 4.1.4.4*.

The dislocation density (Ham, 1961; Hirsch et al, 1977; Hambleton et al, 1997; Yang & Bhadeshia, 1990) was obtained from *equation 4.1.4.4*:

$$\rho_d = 2Nm k/Lt \quad (4.1.4.4)$$

where N is the number of dislocations intersecting a circle of circumference L , m is the magnification of print, t is the foil thickness and k accounts for the number of dislocations which are not visible in the image for a given operating condition; for the $\{220\}$ reflection used throughout, $k = 6/5$.

Foil thickness was estimated by counting extinction contours. The foil thickness is given by *equation 4.1.4.4a*. Typical values of η_g , ξ_g , and t are listed in *Table 4.1.4.3*.

$$t = \eta_g \xi_g \quad (4.1.4.4a)$$

where η_g is the number of extinction fringes observed at an inclined boundary when the diffracted beam is represented by the reciprocal lattice vector g . The ξ_g is the extinction distance for that g vector and accelerating voltage.

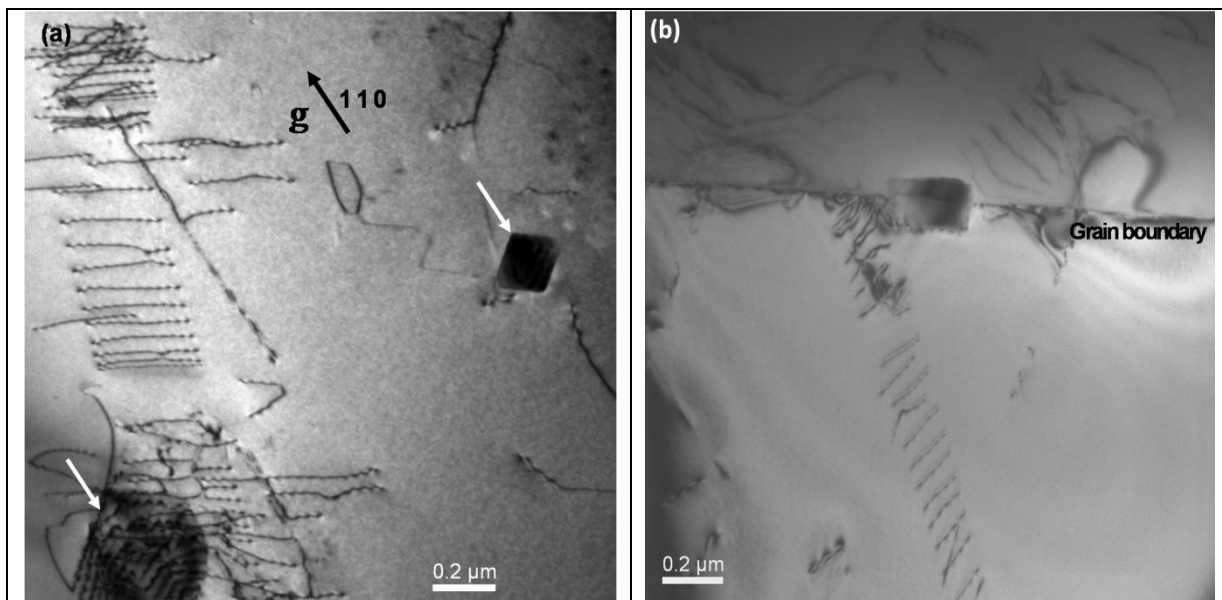


Figure 4.1.4.4: BF TEM micrographs illustrating (a) dislocation structure, precipitates particles and dislocation-particle interactions (b) dislocations piled up at the grain boundary.

<i>Table 4.1.4.4: Typical values for η_g, ξ_g, t and ρ_d</i>			
η_g	ξ_g (Å) at 200kV	t (Å)	ρ_d (lines/m ²)
5	299.25	1496.24	6.8 X 10 ¹²

The average value of dislocation density was found to be $6.8 \pm 3.2 \times 10^{12}$ lines/m². This estimated value of dislocation density is the average of the twenty TEM images and the standard error was 3.2. The value found appears to be reasonable, but no values of dislocation densities for these materials were found in the literature search. The methodology used here is the same as has been used for obtaining dislocation densities in steels and aluminium (Ham, 1961; Hirsch et al, 1977; Hambleton et al, 1997; Yang & Bhadeshia, 1990).

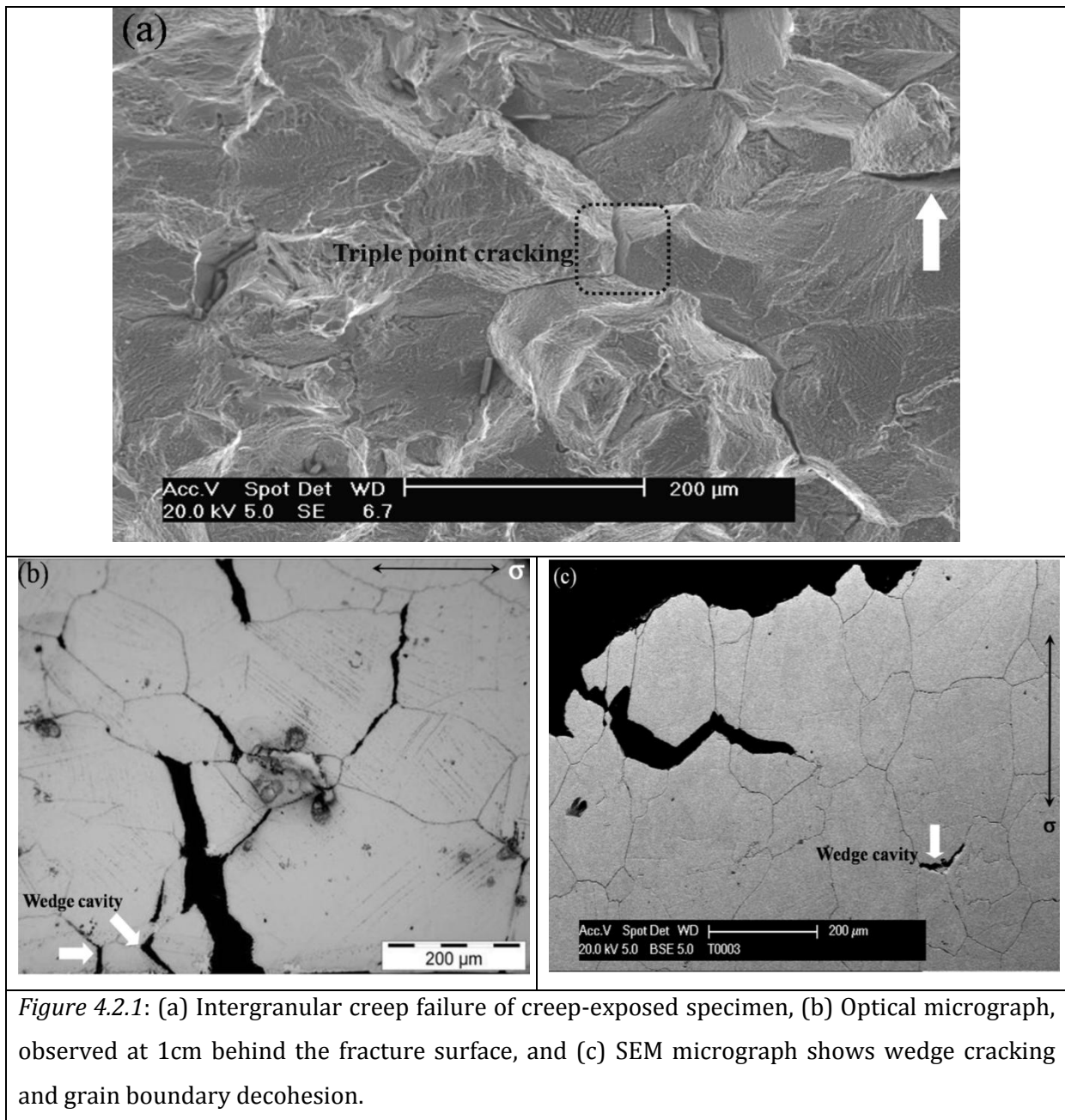
4.2 'Creep-exposed specimen' (T0003) (650°C/ 574Hrs / 350MPa)

Heat-treated Inconel 617 specimen was creep tested at 650°C in air under a uniaxial load of 350MPa (estimated stress value from creep data of IN617, Ennis et al 2007). This specimen ID: T0003 fractured after 574 hours of creep duration. The area reduction was measured as 17.6%.

4.2.1 Fractography

The failure mechanism of the creep fractured specimen was analyzed using scanning electron microscopy and optical microscopy. A fractograph of the creep failed specimen, T0003 is shown in *Figure 4.2.1a*.

The failure mechanism was intergranular fracture by decohesion of the grain boundaries. Intergranular creep fracture involves the nucleation, growth and subsequent linking of voids at grain boundaries to form two differing types of cavities, wedge type cavities and isolated type cavities. Wedge type cavities are associated with cracking at grain boundary triple points and form by grain boundary sliding. The formation of cavities is controlled by diffusion-controlled processes (Kassner and Hayes, 2003). Triple point wedge cracking (marked) and creep cavitation (arrowed) are shown in *Figure 4.2.1(a)*. The failure mechanism of the specimen was further confirmed by optical and scanning electron microscopy of a polished cross-section of the fractured surface. *Figure 4.2.1(b) & (c)* shows further confirmation of wedge cracking, decohesion and crack propagation along the grain boundaries in the creep-exposed specimen. The direction of loading is shown by the arrows in *Figure 4.2.1*. The open cracks intruded inside the specimen to a depth of 100 to 500µm.



4.2.2 Grain Morphology

The austenitic grain structure of 'creep-exposed IN617' specimen is shown in *Figure 4.2.2*. The optical microstructure of the creep-exposed specimen shows an equiaxed austenitic γ -grain structure with an average size of 158 μm . The grain orientation has been shown to be random. Annealing twins and twinning boundaries are observed in a number of grains. Twins have broad faceted appearance, similar to the 'as-received' specimen.

Twin boundaries are observed as flattened and straighter in sides, however in a few areas of the micrograph they are observed as steps (*Figure 4.2.2*). They have a special orientation relationship with the grains and are formed at the grain boundaries. Serrated grain boundaries are observed (arrowed) in *Figure 4.2.2*, after creep exposure duration of 574H at 650°C. Edge, incomplete and complete- types of twins were as common as ‘as-received’ specimen. Grain boundary thickening controls the intergranular deformation mechanism at elevated temperature. This specimen has shown grain boundary thickening (*Figure 4.2.2*).

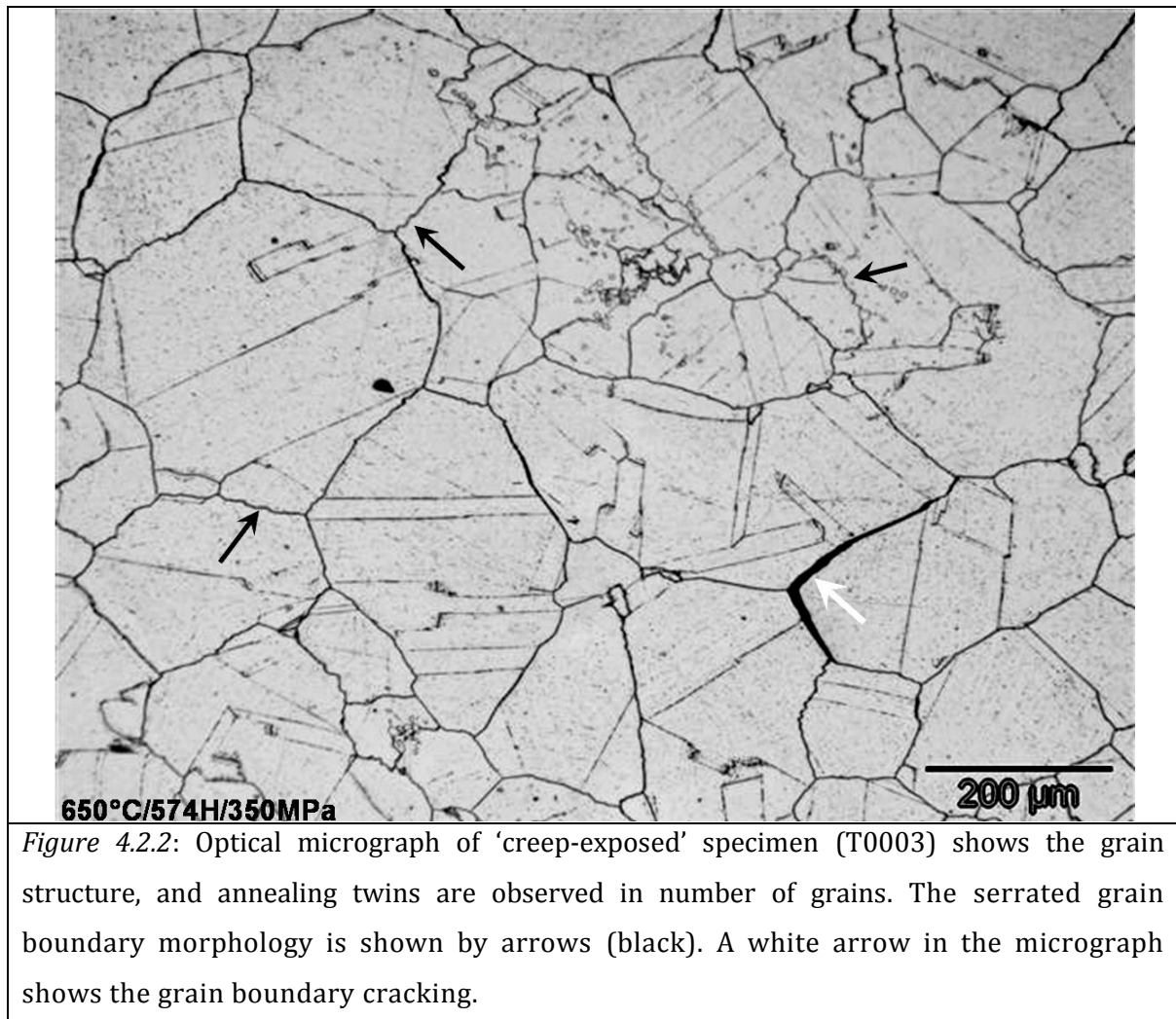


Figure 4.2.2: Optical micrograph of ‘creep-exposed’ specimen (T0003) shows the grain structure, and annealing twins are observed in number of grains. The serrated grain boundary morphology is shown by arrows (black). A white arrow in the micrograph shows the grain boundary cracking.

A summary of the morphology of grains, grain boundary and average hardness of the head and gauge is listed in *Table 4.2.2*. The gauge length hardness substantially increased to average value

of 334Hv whereas head had average hardness of 229Hv. Here, it may be assumed that the major effect on the specimen head is from the thermal effects with minimal effect from stress, therefore, the hardness is lower than that measured along the gauge length.

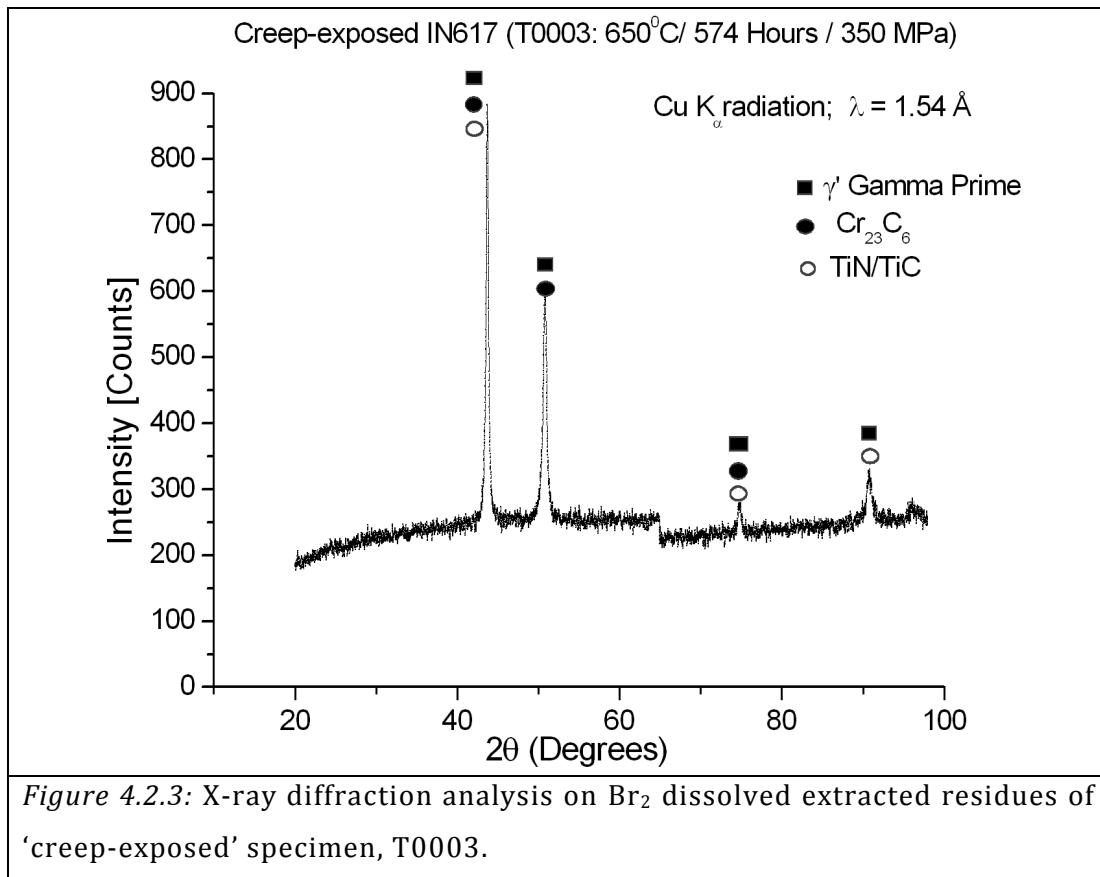
Creep-exposed (650°C/574 Hrs /350MPa)	Grain Morphology			VHN (H _v /20)		Grain- boundary morphology
	Grain-size range (μm)	Avg. grain size (μm)	Grain shape	Head	Gauge	
	46 to 544	158	Equiaxed	229	334	

The materials get hardened during creep exposure from the precipitation of fine carbides of M₂₃C₆ type, from the combined effect of stress and temperature. At elevated temperature there is an increasing tendency for the matrix to soften with continued exposure time due to carbide dissolution and coarsening. This specimen fractured and the test discontinued in a short period (574 H), due to high level stress on the specimen.

4.2.3 Phase Identification

The precipitates were identified through X-ray powder diffraction analysis. XRD was conducted on electrolytic and Br₂ dissolved extracted residues from alloy specimen. The potential precipitate's peaks overlapped with the austenitic γ-matrix peaks were identified using PeakFit® software. An X-ray diffraction pattern analysis of 'creep-exposed' specimen is shown in *Figure 4.2.3*. The precipitates in the creep-exposed specimen were identified as γ'-gamma prime, Cr₂₃C₆ and TiN/TiC by analysis of the XRD traces, similar to the as 'as-received' specimen.

The phases were further identified by using EDX measurements in transmission electron microscopy (TEM) and by analysis of selected area electron diffraction (SAED) patterns, discussed later in this chapter.



4.2.4 Precipitate Morphology and Location

The precipitate morphology and their locations are discussed in this section. A backscattered electron (BSE) SEM micrograph (*Figure 4.2.4*) shows the evolutions of precipitates in creep-exposed specimen at 650°C. The atomic number (or Z) contrast mechanism that produces BSE images derives that some precipitates have a higher average Z than the austenite grains, whereas some, appearing dark in the image, have a lower average Z than the austenite. EDX spectra acquired from these precipitates indicated the high-Z and low-Z phases are enriched in Cr and Ti, respectively. These therefore, appear as M₂₃C₆-type Cr enriched phase and M(C, N)-type Ti enriched phase. EDX spectra were quantified for elemental analysis using a standardless approximation. The elemental composition of the precipitates was measured by EDX as is shown in *Table 4.2.4.1*. The precipitates were found both intra- and intergranularly in the creep-exposed specimen. Their morphology varied from a regular to a totally irregular morphology.

Table 4.2.4.1: Typical composition of observed phases in creep-exposed condition (T0003) by EDX (wt.%)

$M_{23}C_6$	Cr-28.5Mo-12.9Ni-3Co-2Ti
Ti (C,N)	Ti-1.7Cr

The size of Cr-enriched precipitates varied from $1\mu\text{m}$ to $17\mu\text{m}$. The size of Ti-enriched precipitate varied from $0.25\mu\text{m}$ to $18.75\mu\text{m}$. The Cr-precipitates are extensively precipitated along the grain and twin boundaries in the creep-exposed specimen.

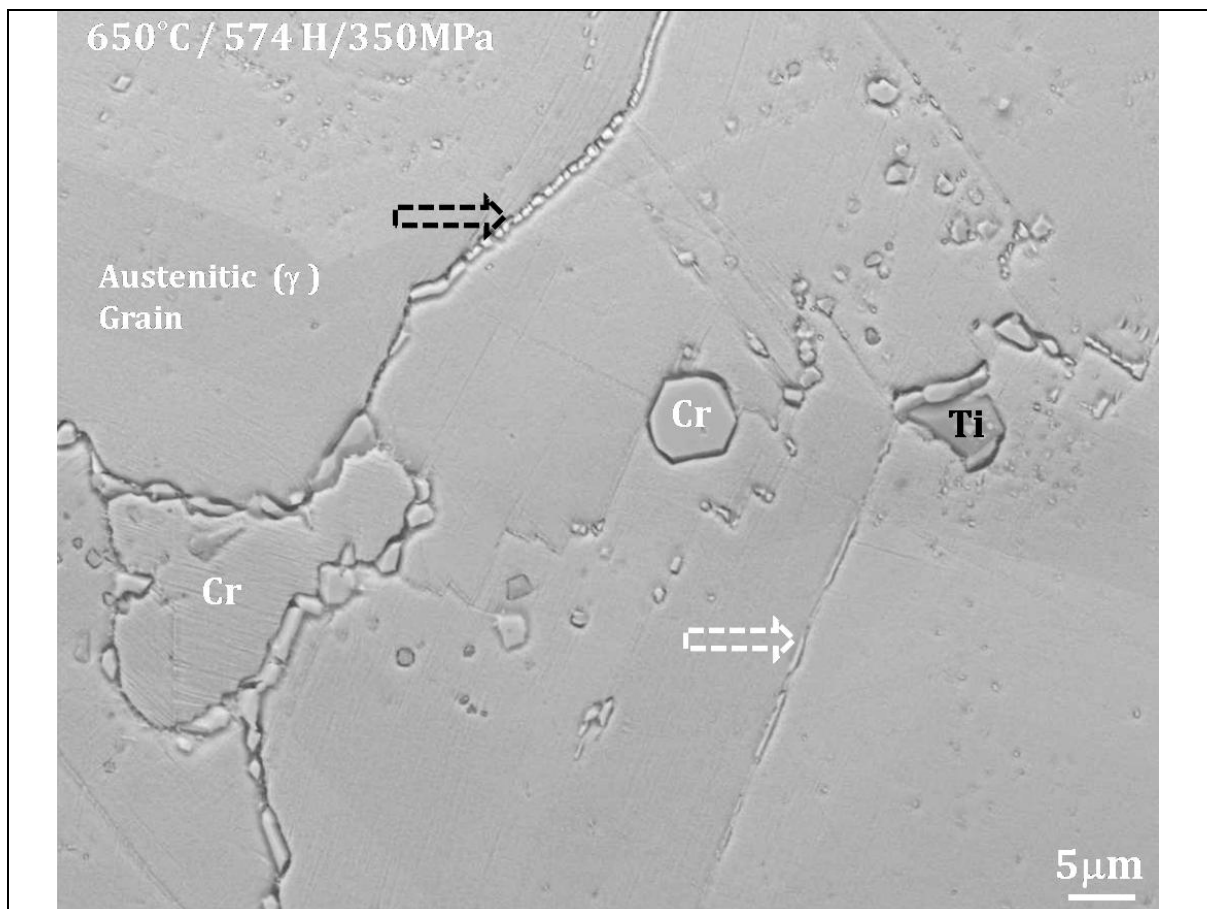


Figure 4.2.4: Scanning electron micrograph of the creep-exposed specimen. The blocky shape (darker contrast, marked 'Ti') near the twin boundary (marked with a white arrow) is Ti-rich phase, TiN; faceted particles (marked 'Cr') are distributed intragranularly, at triple junctions and also decorating the grain boundary (black arrow), and twin boundaries (white arrow) are Cr-rich phase, $Cr_{23}C_6$.

The major precipitates found in the gauge length after creep exposure is shown in *Table 4.2.4.2*. The standard error in the measurement was 2.1-3.3%.

Table 4.2.4.2: Precipitates morphology and location after creep exposure at 650°C

Specimen ID	Precipitate location	Precipitates Morphology			
		Phases	Size	Shape	Area fraction (%)
T0003	throughout the matrix	γ' - Ni ₃ (Ti, Al)	10-65nm	Spherical	6.0
	Extensive precipitation of Cr-enriched carbides (M ₂₃ C ₆) on grain boundaries and twin boundaries	Ti (C, N)	0.25-19 μ m	Regular to totally irregular geometry	0.4
		M ₂₃ C ₆	<1-17 μ m		4.3

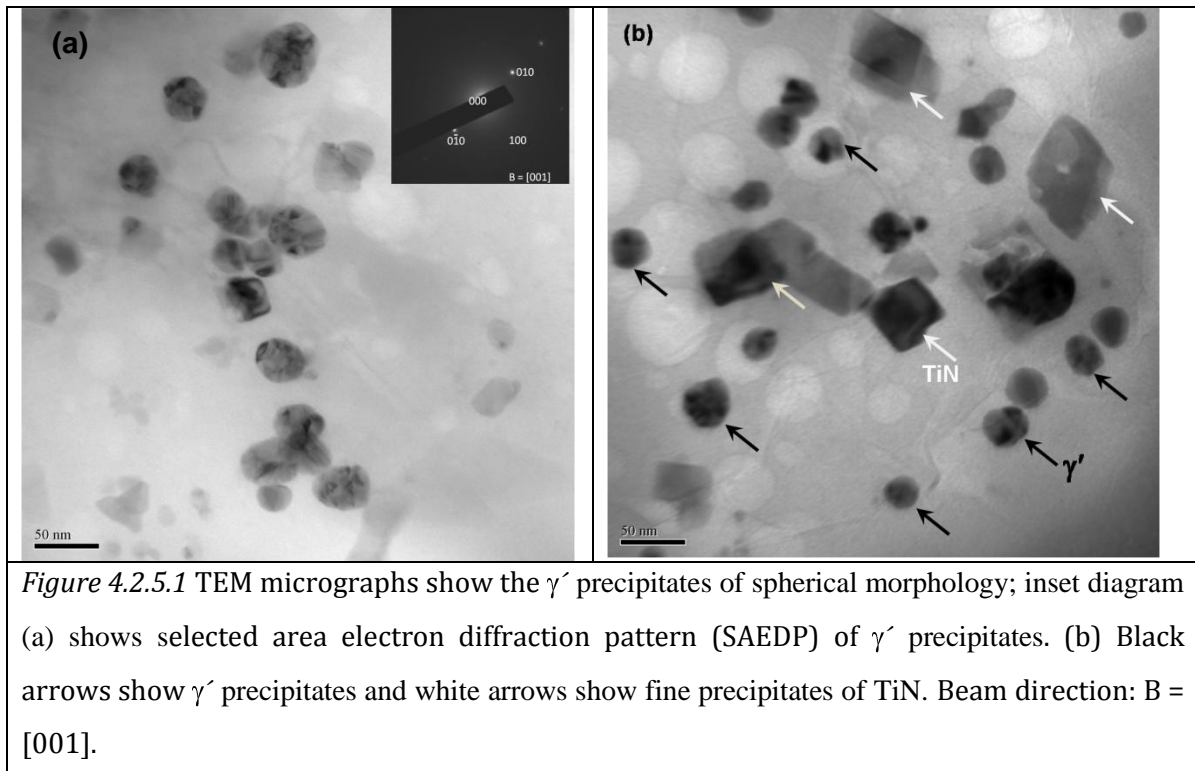
The precipitation strengthening phase in austenitic gamma (γ) matrix is ordered intermetallic gamma prime (γ') precipitates. Their morphology and locations were identified using transmission electron microscopy, and are discussed in the next section. The shape and size of the coherent precipitates of γ' were identified as spherical and varied from 10nm to 65nm.

4.2.5 Transmission Electron Microscopy (TEM) Observations

The microstructure of 'creep-exposed IN617 specimen (T0003; 650°C/574Hours/350MPa) was analysed using analytical transmission electron microscopy and the results are presented in this section. The phases noted in *Figure 4.2.4* were further identified using selected area electron diffraction patterns and energy dispersive X-ray spectrometry (EDX), in TEM. The microstructure of the 'creep-exposed' specimen consists of γ -austenitic matrix, coherent precipitate of γ' , and semi coherent dominant precipitates of M₂₃C₆ (M = Cr, Mo, Co) and Ti (C, N), with an array of dislocations. These semi-coherent precipitates were mainly located at prior austenite grain boundaries and sub-grain boundaries and also appear randomly within the matrix. The morphological geometries of the precipitates were discussed in previous section and further discussion continued in the following subsections.

4.2.5.1 Gamma Prime (γ')

Finely dispersed γ' precipitates strengthen the grains at high temperature. However, this γ' coarsens during service exposure condition, which reduces high temperature strength. Additionally, exposure at higher temperature and higher stress accelerates the coarsening behaviour. Creep exposed specimen (T0003; 650°C/574Hours/350MPa) was examined in the TEM. The morphology of the γ' precipitates was spherical shape and their average size varied from a minimum 10nm to a maximum 65nm with an average size of 42nm. Their morphology is shown in *Figure 4.2.5.1*.



The reflections from γ' and their indexed planes are shown in inset micrograph in *Figure 4.2.5.1*.

The beam direction was along B= [001].

4.2.5.1 (a) Volume fraction of Gamma Prime

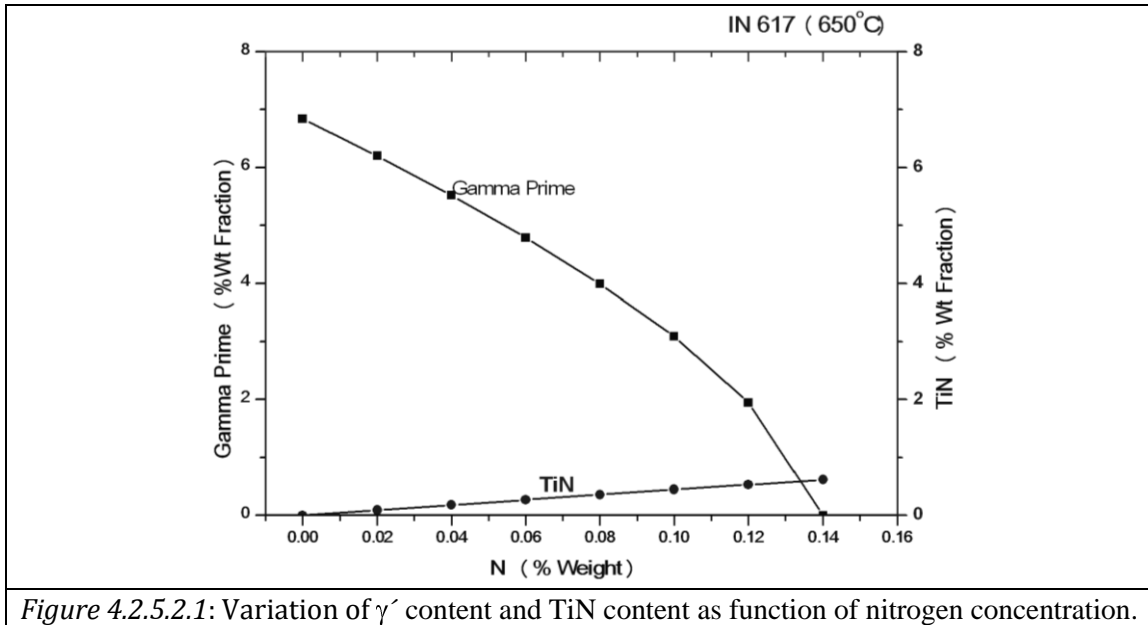
The method for volume fraction estimation of gamma prime precipitates is discussed in previous section 3.7. The thickness of carbon replica was measured using AFM. The carbon replica thickness (h) was in range from 18-24nm. The estimation was taken on 20 TEM images and the estimated typical value is shown in *Table 4.2.5.1*.

Average Diameter (2R, nm)	$A_{ext} = \frac{N\pi R^2}{A_0}$	A_0 (nm ²)	$A_f = 1 - \exp(-A_{ext})$	$V_f = 1 - (1 - A_f)^{\frac{4R}{3h}}$
42	0.056	116506.2	0.0549	0.0598

The volume fraction of gamma prime in this specimen was estimated approximately 6%, i.e smaller than that seen in the as-received specimen. The standard error in the measurement was 2.2%.

4.2.5.2 TiN

The precipitation of carbo-nitrides and nitrides occurred during the creep exposure. The gamma prime, Ni₃ (Ti, Al) precipitate dissolved and carbo-nitride of titanium formed. *Figure 4.2.5.2.1* shows the Thermo-calc result on the effect of nitrogen content in the alloy on its weight% of γ' and TiN. The residual nitrogen content in the alloy matrix is critical in determining the wt.% of strengthening phase, γ' : Ni₃(Ti, Al), in the alloy matrix. A low nitrogen content (< 0.2 wt.%) in the alloy does have a significant effect on the weight% of γ' . However, on increasing nitrogen content in the alloy through atmospheric diffusion, the weight% of TiN increases due to nucleation of secondary TiN of size less than 0.1 μ m. The necessary titanium diffuses out from the γ' to form TiN, and therefore that may be one reason for reduction in weight% of γ' precipitates in the matrix. That leads to weakening of the matrix.



TiN is one of the predominant phases present at higher concentration of N in the alloy. However, the weight% of Ti is 0.48 in this alloy and titanium diffusing from the γ' is important in decreasing its volume fraction in the alloy. The fine distribution of Ti (C, N) cuboidal particles contributing to hardness in this specimen and has shown harder than the 'as-received' specimen. The fine distribution of cuboidal Ti (C, N) particles is shown in *Figure 4.2.5.2.2*.

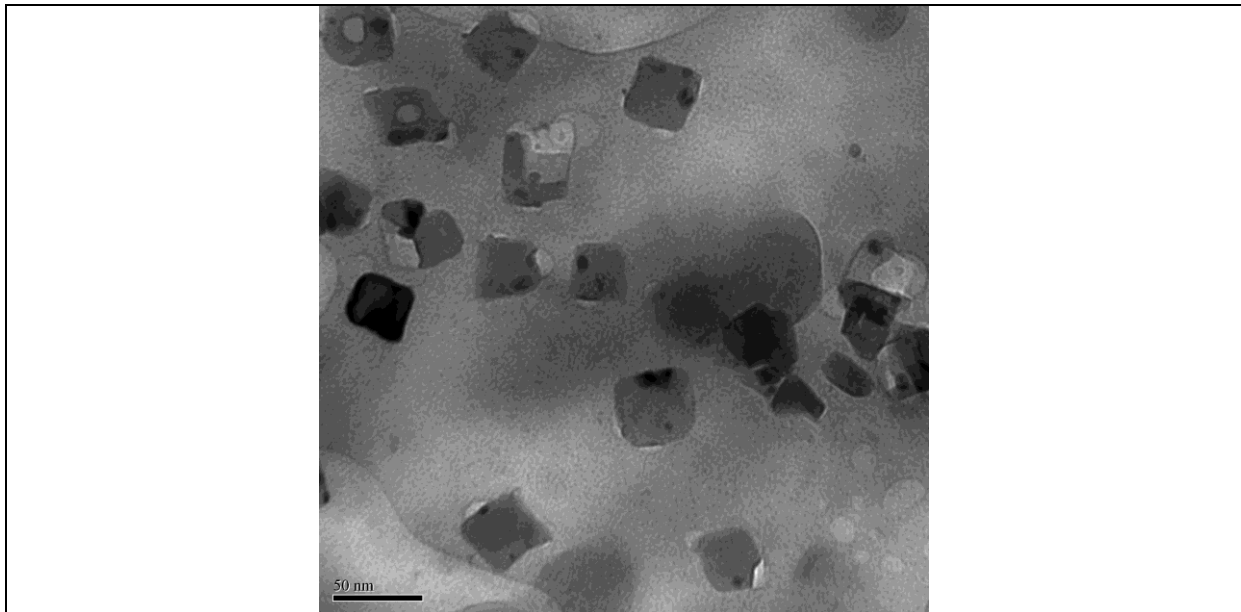
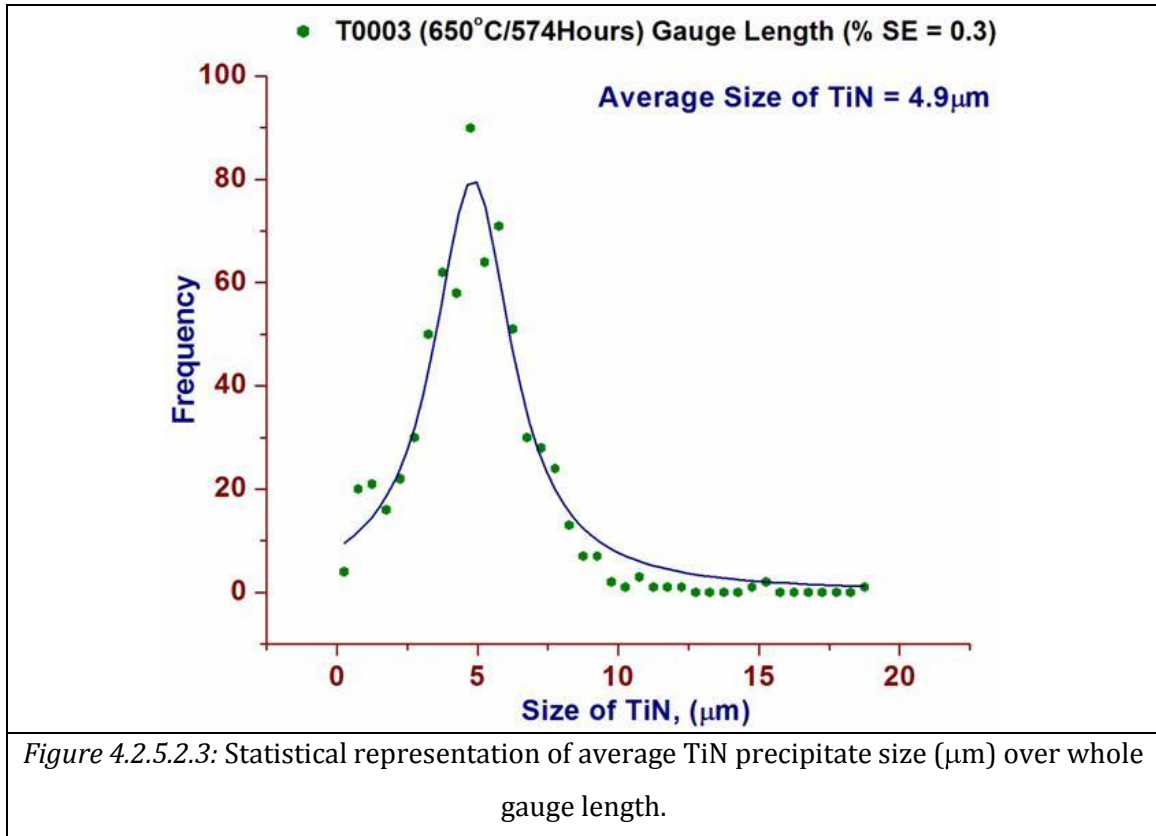


Figure 4.2.5.2.2: BF-TEM micrograph shows the fine distribution of cuboidal Ti (C, N) precipitates, second generation precipitates contribution as strengthening phase to the matrix.

The distribution of TiN phase over whole the gauge length of creep-exposed specimen is shown in the *Figure 4.2.5.2.3*. It is a statistical representation of frequency of TiN size (μm) found in the gauge length after the creep exposure at 650°C . The TiN precipitate size varied from a minimum $0.25\mu\text{m}$ to a maximum $18.75\mu\text{m}$ with an average size of $4.9\mu\text{m}$.



Typical BF-TEM micrographs of TiN phase are shown in *Figure 4.2.5.2.4*. TiN precipitates of size $0.25\mu\text{m}$ (*Figure 4.2.5.2.4a*) and $3.4\mu\text{m}$ (*Figure 4.2.5.2.4b*) were observed. The fine precipitates of TiN are potentially second generation of nitrides formed in the alloy during the creep exposure. These secondary nitrides as well as large ones were found in large numbers along the surface edge of the creep specimen.

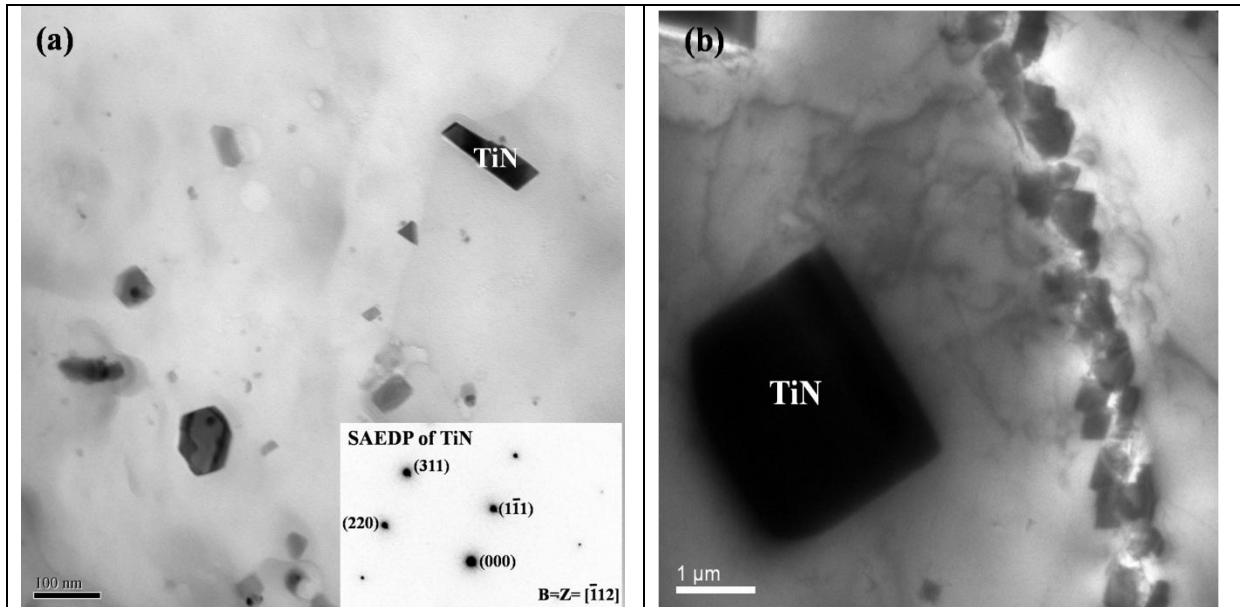


Figure 4.2.5.2.4: BF-TEM micrographs of TiN phase (marked). (a) TiN phase and SAEDP of TiN phase (inset). (b) TiN phase near the grain boundary of size $4.5 \mu\text{m}$. Beam direction and zone axis were along $[112]$.

The quantification of the TiN phase size is shown in Figure 4.2.5.2.5.

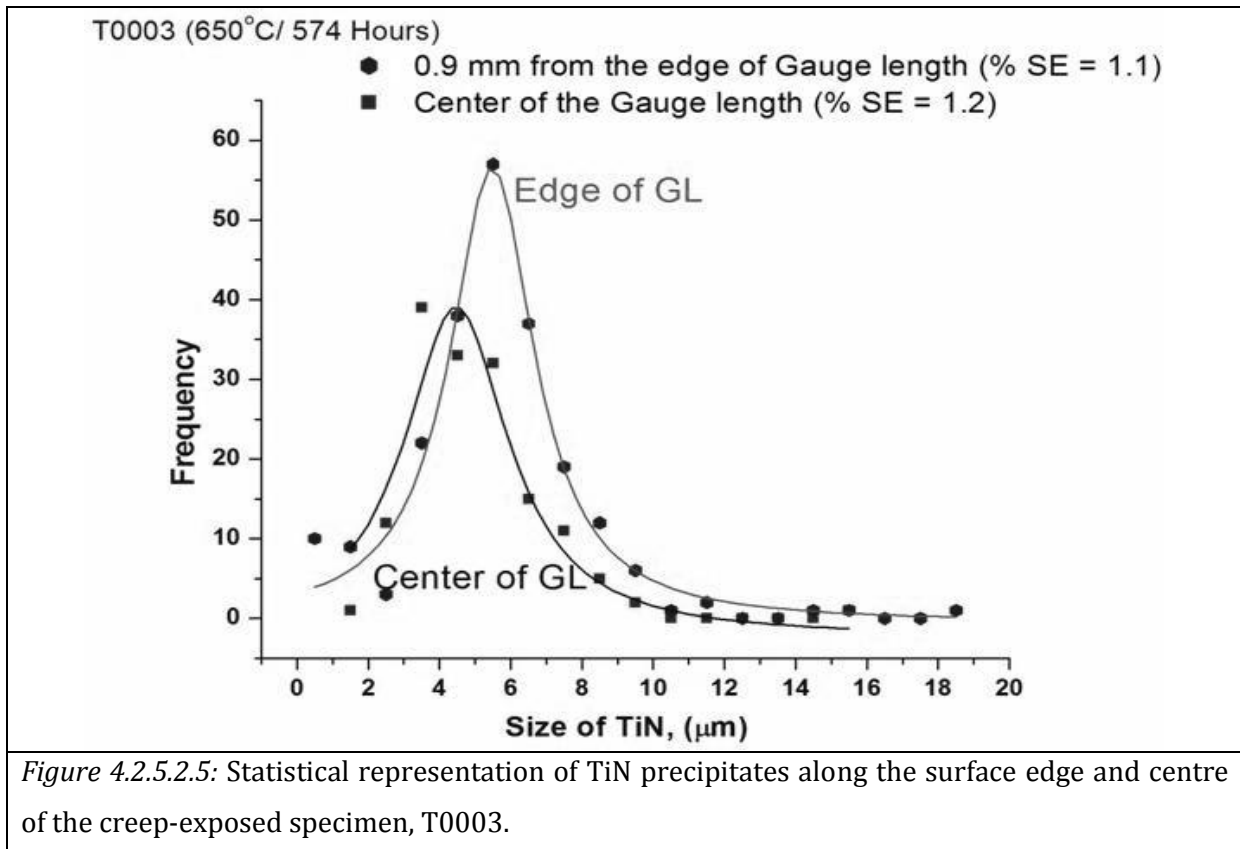


Figure 4.2.5.2.5: Statistical representation of TiN precipitates along the surface edge and centre of the creep-exposed specimen, T0003.

TEM studies (*Figure 4.2.5.2.2*) showed that the secondary fine precipitates of TiN partially may replaced the primary strengthening phase of γ' and act as strengthening phase similar to γ' in the matrix.

4.2.5.3 $M_{23}C_6$

BF-TEM micrographs of $M_{23}C_6$ phase are shown in *Figure 4.2.5.3*. The indexed SAEDP is shown in *Figure 4.2.5.3a*. The beam direction and zone axis were along $[\bar{1}11]$. EDX shows that the predominant carbide formed was $M_{23}C_6$ enriched in chromium approximately of stoichiometric composition, $Cr_{16} (Ni, Mo, Co)_7 C_6$.

$M_{23}C_6$ carbides have a cubic structure with a lattice constant $a_{M_{23}C_6} = 10.65 \text{ \AA}$ and these precipitates have shown its crystallographic relationship with the matrix as $\{001\}_{M_{23}C_6} \parallel \{001\}_{\text{matrix}}$ & $\langle 001 \rangle_{M_{23}C_6} \parallel \langle 001 \rangle_{\text{matrix}}$.

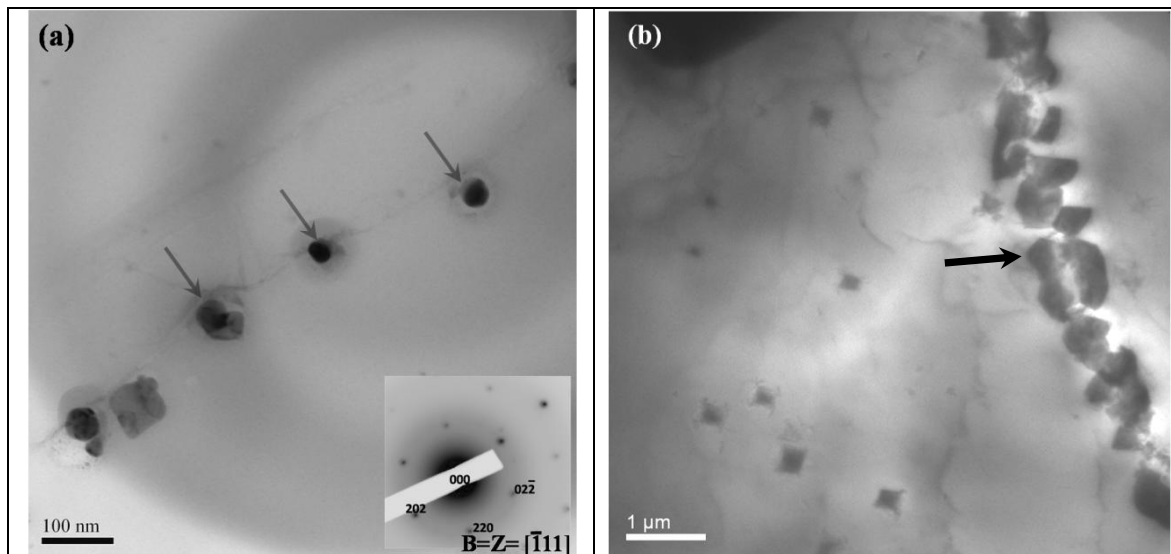


Figure 4.2.5.3: BF-TEM micrographs show the $M_{23}C_6$ (Cr-enriched) carbides, (noted in *Figure 4.2.4*) (a) SAEDP of $M_{23}C_6$ precipitates shown in inset. (b) Precipitates of $M_{23}C_6$ are located along the grain boundary.

The additional precipitation of carbides and evolution of primary carbides during creep exposure are from degradation of MC carbides and from soluble carbon residual in the alloy matrix (Davis, 1999). The precipitation appears at different locations, such as near to/on twin

boundaries, within the grains, but typically on the austenite grain boundaries and on sub-grain boundaries. The discrete $M_{23}C_6$ particles formed intra- and intergranularly are favourable to high temperature strength through blocking of dislocation movements by pinning. However, they take out solid solution strengthening elements from matrix, which affects the high temperature mechanical properties. Therefore, there is a combined action of strengthening and weakening effects on creep tests. The weakening effect was stronger than the strengthening one; therefore, this creep test condition (650°C/ 574Hrs / 350MPa) specimen showed a short life.

4.2.5.4 Quantitative Measurements of Dislocation density

The dislocation density was calculated using *Equation 4.1.4.4*, as discussed in section 4.1.4.4. The average dislocation density in gauge region of T0003 specimen was estimated as $8.3 \pm 2.0 \times 10^{12}$ lines/m². The standard deviation in the measurement was 1.9.

Typical values of ρ_d , η_g , ξ_g , and t are listed in *Table 4.2.5.4*.

η_g	ξ_g (Å) at 200kV	t (Å)	ρ_d (lines/m ²)
5	299.25	1496.24	8.3×10^{12}

The value of dislocation density in this specimen is higher than that of 'as-received' specimen by an order of 10. *Figure 4.2.5.4* shows a montage of BF-TEM micrographs illustrating dislocation structure, and dislocation-precipitate interaction in the austenitic γ -matrix.

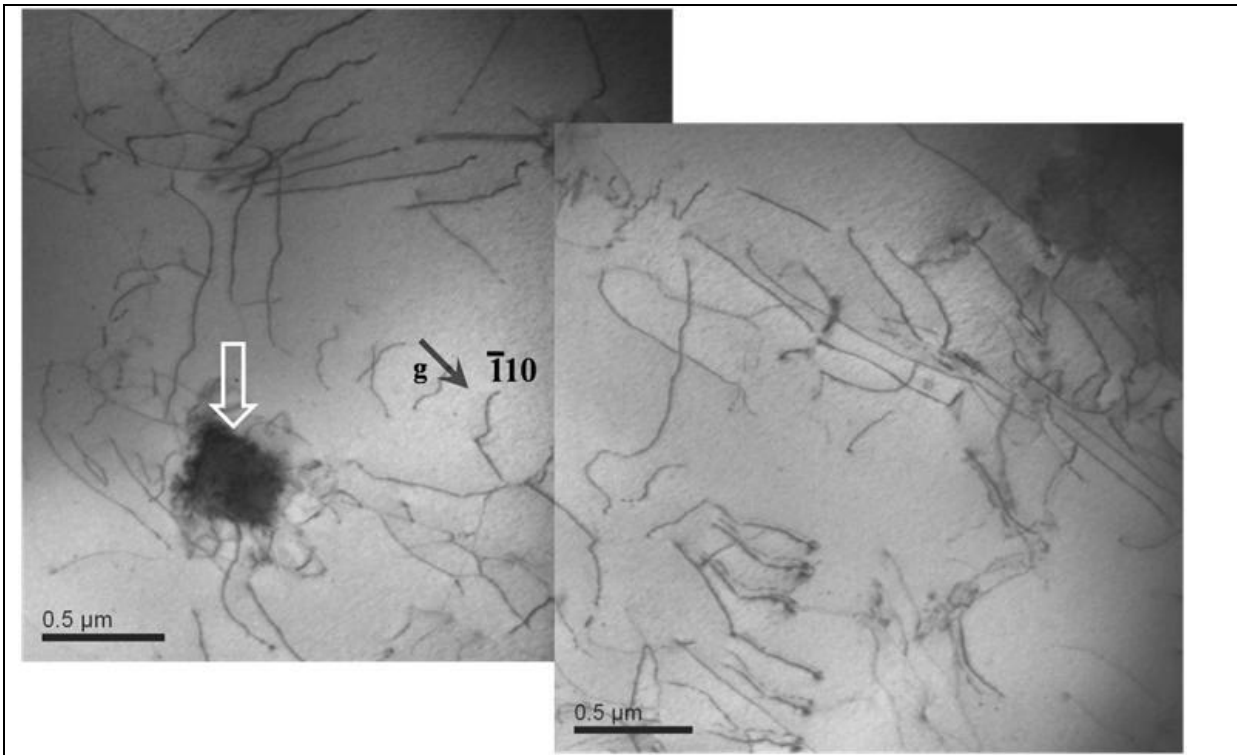


Figure 4.2.5.4: Montage of BF-TEM micrographs illustrating dislocation structure, and dislocation-precipitate interaction in austenitic γ -matrix (arrowed). Burger vector is along $g=\langle\bar{1}10\rangle$ direction.

The Burgers vector of dislocations is along the $g=\langle\bar{1}10\rangle$ direction. The coherent precipitates (such as γ') act as a barrier for dislocations and also, strengthen the matrix. Precipitates interacted with dislocation and formed interfacial dislocations (arrowed) are shown in *Figure 4.2.5.4*. Such precipitate-dislocation interaction decreased the dislocation spacing (*Figure 4.2.5.4*) and the interaction contributed to the strength of the matrix at exposed temperature.

4.3 'Creep-exposed specimen' (T0008) (650°C/45,000Hrs/275MPa)

Solution-annealed 'as-received' Inconel 617 alloy was creep tested at 650°C in air under a uniaxial load of 275MPa (estimated stress value from creep data of IN617, Ennis et al 2007). This specimen ID: T0008 fractured after 45,000 hours of creep duration. The area reduction was measured as 16.9%.

4.3.1 Fractography

The failure mechanism of the creep fractured specimen was analyzed using scanning electron microscopy and optical microscopy. A fractograph of the creep failed specimen, T0008 is shown in *Figure 4.3.1a*.

The failure mechanism was intergranular by decohesion along the grain boundaries. Intergranular mechanism involves nucleation, and growth of micro-voids. The subsequent linking of voids at grain boundaries were found to form wedge and isolated type cavities. The formation of these cavities was controlled by diffusion-controlled processes. Wedge type cavities were associated with cracking at grain boundary triple points. Triple point wedge cracking (marked) and creep cavitation (arrowed) are shown in *Figure 4.3.1(a)*. The failure mechanism in this specimen was further confirmed by optical and scanning electron microscopy of a polished cross-section of the fractured surface. *Figures 4.3.1(b) & (c)* show further confirmation of wedge cracking, decohesion and crack propagation along the grain boundaries. The direction of loading is shown by the arrows in *Figures 4.3.1 (b) & (c)*. The open cracks intruded inside the specimen to a depth of 200 to 800µm.

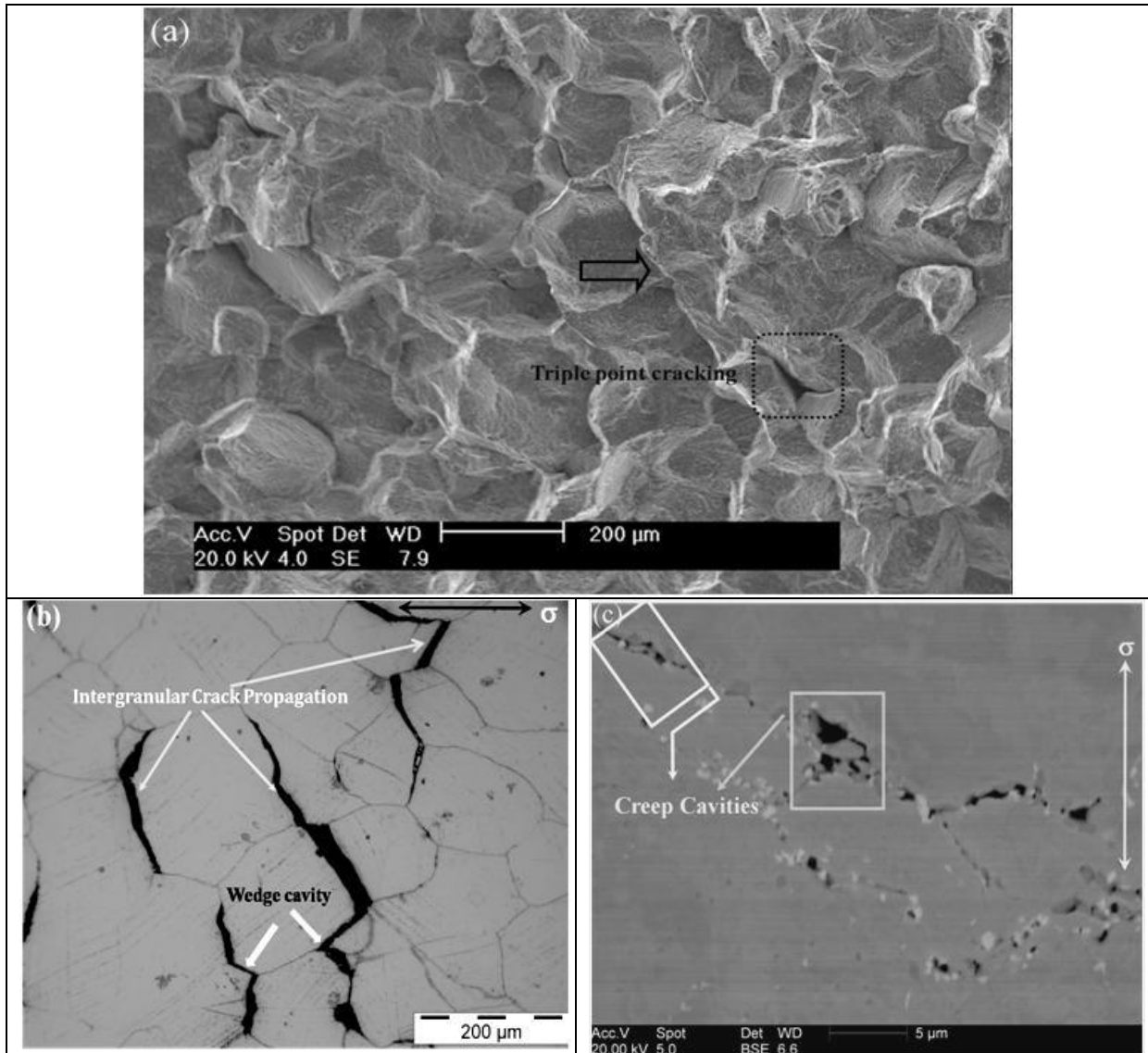


Figure 4.3.1: (a) Intergranular creep failure of creep-exposed specimen at 650°C, (b) Optical micrograph, 1cm behind the fracture surface, shows intergranular decohesion and intergranular crack propagation and (c) SEM micrograph showing creep cavities along the grain boundaries.

4.3.2 Grain Morphology

The austenite grain structure of 'creep-exposed IN617' specimen is shown in Figure 4.3.2. The optical microstructure of the creep-exposed specimen shows an equiaxed austenitic γ -grain structure with an average size of 146 μm .

The grain orientation was random (Krishna et al 2009). Annealing twins and twin boundaries were observed in a number of grains. Twins have a faceted appearance and

are broad, similar to the 'as-received' specimen. Twin boundaries were observed to be flattened and straighter in the sides; however in a few areas of the micrograph they were observed as steps (*Figure 4.3.2*).

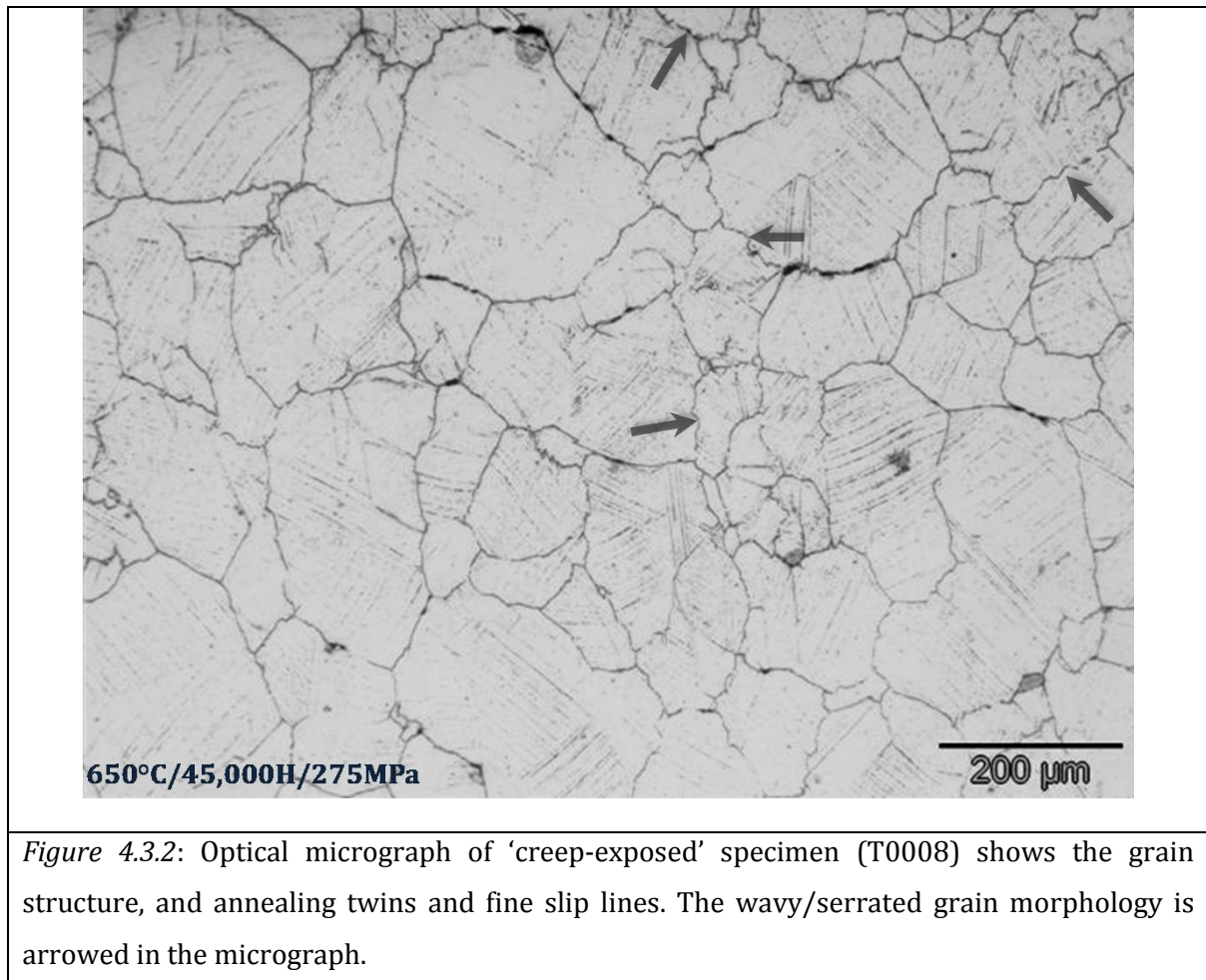


Figure 4.3.2: Optical micrograph of 'creep-exposed' specimen (T0008) shows the grain structure, and annealing twins and fine slip lines. The wavy/serrated grain morphology is arrowed in the micrograph.

They were found to have special orientation relationship with grains and formed at grain boundaries. Serrated grain boundaries were observed (arrowed in *Figure 4.3.2*) in the micrograph, similar to the T0003 specimen. Edge, incomplete and complete- types of twins were common as was found for the 'as-received' specimen. Grain boundary thickening is an important intergranular deformation mechanism at elevated temperature. Grain boundary thickening was observed for this sample, similar to the T0003 (*Figure 4.3.2*). A summary of the morphology of grains, grain boundary and average hardness of the head and gauge is listed in Table 4.3.2. The gauge length hardness had substantially increased to an average value of 353Hv whereas head had an average hardness of 267Hv. Here, again similar reason as discussed

in previous specimen T0003, that the major effect on the head is from the thermal effects with minimal effect from strain, therefore, the hardness is lower than the gauge length value.

Creep-exposed (650°C/45,000 Hrs /275MPa)	Grain Morphology			VHN (H _v /20)		Grain- boundary morphology
	Grain-size range (μm)	Avg. grain size (μm)	Grain shape	Head	Gauge	
	65 to 487	146	Equiaxed	267	353	

The high hardness value in the gauge region was due to extensive precipitation of carbides ($M_{23}C_6$), carbo-nitrides [Ti (C, N)], μ -phase, and of increased dislocation density during the creep exposure.

4.3.3 Phase Identification

An X-ray diffraction pattern analysis of T0008 specimen is shown in Figure 4.3.3. Precipitates in this specimen were identified as γ' -gamma prime, $Cr_{23}C_6$ TiN/TiC and μ -phase.

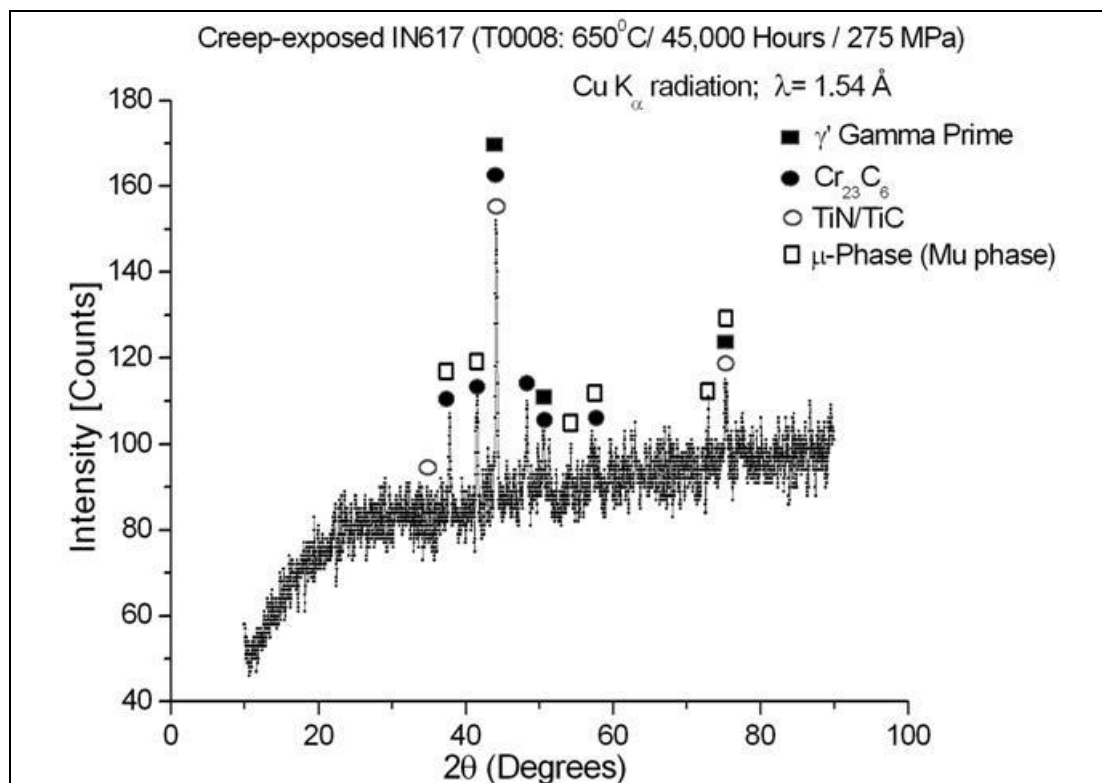


Figure 4.3.3: X-ray diffraction analysis on Br₂ dissolved extracted residues of creep-exposed T0008 specimen.

Here it is important to note that, μ -phase was not observed in the 'as-received' and T0003 specimens. It appears in the alloy after long duration of exposure and this creep-exposed specimen was longest exposed duration of 45,000 hours at 650°C.

4.3.4 Precipitate Morphology and Location

The morphology of precipitates and their locations were studied in the same way as for previous samples. *Figure 4.3.4* shows the evolutions of precipitates in a specimen creep-exposed at 700°C. BSE micrograph in *Figure 4.3.4* shows that precipitates have a higher average Z than the austenite grains appear white, whereas some, appearing dark in the image, have a lower average Z than the austenite grains. EDX spectra acquired from these precipitates indicated the high-Z and low-Z phases are enriched in Mo, Cr and Ti, respectively. These therefore, appear as μ -phase (μ -phase, Mo enriched), $M_{23}C_6$ -type Cr enriched phase and M(C, N)-type Ti enriched phase, in contrast to the as-received and T0003 specimens, which only showed Cr- and Ti-rich phases. In the SEM, EDX spectra were measured from these precipitates and quantified for elemental analysis using a standardless approximation. The elemental composition of these precipitates is shown in *Table 4.3.4.1*. These precipitates were found both intra- and intergranularly in the specimen. Their morphology varied from a regular to a totally irregular morphology.

<i>Table 4.3.4.1: A typical composition of observed phases in creep-exposed condition (T0008) by EDX (wt.%)</i>	
$M_{23}C_6$	Cr-27Mo-8.3Ni-3.2Co-4.1Ti
Ti (C,N)	Ti-1.8Cr-1.3Al
$(Ni, Co, Fe)_7Mo_6$	Mo-28.1Ni-17.7Cr-11.1Co

The size of the Cr-enriched precipitates varied from <0.1 μ m to 5 μ m. The size of the Ti-enriched precipitates varied from 0.5 μ m to 14 μ m. The size of the Mo-enriched precipitates varied from less than 0.1 μ m to 6 μ m. The Cr-enriched and Mo-enriched

precipitates were extensively precipitated along the grain and twin boundaries, in the creep-exposed specimen.

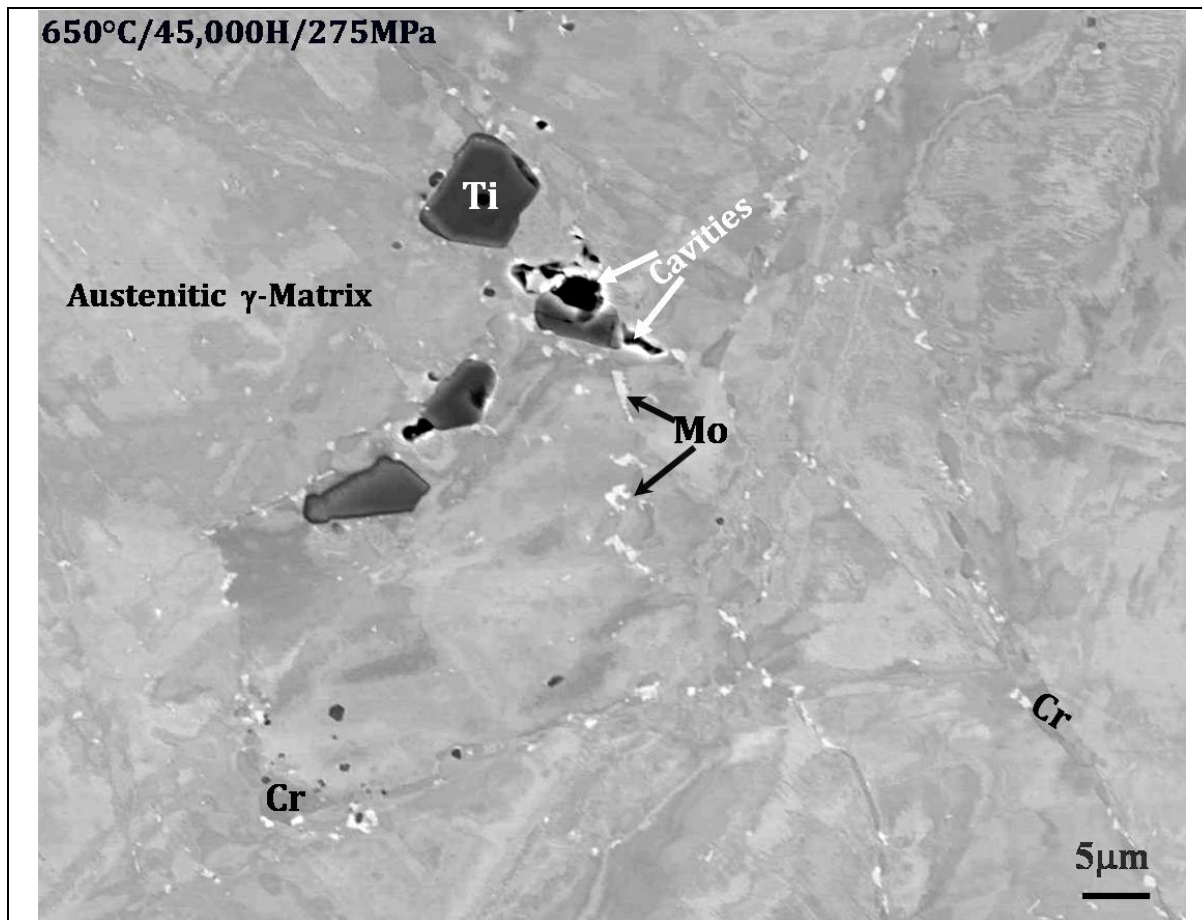


Figure 4.3.4: Backscattered scanning electron micrograph of the creep-exposed specimen shows the blocky shape (darker contrast, marked 'Ti') near to the twin boundary is Ti-rich phase, TiN; particles (marked 'Cr') at grain boundary, triple junctions and twin boundaries are Cr-rich phase, Cr_{23}C_6 . Mo-enriched precipitates are also observed along the grain boundaries and near to Cr-enriched precipitates (marked 'Mo'), are μ -phase.

Here it is note worthy that the extensive precipitation of Cr- and Mo-enriched precipitates was not observed in the T0003 specimen. In this specimen, precipitates were not only increased in number but also in size. Therefore, precipitation was the function of creep conditions. Extensive precipitation weakened the matrix strength due to diffusion of strengthening elements from the matrix to precipitates and weakening leads to rupture of the specimen. The major precipitates found in the gauge length after microstructural evolutions during creep are shown in *Table 4.3.4*. The standard error in the measurement was 2.4 to 3.9%.

Table 4.3.4.2: Precipitates morphology and location after creep exposure

Specimen ID	Precipitate location	Precipitates Morphology			Area fraction (%)
		Phases	Size	Shape	
T0008(650°C/45,000 Hrs /275MPa)	throughout the matrix	γ' - Ni ₃ (Ti, Al)	10-70nm	Spherical	3.12
	Extensive precipitation throughout the matrix	Ti (C, N)	0.5-14 μ m	Regular to totally irregular geometry	0.67
		M ₂₃ C ₆	<0.1-7 μ m		2.8
		μ -phase	<0.1-4 μ m	Blocky	1.2

The strengthening phase in the austenitic gamma (γ) matrix is the ordered intermetallic gamma prime (γ') precipitate. Their morphology and coherency were identified using transmission electron microscopy, as discussed in the next section. The shape and size of the coherent precipitates of γ' were identified as spherical and 10nm to 50nm, respectively.

4.3.5 Transmission Electron Microscopy (TEM) Observations

The microstructure of the 'creep-exposed IN617 specimen (T0008; 650°C/45,000Hours/275MPa) has been analysed using analytical transmission electron microscopy and the results are presented in this section. The microstructure of the 'creep-exposed' specimen for longer duration of 45,000 hours at 650°C consists of a γ -austenitic matrix, coherent precipitates of γ' , Ti (C, N), semi coherent precipitates of M₂₃C₆ (M = Cr, Ni, Mo, Co) and the topologically-closed-packed μ -phase (Mo-enriched). The presence of μ -phase is detrimental to the properties of alloys because it is brittle in nature. The semi-coherent precipitates were mainly located at austenite grain boundaries, sub-grain boundaries and also, randomly appear within the austenite grains, in the alloy. The morphological geometries of these precipitates are discussed in following sections.

4.3.5.1 Gamma Prime (γ')

Finely dispersed γ' precipitates strengthen the alloy matrix at high temperatures. However, γ' coarsens during service exposure conditions, which reduces the high temperature strength. Additionally, exposure of the alloy at high temperature and high strain coarsening was observed. The morphology of the γ' precipitates varied from spherical shape and their average size varied from a minimum 10nm to a maximum 55nm with an average size of 36nm. Their morphology is shown in *Figure 4.3.5.1*.

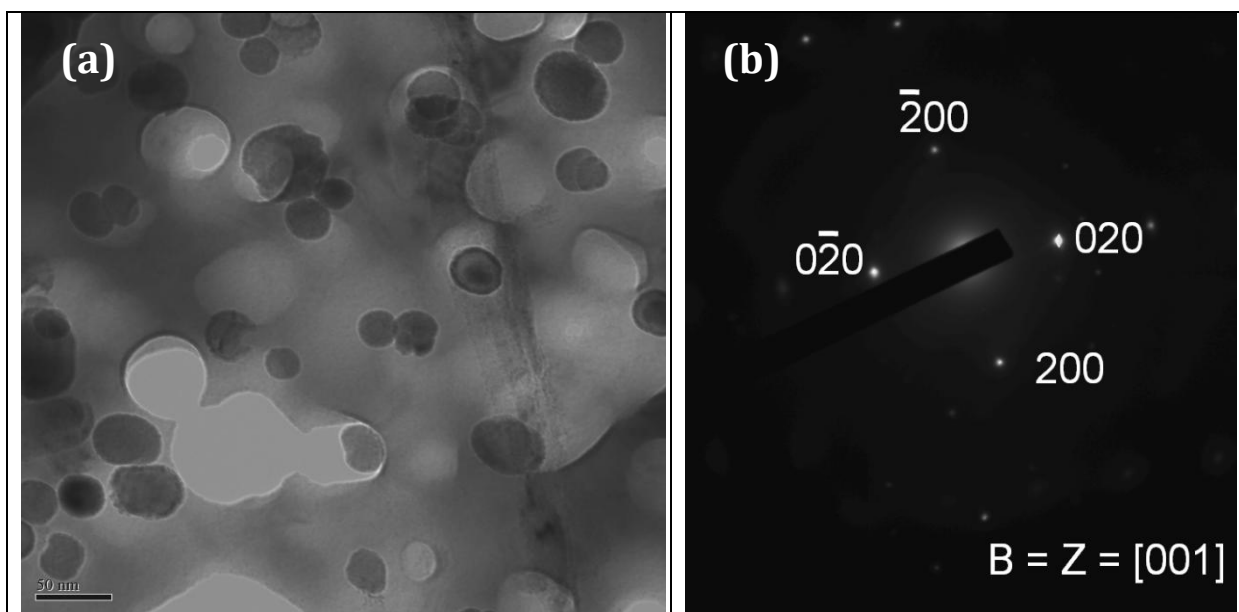


Figure 4.3.5.1: TEM micrographs show the γ' precipitates of spherical morphology; inset diagram is selected area electron diffraction pattern (SAEDP) from γ' . Beam direction and zone axis were along $B = z = [001]$.

The reflections from γ' and their indexed planes are shown in *Figure 4.3.5.1 (b)*. The beam direction and zone axis were along $B = [001]$.

4.3.5.1 (a) Volume fraction of Gamma Prime

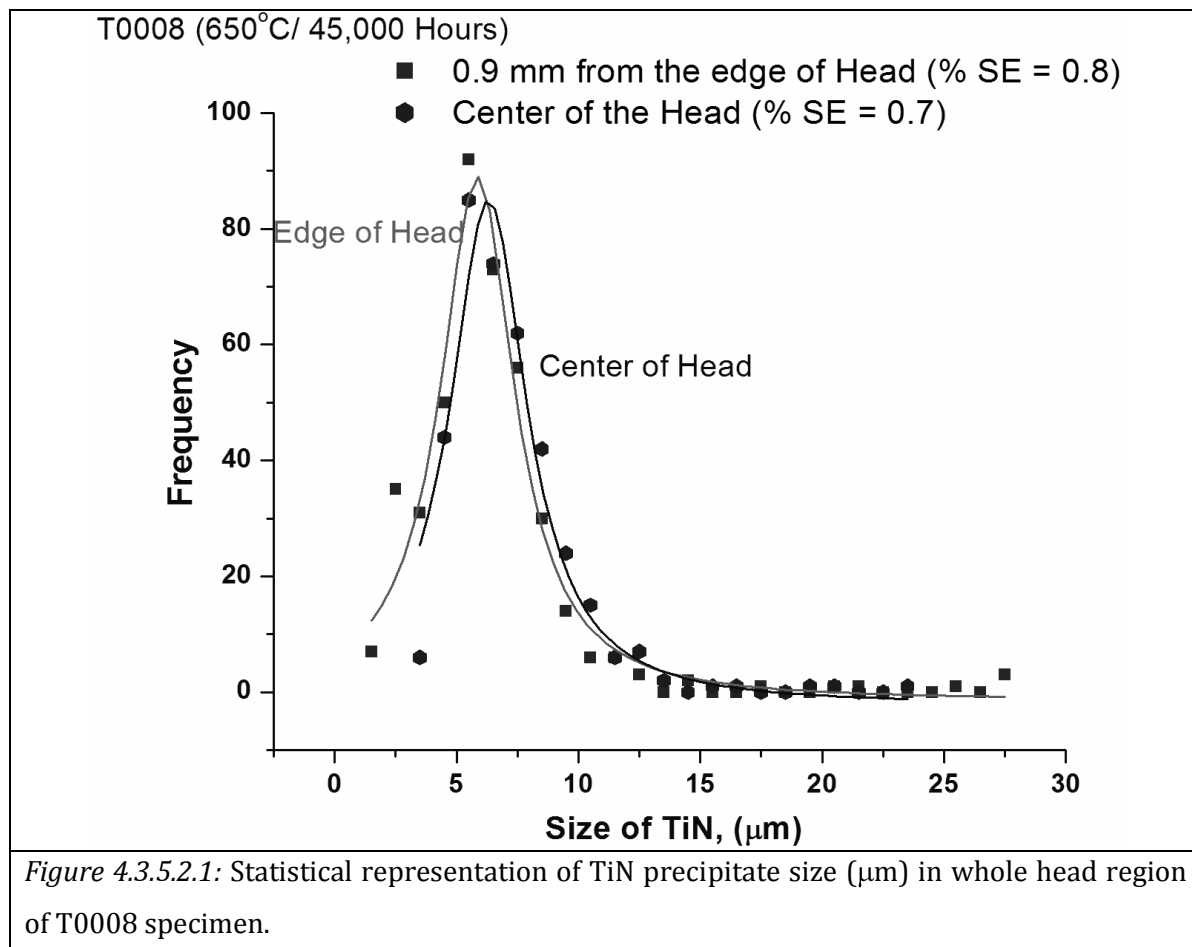
Typical values for the γ' volume fraction are shown in *Table 4.3.5.1*. The carbon replica thickness was measured using AFM. The replica thickness (h) was in range from 18-24nm.

Average Diameter (2R, nm)	$A_{ext} = \frac{N\pi R^2}{A_0}$	A_0 (nm ²)	$A_f = 1 - \exp(-A_{ext})$	$V_f = 1 - (1 - A_f)^{\frac{4R}{3h}}$
36	0.036	562500	0.0349	0.0312

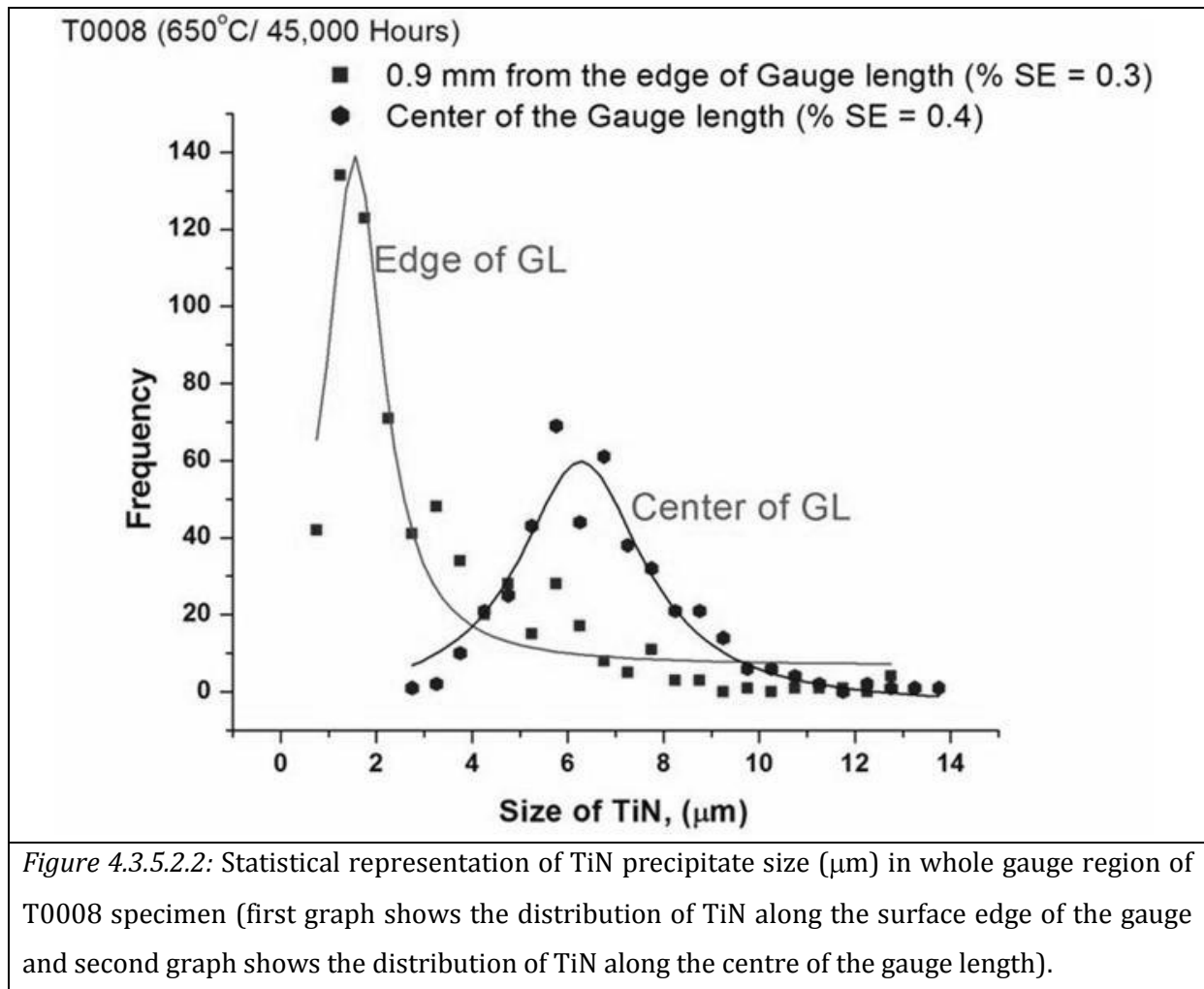
The volume fraction of gamma prime in this specimen was estimated to be approximately 3.12%. This is lower than for the sample, T0003 exposed for 574 hours which is as would be expected from the increased area fraction of TiN found in this sample, as discussed in the following section.

4.3.5.2 TiN

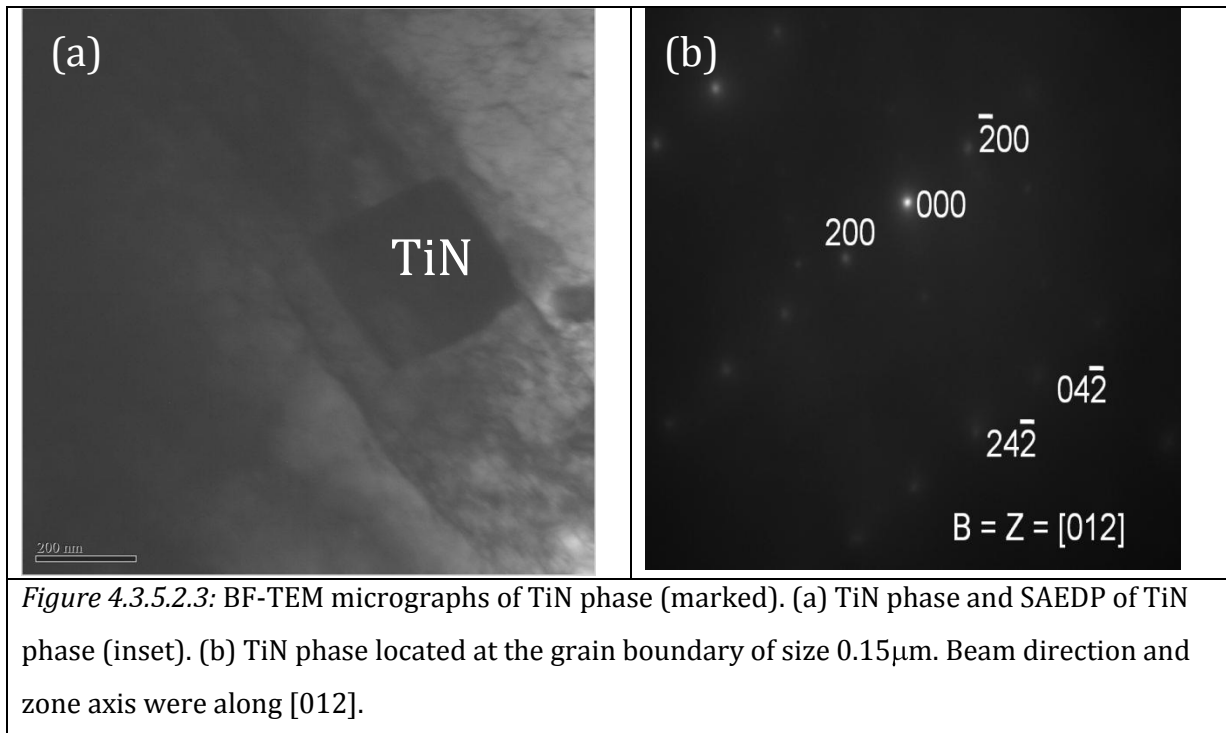
The distribution of TiN phase in the head and gauge length of creep-exposed specimen, T0008 are shown in the *Figures 4.3.5.2.1* and *Figure 4.3.5.2.2*.



The TiN precipitate size varied in the head region from a minimum of $0.1\mu\text{m}$ to a maximum of $27.75\mu\text{m}$ with an average size of $6.9\mu\text{m}$. The TiN precipitate size varied in gauge region from a minimum of $0.5\mu\text{m}$ to a maximum of $14\mu\text{m}$ with an average size of $6.9\mu\text{m}$. The size of TiN particles in the gauge length is shown in *Figure 4.3.5.2.2*. The fine TiN precipitates of size less than $0.1\mu\text{m}$ are expected to act as a strengthening phase. It was observed that γ' was coarsened from the initial size of 10nm to final size of 36nm after $45,000$ hours and this coarsening behaviour reduces the strength of the alloy, however TiN precipitates were not shown coarsening. Therefore, fine TiN precipitates are expected to act as a promising strengthening phase in this alloy.



A typical BF-TEM micrograph of TiN phase is shown in *Figure 4.2.5.2.3*. A rectangular TiN precipitate of size $0.15\mu\text{m}$ can be observed in *Figure 4.3.5.2.3a* and the indexed SAEDP pattern is shown in *Figure 4.3.5.2.3b*. The zone axis and beam direction were along $[012]$.



4.3.5.3 $M_{23}C_6$

$M_{23}C_6$ precipitate was formed during the heat-treatment and service exposure conditions from the degradation of carbo-nitrides, $M(C, N)$, as discussed in section 1.1.6 and reaction of chromium with soluble residual carbon in the alloy matrix. They usually found at the grain boundaries, twin boundaries and occasionally in the grain interior. The approximate composition of $M_{23}C_6$ precipitate was quantified by EDX as Cr-6.8Ni-28.6Mo (wt %). It was observed that the discrete precipitates of $M_{23}C_6$ influence the high temperature strength of the alloy by inhibiting the grain-boundary sliding (Mankins et al, 1974). A large $M_{23}C_6$ precipitate of size $0.2\mu\text{m}$ is shown in *Figure 4.3.5.3*. The indexed SAEDP is shown in *Figure 4.3.5.3 (b)*. An extensive precipitation of $M_{23}C_6$ precipitates was observed along the boundaries and near to the large precipitates of $M_{23}C_6$ or $Ti(C, N)$ in this specimen.

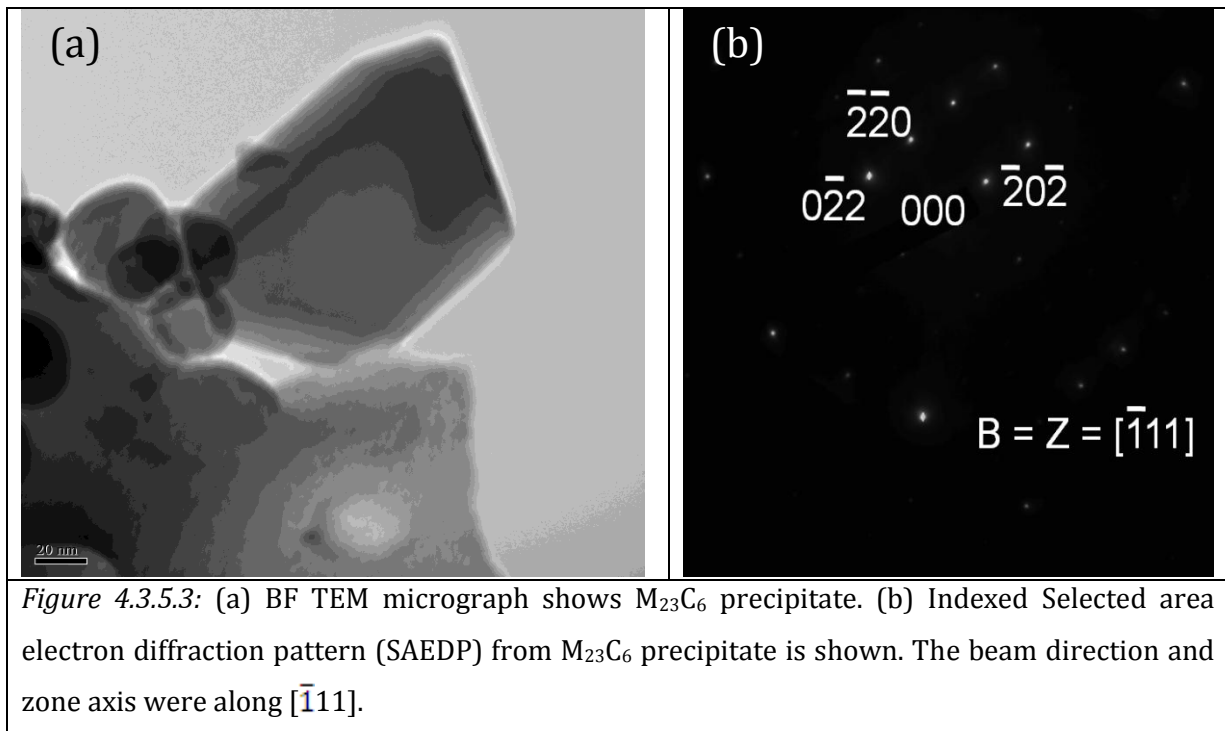


Figure 4.3.5.3: (a) BF TEM micrograph shows $M_{23}C_6$ precipitate. (b) Indexed Selected area electron diffraction pattern (SAEDP) from $M_{23}C_6$ precipitate is shown. The beam direction and zone axis were along $[\bar{1}11]$.

The morphology of $M_{23}C_6$ precipitates was almost similar to the 'as-received' and T0003 specimen. However, their numbers were increased extensively, in this specimen.

4.3.5.4 μ -phase

μ -phase is a thermodynamically stable phase in IN617 alloy up to 800°C. This phase is rich in refractory element, Mo, and known as topologically close-packed (TCP) phase. It was observed to precipitate during exposure conditions at high temperature and intermediate stress, in alloys having high refractory elements Mo and W (Pollock and Argon, 1992). This phase has a detrimental effect on the high temperature strength and creep properties of IN617 alloy, due to its brittleness. The precipitation of μ -phase in the alloy depletes the strengthening elements, Mo, Cr, and Co from the γ matrix and therefore, decreases its strength (Rae et al, 2005). The presence of large area fraction of TCP phase in the alloy produces multiple internal cracks and interfacial decohesion during the high temperature fracture. (Simonetti & Caron, 1998). This specimen showed a large number of internal cracks and decohesion along the boundaries, as discussed in the previous Section 4.3.1. This phase was nucleated at the Mo rich grain boundaries and near to the carbides. Figure 4.3.5.4 shows the BF TEM micrograph of μ -

phase having blocky morphology. Inset in *Figure 4.3.5.4* shows the SAEDP of μ -phase. A stacking fault defect in its structure can be observed in the micrograph (*Figure 4.3.5.4*). The standardless quantitative analysis from EDX shows that the μ -phase was enriched by Mo and Cr and a typical quantitative analysis was Mo-28.1Ni-17.7Cr-11.1Co (wt. %).

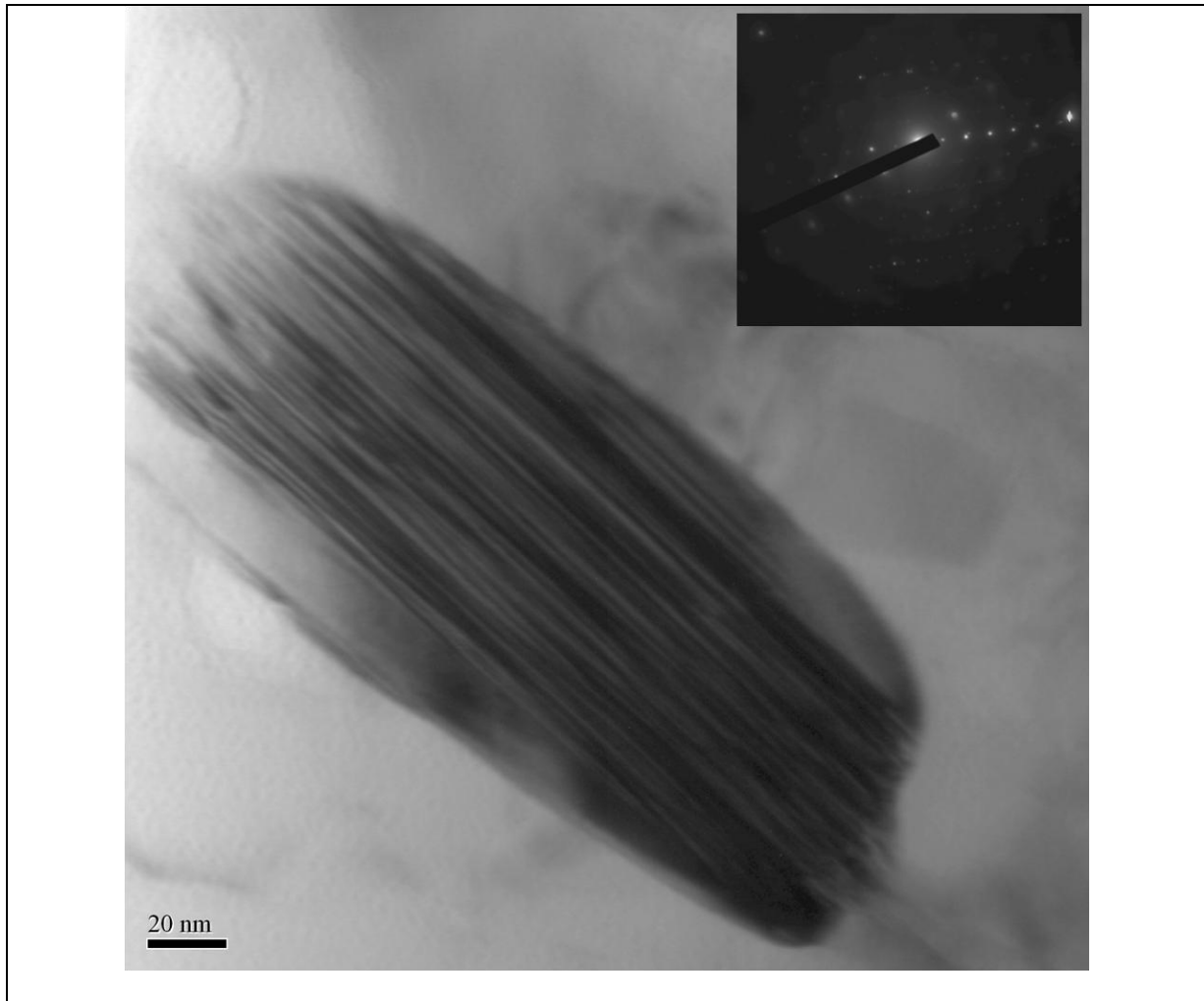


Figure 4.3.5.4: BF-TEM micrograph shows μ -phase. It is a TCP phase, and potentially detrimental to strength of the matrix, due to the presence of stacking faults and twins in its structure. The beam direction and zone axis were along $[12\bar{1}]$.

4.3.5.5 Quantitative Measurement of Dislocation density

The dislocation density was estimated in gauge region of the specimen T0008, as the similar method discussed in section 4.1.4.4. The average dislocation density was estimated to be

$2.5 \pm 1.6 \times 10^{13}$ lines/m². The standard deviation in the measurement was 1.6. The average dislocation density in this specimen was increased in the order of 10, than that of 'as-received' specimen. *Figure 4.3.5.5* shows a typical BF-TEM micrograph illustrating the dislocation structure, and dislocation-precipitate interaction in austenitic γ -matrix. The coherent γ' precipitates act as a barrier for the movement of dislocations and this provides strengthening to the matrix. The interaction of dislocations with γ' precipitates and interfacial dislocations can be observed in *Figure 4.3.5.5*.

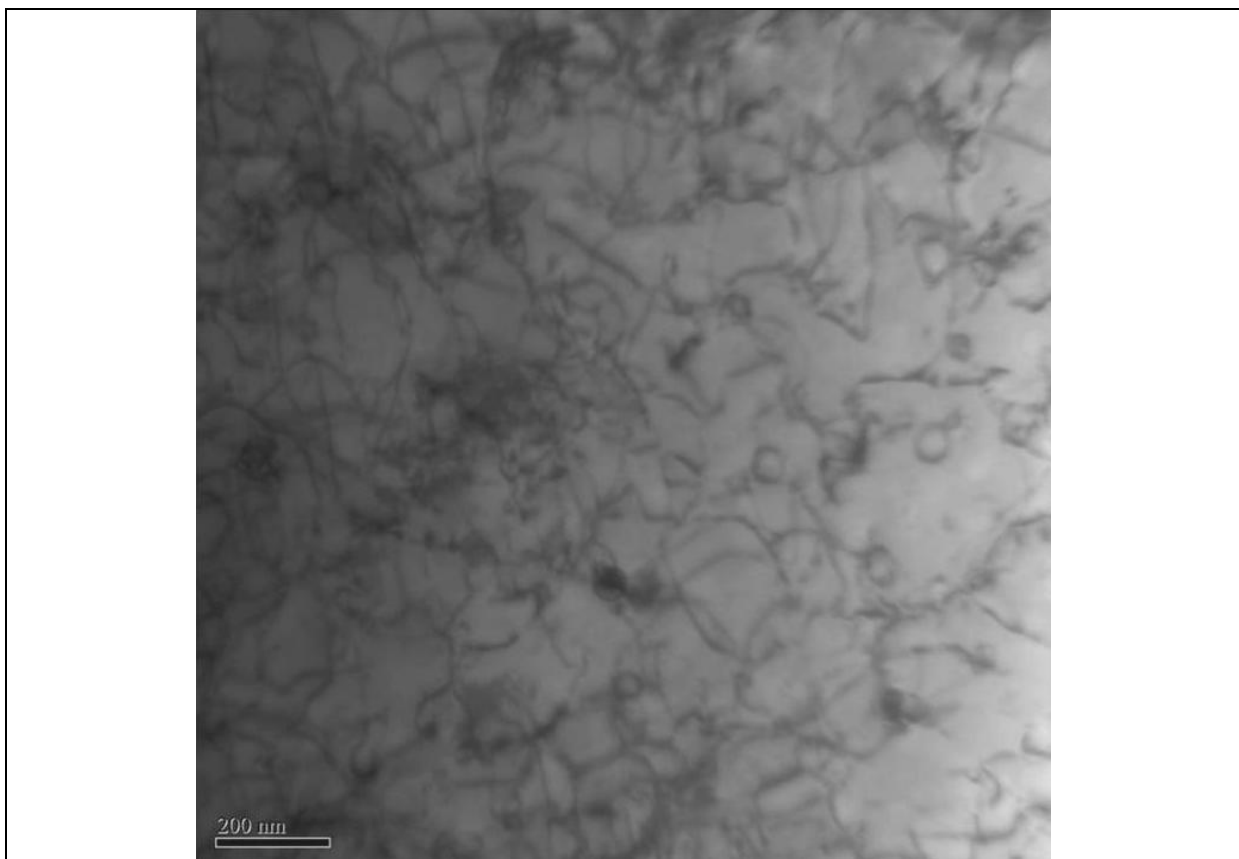


Figure 4.3.5.5: BF-TEM micrograph shows the dislocation structure, and dislocation-precipitate interaction in austenitic γ -matrix.

Typical values of dislocation density (ρ_d), η_g , ξ_g , and t are listed in *Table 4.3.5.5*.

<i>Table:4.3.5.5: Typical values for η_g, ξ_g, t and ρ_d</i>			
η_g	ξ_g (Å) at 200kV	t (Å)	ρ_d (lines/m ²)
5	299.25	1196.24	2.45×10^{13}

4.4 'Creep-exposed specimen' (T0151) (700°C/ 4,000Hrs / 200MPa)

A solution annealed IN617 alloy sample was machined for creep test and creep tested at 700°C in air under a uniaxial load of 200MPa (stress value estimated from creep data of IN617, Ennis et al 2007). This specimen ID: T0151 fractured after short creep duration of 4,000 hours. The area reduction was 45.1% for this specimen.

4.4.1 Fractography

The failure mechanism of the creep fractured specimen was analyzed in a similar way as discussed for the previous specimens, by using scanning electron and optical microscopy. A fractograph of the creep failed specimen, T0151 is shown in *Figure 4.4.1a*.

This specimen showed mixed mode of failure mechanisms, intergranular and transgranular. The fast crack propagation shows that transgranular failure possibly a rapid failure mechanism. The fracture was propagated along the grain boundaries resulting in bulk deformation in the alloy. The failure mechanism in this specimen was further confirmed by optical and scanning electron microscopy, as discussed for the previous specimens. *Figures 4.4.1(b) & (c)* show wedge cavities, bulk creep voids and decohesion along the grain boundaries. The direction of loading is shown by the arrows in *Figure 4.4.1*. The open cracks intruded inside the specimen to a depth of 50 to 700 μm .

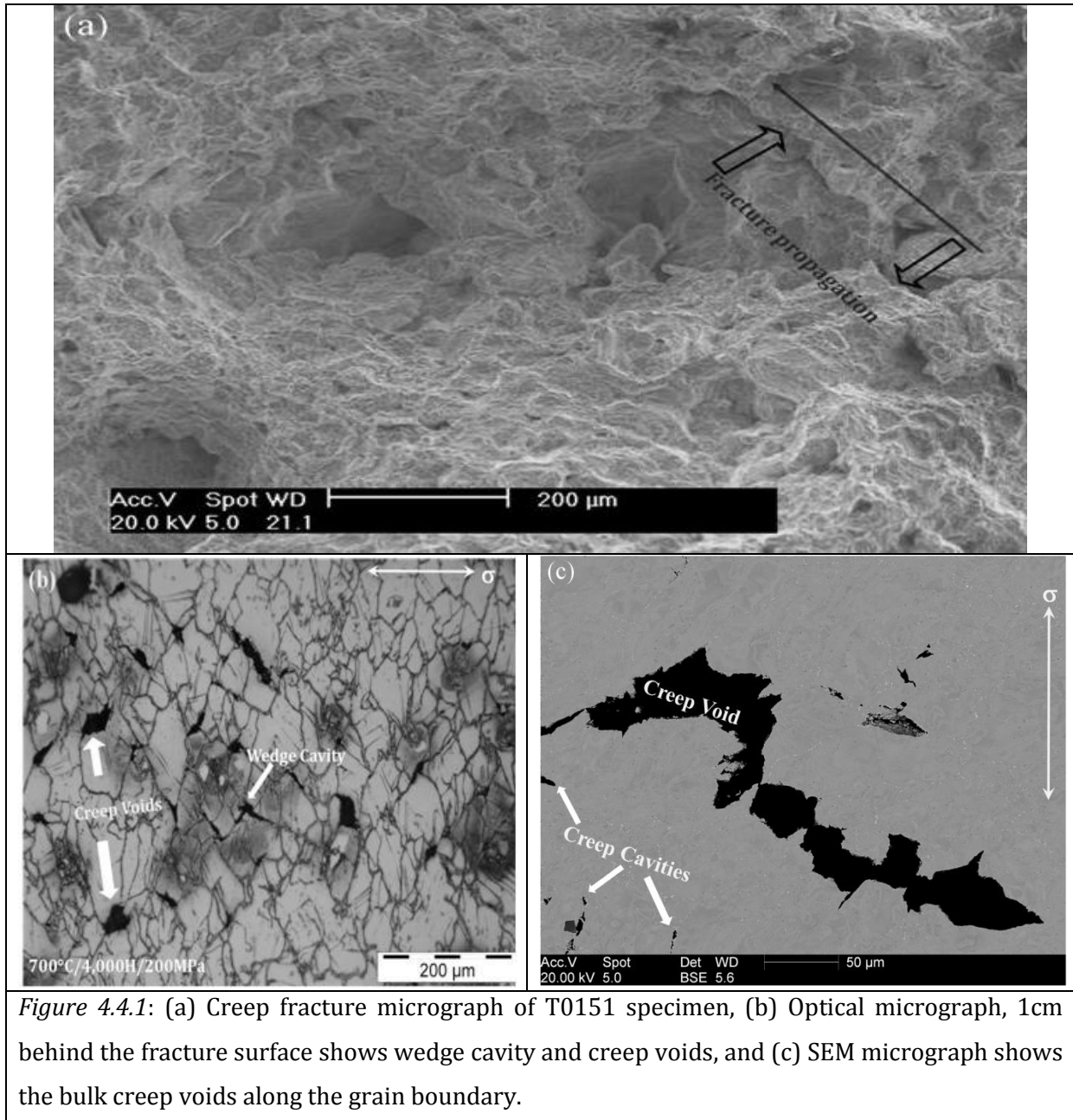


Figure 4.4.1: (a) Creep fracture micrograph of T0151 specimen, (b) Optical micrograph, 1cm behind the fracture surface shows wedge cavity and creep voids, and (c) SEM micrograph shows the bulk creep voids along the grain boundary.

4.4.2 Grain Morphology

The austenite grain structure of specimen T0151 is shown in *Figure 4.4.2*. An optical micrograph of this specimen in *Figure 4.4.2* shows an equiaxed and elongated austenite grain structure with an average size of 133 μm , in contrast to grain morphology observed in ‘as-received’, T0003 and T0008 specimens.

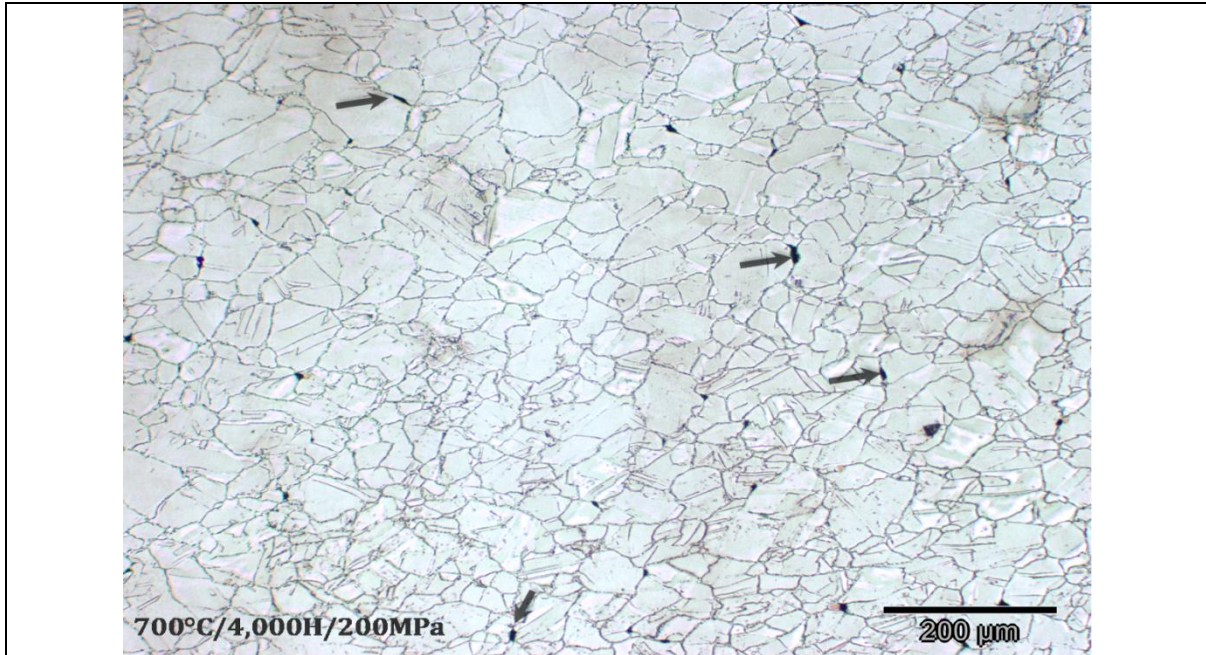


Figure 4.4.2: Optical micrograph of creep-exposed specimen T0151 shows the grain structure and its morphology. Annealing twins and creep cavities (arrows) are clearly observed in the micrograph.

The grain orientation and grain size observed in this specimen was random (Krishna et al, 2009). Annealing twins and twin boundaries were observed in the grains, similar to the ‘as-received’, T0003 and T0008 specimens. All the grain boundaries were wavy along their lengths; this was in contrast to the specimens T0003 and T0008. A summary of the morphology of grains, grain boundary and average hardness of the head and gauge is listed in *Table 4.4.2*.

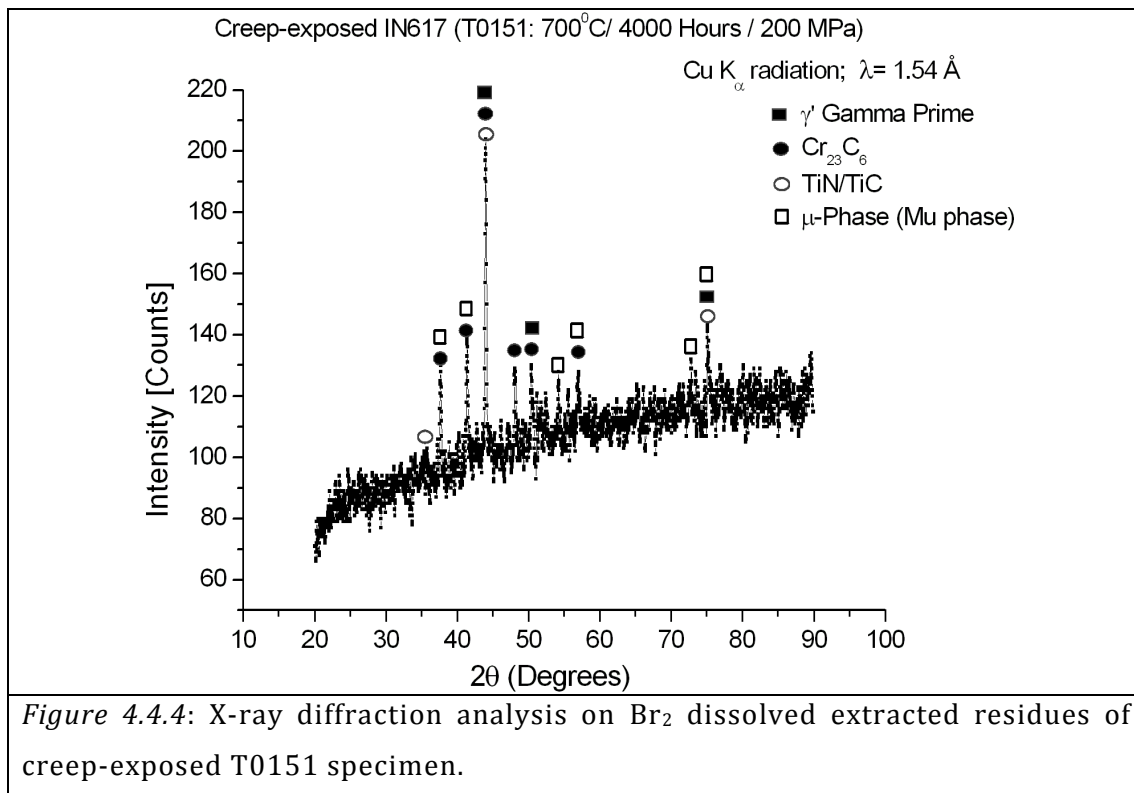
Creep-exposed (700°C/4,000 Hrs /200MPa)	Grain Morphology			VHN ($H_V/20$)		Grain- boundary morphology
	Grain-size range (μm)	Avg. grain size (μm)	Grain shape	Head	Gauge	
	28 to 269	133	Elongated	272	343	

The gauge length hardness substantially increased to an average value of 343Hv where as head had an average hardness of 272Hv. Here, the higher value of hardness in gauge length was from the thermal and stress effects, whereas lower hardness observed in the head of the specimen was only from the thermal effect and minimal from stress. This specimen also showed extensive precipitation of carbides of $M_{23}C_6$ type and work hardening was the

primary reason of the high hardness value in the gauge length. The hardness value in the gauge length of T0151 specimen was lower than the hardness value in gauge length of the specimen T0008 but higher than the specimen T0003. T0151 specimen was exposed to 4000 hours and the precipitation in this specimen was not as extensive as that of the T0008 specimen, even if the T0151 specimen was exposed at 700°C. The extensive precipitation was the reason for high hardness value in T0008 specimen.

4.4.4 Phase Identification

An XRD was conducted on electrolytically and Br₂ dissolved T0151 specimen residues of carbides, nitrides and intermetallics. An analysed X-ray diffraction pattern of specimen T0151 is shown in *Figure 4.4.4*.



The identified precipitates in this specimen were γ'-gamma prime, Cr₂₃C₆, TiN/TiC and μ-phase, as similar to the T0008 specimen, exposed for 45,000 hours at 650°C.

4.4.4 Precipitate Morphology and Location

The morphology of precipitates and their locations in this T0151 specimen are discussed here using a backscattered electron (BSE) SEM micrograph. *Figure 4.4.4* shows the precipitates morphology and their locations in the T0151 specimen. The precipitates were enriched in Mo, Cr and Ti. They were identified from the XRD as μ -phase, enriched in Mo, $M_{23}C_6$ -type carbides enriched in Cr and $M(C, N)$ -type carbo-nitrides enriched in Ti. The quantified elemental analysis from EDX spectra is shown in *Table 4.4.4.1*. The precipitates were found randomly in the matrix and at the grain boundaries. Their morphology varied from a regular to a totally irregular, as similar to the 'as-received', T0003 and T0008 specimens.

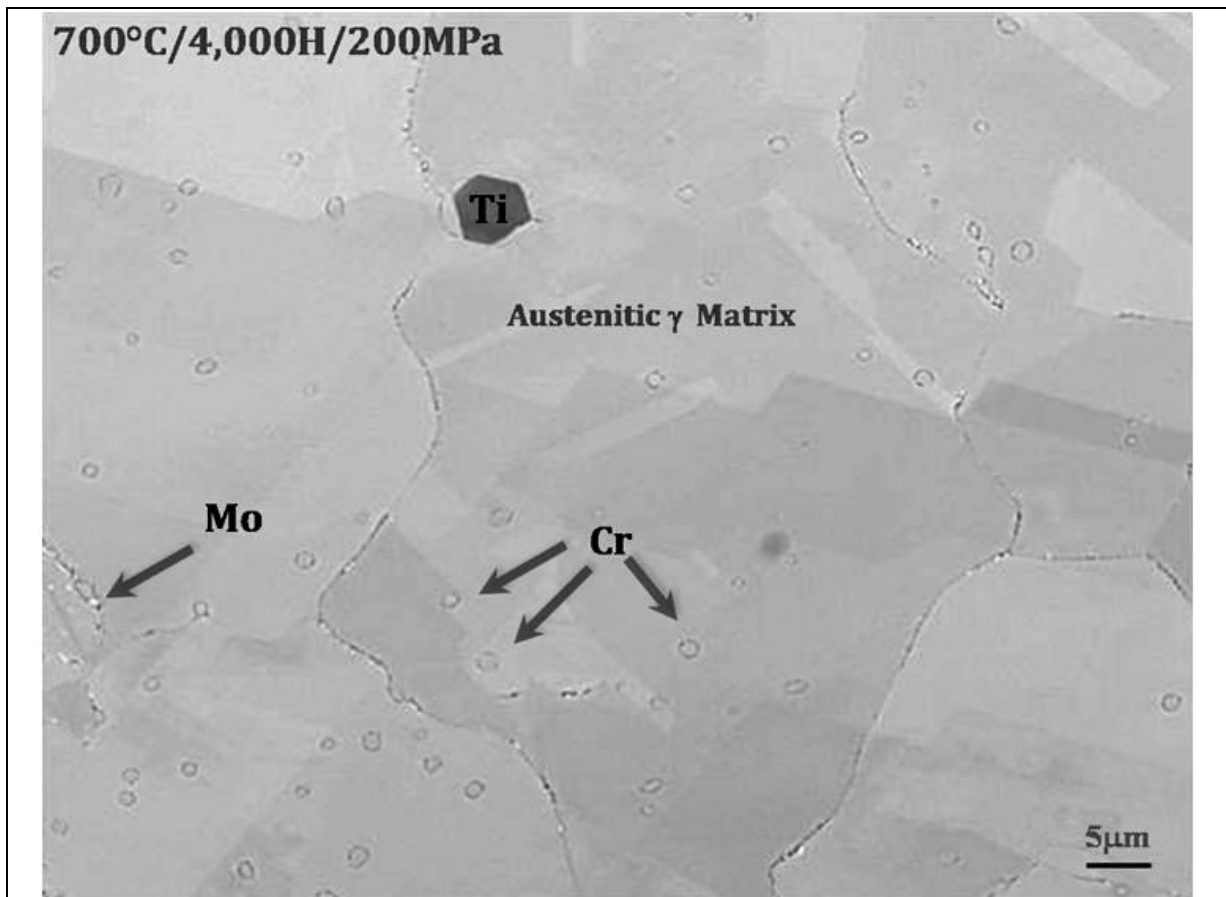


Figure 4.4.4: Backscattered SEM micrograph of the creep-exposed T0151 specimen. The blocky shape (dark in figure, marked 'Ti') at the boundary is Ti-enriched precipitate. The particles (marked 'Cr') are at inter- and intragranular, are $M_{23}C_6$ type carbides. Mo-enriched precipitates are observed along the grain boundaries and near to Cr-enriched precipitates (marked 'Mo'), are μ -phase of $(Ni, Co, Fe)_7 Mo_6$ type.

The size of the Cr-enriched ($M_{23}C_6$) precipitates varied from less than $0.1\mu\text{m}$ to $4\mu\text{m}$. The size of the Ti-enriched (TiN/TiC) precipitate varied from $2\mu\text{m}$ to $7\mu\text{m}$. The size of the Mo-enriched, $[(\text{Ni}, \text{Co}, \text{Fe})_7 \text{Mo}_6]$ precipitate varied from less than $0.1\mu\text{m}$ to $2\mu\text{m}$. The Cr-enriched and Mo-enriched precipitates were extensively precipitated along the grain and twin boundaries, in this specimen.

Table 4.4.4.1: Typical composition of observed phases in T0151 specimen by EDX (wt. %)

$M_{23}C_6$	Cr-21.5Mo-17.9Ni-7.9Co-0.4Ti-0.2Al
Ti (C,N)	Ti-1.7Cr
$(\text{Ni}, \text{Co}, \text{Fe})_7 \text{Mo}_6$	Mo-19.9Ni-20.8Cr-9.1Co-0.1Ti-0.4Al

The morphology of these precipitates was similar to the T0008 specimen. However, sizes of the precipitates were less than the size of the precipitates observed in the T0008. This was due to the lower exposure duration for the T0151 specimen. The morphology of γ' precipitates was not resolved in SEM, due to fine precipitate size. Therefore, its morphology and locations was identified using transmission electron microscopy, and are discussed in the following section.

The major precipitates found in the creep-exposed gauge length of T0151 specimen are listed in *Table 4.4.4.2*. The standard error in measurement was in the range of 1.3 to 4.1%.

Table 4.4.4: Precipitates morphology and location after creep exposure in T0151 specimen

Specimen ID	Precipitate location	Precipitates Morphology			
		Phases	Size	Shape	Area fraction (%)
T0151(700°C/4,000 Hrs /200MPa)	throughout the matrix	γ' - $\text{Ni}_3(\text{Ti}, \text{Al})$	10-55nm	spherical	4.71
	Precipitation intra- and intergranularly	Ti (C, N)	2-7 μm	regular to totally irregular geometry	0.7
		$M_{23}C_6$	<1-4 μm		2.2
		μ -phase	<0.1-2 μm	Globular	0.3

4.4.5 Transmission Electron Microscopy (TEM) Observations

The creep-exposed T0151 specimen (700°C/4,000Hours/200MPa) was analysed using analytical transmission electron microscopy. The phases noted in *Figure 4.4.4* were further identified using selected area electron diffraction patterns and energy dispersive X-ray spectrometry (EDX). The microstructure consists of γ -austenitic matrix, coherent precipitate of γ' , Ti (C, N), semi coherent precipitate $M_{23}C_6$ (M = Cr, Ni, Mo, Co) and topologically-closed-packed μ - phase, enriched in Mo. μ -phase was found to detrimental to the strength of the alloy (Simonetti, and Caron, 1998). The semi-coherent precipitates of carbides were mainly found at the austenite grain boundaries, sub-grain boundaries and also, randomly found within the austenite grains. A detailed morphological geometry of these precipitates is further discussed in the following subsections.

4.4.5.1 Gamma Prime (γ')

The coherency of finely dispersed γ' precipitates with the matrix strengthens the alloy at high temperature. However, coarsening of precipitates during service exposure reduces the strength of the matrix. T0151 specimen was examined in the TEM for identifying the γ' precipitates. The morphology of the γ' precipitates varied from spherical shape and their average size varied from a minimum 10nm to a maximum 55nm with an average size of 32nm. The micrographs in *Figure 4.4.5.1* show the morphology of the γ' precipitates. The indexed SAEDP is shown in *Figure 4.4.5.1 (b)*. The beam direction and zone axis were along $B = [011]$.

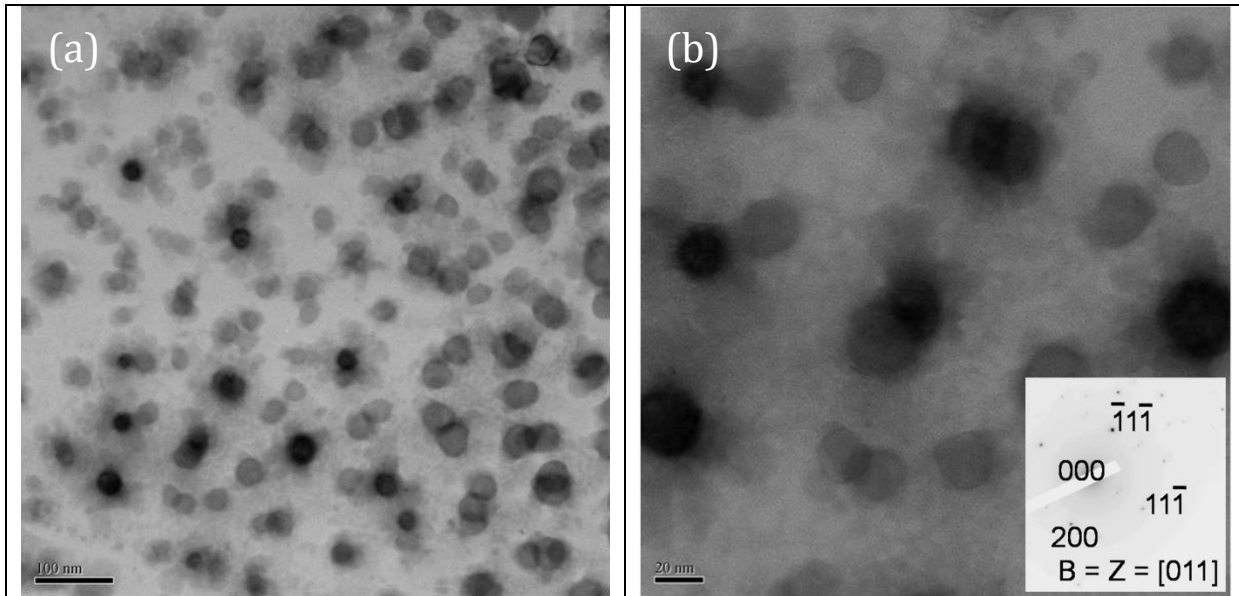


Figure 4.4.5.1: TEM micrographs show the γ' precipitates of spherical morphology; inset diagram is selected area electron diffraction pattern (SAEDP) from γ' . Beam direction and zone axis were along $B = Z = [011]$.

A random dispersion of γ' expected to strengthened the disordered FCC austenitic γ matrix (Mankins, 1974). The coherent interfaces of γ' precipitates are in orientation relationship with γ - matrix as $(100)_{\{\text{matrix-}\gamma\}} \parallel (100)_{\{\gamma\}}$; $[010]_{\{\text{matrix-}\gamma\}} \parallel [010]_{\{\gamma\}}$. The average size of γ' precipitates in this T0151 specimen was higher than the average size of precipitates in the 'as-received', T0003 and T0008 specimens. The obvious growth of γ' precipitates was due to the combined effect of temperature and strain.

4.4.5.1 (a) Volume fraction of Gamma Prime

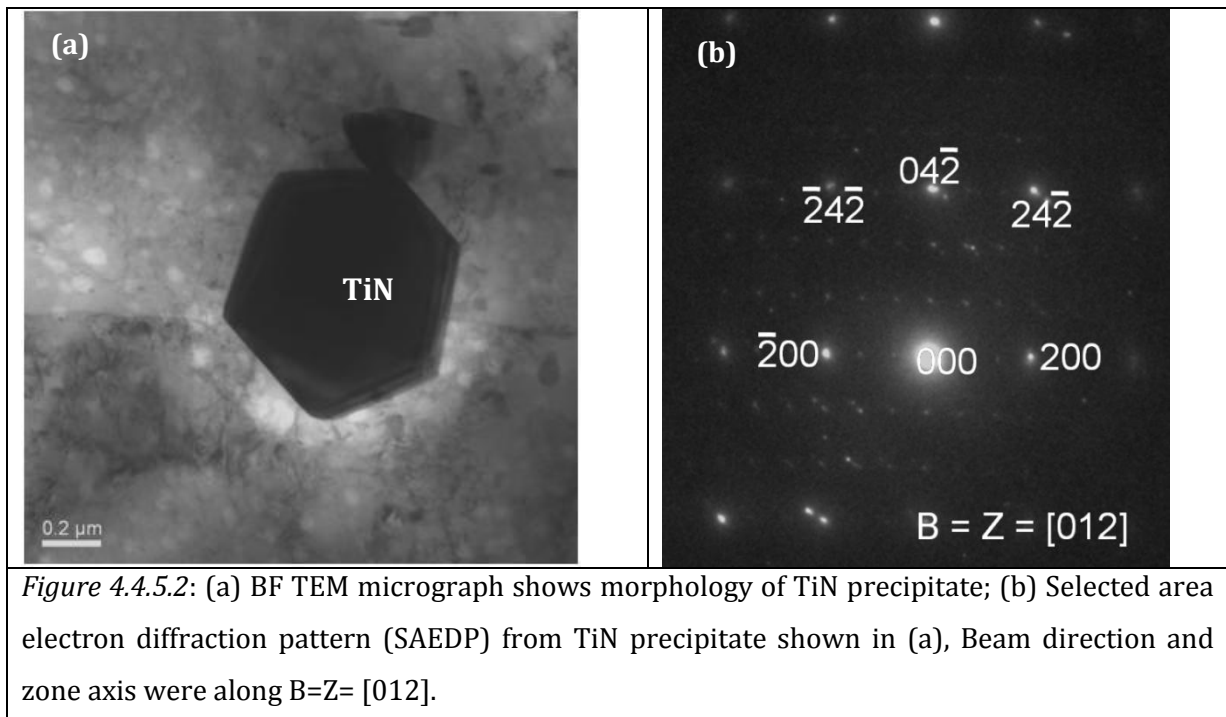
The volume fraction of gamma prime in T0151 specimen was estimated as similar to the previous specimens. The average measured carbon replicas thickness (h) was 22nm. Typical values of average size, area fraction and volume fraction of gamma prime is shown in Table 4.4.5.1.

Table 4.4.5.1: Estimated value of gamma prime, γ' volume fraction in T0151 specimen				
Average Diameter (2R, nm)	$A_{ext} = \frac{N\pi R^2}{A_0}$	A_0 (nm ²)	$A_f = 1 - \exp(-A_{ext})$	$V_f = 1 - (1 - A_f)^{\frac{4R}{3h}}$
32	0.086	562500	0.0827	0.0471

The volume fraction of γ' in this specimen was estimated to be approximately 4.71%, which is smaller than the estimated in 'as-received' and T0003 specimen but larger than the T0008 specimen. The coarsening effect due to high temperature exposure results in decrease in volume fraction. It was found to reduce with increased exposed duration and temperature, due to the diffusion of Ti from γ' and the formation of TiN precipitate. This specimen exposed for 4000 hours at 700°C and the low volume fraction in this specimen is due to increased area fraction of TiN precipitates.

4.4.5.2 TiN

Ti-enriched precipitates in T0151 specimen as noted in *Figure 4.4.4* were examined in the TEM. *Figure 4.4.5.2* shows BF-TEM micrograph of Ti-enriched precipitate, TiN in T0151 specimen.

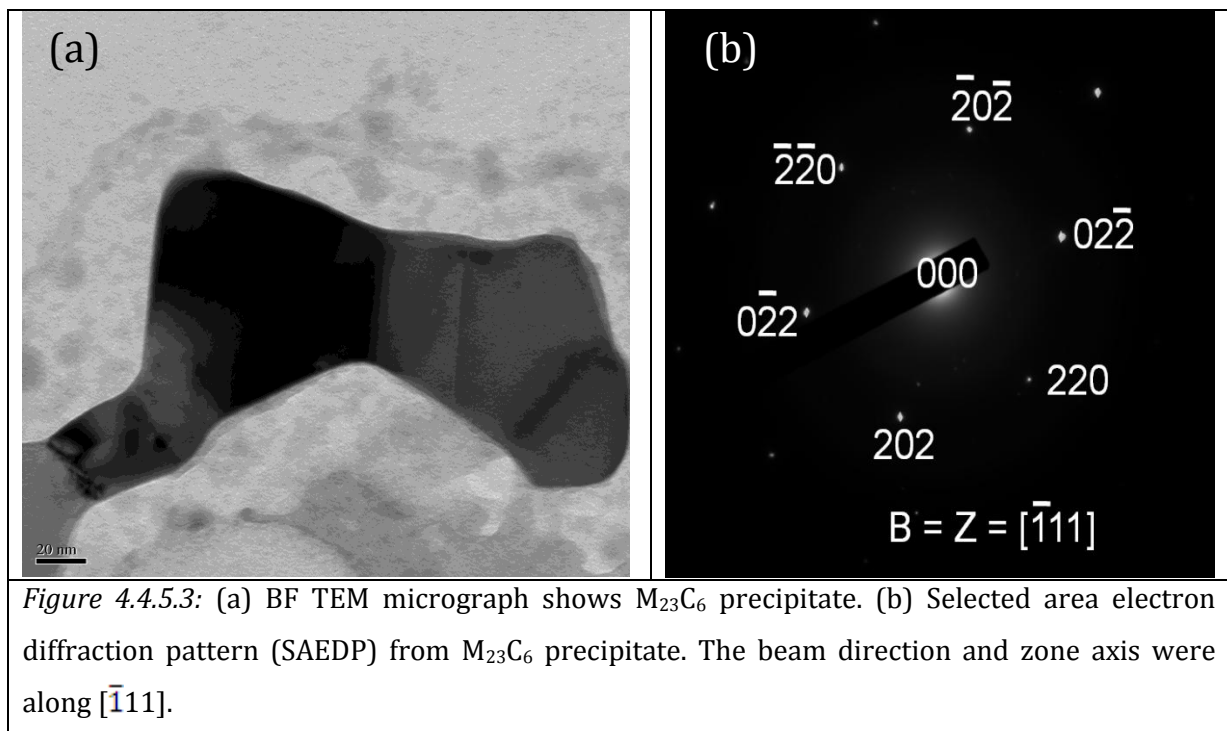


The indexed selected area electron diffraction pattern (SAEDP) is shown in *Figure 4.4.5.2b*. Beam direction and zone axis were along $[012]$ direction. EDX analysis showed that the dark feature in *Figure 4.4.4* is enriched in Ti relative to grain interiors. A standard less typical

quantitative analysis of TiN phase was Ti-1.7Cr. The size of blocky TiN phase in *Figure 4.4.5.2a* is $1.2\mu\text{m}$.

4.4.5.3 $M_{23}C_6$

$M_{23}C_6$ precipitates are expected to strengthen the grain boundary at high temperature (Mankins et al, 1974; Davis, 1999). It was found that grain boundaries were decorated with fine $M_{23}C_6$ precipitates. It was also observed at twin boundaries, twin ends and occasionally in the grain interior. The approximate composition of $M_{23}C_6$ precipitate was Cr-21.5Mo-17.9Ni-7.9Co-0.4Ti-0.2Al (wt. %). The precipitate of $M_{23}C_6$ is shown in *Figure 4.4.5.3*. The indexed SAEDP is shown in *Figure 4.4.5.3 (b)*. The beam direction and zone axis were along $[\bar{1}11]$. The size of the precipitate shown in *Figure 4.4.5.3* is of $0.12\mu\text{m}$.

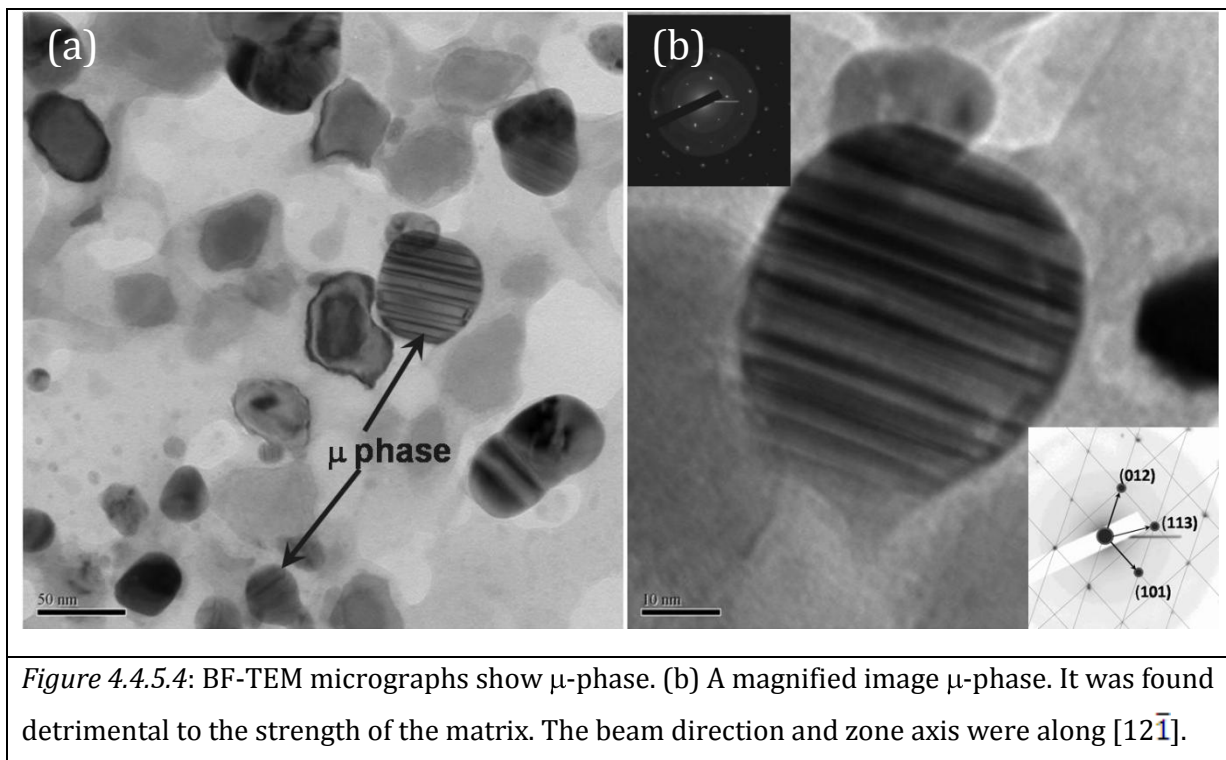


4.4.5.4 μ -phase

μ -phase was found in T0151 specimen after the exposed conditions of high temperature at 700°C and stress of 200MPa. This phase was nucleated at the grain

boundaries and near to carbides. *Figure 4.4.5.4* shows the BF TEM micrographs of μ -phase having globular morphology. *Figure 4.4.5.4 (b)* shows the higher magnification of μ -phase precipitate.

The stacking faults and twins in the structure were the potential reason for its brittle behaviour. The quantitative analysis from EDX showed that the μ -phase was rich in Mo and Cr and a typical quantitative analysis was Mo-19.9Ni-20.8Cr-9.1Co-0.1Ti-0.4Al (wt. %). This phase was also found in T0008 specimen, which was exposed at 650°C for 45,000 hours. However, it was not observed in T0003 specimen, which was exposed at 650°C for 574 hours.



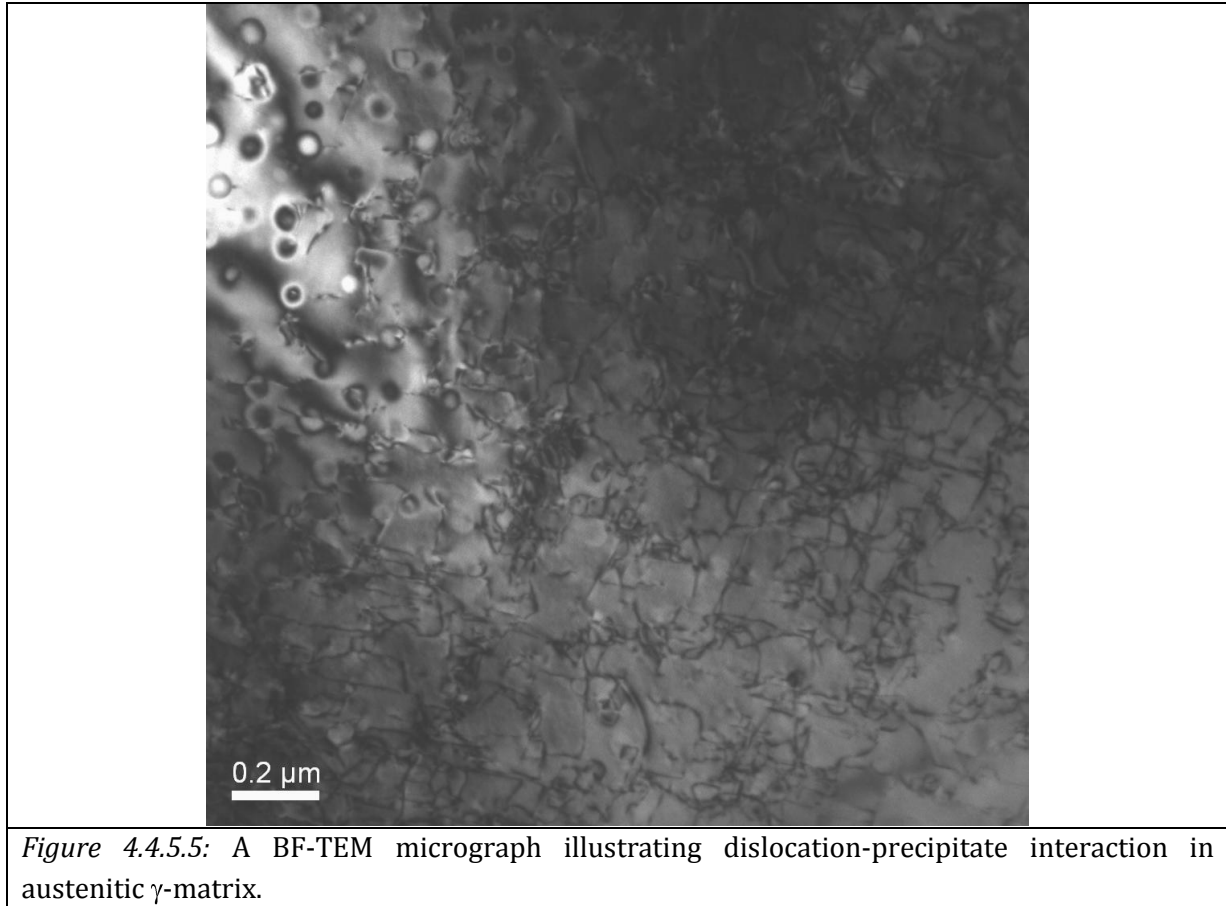
Therefore, μ -phase was found to precipitate in the alloy at high temperature of 700°C or at 650°C when exposed for a longer durations of time.

4.4.5.4 Quantitative Measurements of Dislocation density

The dislocation density was calculated in a similar way as discussed in the previous sections. *Figure 4.3.5.5* shows a typical BF-TEM micrograph illustrating the dislocation structure, and dislocation-precipitate interaction in austenitic γ -matrix. It was found cells almost free from

dislocations and tangles of dislocations in this creep deformed T0151 specimen. Typical values of ρ_d , η_g , ξ_g , and t are listed in Table 4.4.5.5.

<i>Table:4.4.5.5: Typical values for η_g, ξ_g, t and ρ_d</i>			
η_g	ξ_g (Å) at 200kV	t (Å)	ρ_d (lines/m ²)
5	299.25	1296.24	3.35 X 10 ¹³



The average dislocation density was estimated in this T0151 specimen exposed at 700°C to be approximately $3.4 \pm 2.1 \times 10^{13}$ lines/m². The standard deviation in the measurement was 2.1. The coherent precipitates act as a barrier for movement of dislocations. The interaction of precipitates with dislocations was observed in the alloy (*Figure 4.4.5.5*).

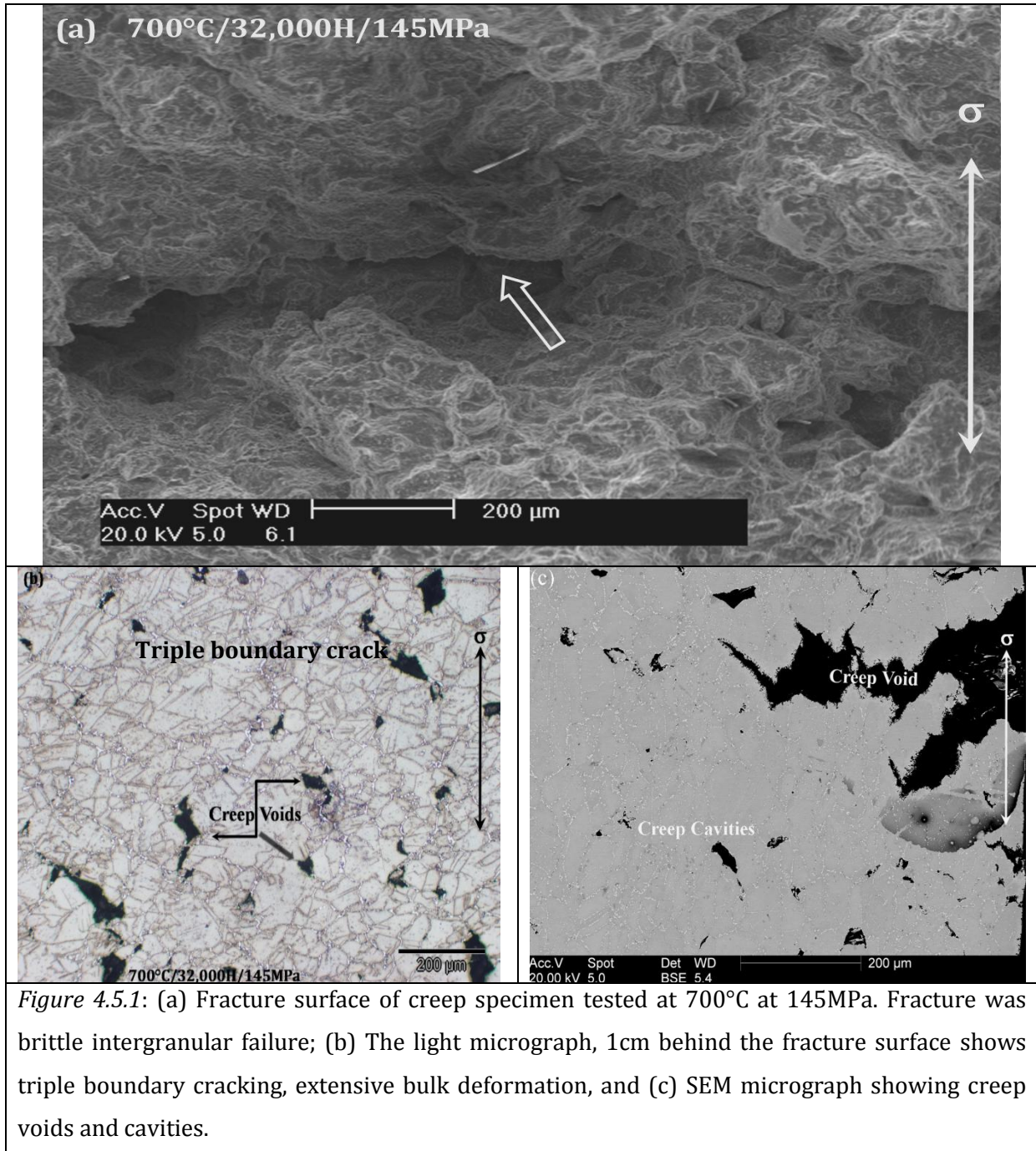
4.5 'Creep-exposed specimen' (T0154) (700°C/32,000Hrs/145MPa)

A solution-annealed IN617 alloy sample was creep tested at 700°C in air under a uniaxial load (estimated) of 145MPa (estimated stress value from creep data of IN617, Ennis et al 2007). This specimen ID: T0154 fractured after long creep duration of 32,000 hours. The reduction in area was not measured for this specimen.

4.5.1 Fractography

The failure mechanism of the creep fractured specimen was analyzed using scanning electron and optical microscopy. A fractograph of the creep failed specimen, T0154 is shown in Figure 4.5.1a.

This specimen showed similar fracture mechanism as observed in T0151 specimen. The fracture mode was intergranular and transgranular for the high temperature exposure. The bulk deformation along the grain boundary was observed as similar to the T0151 specimen. Creep fracture was found to involve with nucleation and growth of micro voids. The coalescence of voids at the grain boundaries was found to form cavities. Crack propagation is shown by arrow in *Figure 4.5.1(a)*. The failure mechanism was further confirmed by optical and scanning electron microscopy. *Figures 4.5.1(b) & (c)* show triple boundary cracking, decohesion and crack propagation along the grain boundaries and creep voids. The direction of loading is shown by the arrows in *Figure 4.5.1*. Creep cavity of size 5 to 20µm (dark spots: marked) is shown in the micrograph, with elongated grains and extensive precipitation along boundaries. This was believed to be longer duration of 32,000 hours at 700°C. High temperature exposure was found to induce recrystallization in the alloy. The open cracks intruded inside the specimen to a depth of 500µm to 1mm.



4.5.2 Grain Morphology

The austenite grain structure of specimen T0154 is shown in *Figure 4.5.2*. The optical microstructure of creep-exposed specimen shows an equiaxed and elongated austenite grain structure with an average size of 93μm, as similar to the grain morphology observed in T0151 specimen, but in contrast to the T0003 and T0008 specimens.

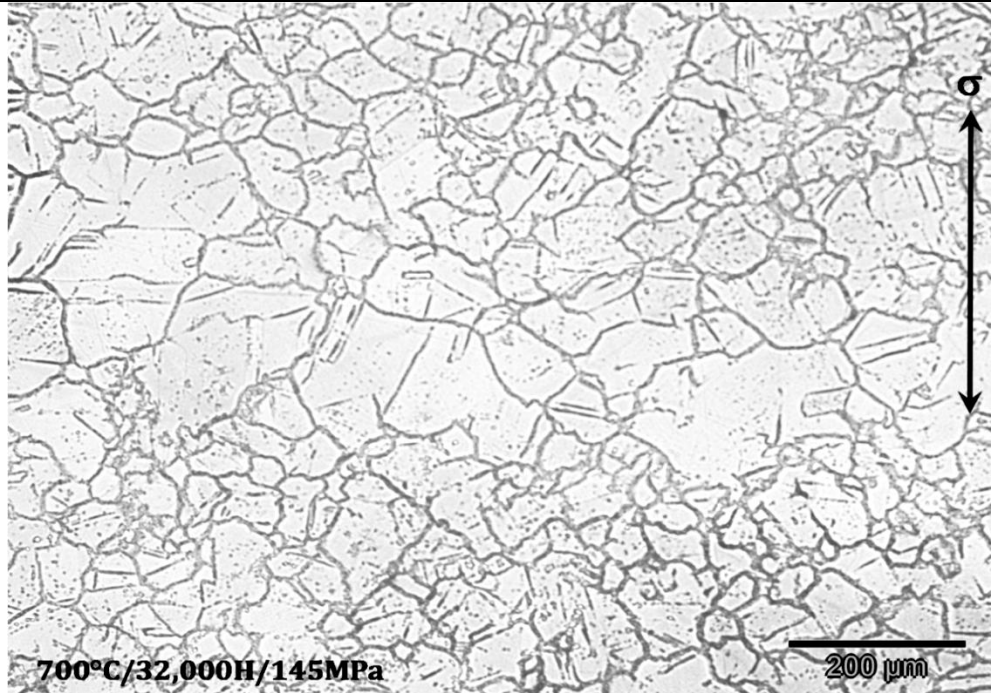


Figure 4.5.2: Optical micrograph of creep exposed specimen T0154 at 700°C shows the typical grain structure, annealing twins are observed in the specimen.

The grain orientation was found to random (Krishna et al, 2009). Annealing twins and twinning boundaries were found in a number of grains, as similar to the as-received and other exposed specimens. They were showed a specific orientation relationship with the grains and formed at the grain boundaries. The gain boundaries appeared serrated along their lengths, as similar to the T0151 specimen. Grain boundary thickening was also found in this specimen and is shown in the optical micrograph (Figure 4.5.2). A summary of morphology of grains, grain boundary and average hardness of the head and gauge is listed in Table 4.5.2.

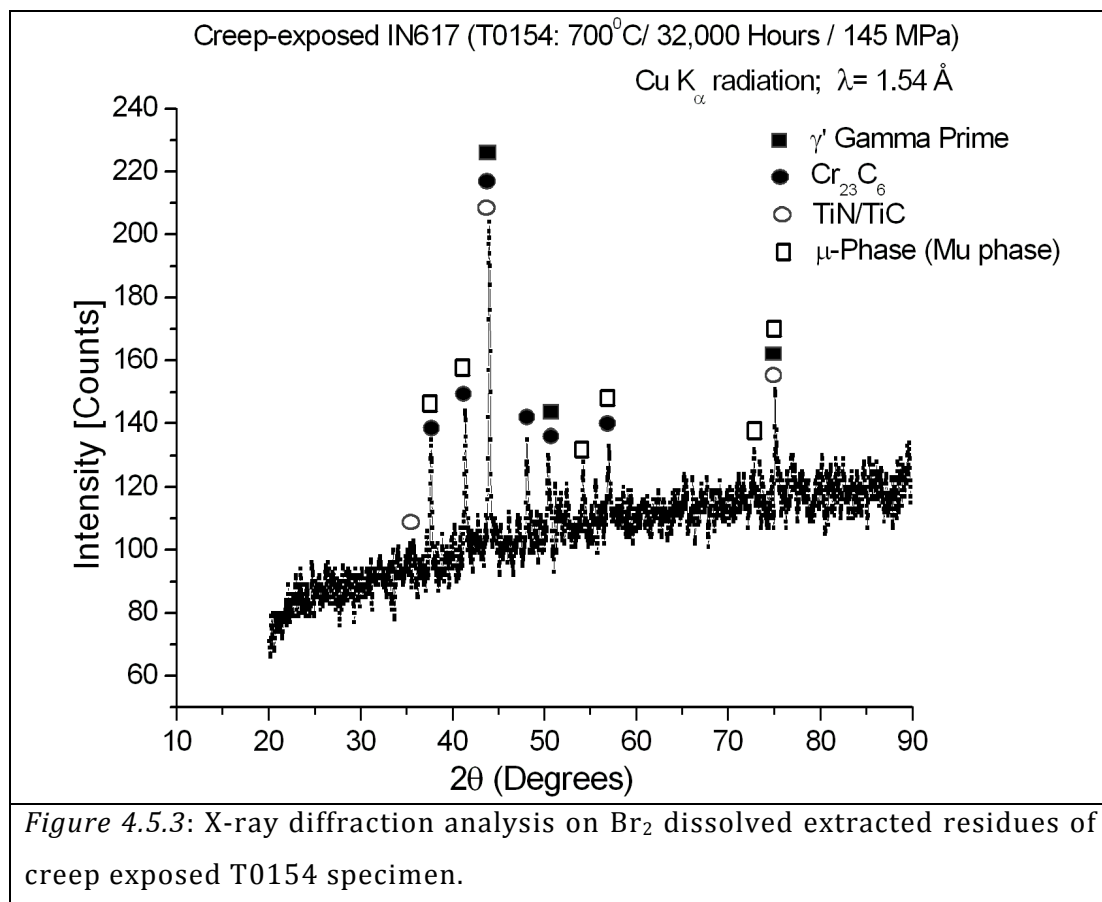
Creep-exposed (700°C/32,000 Hrs /145MPa)	Grain Morphology			VHN (H _v /20)		Grain- boundary morphology
	Grain-size range (μm)	Avg. grain size (μm)	Grain shape	Head	Gauge	
	15 to 222	93	Elongated & Equiaxed	287	313	Serrated

The gauge length hardness substantially increased to an average value of 313Hv whereas head had an average hardness of 287Hv. The higher value of hardness in the gauge length was found due to the extensive precipitation of phases, later it is shown that the are carbides, TCP μ-phase and coarsening of fine carbides. The gauge region was under the effects

of thermal and stress, whereas head region was under the effect of thermal, therefore, hardness was lower in the head than the hardness in the gauge length. The hardness value in the gauge length of T0154 is lower than the hardness value of T0151 specimen; both specimens were exposed at 700°C. T0154 was exposed for a longer durations of 32,000 hours, where as T0151 exposed only for 4,000 hours. The precipitation coarsening due to continued exposure duration in the T0154 specimen was the reason for its lower hardness in the gauge length. The hardness graph of along the head and gauge length is shown in Appendix I.

4.5.3 Phase Identification

A similar technique was used to produce the phase extract powder from the alloy for XRD as discussed in section 3.5. An analysed XRD pattern of T0154 specimen is shown in *Figure 4.5.3*. The precipitates in the creep-exposed specimen were identified as γ' , Cr_{23}C_6 , TiN/TiC and μ -phase, as similar to the T0151 and T0008 specimens.



4.5.4 Precipitate Morphology and Location

In this section precipitates morphology and their locations of specimen T0154 are discussed. *Figure 4.5.4* shows precipitates morphology and their locations in a BSE-SEM micrograph. The identified phases were enriched in Mo, Cr and Ti. They were identified from the XRD as μ -phase, enriched in Mo, $M_{23}C_6$ -type carbides enriched in Cr and $M(C, N)$ -type carbo-nitrides enriched in Ti.

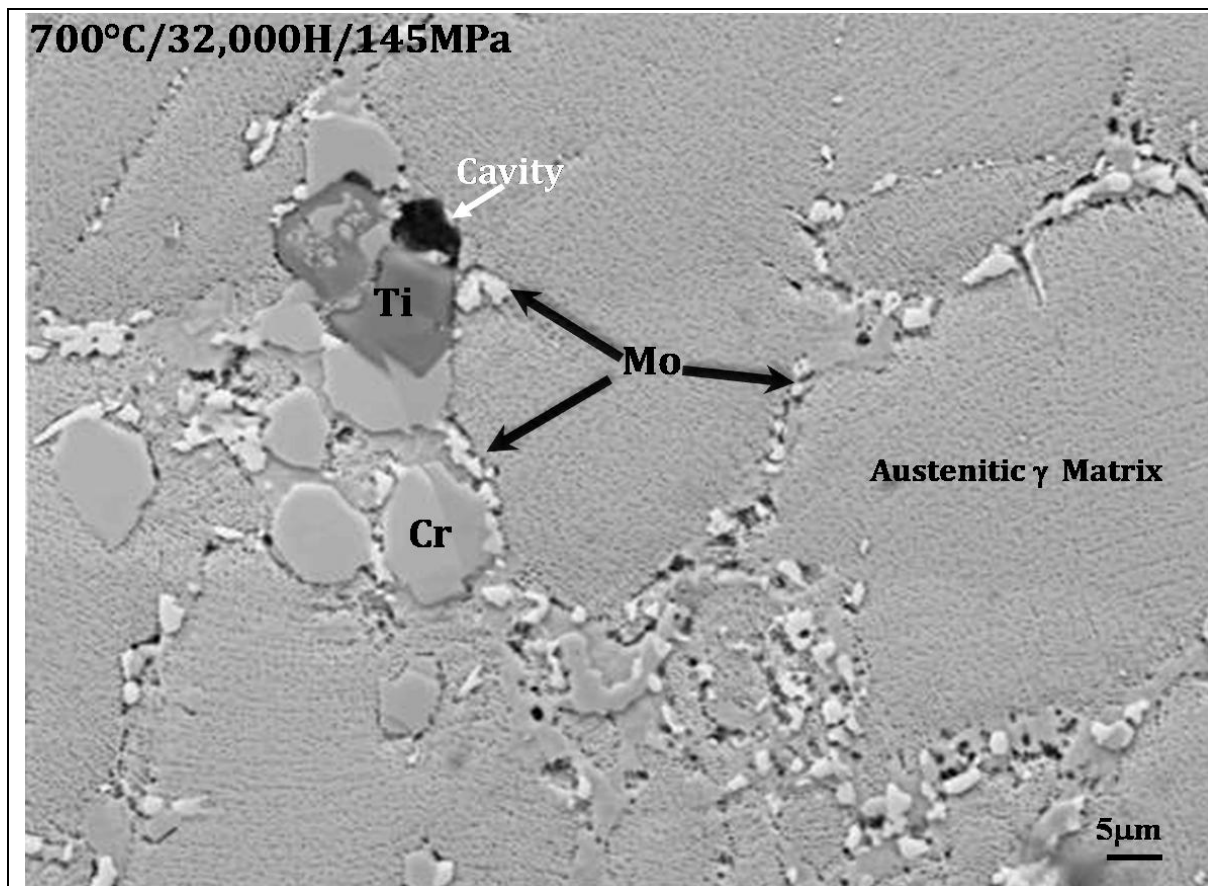


Figure 4.5.4: Backscattered SEM micrograph of T0154 specimen. The blocky shape (dark in figure, marked 'Ti') at the boundary is Ti-enriched precipitate of $Ti(C, N)$ phase. The faceted particles (marked 'Cr'), at inter- and intra-granularly are of $M_{23}C_6$ type carbides. Mo-enriched precipitates are observed along the grain boundaries and near to Cr-enriched precipitate (marked 'Mo'), elemental composition as $(Ni, Co, Fe)_7 Mo_6$.

The elemental analysis of the precipitates from EDX spectra is shown in *Table 4.5.4.1*. The precipitates were found randomly in the matrix and primarily at the grain boundaries.

Their morphology varied from a regular to a totally irregular shape, as similar to the T0151 and T0008 specimens.

$M_{23}C_6$	Cr-29.2Mo-6.3Ni-2Co-2.5Ti
Ti (C,N)	Ti-1.8Cr
$(Ni, Co, Fe)_7Mo_6$	Mo-23.3Ni-22.3Cr-8.6Co-1.7Ti-0.4Al

The size of the Cr-enriched ($M_{23}C_6$) precipitates varied from $0.5\mu\text{m}$ to $7\mu\text{m}$. The size of the Ti-enriched precipitate (TiN/TiC) varied from $6\mu\text{m}$ to $8\mu\text{m}$. The size of Mo-enriched precipitate $(Ni, Co, Fe)_7 Mo_6$ varied from less than $0.1\mu\text{m}$ to $5\mu\text{m}$. The Cr-enriched and Mo-enriched precipitates were extensively precipitated at the grain and twin boundaries, as similar to specimen T0008. The size of the precipitates in T0154 specimen was larger than the size of precipitates in T0008 and T0151 specimens. This was due to the higher exposure temperature for longer duration of 32,000 hours.

The morphology of γ' precipitates was not resolved in SEM, due to their fine precipitate size.

The major precipitates found in the creep exposed T0154 specimen are shown in Table 4.5.4.2. The standard error in the measurement was 0.5- 3.1%.

Specimen ID	Precipitate location	Precipitates Morphology			
		Phases	Size	Shape	Area fraction (%)
T0154	Precipitation intra- and intergranularly and localised precipitation of Mu-phase along the grain and twin boundaries, and near to Cr-enriched precipitates	Ti (C, N)	$6-8\mu\text{m}$	regular to totally irregular geometry	1.1
		$M_{23}C_6$	$0.5-7\mu\text{m}$		6.7
		μ -phase	$<0.1-5\mu\text{m}$	Globular	3.7

Summary

This specimen was not analyzed using the transmission electron microscopy. The exact nature of the different precipitates identified in the SEM can only be resolved after the TEM analysis. However, XRD identified the phases present in this specimen after long creep durations were γ' , TiN/TiC, $M_{23}C_6$ and μ phase. The morphology of the primary precipitates of TiN/TiC, and $M_{23}C_6$ were observed in the SEM micrographs. SEM did not able to resolve the morphology of the γ' precipitates, due to its fine size.

References

- Davis, J.R. (Ed.) (1999). ASM Specialty Handbook: Heat Resistant Materials, ASM International®, Material Park, OH 44073-0002.
- Davies P. and Randle V. Grain boundary engineering and the role of the interfacial plane, *Materials Science and Technology*, 2001, 17 (6), 615-626.
- Dieter. G.E. (1986). *Mechanical Metallurgy*. 3rd ed., Mc Graw-Hill Book Co., New York 1986.
- Garofalo, F. (1965). *Fundamentals of Creep and Creep-Rupture in Metals*, McMillan. Series in Materials Science, McMillan, New York, 1965.
- Gemmell, G. D. and Grant, N. J. (1957). *Trans. AIME*, 209, 417.
- Ham, R. K. 1961. The determination of dislocation densities in thin foils. *Phil. Mag.* 6: 1183-1184.
- Hambleton, R., Rainforth, W.M. and Jones, H. (1997). Dislocation densities, dispersoid identities and the origins of thermal stability and strengthening in three mechanically alloyed aluminium alloys, *Philosophical Magazine A*, 76 (5), 1093-1104.
- Hirsch, P., Howie, P., Nicholson, R.B. Pashley, D. W., and Whelan, M. J. (1977). *Electron Microscopy of Thin Crystals*, Krieger, New York, N.Y.1977.
- Kassner, M. E. and Hayes, T. A. (2003). Creep cavitation in metals, *International Journal of Plasticity*, 19(10), 1715-1748.
- Krishna, R., Hainsworth, S.V., Gill, S.P.A., Strang, A. and Atkinson, H. V. 'Microstructural evolution in creep exposed IN617' 2nd International Creep Conference Creep & Fracture in High Temperature Components: Design & Life Assessment Issues, Proceedings, Shibli IA; Holdsworth SR (Eds.), 1223- 1235. Zurich, Switzerland, 21-23 April, 2009.
- Mankins, W.L., Hosier, J.C and Bassford, T.H. (1974). Microstructure and phase stability of Inconel alloy 617. *Metallurgical Transactions* 1974; 5 (12): 2579-2590.
- Mazur, Z., Ramirez, A.L., Islas, J.A. J. and Amezcua, A.C. Failure analysis of a gas turbine blade made of Inconel 738LC alloy, *Engineering Failure Analysis* 2005; 12: 474-486.
- McLean, D. (1957) *Grain Boundaries in Metals*, Oxford University Press, London (1957).

- Murr, L.E. (1975). Some observations of grain boundary ledges and ledges as dislocation sources in metals and alloys, *Met. Trans.* 6A (1975), 505–515.
- Pollock, T.M. and Argon, A.S. (1992). Creep resistance of CMSX-3 nickel base superalloy single crystals, *Acta Metallurgica et Materialia*, 40 (1), 1-30.
- Rae, C.M.F., Hook, M.S. and Reed, R.C. (2005). The Effect of TCP Morphology on the Development of Aluminide Coated Superalloys, *Materials Science and Engineering*, A396, 231-239.
- Simonetti, M and Caron, P. (1998). Role and behaviour of μ phase during deformation of a nickel-based single crystal superalloy *Materials Science & Engineering. A, Structural Materials: Properties, Microstructure and Processing*, 254, 1-2, 1-12.
- Wilms, G. R., and Wood, W. A. (1948-49). *J.Inst. Met.*, 75, 693.
- Wusatowska-Sarnek, A.M., Blackburn, M.J. and Aindow, M. Techniques for microstructural characterization of powder-processed nickel-based superalloys, *Materials Science and Engineering A* 2003; 360 (1-2): 390-395.
- Yang, J.R. and Bhadeshia, H.K.D.H (1990). The dislocation density of acicular ferrite in steel welds, *Welding Research Supplement*, 3005-307s.

The nickel-chromium Inconel 625 alloy was developed to be a solid-solution-strengthened alloy with relatively high levels of molybdenum and niobium. The strength, mechanical and oxidation properties of Inconel 625 alloy are generally correlated to the solid-solution-strengthened γ phase, the presence of metastable Ni_3Nb phase γ'' (on exposure metastable γ'' transforms to equilibrium δ phase of the same nominal composition), strengthening phases and grain boundary stabilizing phase. The objective of this chapter is to investigate the precipitate evolution in IN625 alloy after short to long term creep tests.

5.1 'As-received'

5.1.1 Grain Morphology

The grain structure and morphology are the controlling microstructural factor for determining the high temperatures creep and fracture behaviour in nickel base superalloys. Therefore, it is vital to control the grain size to avoid excessively fine grains, which decrease the creep and rupture strength and excessively large grains, which lower the tensile strength. An optimal microstructural state is necessary in the alloys and this can be achieved by way of single or multi-stage heat treatments. In this section metallographic observations of grain structure and its morphology for the 'as-received' sample of Inconel 625 (IN625) alloy are discussed.

The 'as-received' sample was in the solution-annealed condition (heat-treated at 670°C/ 10 Hrs/ AC after solutionization for 3 hours at 1100°C followed by water quenching). The optical microstructure of the 'as-received' IN625 sample is shown in *Figure 5.1.1*. The 'as-received' sample showed an equiaxed austenitic γ -grain structure. The grain size varied from a minimum of 35 μm to a maximum of 464 μm , with an average size of 90 μm . This coarse grain

structure in the solution-annealed condition is a prerequisite for high temperature creep rupture strength. EBSD results showed that the grain orientation was found to be random. Annealing twins and twinning boundaries were observed in a number of grains. Twins have a faceted appearance which is a very common feature in IN625 alloy, whereas twin boundaries have flat and straighter sides. Twin bands and boundaries can be observed inside the grains (*Figure 5.1.1*). Twins have a special orientation relationship with the grains and grain boundaries. Twin boundaries are high-energy boundaries and are readily visible. They were formed at the grain boundaries and oriented in specific directions inside the grains. The twin bands were 30-120 μm in width and of the grain size in length. A summary of the morphology of grains and grain boundary is listed in *Table 5.1.1*.

As-received IN625	Grain Morphology			ASTM grain size No.	Grain-boundary morphology
	Grain-size range (μm)	Avg. grain size (μm)	Grain shape		
	35 to 464	90	Equiaxed		

The Vickers hardness value of the ‘as received’ sample was found to be $190.5 \pm 6 \text{ H}_V/20$.

Intergranular precipitates were found in the alloy to strengthen matrix at high temperature (Mankins et al 1974; Davis 1999). Solutionization and ageing heat treatments were used to dissolve the intragranular precipitates (mainly carbides) and to enhance the localized precipitation of carbides along the grain boundaries. *Figure 5.1.1* shows that there are fine inter- and intragranular precipitates are randomly distributed in the alloy.

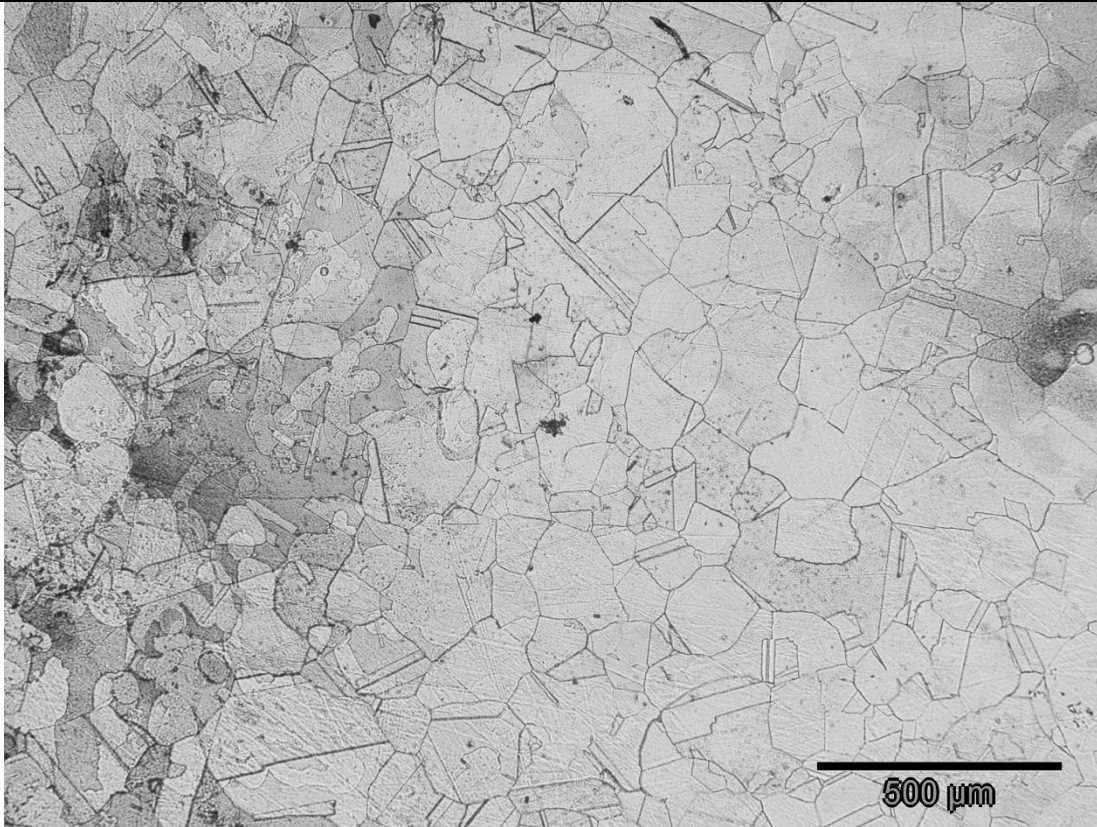
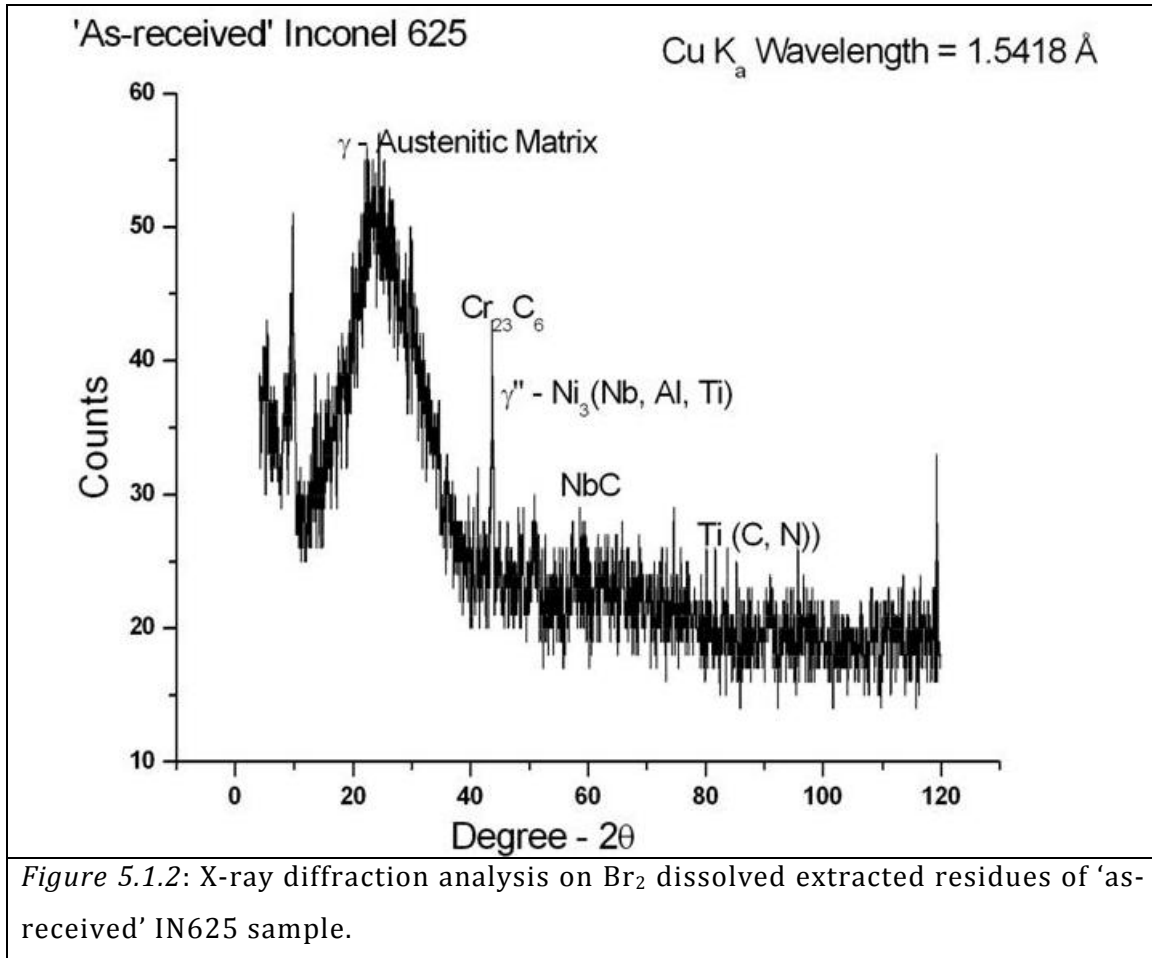


Figure 5.1.1: Optical micrograph of the 'as-received' (solution-annealed) IN625 shows the grain structure and annealing twins in a number of grains.

5.1.2 Phase Identification

An analysed X-ray diffraction pattern of the 'as-received' IN625 sample is shown in *Figure 5.1.2*. The identified phases were austenitic γ - matrix, γ'' - gamma double prime, Nb-enriched and Ti-enriched MC type carbides, and $M_{23}C_6$ type Cr-enriched carbides. The presence of γ'' in the 'as-received' IN625 was difficult to register, since the morphology of the precipitate was very fine and of nanometres in size range. However, peaks from γ'' were registered in XRD from the matrix dissolved residue of the 'as-received' IN625 sample.



The identified phases were further confirmed by the EDX measurements in the transmission electron microscopy (TEM) and by the analysis of selected area electron diffraction (SAED) patterns, discussed later in this chapter.

5.1.3 Precipitate Morphology and Location

The role of precipitate morphology and their location were found to influence the high temperature creep-rupture behaviour in nickel base alloys. In this section precipitate morphology and their locations in 'as-received' IN625 sample are discussed. A BSE-SEM micrograph in *Figure 5.1.3* shows the precipitates morphology and their locations in the 'as-received' sample. Three major precipitates were found in the 'as-received' IN625 sample. They were enriched in Nb, Ti and Cr. All the three enriched precipitates were marked in the *Figure 5.1.3*.

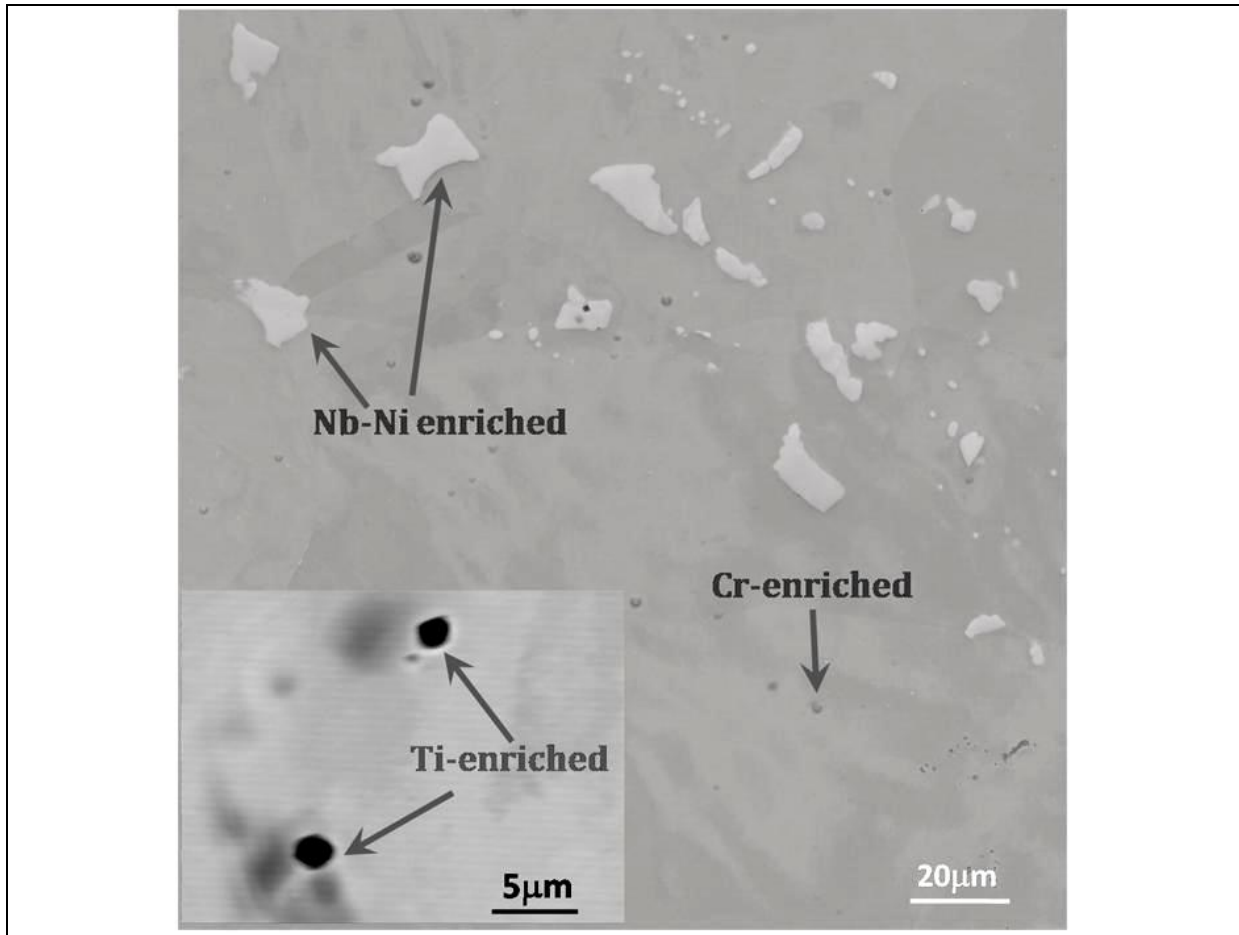


Figure 5.1.3: Backscattered scanning electron micrograph of 'as-received' IN625. Inset micrograph shows Ti-enrich precipitates (arrowed). Cr- and Nb-enriched precipitates are found intra- and intergranularly in the matrix.

The precipitates enriched in Cr, Ti, and Nb, appeared as $M_{23}C_6$ -type carbides, TiN/TiC and NbC. These precipitates were distributed randomly in the alloy. Their morphology varied from a regular to a totally irregular. The elemental composition of these precipitates was measured by EDX and is shown in *Table 5.1.3.1*.

Austenitic γ -Matrix	Ni-20.3Cr-6.7Mo-2.2Fe-2.7Nb
$M_{23}C_6$	Cr-7.1Mo-19.6Ni-2.1Fe-2.2Nb
Ti (C, N)	Ti-10.1Cr-18.9Ni-20.5Nb-9.2Mo
NbC	Nb-13.5Mo-6.9Ni-2.3Cr-1.7Ti

The hardening phase in the austenitic gamma (γ) matrix, in the majority of Ni-base superalloys, is the ordered intermetallic metastable γ' - phase, however, in IN625 alloy,

hardening is caused primarily by the precipitates of γ'' or Ni_3 (Nb, Al, Ti). The presence of γ'' and morphology in 'as-received' IN625 was observed in transmission electron microscopy, and is discussed in the next section. The shape and size of the γ'' precipitates were of circular disc morphology with an average size of 5.5 ± 1 nm. The size of the Cr-enriched ($M_{23}C_6$) precipitates varied in size from less than $0.04 \mu m$ to $1 \mu m$. The size of the Ti-enriched [Ti (C, N)] precipitate varied from $0.1 \mu m$ to $2 \mu m$. The size of the Nb-enriched (NbC) precipitate varied from $0.1 \mu m$ to $12 \mu m$. The precipitates morphology and their locations, in 'as-received' IN625, are listed in *Table 5.1.3.2*.

Specimen ID	Precipitate location	Precipitates Morphology			
		Phases	Size	Shape	Area fraction (%)
As-received IN625	Throughout the matrix	γ''	3-8nm	disc	7.65
	Intra- and inter-granularly, at twin boundaries	Ti (C,N)	0.1-4 μm	regular to totally irregular geometry	0.05
		$M_{23}C_6$	0.04-1 μm		0.21
		NbC	0.1-12 μm		14.4

The precipitates of size less than $1 \mu m$ were intergranularly dispersed and some larger particles were observed within the grains. Ti-enriched precipitates, of M(C, N) type carbo-nitrides were randomly distributed inside the grains and at the twin boundaries. XRD analysis confirmed the precipitates of Cr-rich, Ti-rich and Nb-rich are $M_{23}C_6$ type carbides, Ti (C, N) type carbo-nitrides and NbC type carbides. Carbides were present in the matrix and primarily, at the grain boundaries. The energy dispersive X-ray microanalysis (EDX) showed that the grain boundary precipitates were mostly rich in chromium. The blocky particles were mainly of niobium enriched, in contrast to as-received IN617. The large primary NbC carbides were un-dissolved primary carbides after solution-annealing; however most of $M_{23}C_6$ carbides were dissolved during the solution annealing and precipitated along the grain boundaries.

5.1.4 Transmission Electron Microscopy (TEM) Observations

The microstructure of 'as-received' IN625 was analysed using analytical transmission electron microscopy and the results are discussed in this section. The precipitates of different phases observed in *Figure 5.1.3* were further identified in TEM. The microstructure of 'as-received' sample consists of γ -austenitic matrix, precipitation hardened ordered BCT precipitates of γ'' (DO₂₂ structure) or Ni₃ (Nb, Ti, Al) phase, NbC carbides, dominant intergranular precipitates of M₂₃C₆ (M = Cr, Mo, Co) phase and Ti (C, N), with an array of dislocations (Brown and Muzyka, 1987; Bhom et al, 1970; Floreen et al, 1994; Tawancy et al, 1990; Sundararaman et al, 1988 and Sundararaman et al, 1997). The precipitates were mainly located at prior austenite grain boundaries and sub-grain boundaries and also appeared randomly within the matrix. The morphological geometries of these precipitates are discussed in the following subsections. The dislocations were generated during the quenching operation and typical precipitate-dislocation interactions with regular precipitates are shown in *Figure 5.1.4*.

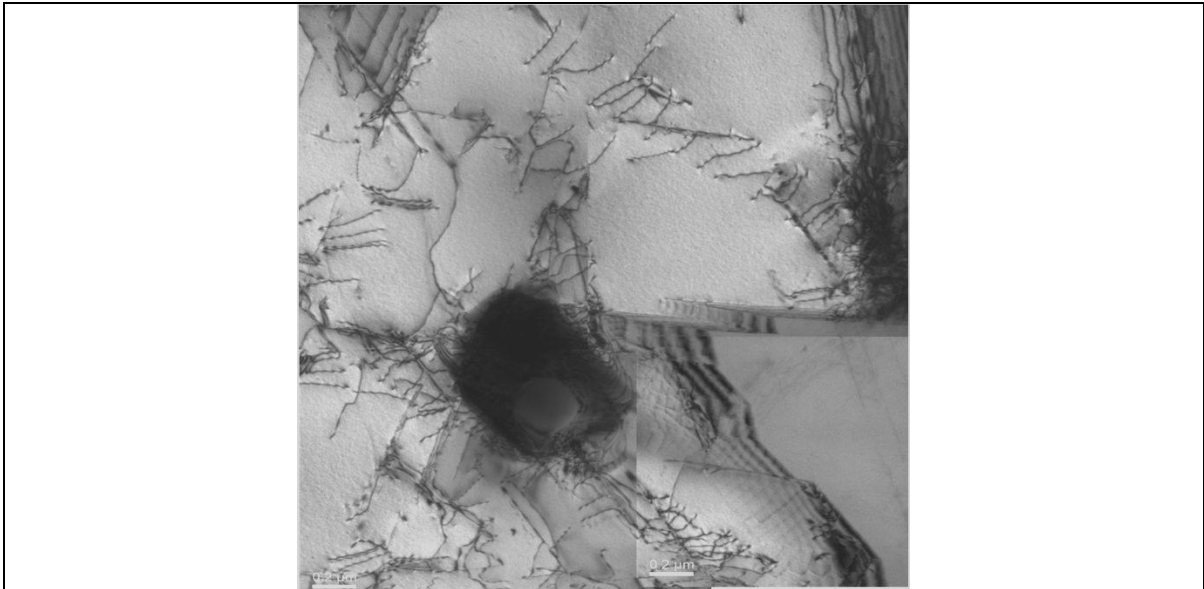
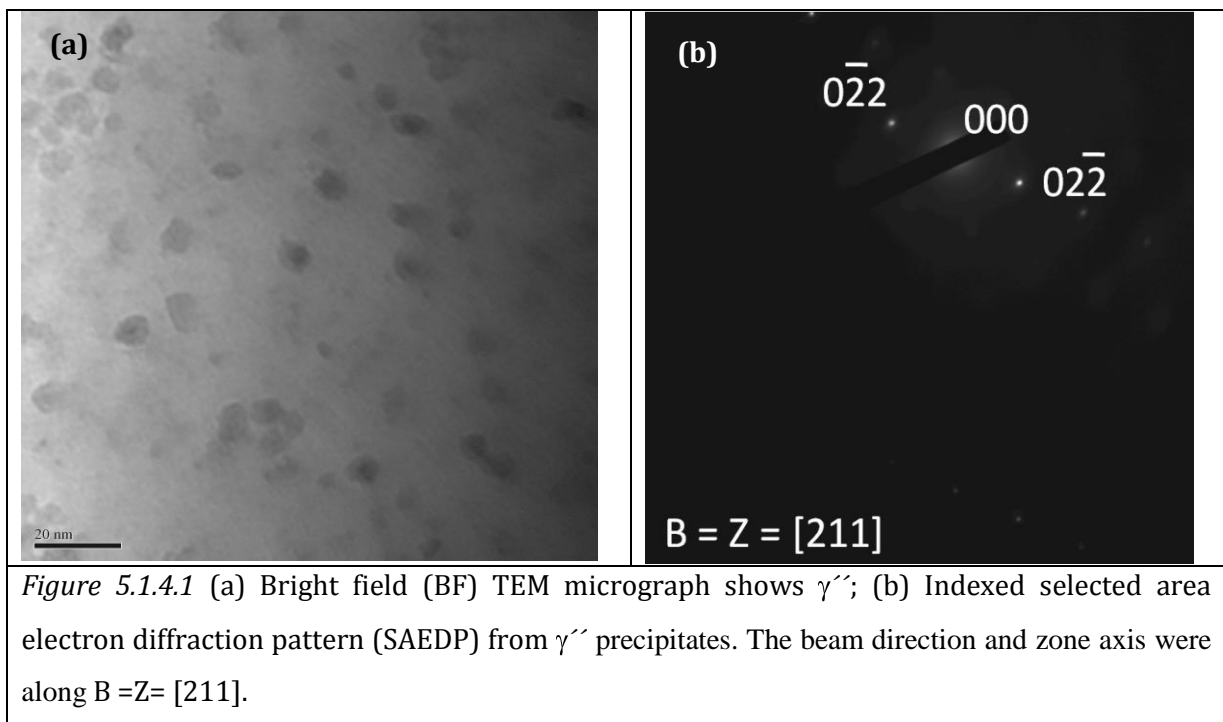


Figure 5.1.4: Montage of BF-TEM micrographs of 'as-received' IN625 alloy shows the dislocation structure, precipitate and dislocation-particle interaction in a solid solution strengthened austenitic γ - matrix. A blocky carbide precipitate in the micrograph, is of NbC.

Figure 5.1.4 shows a high density of dislocations is uniformly distributed in the austenitic matrix and dislocations are pinned by the precipitate of NbC carbide phase.

5.1.4.1 Gamma Double Prime (γ'')

γ'' phase has an ordered body-centered-tetragonal DO_{22} crystal structure (Cozar and Pineau, 1973). A coherent strain from the lattice distortions of γ'' was found to provide strengthening to the γ matrix (Oblak et al, 1974). The γ'' phase is metastable and its thermodynamically stable equilibrium form is δ phase, which has an incoherent, orthorhombic crystal structure. The γ'' phase is an ordered phase containing Nb, Al, Ti and Ni, which is coherent with the disordered FCC austenitic γ phase. *Figure 5.1.4.1* shows a TEM micrograph of fine γ'' precipitates and indexed selected area electron diffraction pattern from these precipitates.



The indexed SAEDP from γ'' is shown in *Figure 5.1.4.1b*. The beam direction and zone axis are shown in *Figure 5.1.4.1b* $\{B=Z= [211]\}$. The γ'' precipitates coherent interfaces were in an orientation relationship with γ -matrix as $(100)_{\{\text{matrix-}\gamma\}} \parallel (100)_{\{\gamma''\}}$; $[010]_{\{\text{matrix-}\gamma\}} \parallel [010]_{\{\gamma''\}}$.

5.1.4.1 (a) Volume fraction of Gamma Double Prime

The estimated volume fraction of γ'' precipitate is listed in *Table 5.1.4.1*. The procedure for the estimation was similar as used for other samples of IN617 and was discussed in section 3.7. The measured carbon replica thickness was 24nm.

<i>Table 5.1.4.1: Estimated values of volume fraction in 'as-received' IN625</i>				
Diameter (2R, nm)	$A_{ext} = \frac{N\pi R^2}{A_0}$	A_0 (nm ²)	$A_f = 1 - \exp(-A_{ext})$	$V_f = 1 - (1 - A_f)^{\frac{4R}{3h}}$
5.46	0.154	25600	0.143	0.0765

The volume fraction of gamma double prime in the specimen was estimated to be approximately 8%.

5.1.4.2 TiN

Ti-enriched precipitates in 'as-received' IN625 sample, (noted in *Figure 5.1.3*), were identified in TEM. *Figure 5.1.4.2* shows BF-TEM micrograph of blocky TiN precipitate. Selected area electron diffraction pattern (SAEDP) confirmed this precipitate as TiN. EDX analysis was further confirmed that dark feature was enriched in Ti relative to the grain interiors.

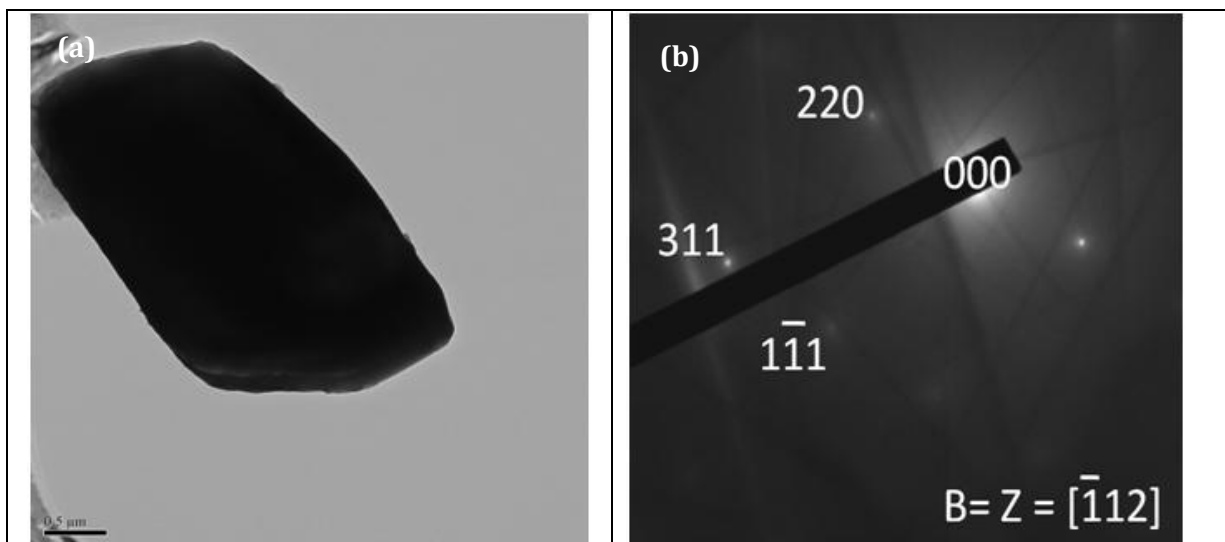


Figure 5.1.4.2: (a) BF TEM micrograph shows morphology of TiN precipitate; (b) Selected area electron diffraction pattern (SAEDP) from TiN precipitate shown in (a), Beam direction was $B=Z=[\bar{1}12]$.

Beam direction and zone axis were along $[\bar{1}12]$ direction. The size of the blocky TiN in *Figure 5.1.4.2a* is $\sim 3\mu\text{m}$. An indexed SAEDP is shown in *Figure 5.1.4.2b*.

5.1.4.3 $M_{23}C_6$

$M_{23}C_6$ precipitates form during ageing heat-treatment from the degradation of M(C, N) carbo-nitrides and reaction of chromium with soluble residual carbon in the alloy matrix, as discussed in section 1.1.6.

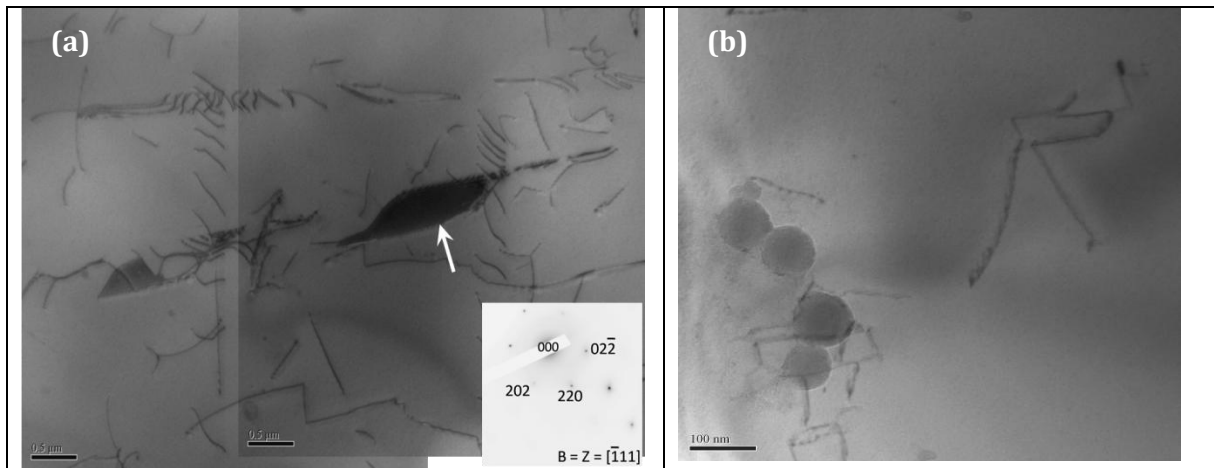


Figure 5.1.4.3: (a) BF TEM micrograph shows $M_{23}C_6$ precipitate near the dislocation arrays (arrowed), inset shows selected area electron diffraction pattern (SAEDP) from $M_{23}C_6$ precipitate. (b) A typical TEM micrograph shows circular $M_{23}C_6$ precipitates.

Their presence at the grain boundaries, near twin boundaries strengthens the grain boundaries by pinning it. The approximate composition of $M_{23}C_6$ precipitate is Cr-17.7Ni-17.1Nb-5.1Mo-1.8Fe (wt.%). The precipitate of $M_{23}C_6$ is shown in the BF-TEM micrograph in *Figure 5.1.4.3*. Other features such as interfacial dislocations and dislocation arrays can also be seen in the BF-TEM micrograph (*Figure 5.1.4.3*). The circular precipitates of $M_{23}C_6$ are also observed in the sample in size range from 50 to 80nm (*Figure 5.1.4.3b*).

5.1.4.4 NbC

Figure 5.1.4.4 shows the NbC carbide in 'as-received' IN625. The indexed SAEDP is shown in *Figure 5.1.4.4b*. The beam direction and zone axis were along $[001]$. The standardless quantitative analysis of NbC is Nb-13.5Mo-6.9Ni-2.3Cr-1.7Ti (wt.%). NbC

precipitates were found in different morphology from irregular to regular of varying sizes from 250nm to 12 μ m. It was found inter- and intragranularly in the alloy.

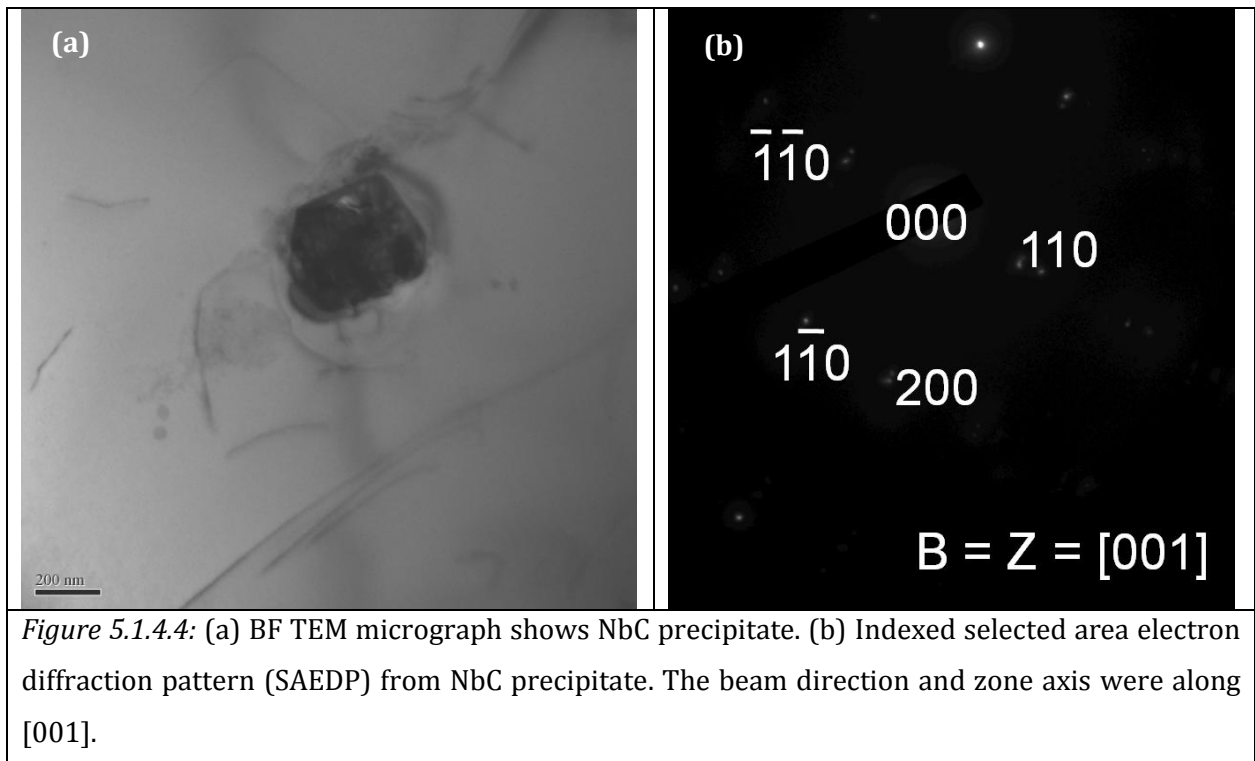


Figure 5.1.4.4: (a) BF TEM micrograph shows NbC precipitate. (b) Indexed selected area electron diffraction pattern (SAEDP) from NbC precipitate. The beam direction and zone axis were along [001].

5.1.4.5 Quantitative Measurements of Dislocation density

The quantitative measurement of dislocation density was estimated as a similar way used for previous IN617 samples and briefly discussed here. An array of dislocations and piled-up dislocations near to the grain boundary and around the precipitate are shown in *Figure 5.1.4.5*. The dislocation density was estimated to be $13.5 \pm 6.1 \times 10^{12}$ lines/m². The standard deviation in the measurements was 6.1.

The dislocation density was obtained from the *equation 4.1.4.4*, as discussed in subsection 4.1.4.4 for IN617 alloys. The value of dislocation density was for steel and aluminium was discussed in Ham, 1961; Hirsch et al, 1977; Hambleton et al, 1997; Yang & Bhadeshia, 1990. But, no literature was found for nickel base superalloys, IN625.

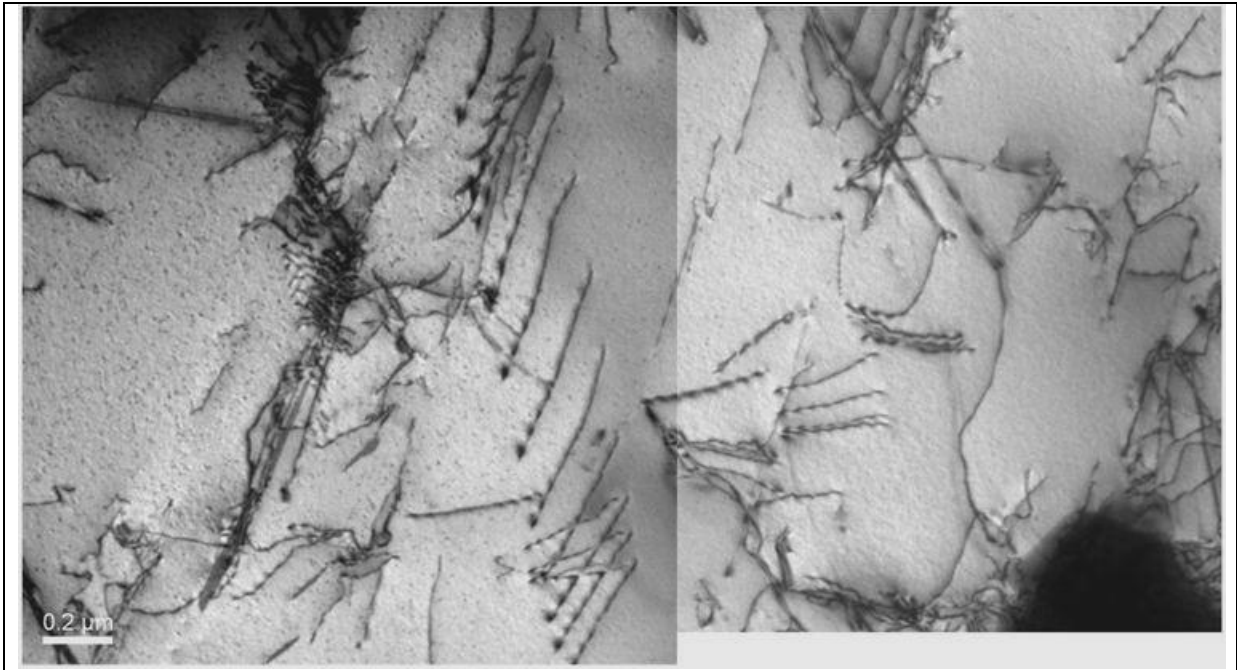


Figure 5.1.4.5: BF TEM micrographs illustrating (a) dislocation structure, precipitates particle, dislocation-particle interaction and dislocations piled up.

The foil thickness was estimated by counting the extinction contours as discussed in the previous subsection 4.1.4.4. Equation 5.1.4.4a was used to calculate the foil thickness. The typical values of η_g (extinction contours), ξ_g , and t (foil thickness) are listed in Table 5.1.4.5.

$$t = \eta_g \xi_g; \quad (5.1.4.5a)$$

where η_g is the number of extinction fringes observed at an inclined boundary when the diffracted beam is represented by the reciprocal lattice vector g . The ξ_g is the extinction distance for that g vector and accelerating voltage.

Table 5.1.4.5: Typical values for η_g , ξ_g , t and ρ_d			
η_g	ξ_g (Å) at 200kV	t (Å)	ρ_d (lines/m ²)
5	299.25	1496.24	13.5 X 10 ¹²

5.2 'Creep-exposed specimen' (S9980) (650°C/ 33000Hrs)

The solution-annealed condition (heat-treated at 670°C/ 10 Hrs/ AC after solutionization for 3 hours at 1100°C followed by water quenching) alloy was machined for creep test specimen. The creep test was conducted at 650°C in air under a uniaxial intermediate load. This specimen ID: S9980 fractured after 33,000 hours of creep duration. The area reduction was measured from the fractured specimen as 21.8%.

5.2.1 Grain Morphology

An optimal grain structure is necessary for the potential high temperature alloys. In this section the morphology of the grains in creep-exposed IN625 specimen is discussed. The optical microstructure of the 'creep-exposed' IN625 specimen is shown in *Figure 5.2.1*.

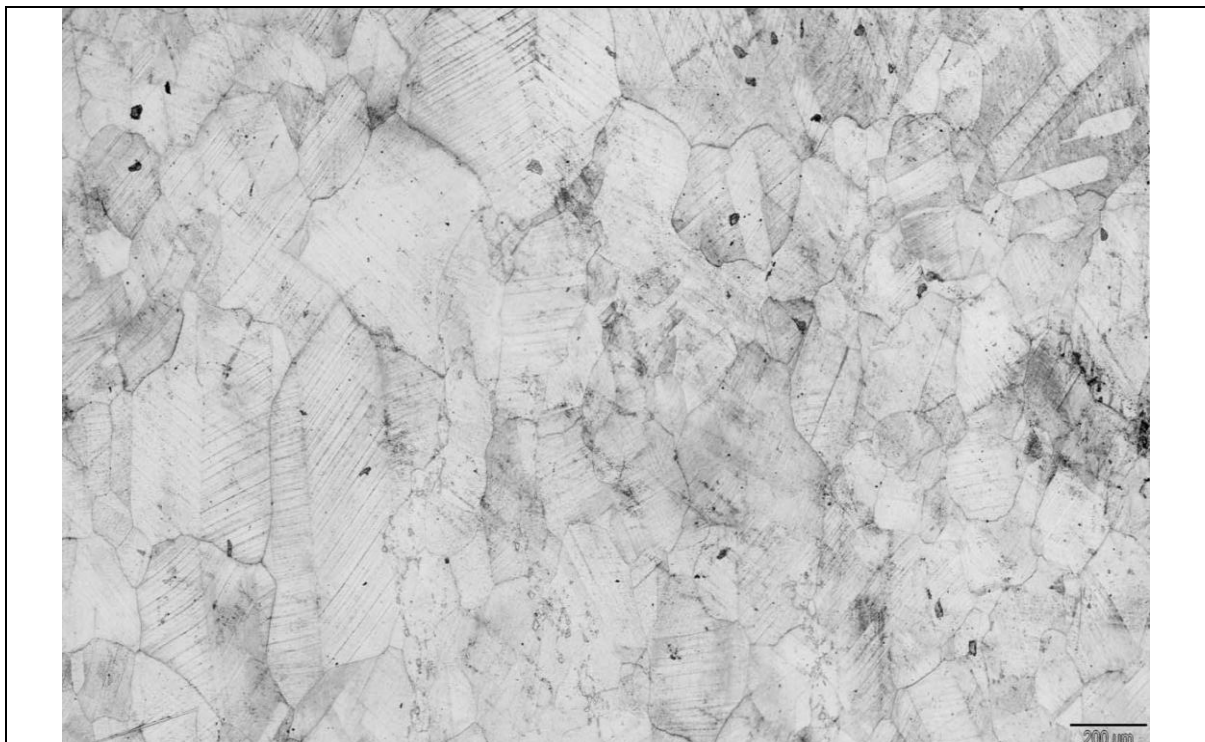


Figure 5.2.1: Optical micrograph of grain structure of gauge length, observed in specimen (S9980) after creep test at 650°C. A typical cell structure and sub-grains can be observed in the micrograph after 33, 000 h of creep exposure. Fine slip lines and slip bands can be seen in almost each grain, and are oriented along (111) plane.

The creep-exposed specimen showed an equiaxed austenitic γ -grain structure. The austenite grain size varied from a minimum of $70\mu\text{m}$ to a maximum of $633\mu\text{m}$, with an average size of $132.8\mu\text{m}$. The ASTM grain size number was in the range of 2-3. Fine slip lines and slip bands were observed in a number of grains. The coarse slip lines can be observed in the grain at different orientation (*Figure 5.2.1*). Clustering of these fine slip lines were found to form coarse slip band, and can be observed in optical micrograph (*Figure 5.2.1*). Slip was active on $\{111\} \langle 110 \rangle$ slip system. However, multiple slip was also found in some grains, and in those grains more than one slip systems were active. Fine slip lines is shown in the micrograph in *Figure 5.2.1*. They were observed in almost all the grains oriented along the $\{111\}$ planes. Slip bands were discontinuous and straight and of grain diameter in size. The average length of slip bands was observed in the range of $5\text{-}215\mu\text{m}$. The average slip-line spacings were in range of $1\text{-}5\mu\text{m}$. This slip-band spacing was found to depend on composition, stress and temperature (Gemmel et al., 1957; Wilms et al., 1958-59). It was observed that the decrease in creep stress, lead to increase in the distance between the slip bands. The slip-band spacing was found to increase with an increase in the temperature. The mode of deformation at high temperature was observed as deformation or kinks bending, multiple slip, cross-slip, climb, lattice bending and rotation, twinning and grain-boundary sliding. At sufficiently high temperature more than one deformation modes were found to become operative. A kink/deformation bending was found to result from the lattice rotation and consequently form deformation bands. A schematic representation of deformation band is shown in *Figure 5.2.1(i)* as observed in optical micrograph of *Figure 5.2.1*. The formation of these deformation bands was found to be followed by the appearance of slip bands on the primary slip systems (Garofalo, 1965). A summary of the morphology of grains and grain boundary is listed in *Table 5.2.1*.

Creep-exposed (650°C/ 33,000 Hrs)	Grain Morphology			ASTM No.	VHN(Hv/20)		GB morphology
	Grain-size range (μm)	Avg. grain size (μm)	Grain shape		Head	Gauge	
					70 to 633	132.8	

The substantial increase in hardness in the gauge length to an average value of 403Hv from the head region of average hardness from 334.5Hv was due to the combined effects of strain and temperature.

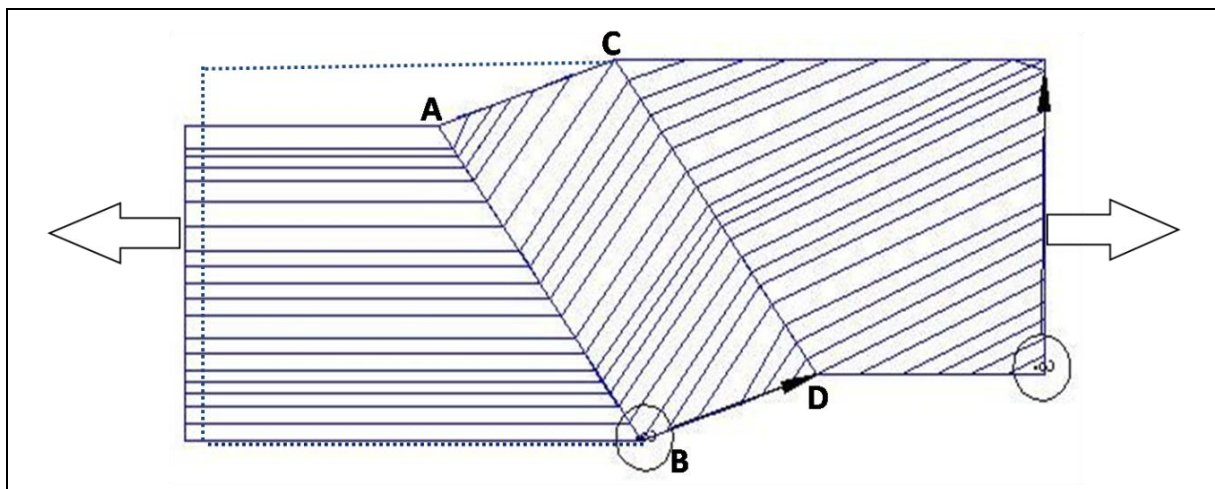


Figure 5.2.1 (i): Schematic representation of the formation of a deformation band under a uniaxial tensile stress. The bend planes (AB & CD) are perpendicular to the slip direction and orientation change can be noted across the single twin plane.

The increase in hardness during the creep exposure for 33,000 hours was due to the precipitation of fine carbides along the grain boundaries, grain interiors and work hardening due to dislocations. The long creep exposure led to softening the matrix due to carbides coarsening and precipitation. This specimen fractured after a long duration of creep exposure.

5.2.2 Fractography

The failure mechanism of the creep fractured specimen S9980 was analyzed using scanning electron and optical microscopy. Fractographs of the creep failed specimen, S9980, are shown in Figure 5.2.2.

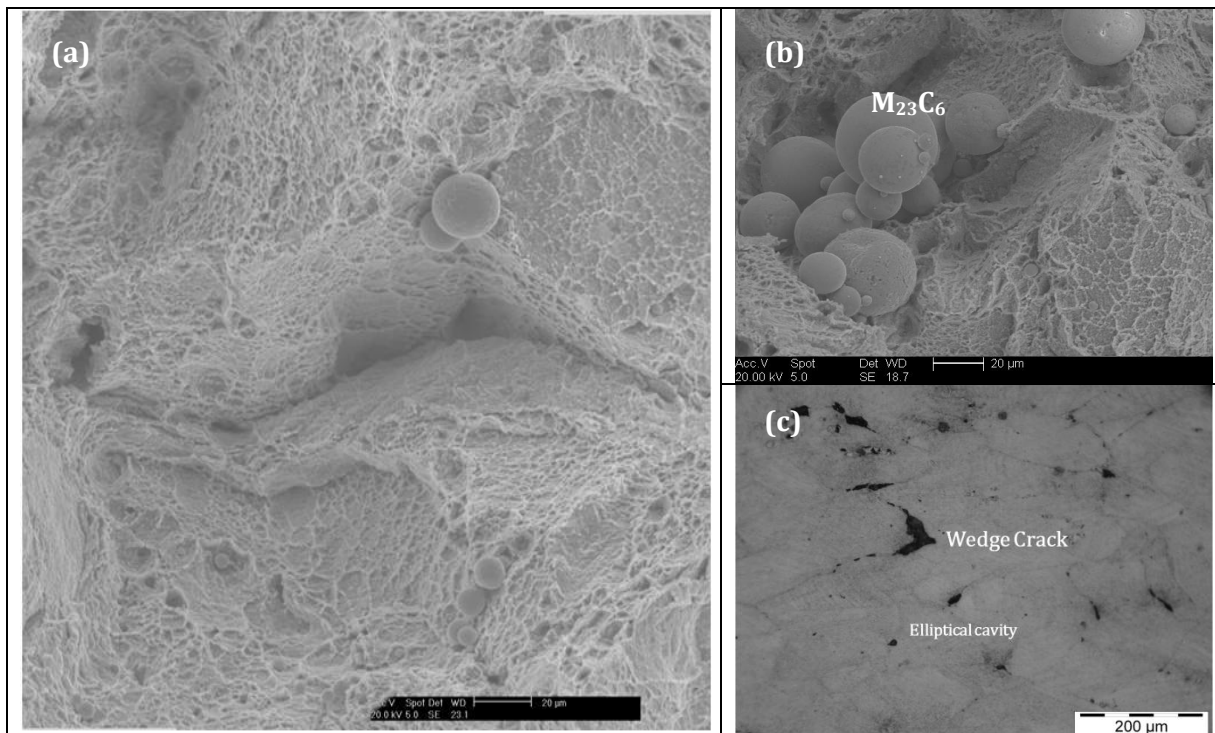
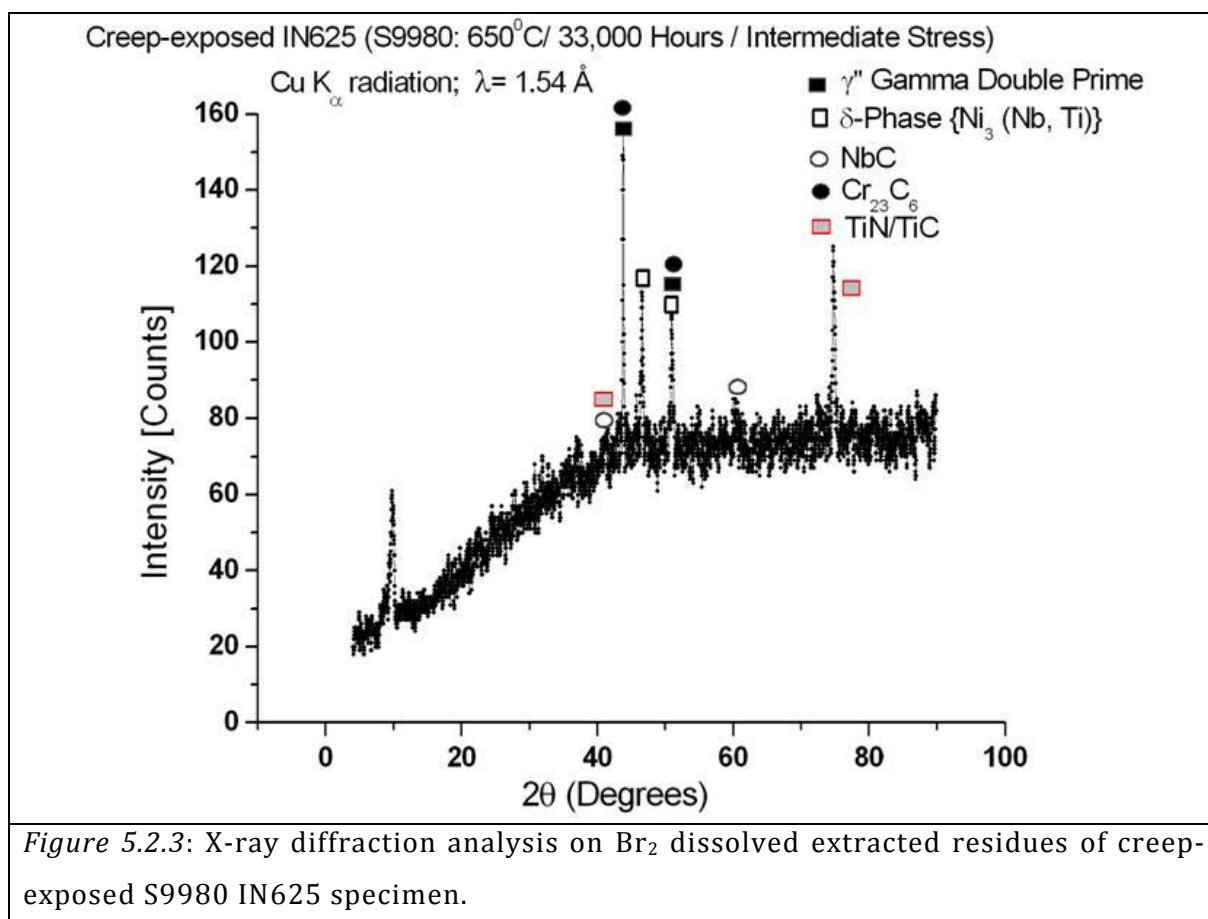


Figure 5.2.2: SEM micrographs show mixed mode of (intergranular & transgranular) creep failure in creep-exposed specimen S9980. Grain boundaries decohesion and very big spherical precipitates of chromium carbides are shown in the micrographs. The direction of loading is perpendicular to the wedge crack propagation.

The failure mechanism was mixed mode, intergranular and transgranular fracture. Grain boundary creep cavitation (arrowed) and spherical chromium carbides precipitates (identified by EDX) on the fracture surface are shown in the *Figure 5.2.2*. The failure mechanism of this exposed specimen was further confirmed by optical microscopy of a polished cross-section of the fractured surface. The spherical chromium precipitates shown in the *Figure 5.2.2b*, were formed during the heat treatment process, since lower surface energy favours the formation of the spherical shape. The presence of these spherical precipitates favours the fracture initiation and crack propagation along the grain boundaries where spherical precipitates are situated. *Figure 5.2.2c* shows further confirmation of wedge cracking, and formation of elliptical cavities at the grain boundaries. The direction of loading is perpendicular to the wedge crack. The open cracks intruded inside the specimen to a depth of 90 to 490 μm.

5.2.3 Phase Identification

The precipitates were identified through X-ray powder diffraction analysis on electrolytic and Br₂ dissolved extracted residues of carbides, nitrides and intermetallics.



The resultant X-ray patterns were analysed by comparing experimental diffraction data with the standard (JCPDS) diffraction data. An analysed X-ray diffraction pattern of this creep-exposed specimen is shown in *Figure 5.2.3*. The identified phases were an austenitic γ-matrix, γ''-gamma double prime, δ-phase: Ni₃ (Nb, Ti, Al), Nb-enriched and Ti-enriched MC type carbides, and M₂₃C₆ (Cr-enriched).

5.2.4 Precipitate Morphology and Location

The precipitate morphology and its precipitation location in creep exposed specimen S9980 are discussed in this section. A backscattered electron (BSE) SEM micrograph of specimen S9980 in *Figure 5.2.4* shows the precipitate morphology and its locations. The precipitates found in S9980 specimen were needle type Nb-enriched δ -phase in two-near orthogonal directions, and Nb-, Ti- and Cr-enriched precipitates.

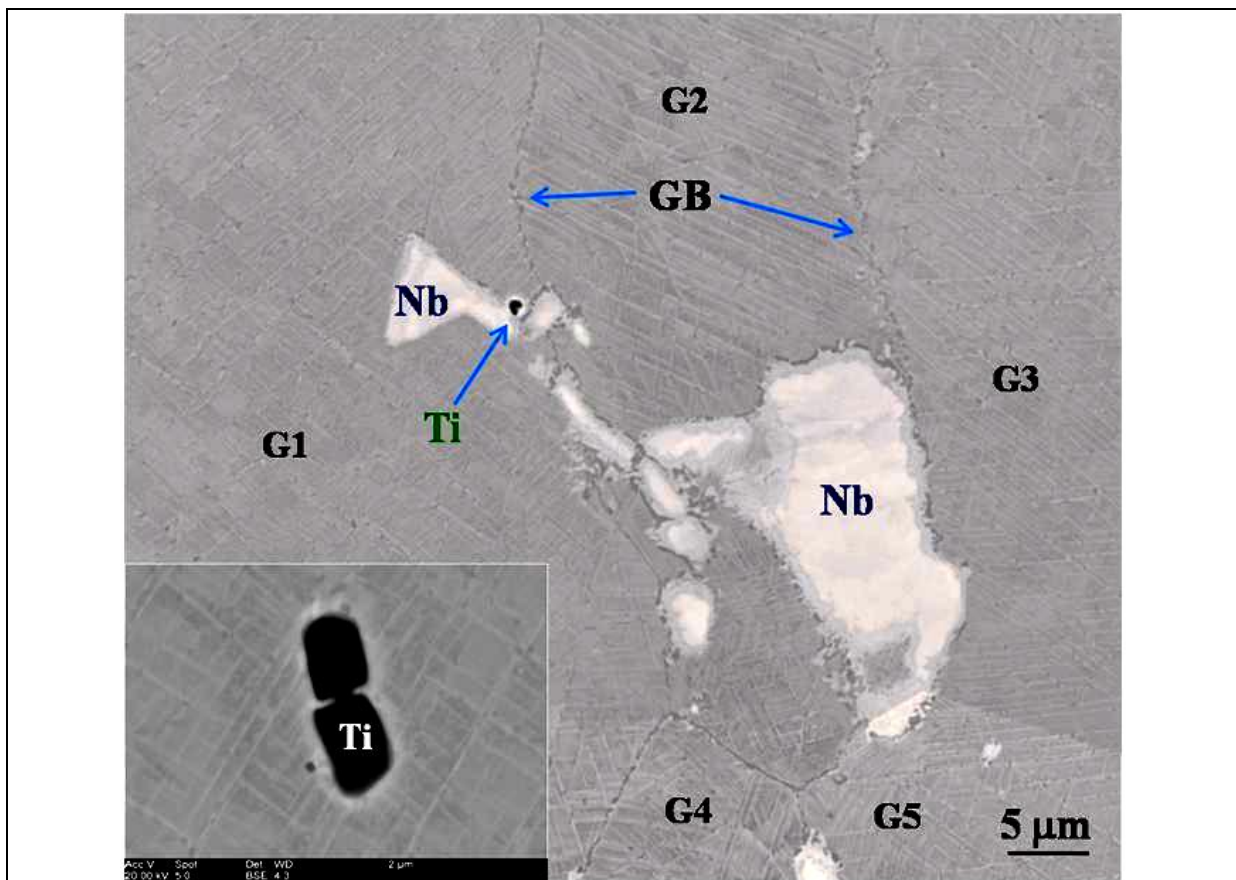


Figure 5.2.4: Backscattered scanning electron micrograph of creep-exposed specimen S9980. Inset micrograph shows Ti-enrich precipitates. Cr- and Nb-enriched precipitates are found intra- and intergranularly in the creep-exposed specimen.

EDX spectra were acquired from these precipitates indicated high-Z and low-Z phases are enriched in Nb, Cr and Ti, respectively. The identified phases from the XRD analysis were $M_{23}C_6$ -type Cr enriched phase, M(C, N)-type Ti & Nb enriched phase and needle shaped precipitates of δ -phase. The precipitates were found intra- and intergranularly in the alloy. The

morphology varied from symmetric to totally asymmetric. The elemental composition of the precipitates was measured by EDX and is listed in *Table 5.2.4*.

Austenitic γ -Matrix	Ni-24.3Cr-10.7Mo-2.5Fe-12.7Nb
$M_{23}C_6$	Cr-4.1Mo-20.6Ni-1.4Fe-3.8Nb
δ -phase (needle shape)	Nb-45.3Ni-18.1Cr-15.6Mo-1.2Fe
Ti (C, N)	Ti-17.1Cr-28.9Ni-11.5Nb-6.2Mo
NbC	Nb-8.4Mo-1.9Ni-0.8Cr-1.8Ti

The precipitation hardening phase of γ'' in the creep-exposed specimen S9980 was identified but the morphology of this hardening phase was different from the 'as-received' IN625. The shape and size of the γ'' precipitates were circular to thin ellipsoidal discs and an average size of 12.3 ± 6.2 nm, in S9980 specimen. The size of the Cr-enriched ($M_{23}C_6$) precipitates varied in size from $0.01 \mu\text{m}$ to $3 \mu\text{m}$. The size of the Ti-enriched [Ti (C, N)] precipitate varied from $0.5 \mu\text{m}$ to $2.5 \mu\text{m}$. The size of the Nb-enriched (NbC) precipitate varied from $0.1 \mu\text{m}$ to $20 \mu\text{m}$. The size of the δ -phase (needle shape) was of varying size and the largest one observed was of grain size in length. The precipitate morphology and locations are listed in *Table 5.2.4.I*.

Specimen ID	Precipitate location	Precipitates Morphology			
		Phases	Size	Shape	Area fraction (%)
Creep-exposed (650°C/33,000 Hrs/Intermediate stress)	Throughout the matrix	γ''	5-26nm	Circular To Thin Ellipsoidal Discs	3.2
		δ -phase (orthogonal)	<1-23 μm	needle shape	13.6
	Intra- and inter-granularly, near to twin boundaries	Ti (C,N)	0.5-2.5 μm	regular to totally irregular geometry	0.02
		$M_{23}C_6$	0.01-3 μm		0.64
		NbC	0.1-20 μm		16.1

The Ti-enriched phase, TiN was randomly distributed in the matrix. The identified phases in XRD were confirmed the precipitates of Cr-rich, Ti-rich, Nb-rich and needle shaped precipitates as $M_{23}C_6$ type carbides, Ti (C, N) type carbo-nitrides, NbC type carbides and δ -phase respectively. Carbides were present in the matrix and at the grain boundaries. A series of discrete carbides along the grain boundaries were also observed. The blocky particles are mainly composed of niobium, as similar to the as-received IN625.

5.2.5 Transmission Electron Microscopy (TEM) Observations

The creep-exposed S9980 specimen was analysed using analytical transmission electron microscopy and the results are presented in this section. The precipitates of different phases, shown in *Figure 5.2.4*; were further confirmed using selected area electron diffraction patterns and energy dispersive X-ray (EDX) analysis, in the TEM, as discussed for previous specimens.

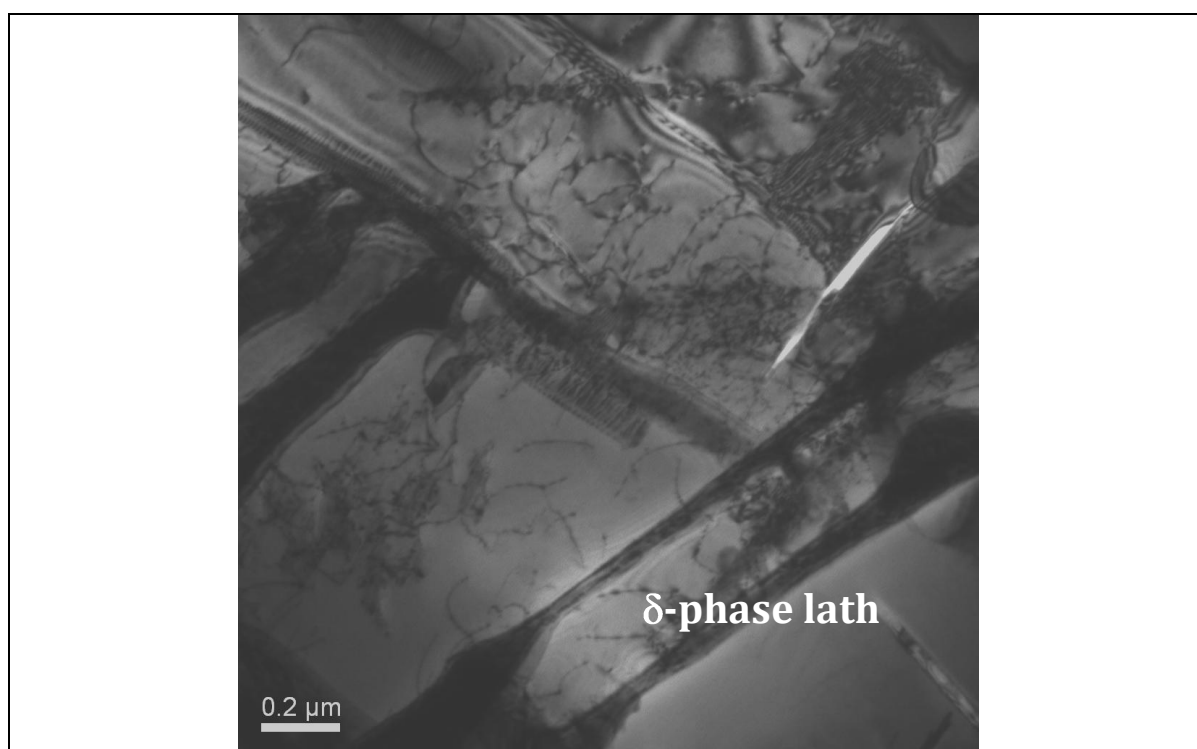


Figure 5.2.5: BF-TEM micrograph of creep-exposed S9980 shows the dislocation structure, and dislocation-particle interaction in austenitic γ - matrix. Laths of the δ - phase can be observed in the micrograph.

The microstructure consisted of γ -austenitic matrix, γ'' -phase, NbC carbides, $M_{23}C_6$ carbides and TiN phase. These precipitates were mainly located at the prior austenite grain boundaries and sub-grain boundaries.

The morphological geometries of these precipitates are discussed in the following subsections. A large number of distributed dislocations resulted from the creep deformation and typical precipitate-dislocation interactions with regular and irregular precipitates were observed in this creep-exposed alloy.

5.2.5.1 Gamma Double Prime (γ'')

Figure 5.2.5.1 shows TEM micrograph of fine γ'' precipitates. The reflections from γ'' and their indexed SAEDP are shown in Figure 5.2.5.1b.

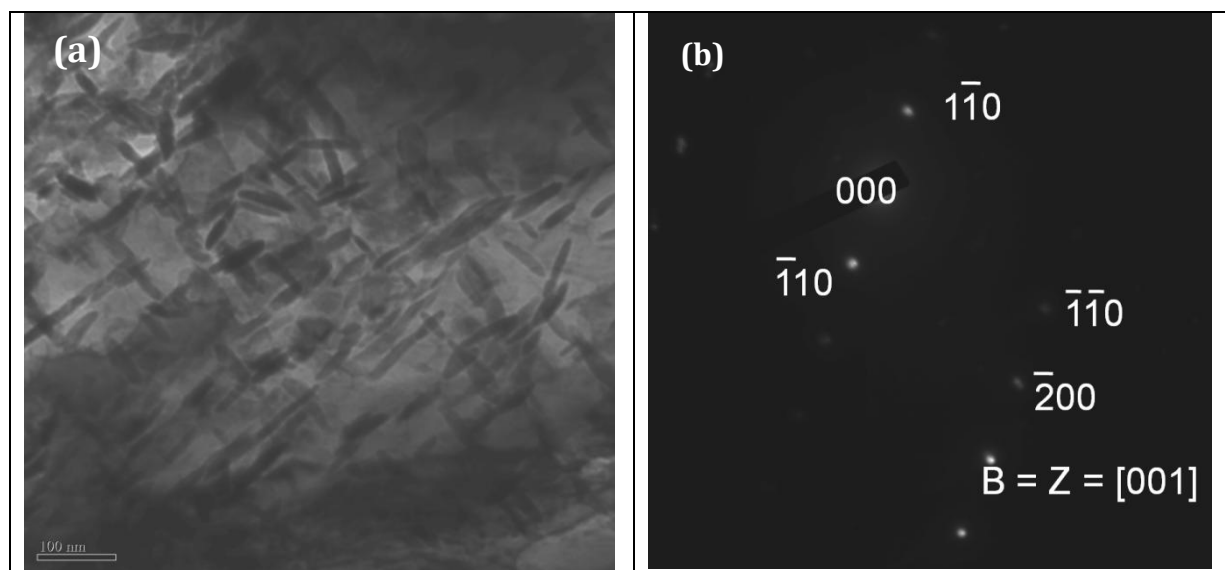


Figure 5.2.5.1 (a) BF-TEM micrograph shows γ'' ; (b) the indexed selected area electron diffraction pattern (SAEDP) from γ'' precipitates. The beam direction and zone axis were along $B = Z = [001]$.

The beam direction and zone axis were shown in Figure 5.2.5.1b $\{B=Z= [001]\}$. Their random dispersion strengthened the disordered FCC austenitic gamma (γ) matrix. The γ'' precipitates coherent interfaces are in orientation relationship with γ -matrix as $(100)_{\{\text{matrix-}\gamma\}} \parallel (100)_{\{\gamma''\}}$; $[010]_{\{\text{matrix-}\gamma\}} \parallel [010]_{\{\gamma''\}}$.

5.2.5.1 (a) Volume fraction of Gamma Double Prime

The volume fraction of gamma double prime was estimated in a similar way as discussed in the previous section. The shapes of the γ'' precipitates found in this specimen were thin ellipsoidal discs or thin lens shaped particles and the average size was 12.3 ± 6.2 nm. The volume fraction of gamma double prime in this specimen was estimated to be approximately 3.2%, which is smaller than that observed in the 'as-received' IN625.

5.2.5.2 TiN

Figure 5.2.5.2 shows BF-TEM micrograph of TiN precipitate, in this creep-exposed specimen. The indexed diffraction pattern (SAEDP) from TiN precipitate is shown in Figure 5.2.5.2b. The Beam direction and zone axis were along $[\bar{1}12]$ direction. EDX confirmed the precipitate in Figure 5.2.5.2 is enriched in Ti relative to the grain. The size of the blocky TiN rich phase in Figure 5.2.5.2a was $0.5 \mu\text{m}$.

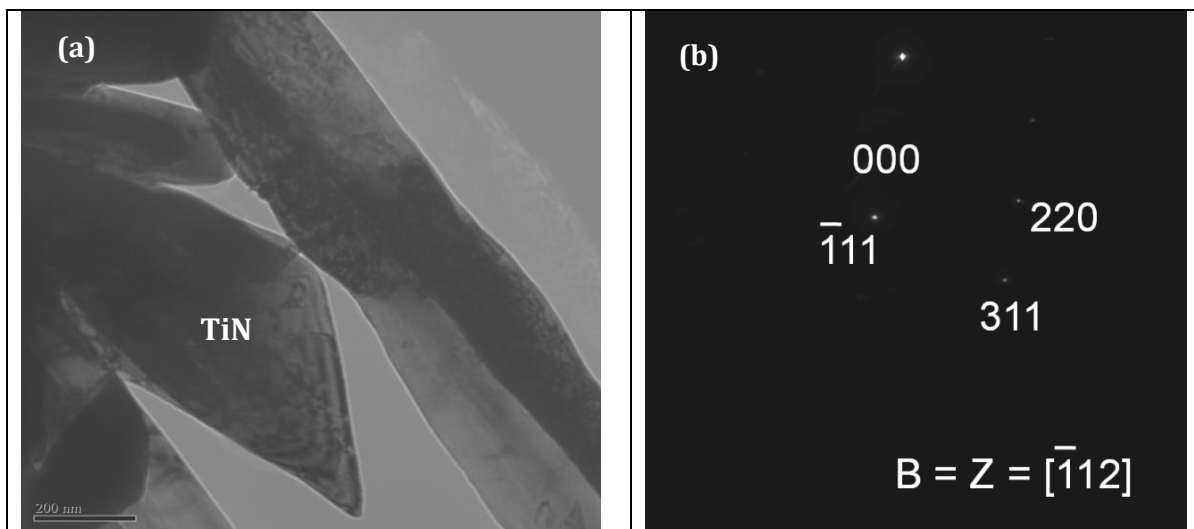
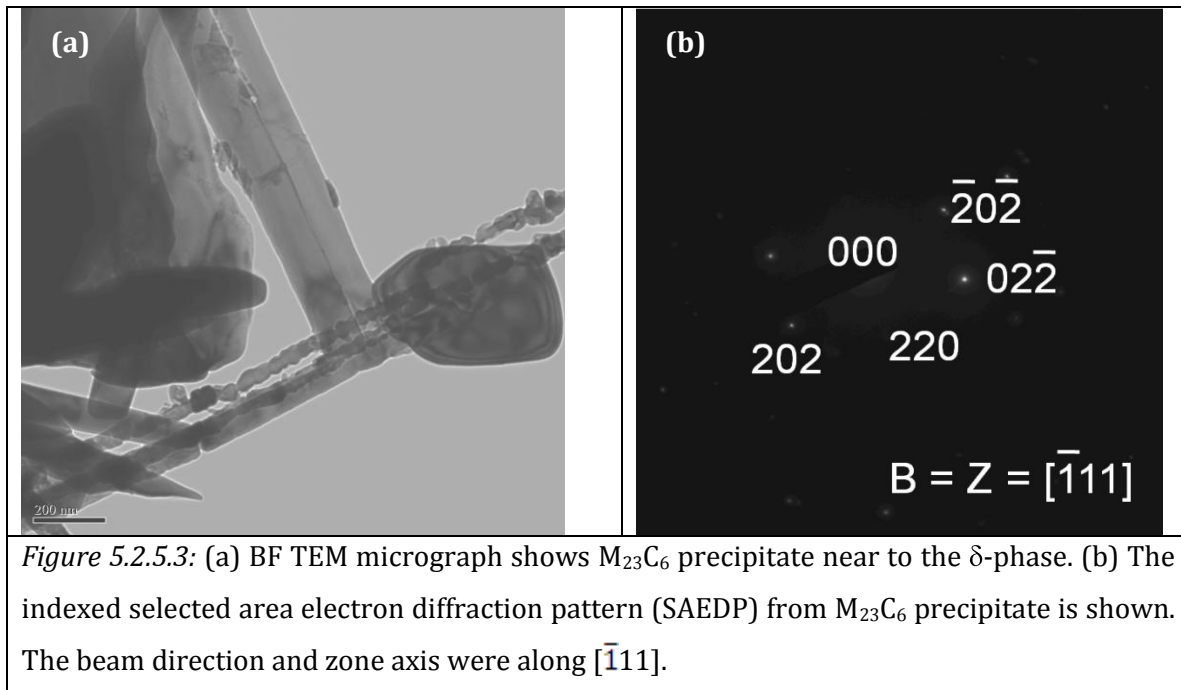


Figure 5.2.5.2: (a) BF TEM micrograph shows morphology of TiN precipitate; (b) The indexed selected area electron diffraction pattern (SAEDP) from TiN precipitate (a), Beam direction was along $B=Z=[\bar{1}12]$.

5.2.5.3 $M_{23}C_6$

The approximate of $M_{23}C_6$ precipitate composition was found to be Cr-6.7Ni-4.4Nb-21.1Mo (wt. %). The discrete particles of $M_{23}C_6$ at the grain boundaries were found to influence

the high temperature properties of the alloy through pinning grain-boundary sliding. A precipitate of $M_{23}C_6$ is shown in *Figure 5.2.5.3a*. The indexed SAEDP is shown in *Figure 5.2.5.3 (b)*.



5.2.5.4 δ -phase

δ -phase is a thermodynamically stable phase in IN625 alloy. This phase was found to occur during the exposure to temperatures in excess of 650°C and leads to degradation in the creep and strength properties. It is observed that the formation of δ -phases at 650°C and above is a major consideration in limiting the alloy use to temperatures below 650°C. The precipitation of intermetallic δ -phase was found to lower the mechanical and creep-rupture properties. δ -phase, $[Ni_3 (Nb, Mo)]$ precipitation was found to occur at Nb and Mo rich carbides and initiated at Nb and Mo rich grain boundaries and matrix carbides. *Figure 5.2.5.4* shows BF-TEM micrographs of δ -phase laths. *Figure 5.2.5.4(b)* shows the higher magnification lath, and stacking faults defects in its structure can be observed in the micrograph. Standard quantitative analysis from EDX showed that these laths were rich in Nb, Mo Cr and Ni. The width of the laths

in this specimen was in the range of 100nm to 0.5 μ m. The long creep duration was believed to be the reason behind the coarsening of these laths.

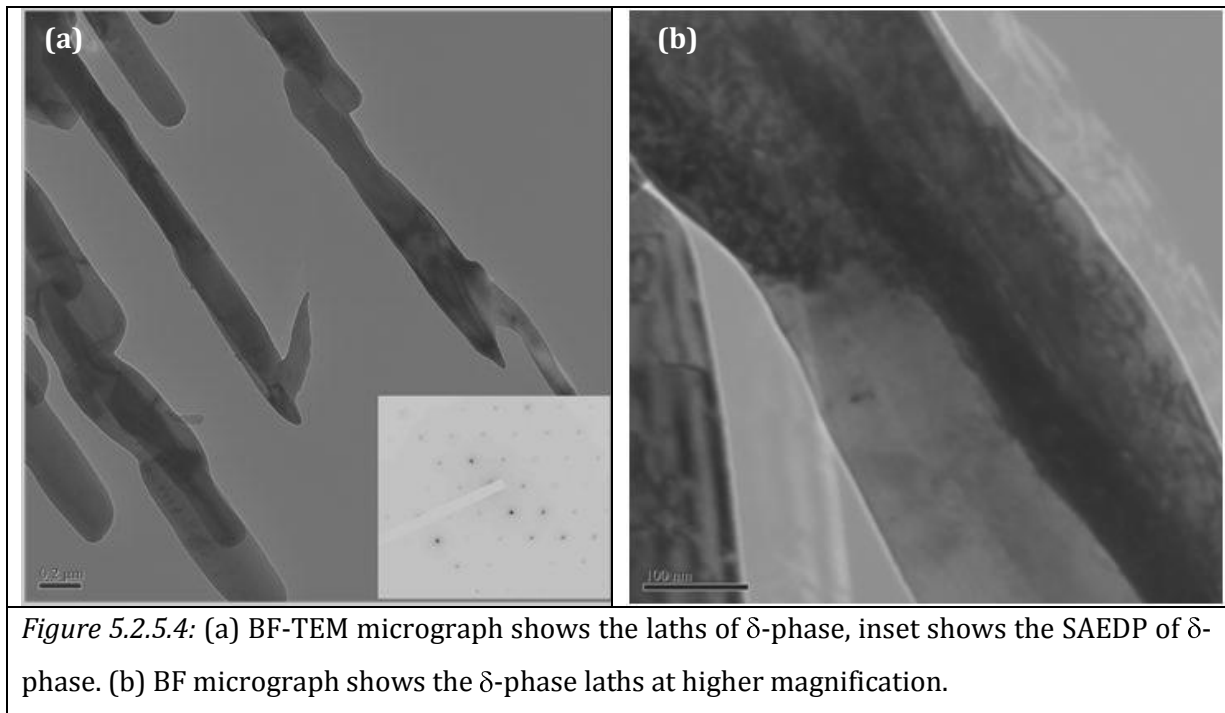


Figure 5.2.5.4: (a) BF-TEM micrograph shows the laths of δ -phase, inset shows the SAEDP of δ -phase. (b) BF micrograph shows the δ -phase laths at higher magnification.

5.2.5.5 NbC

Figure 5.2.5.5 shows the NbC carbide in this creep-exposed specimen and the indexed SAEDP acquired from it. The quantitative analysis of NbC was found to Nb-30.8Ni-9.4Mo-2.6Cr (wt. %).

NbC carbides were found intra- and intergranularly in the creep-exposed specimen. They were of different morphology from the irregular to symmetric of varied size range from 100nm to 15 μ m.

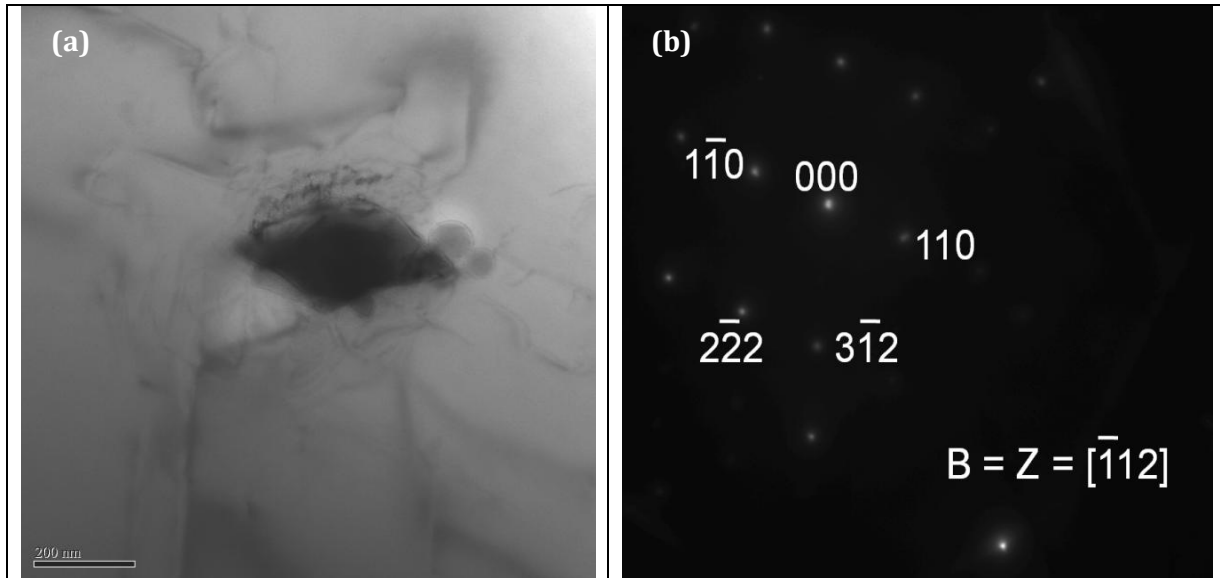


Figure 5.2.5.5: (a) BF TEM micrograph shows NbC precipitate. (b) The indexed selected area electron diffraction pattern (SAEDP) from NbC precipitate is shown. The beam direction and zone axis were along $[\bar{1}12]$.

5.2.5.6 Quantitative Measurements of Dislocation density

The arrays of dislocations near to the precipitates are shown in *Figure 5.2.5.6*. The dark lines in the micrograph are dislocations. The dislocation density (number of dislocations that intersect a unit area of a random surface section) was measured by the method discussed in the previous section 5.1.4.5.

The dislocation density in this creep exposed specimen S9980 was estimated as $19.7 \pm 4.8 \times 10^{13}$ lines/m². The standard deviation for the measurements was 4.8. The value is higher than the as-received IN625 by order of 10. Typical values of η_g (number of extinction fringes), ξ_g (extinction distance for that g vector and accelerating voltage) and t (foil thickness) are listed in *Table 5.1.4.3*.

<i>Table 5.1.4.4: Typical values for η_g, ξ_g, t and ρ_d</i>			
η_g	ξ_g (Å) at 200kV	t (Å)	ρ_d (lines/m ²)
5	299.25	1246.24	19.7×10^{13}

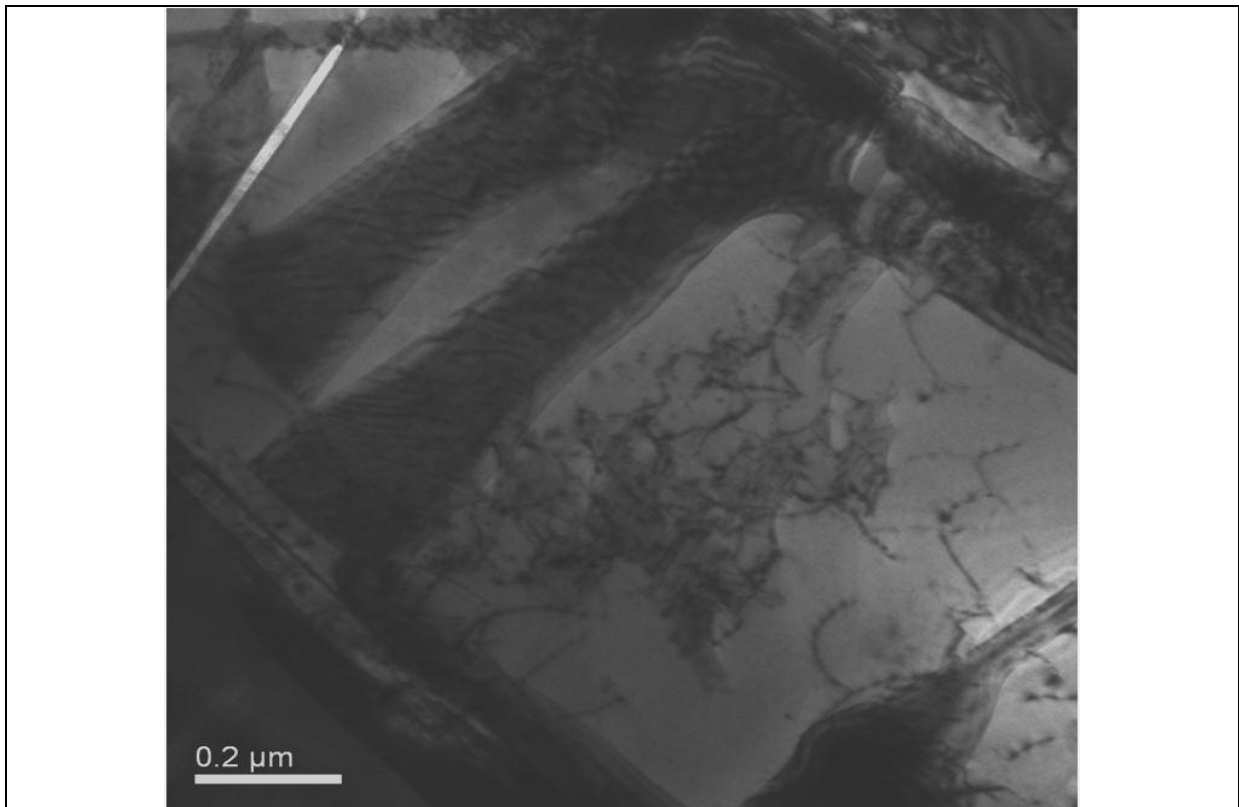


Figure 5.2.5.6: BF TEM micrographs illustrating (a) dislocation structure, precipitates particle, dislocation-particle interaction and dislocations piled up.

The characteristics of dislocations are important with regard to the mechanical properties of alloys. These include strain, temperature, and dislocations ability to multiply. During the deformation, the number of dislocations increases dramatically. The existing dislocations are the important source for the new dislocations; furthermore, grain boundaries, as well as internal defects, and surface irregularities act as dislocation formation sites during deformation. The specimen S9980 was exposed for longest duration at 650°C and the dislocation density was found higher by an order of 10 from the 'as-received' specimen.

5.3 'Creep-exposed specimen' (S9976) (650°C/ 1000Hrs)

The solution-annealed IN625 specimen was creep tested at 650°C in air under a uniaxial high tensile load. This specimen ID: S9976 fractured after 1,000 hours of creep duration. The area reduction was measured from the fractured specimen as 12.7%.

5.3.1 Grain Morphology

In this section metallographic observation of grain structure and its morphology in creep-exposed specimen S9976 is discussed. The optical microstructure of the creep-exposed specimen is shown in *Figure 5.3.1*.

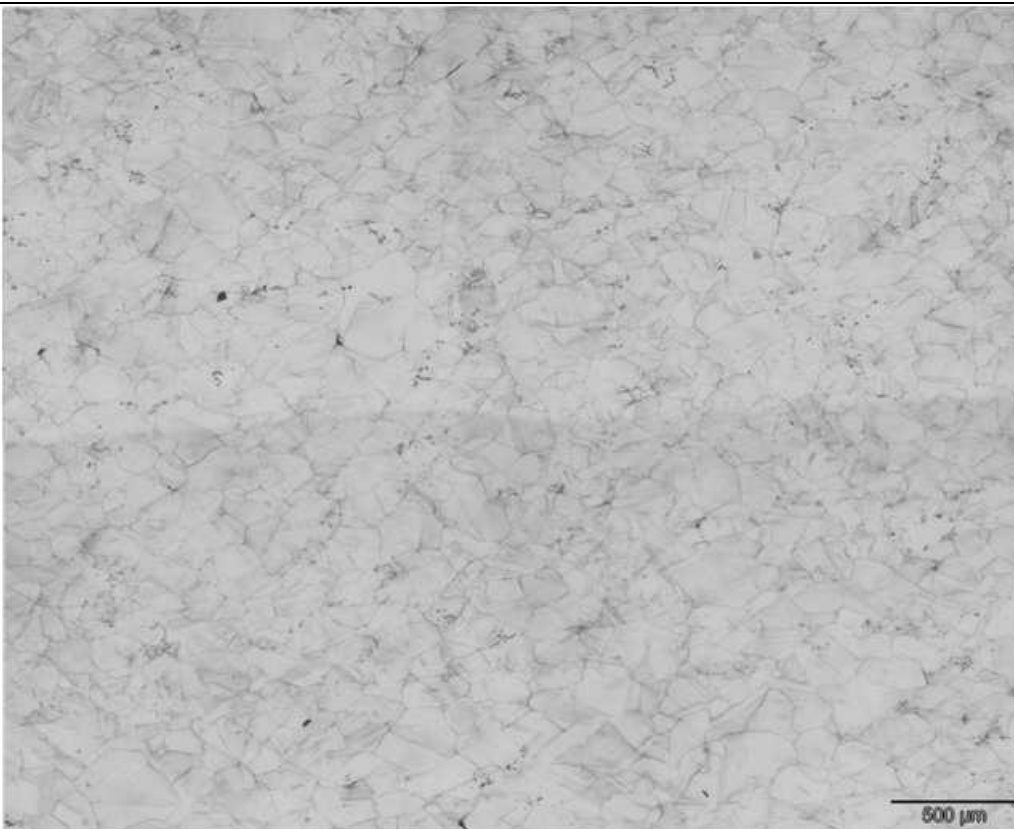


Figure 5.3.1: Optical micrograph of grain structure of gauge length, observed in specimen (S9976) after creep test at 650°C. A typical cell structure and grains can be observed in the micrograph after 1000 hours of creep exposure.

The 'creep-exposed' S9976 specimen showed an equiaxed austenite γ -grain structure. The austenitic grain size varied from a minimum of 45 μm to a maximum of 233 μm , with an average size of 104.7 μm . The ASTM grain size number was in the range of 3-4.

Very fine slip lines were observed in the micrograph. The slip line spacing was not able to be resolved in this specimen. A summary of the morphology of grains and grain boundaries is listed in *Table 5.3.1*.

Creep-exposed (650°C/1000 Hrs/High stress)	Grain Morphology			ASTM grain size No.	VHN(Hv/20)		GB morphology
	Grain-size range (μm)	Avg. grain size (μm)	Grain shape		Head	GL	
	45 to 233	104.7	Equiaxed	5-6	320	433	

The substantially high average value of hardness of 433Hv in the gauge length was believed to be due to the extensive precipitation of phases from the thermal and strain effects. The lower value of average hardness of 320Hv in the head was only from the thermal effect and minimal effect from strain. The hardness value observed in this S9976 specimen was higher than the hardness observed in the S9980 specimen. Specimen S9980 was exposed for the longest duration of 33,000 hours. It can be concluded that strain played an important role in increasing the hardness value, by enhancing the precipitation kinetics.

5.3.2 Fractography

The failure mechanism of the creep fractured specimen S9976 was analyzed using scanning electron microscopy. Fractographs of creep failed specimen, S9976 are shown in *Figure 5.3.2*. The failure mechanism was mixed mode of fracture, intergranular and transgranular. Grain boundary creep cavitation (arrowed) and spherical chromium carbides precipitates are shown in *Figure 5.3.2*. The failure mechanism of this exposed specimen was further confirmed by optical microscopy of a polished cross-section of the fractured surface. *Figure 5.3.2b* shows the spherical chromium precipitates in this specimen, forms during the heat treatment and favours due to lower surface energy in its formation. The direction of loading is perpendicular to the wedge crack. The open cracks intruded inside the specimen to a depth of 50 to 345 μm .

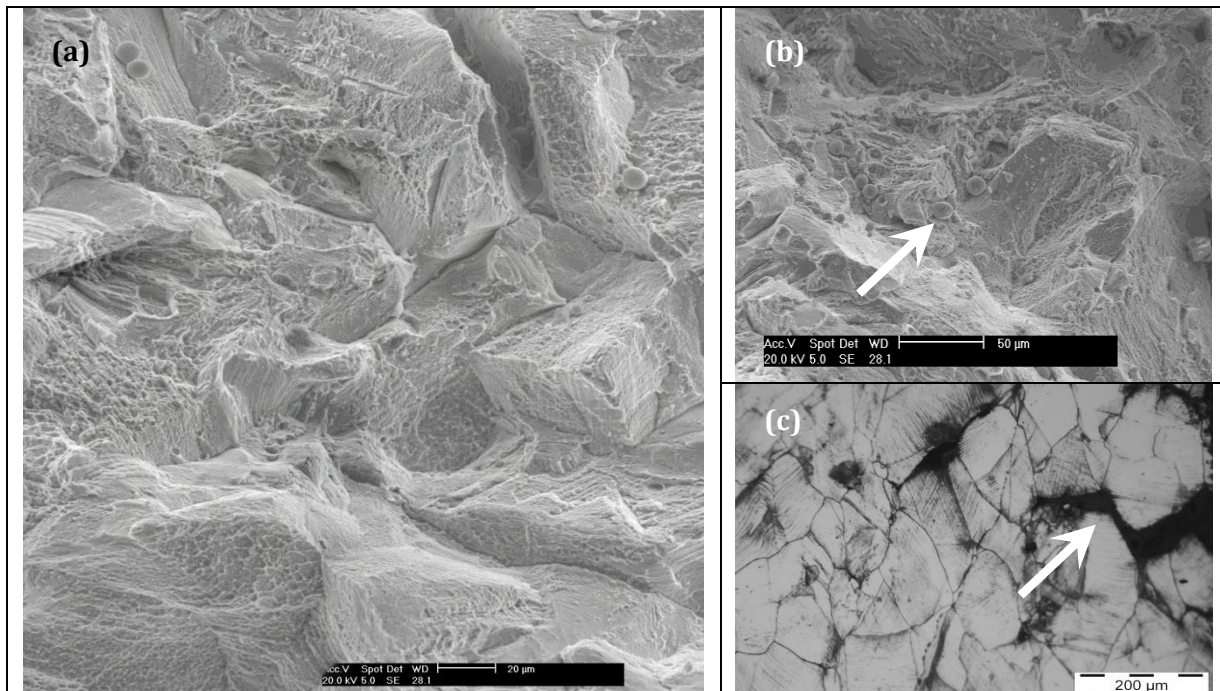
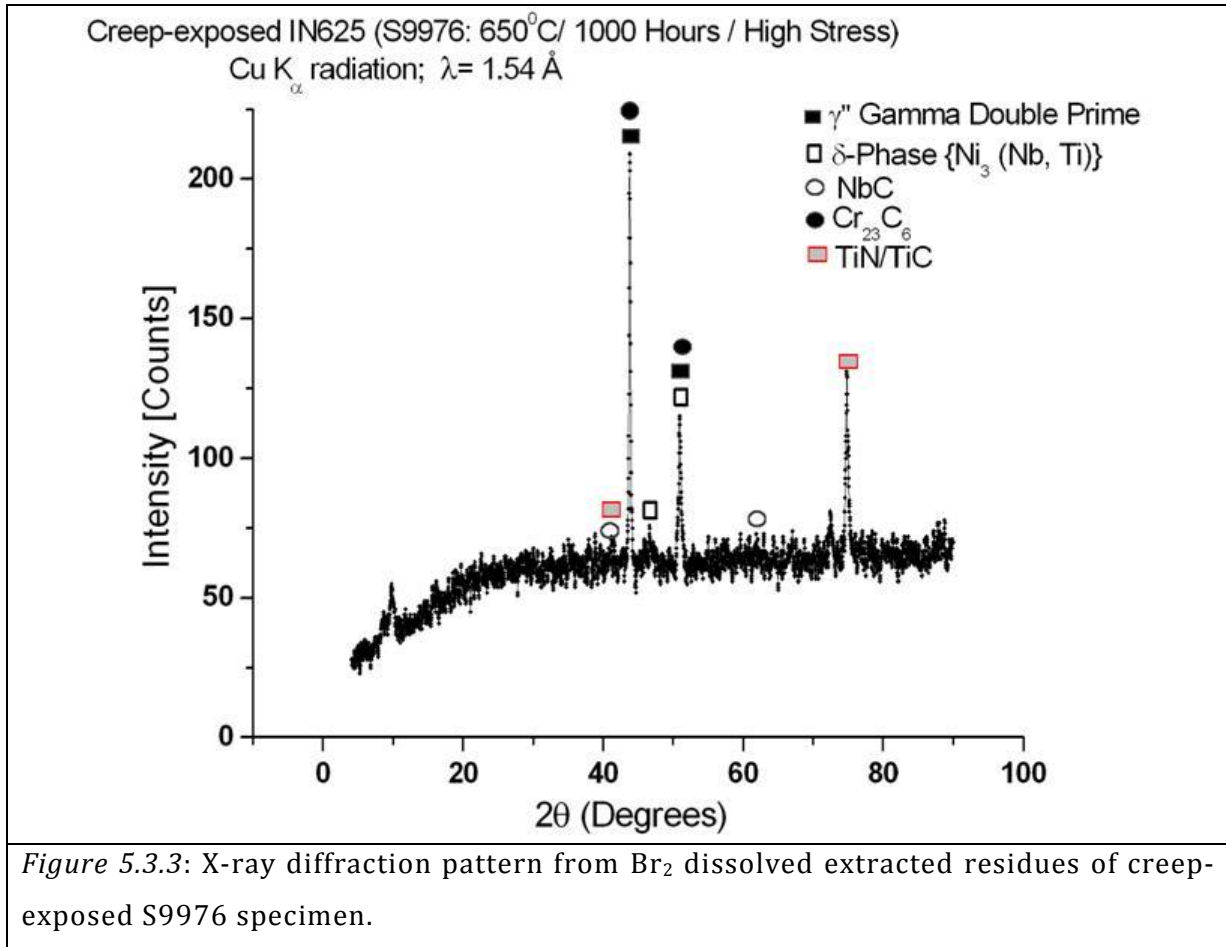


Figure 5.3.2: SEM micrographs show mixed mode of (intergranular & transgranular) creep failure in specimen S9976. Some area of microstructure shows transgranular fracture. Grain boundaries decohesion and spherical precipitates of chromium carbides can be observed in the micrographs. The direction of loading is perpendicular to the wedge crack propagation.

5.3.3 Phase Identification

An analysed X-ray diffraction pattern of creep-exposed S9976 specimen is shown in *Figure 5.3.3*. The phases were identified by the analysis of the XRD traces as austenitic γ - matrix, γ'' - gamma double prime, δ -phase: Ni_3 (Nb, Ti, Al), Nb-enriched and Ti-enriched MC type carbides, and M_{23}C_6 (Cr-enriched).



5.3.4 Precipitate Morphology and Location

The precipitate morphology and their location of precipitation in creep exposed specimen S9976 are discussed, in this section. *Figure 5.3.4* shows BSE-SEM micrograph of precipitate morphology in creep-exposed specimen S9976. The precipitates found in this specimen were laths of Nb-enriched phase located in the grain interior, Nb-, Ti- and Cr-enriched precipitates. The precipitates were identified as M₂₃C₆-type Cr enriched phase and M(C, N)-type Ti- and Nb-enriched phase and lath precipitates of δ-phase. Their morphology varied from regular to totally irregular.

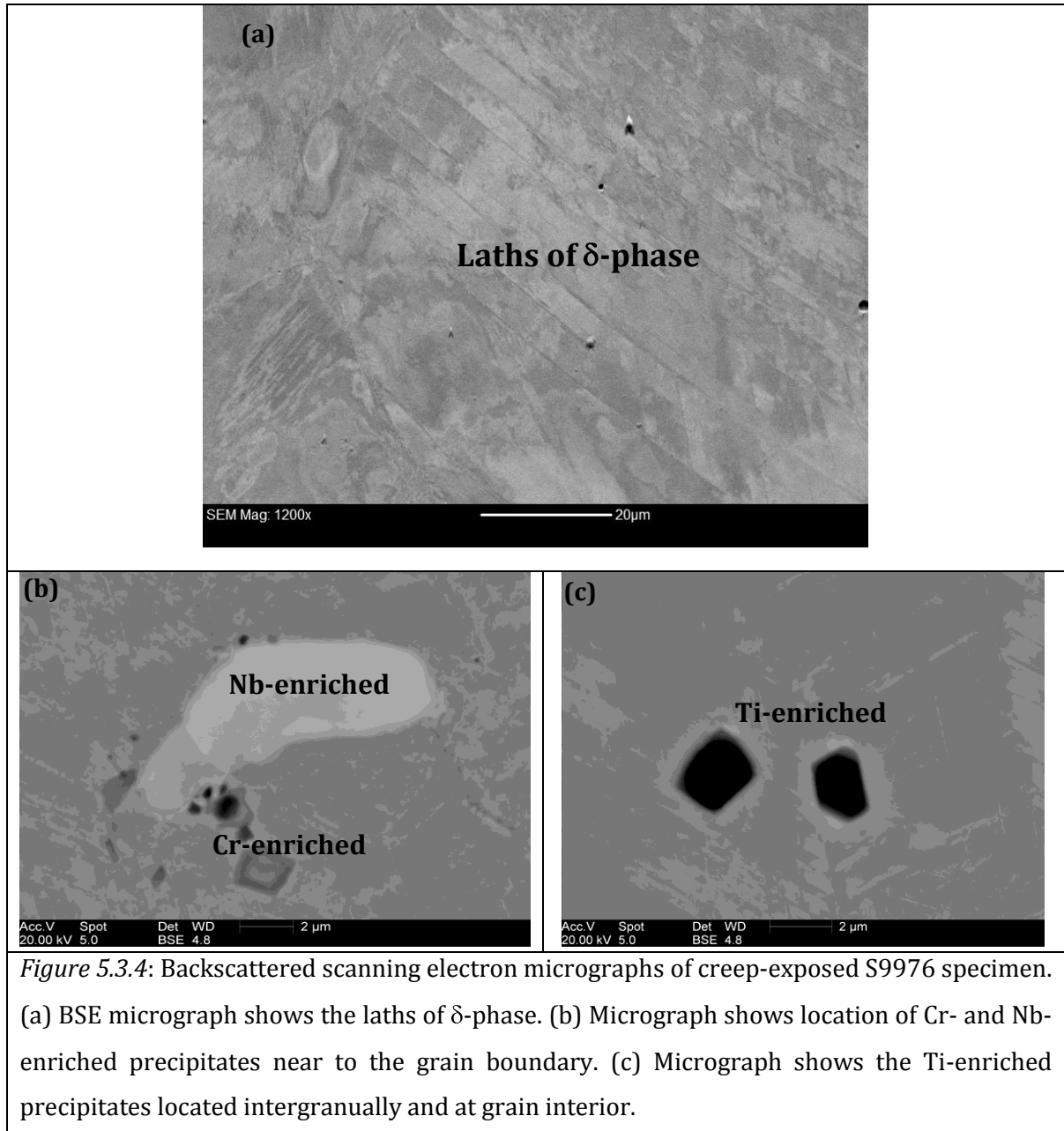


Figure 5.3.4: Backscattered scanning electron micrographs of creep-exposed S9976 specimen. (a) BSE micrograph shows the laths of δ -phase. (b) Micrograph shows location of Cr- and Nb-enriched precipitates near to the grain boundary. (c) Micrograph shows the Ti-enriched precipitates located intergranularly and at grain interior.

The elemental composition of the precipitates was measured by EDX and is shown in *Table 5.3.4*.

Table 5.3.4: Typical composition of phases and austenitic matrix in creep-exposed specimen S9976 by EDX (wt. %)

Austenitic γ -Matrix	Ni-20.3Cr-15.7Mo-2.5Fe-18.7Nb
$M_{23}C_6$	Cr-13.1Mo-20.6Ni-1.2Fe-13.8Nb
Laths of δ -phase	Nb-45.3Ni-18.1Cr-15.6Mo-1.2Fe
Ti (C, N)	Ti-19.5Cr-20.9Ni-11.5Nb-11.2Mo
NbC	Nb-8.1Mo-0.8Ni-0.3Cr-1.5Ti

The precipitate morphology and their locations, in creep-exposed S9976 specimen are listed in *Table 5.3.4.I*.

Specimen ID	Precipitate location	Precipitates Morphology			
		Phases	Size	Shape	Area fraction (%)
Creep-exposed (650°C/1000 Hrs/High stress)	Throughout the matrix	γ''	5-48nm	discs	4.3
		δ -phase (laths)	10-200 μ m	lath shape	15.3
	Intra- and inter- granularly, twin boundary	Ti (C,N)	0.5-2.5 μ m	Regular to totally irregular geometry	0.04
		$M_{23}C_6$	0.01-2 μ m		0.47
		NbC	0.1-15 μ m		18.3

The shape and size of the γ'' precipitates were circular to thin ellipsoidal discs and of average size 21.4 ± 8.1 nm. The size of the Cr-enriched ($M_{23}C_6$) precipitates varied from 0.01 μ m to 2 μ m. The size of the Ti-enriched [Ti (C, N)] precipitate varied from 0.5 μ m to 2.0 μ m. The size of the Nb-enriched (NbC) precipitate varied from 0.1 μ m to 15 μ m. The size of the δ -phase (laths shape) is varying and the largest one is of grain size in length. The precipitates were confirmed by the XRD as Cr-rich, Ti-rich, Nb-rich and lath shaped precipitates were $M_{23}C_6$ type carbides, Ti (C, N) type carbo-nitrides, NbC type carbides and δ -phase respectively.

5.3.5 Transmission Electron Microscopy (TEM) Observations

The microstructural evolution in creep-exposed specimen S9976 was analysed using analytical transmission electron microscopy. The precipitates were further identified using selected area electron diffraction patterns and energy dispersive X-ray spectrometry (EDX), in TEM.

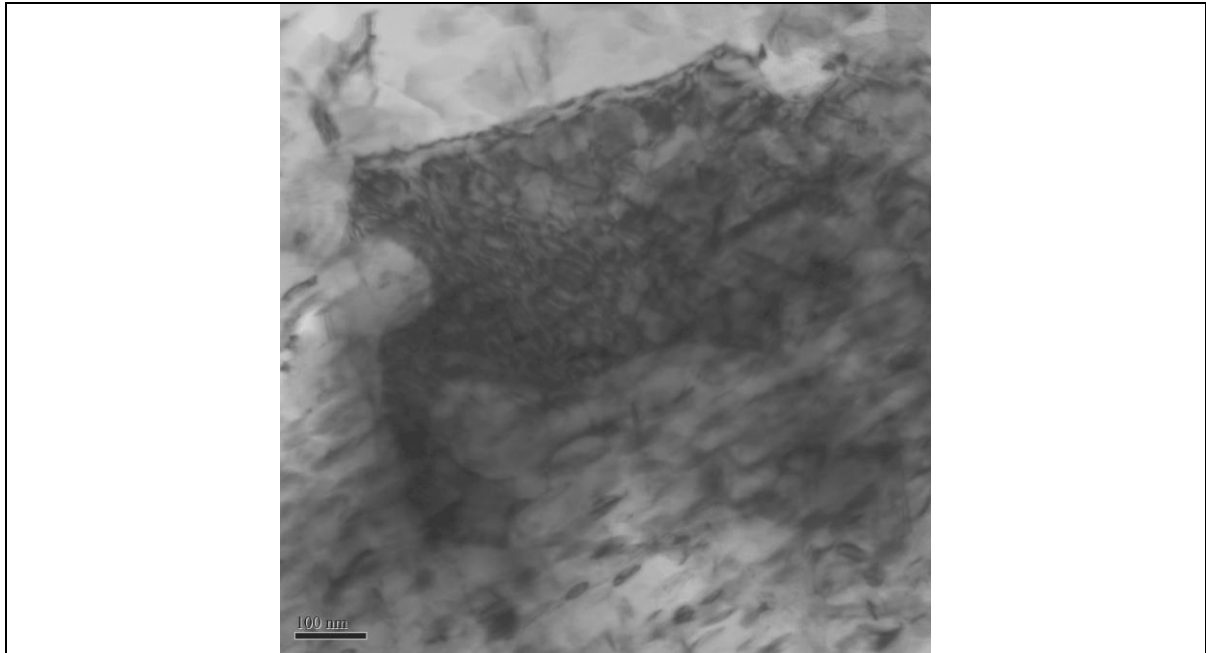


Figure 5.3.5: BF-TEM micrograph of ‘creep-exposed’ IN625 alloy illustrating dislocation structure, on the precipitate.

The microstructure consists of γ -austenitic matrix, γ'' , NbC carbides, laths of δ -phase, intergranular precipitates of $M_{23}C_6$ ($M = Cr, Mo, Co$) and Ti (C, N).

5.3.5.1 Gamma Double Prime (γ'')

The metastable γ'' phase found in S9976 specimen, has complex body-centered-tetragonal DO_{22} crystal structure. *Figure 5.3.5.1* shows TEM micrograph of γ'' precipitates and their indexed selected area electron diffraction pattern. The reflections from γ'' are shown in *Figure 5.3.5.1b*. The beam direction and zone axis are shown in *Figure 5.3.5.1b* $\{B=Z= [\bar{1}12]\}$. The average size of γ'' was 21.4 ± 8.1 nm.

5.3.5.1 (a) Volume fraction of Gamma Double Prime

The volume fraction of gamma double prime precipitates was estimated as discussed in previous sections. The shape of the γ'' precipitates was thin ellipsoidal discs or thin lens shaped particles and their average size was 21.4 ± 8.1 nm. The estimated volume fraction of gamma double prime in this specimen S9976 was 4.3%, which was smaller than that observed in the ‘as-received’ IN625 specimen.

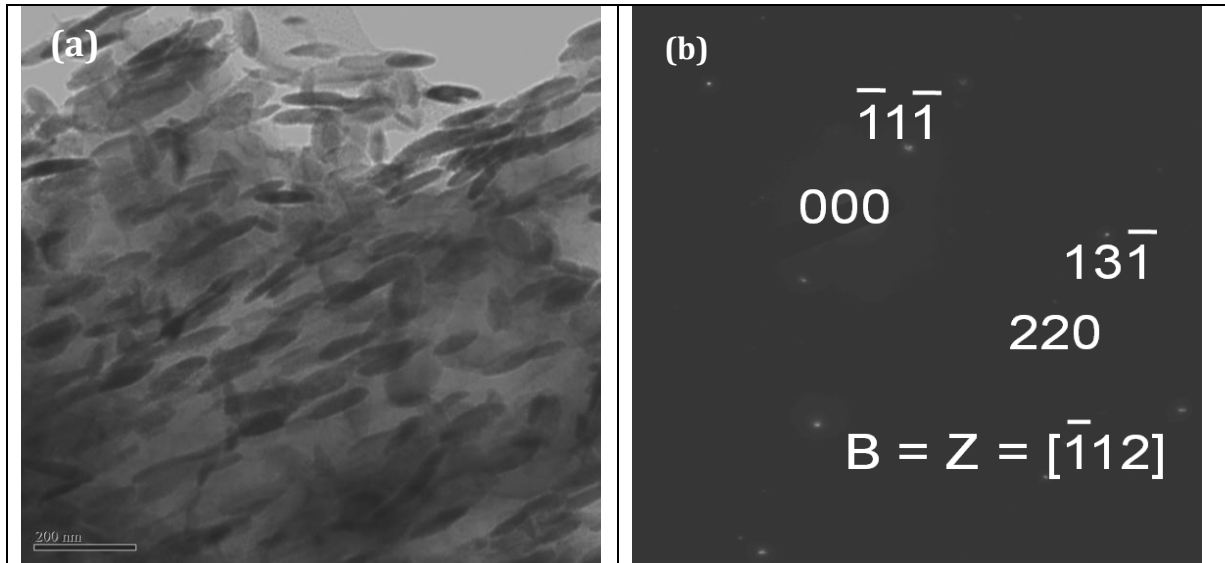


Figure 5.3.5.1 (a) Bright field (BF) TEM micrograph showing the γ'' ; (b) Selected area electron diffraction pattern (SAEDP) from γ'' precipitates. The beam direction and zone axis are along $B = Z = [\bar{1}12]$.

5.3.5.2 TiN

The Ti-enriched precipitates in this specimen (noted in *Figure 5.3.4*) were identified as TiN.

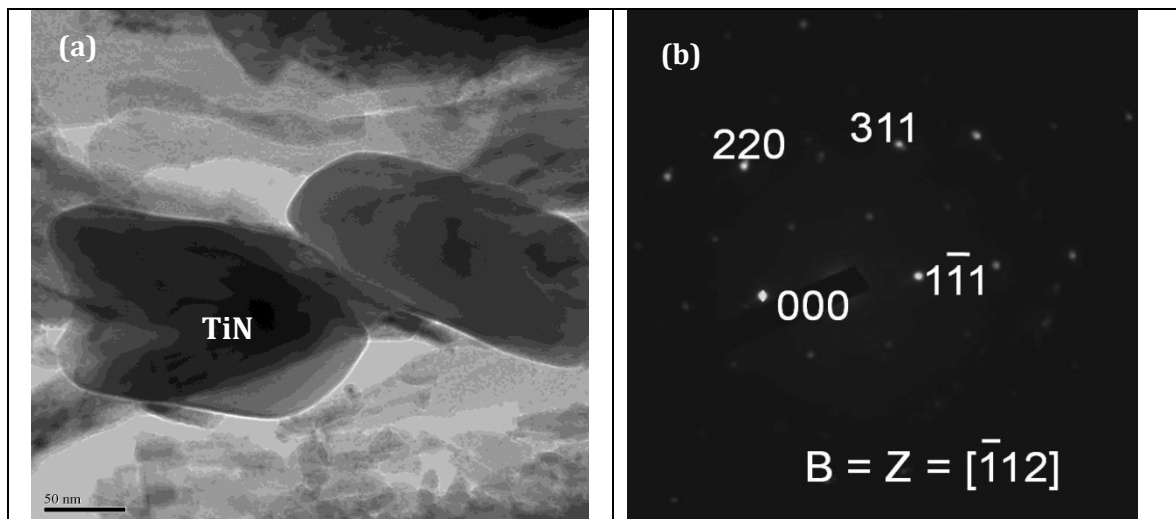


Figure 5.3.5.2: (a) BF-TEM micrograph shows the morphology of TiN precipitate; (b) The indexed selected area electron diffraction pattern (SAEDP) from TiN precipitate (a), The beam direction was along $B = Z = [\bar{1}12]$.

Figure 5.3.5.2 shows BF-TEM micrograph of a TiN precipitate in the creep-exposed specimen S9976. The indexed SAD pattern acquired from the blocky TiN precipitate is shown in

Figure 5.3.5.3b. The beam direction and zone axis were along $[\bar{1}12]$ direction. The size of the blocky TiN phase in Figure 5.3.5.3a was $0.5\mu\text{m}$.

5.3.5.3 $M_{23}C_6$

The evolution of $M_{23}C_6$ precipitates were discussed in previous sections. The approximate composition of $M_{23}C_6$ precipitate was found to Cr-13.1Mo-20.6Ni-1.2Fe-13.8Nb (wt. %). The precipitate of $M_{23}C_6$ is shown in Figure 5.3.5.3. The indexed SAEDP is shown in Figure 5.3.5.3 (b).

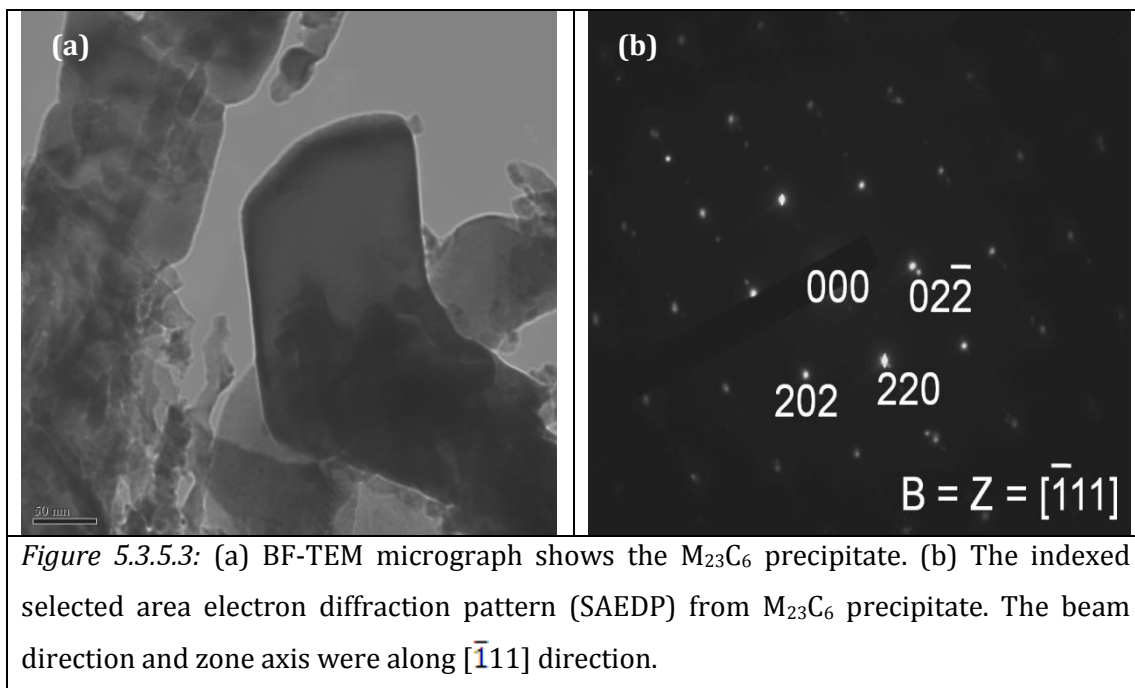


Figure 5.3.5.3: (a) BF-TEM micrograph shows the $M_{23}C_6$ precipitate. (b) The indexed selected area electron diffraction pattern (SAEDP) from $M_{23}C_6$ precipitate. The beam direction and zone axis were along $[\bar{1}11]$ direction.

5.3.5.4 δ -phase

It was observed that the thermodynamically stable δ -phase forms at the expense of metastable γ'' on the exposure to high temperature in the alloy IN625. The formation of intermetallic δ -phase was found to detrimental to the long term creep properties in this alloy (Shankar et al 2001). Figure 5.3.5.4 shows the BF-TEM micrographs of the laths of δ -phase. Figure 5.3.5.4b shows the high magnification laths. The elemental quantitative analysis from EDX shows that these laths were rich in Nb, Mo Cr and Ni. The width of the laths in this specimen was in the range of 20nm to 80nm, which is smaller that that seen in specimen S9976.

The width of laths was smaller due to short duration of 1000 hours exposure in this specimen S9976.

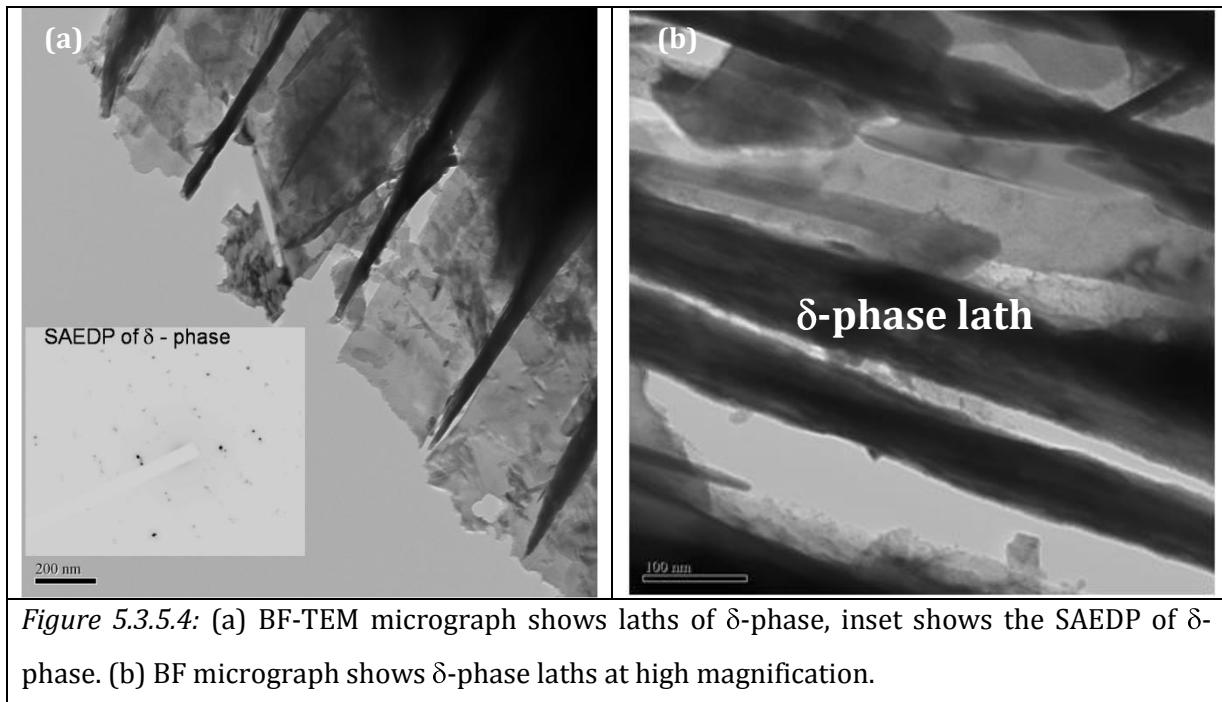


Figure 5.3.5.4: (a) BF-TEM micrograph shows laths of δ -phase, inset shows the SAEDP of δ -phase. (b) BF micrograph shows δ -phase laths at high magnification.

5.3.5.5 NbC

Figure 5.3.5.5 shows the NbC carbide in creep-exposed specimen S9976 and the indexed SAEDP acquired from it.

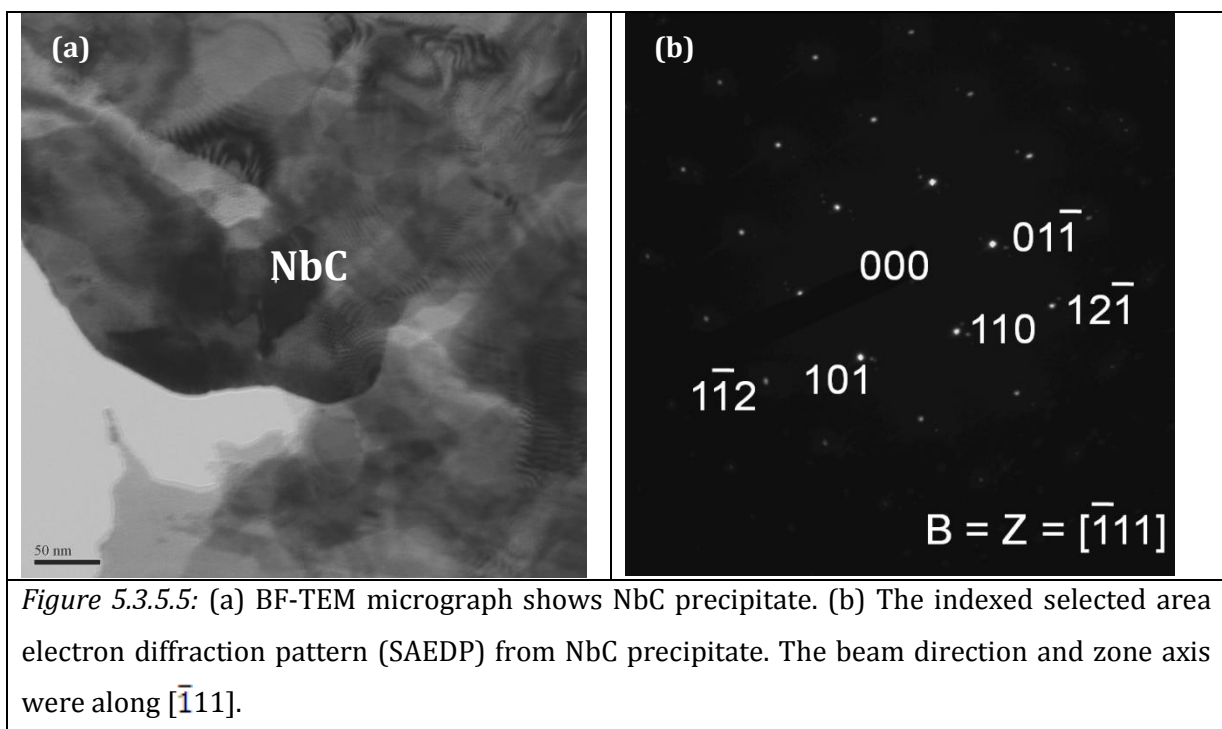


Figure 5.3.5.5: (a) BF-TEM micrograph shows NbC precipitate. (b) The indexed selected area electron diffraction pattern (SAEDP) from NbC precipitate. The beam direction and zone axis were along $[\bar{1}11]$.

The elemental quantitative analysis of NbC was Nb-8.1Mo-0.8Ni-0.3Cr-1.5Ti (wt. %). The precipitate was found to occur intra- and intergranularly in this specimen S9976. The precipitates were found to occur in different morphology from irregular to regular of varying size range from 100nm to 15 μ m.

5.3.5.6 Quantitative Measurements of Dislocation density

The array of dislocations and precipitate-dislocation interactions is shown in *Figure 5.3.5.6*. The similar dislocation measurement technique was used as discussed in previous sections. The dislocation density was estimated as $14.6 \pm 7.8 \times 10^{13}$ lines/m², which is higher than observed in 'as-received' IN625 and specimen S9980. This specimen was exposed for only short duration of 1000 hours at 650°C under a high stress.

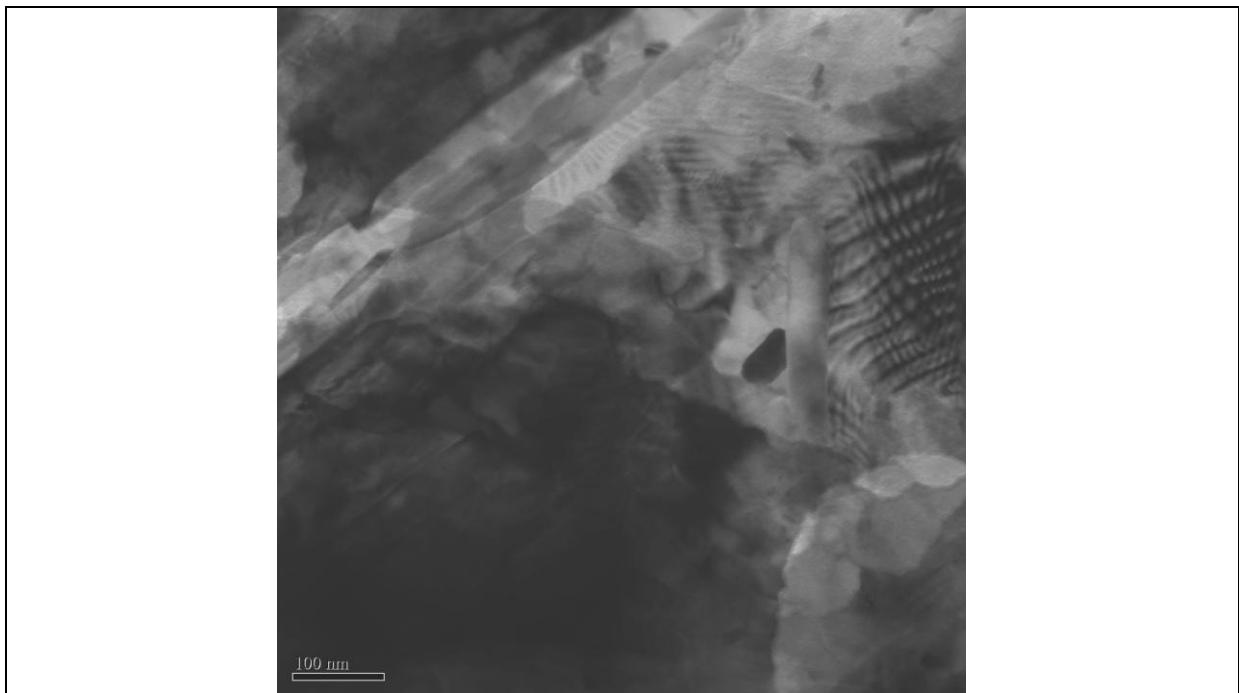


Figure 5.3.5.6: BF TEM micrograph shows dislocation structure, and precipitate in the creep-exposed specimen S9976.

Typical values of η_g (*number of extinction fringes*), ξ_g (*extinction distance*) and t (*foil thickness*) are listed in *Table 5.1.4.3*.

<i>Table 5.1.4.4: Typical values for η_g, ξ_g, t and ρ_d</i>			
η_g	ξ_g (Å) at 200kV	t (Å)	ρ_d (lines/m ²)
5	299.25	1346.24	14.6 X 10 ¹³

Summary

Precipitation of type MC (M=Nb, Mo), MN (M=Ti), metastable precipitates of γ'' , equilibrium δ -phase and $M_{23}C_6$ carbide phases were observed in both creep-exposed S9980 and S9976 samples. The precipitates were found of varying fractions in both samples. It was observed that the metastable γ'' phase is transformed to orthorhombic δ -phase upon creep exposure. However, δ -phase also form directly from the supersaturated solid solution on ageing at high temperature.

References

- Brown, E.E. and Muzyka, D.R. (1987) *The Superalloys II*, C.T. Sims and W.C. Hagel, eds., John Wiley, New York, NY, 165-88.
- Bohm, H., Ehlrich, K. and Krammer, K.H. (1970) *Metallurgy*, 24,139-144.
- Cozar, R. and Pineau, A. (1973). *Metallurgical Transactions*, 4, 47-59.
- Floreen, S., Fuchs, G.E. and Yang, W.J. (1994) in *Superalloys 718, 625, 706 and Various Derivatives*, E.A. Loria, ed., TMS, Warrendale, PA, 13-38.
- Ham, R. K. 1961. The determination of dislocation densities in thin foils. *Phil. Mag.* 6: 1183-1184.
- Hirsch, P., Howie, P., Nicholson, R.B. Pashley, D. W., and Whelan, M. J. (1977). *Electron Microscopy of Thin Crystals*, Krieger, New York, N.Y.1977.
- Hambleton, R., Rainforth, W.M. and Jones, H. (1997). Dislocation densities, dispersoid identities and the origins of thermal stability and strengthening in three mechanically alloyed aluminium alloys, *Philosophical Magazine A*, 76 (5), 1093-1104.
- Oblak, J.M., Paulonis, D.F. and Duvall, D.S. (1974). *Metallurgical Transactions*, 5, 143-153.
- Shankar, V., Rao, K. Bhanu Sankara, and Mannan, S. (2001). Microstructure and mechanical properties of Inconel 625 superalloy, *Journal of Nuclear Materials*, 288, 222-232.
- Sundararaman, M., Mukhopadhyay, P. and Banerjee, S. (1988) Precipitation of the δ -Ni₃Nb phase in two nickel base superalloys, *Metallurgical Transactions A*, 19A (3), 453-465.
- Sundararaman, M., Mukhopadhyay, P., and Banerjee, S. (1997). Carbide precipitation in nickel base superalloys 718 and 625 and their effect on mechanical properties, *Superalloys 718, 625, 706 and Various Derivatives*, 367-378.
- Sundararaman, M; Kumar, Lalit; Prasad, G Eswara; Mukhopadhyay, P; and Banerjee, S (1999). Precipitation of an intermetallic phase with Pt₂Mo-type structure in alloy 625. *Metallurgical and Materials Transactions A*, 30A, 41-52.
- Tawancy, H.M., Allam, I.M. and Abbas, N.M. (1990) Effect of Ni₃Nb precipitation on the corrosion resistance of Inconel alloy 625, *Journal of Materials Science Letters*, 9, 343-347.

Nimonic 263 is a nickel-based alloy that has good welding properties. The main strengthening phase in this alloy is γ' with $M_{23}C_6$ particles on the grain boundaries and TiN, η -phase precipitates within the grains and on the grain boundaries. This chapter presents results of microstructural observations on the samples that were detailed in chapter 3. The aim of the work in this chapter was to establish how creep at varying temperatures and stresses affected the evolution of precipitates. The microstructural work has been confined to optical and FEGSEM observations, TEM and EBSD have not been performed owing to time constraints and the large number of samples.

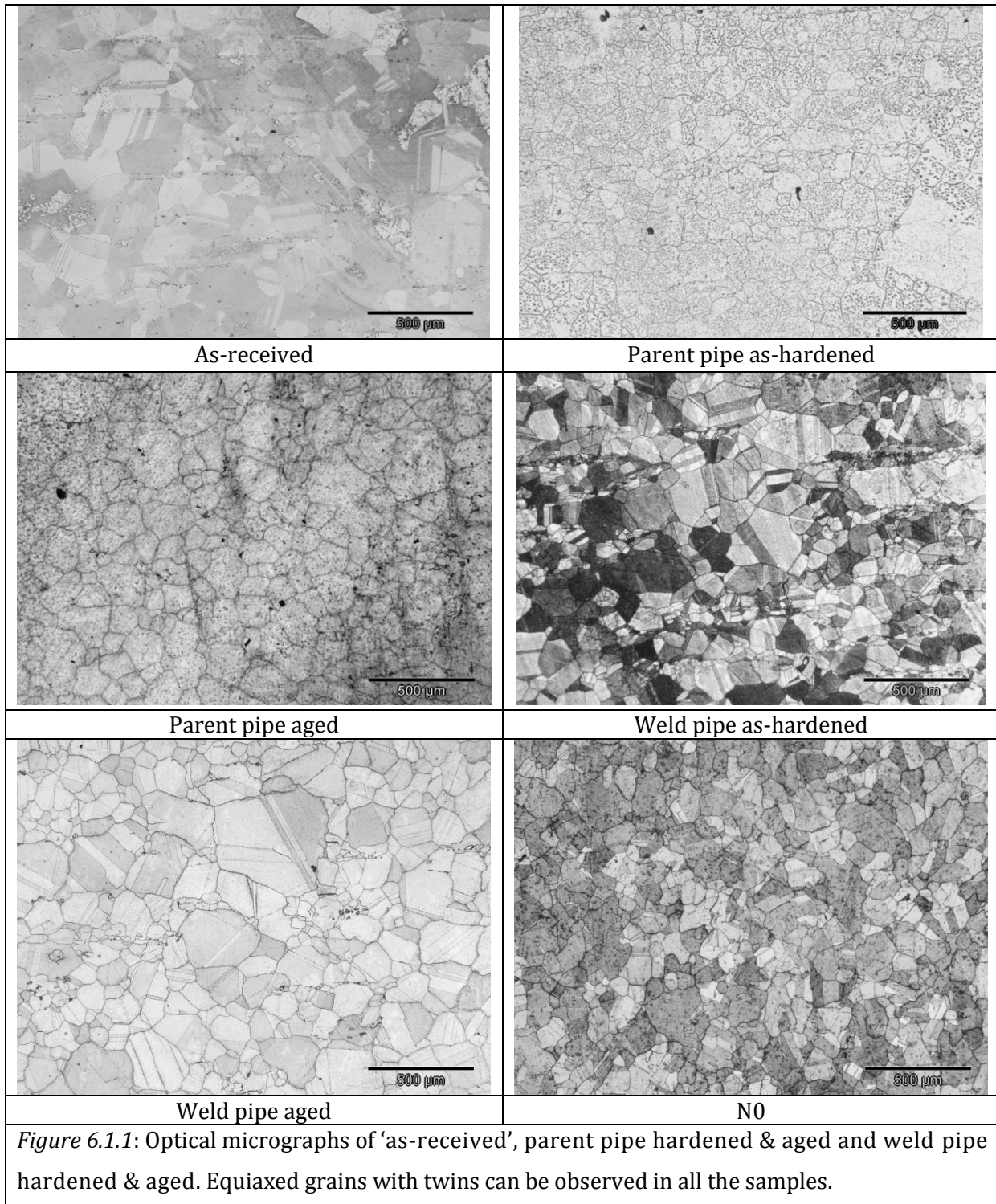
6.1 Grain Morphology

In this section the metallographic observations of the grain morphology and structure for the 'as-received', thermal and creep exposed Nimonic 263 samples are discussed. The 'as-received' sample was solution-annealed at 800°C/ 8 Hrs/ AC after solutionization for 1150°C/ 2 Hrs/ WQ. The solution annealed samples were machined for creep tests. The creep tests were conducted at 725 and 775°C in air under a uniaxial load. *Table 6.1.1* gives the main results for grain size range and average, grain shape, grain boundary morphology and hardness for all the thermally exposed alloys studied.

Table 6.1.1: Summary of Grain/Grain Boundary Morphology, ASTM grain size No. and Hardness

Thermal-exposed Samples	Grain Morphology			ASTM grain size No.	VHN (Hv/20)	Grain-boundary morphology
	Grain-size range (μm)	Avg. grain size (μm)	Grain shape			
As-received	25 to 470	54	Equiaxed	10-11	305.6 \pm 14	Flat
Parent pipe as-hardened	13 to 288.5	90.3	Equiaxed	5-6	283.8 \pm 8	Flat & wide
Parent Pipe aged	14 to 427.6	118.7	Equiaxed	5-6	337.8 \pm 12.3	Flat & wide
Weld as-hardened	16 to 340	75.0	Equiaxed	5-6	278.8 \pm 4	Flat
Weld aged	40 to 145	97.5	Equiaxed	5-6	310 \pm 14	Flat
NO (Hardened)	10 to 420	88.5	Equiaxed	5-6	284.2 \pm 14.7	Flat

The table shows that the grain size of the as-received alloy is small compared to the parent pipe and welded pipe samples. The ageing treatment on both the pipe and the weld-pipe increases the grain size. The hardness also increases for the pipes after the ageing treatments. The microstructures of the initial alloys are shown in *Figures 6.1.1*.



The micrographs show the equiaxed nature of the different samples. Twins can also be observed in all the different samples.

Table 6.1.2 shows the effect of creep exposure on the different samples. It can be seen that the grain size remains relatively constant over the temperatures, creep durations and stresses studied.

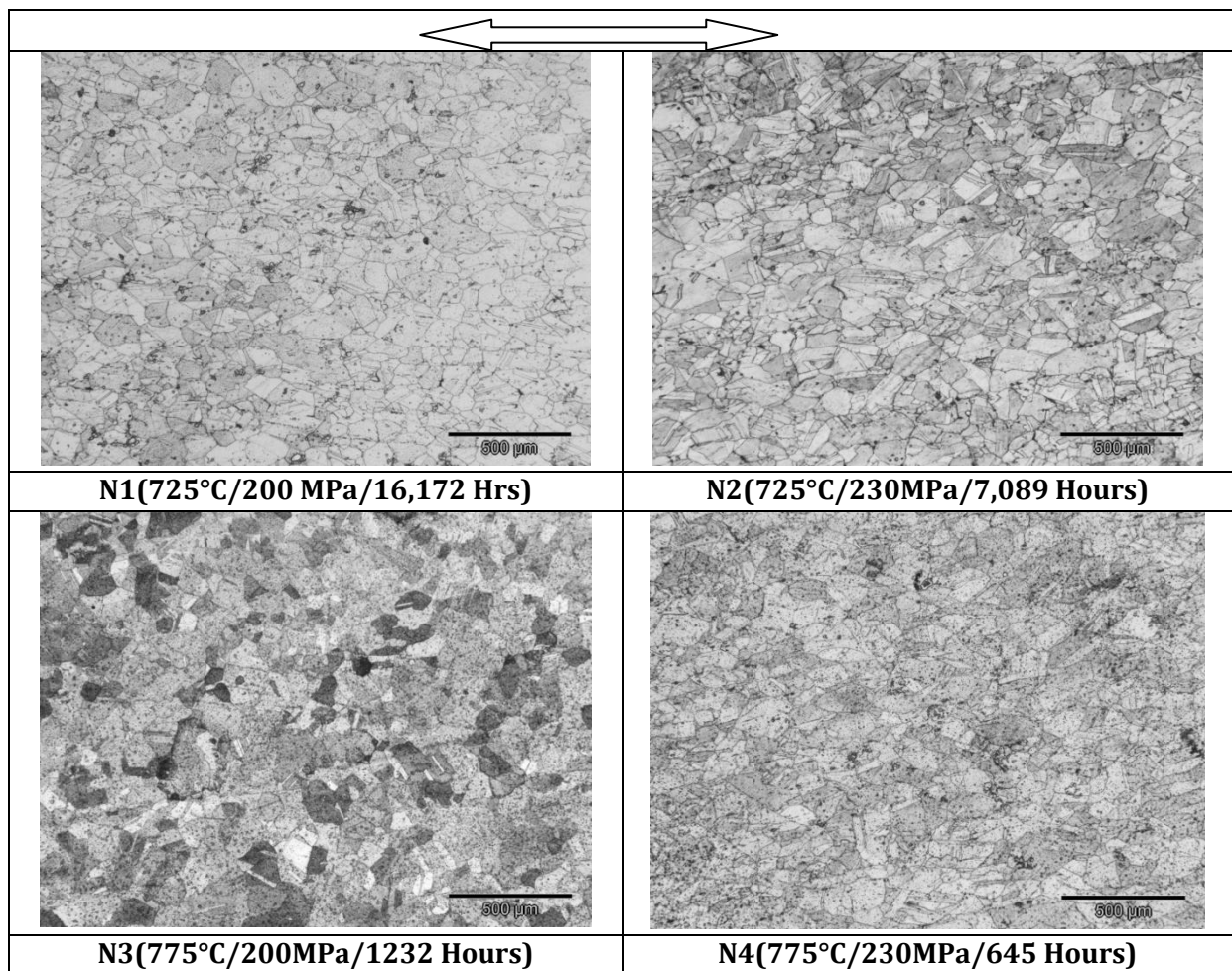
Table 6.1.2: Summary of Grain & Grain boundary morphology, Average grain size, and Hardness in head & gauge length of creep exposed samples

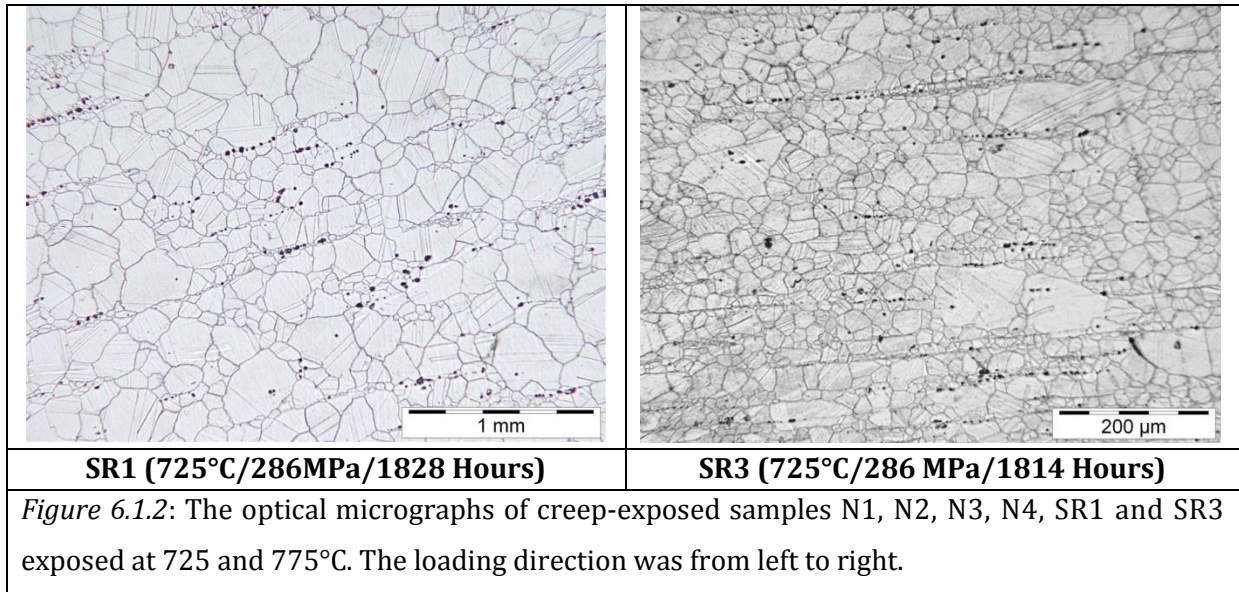
Creep-exposed samples	Grain Morphology			VHN (Hv/20)		Grain-boundary morphology
	Grain-size range (μm)	Avg. grain size (μm)	Grain shape	Head	Gauge	
N1 (725°C/200 MPa/16,172 Hrs)	20 to 340	81.5	Equiaxed & Elongated	290	345	Flat
N2 (725°C/230MPa/ 7,089Hrs)	10 to 295	72.5	Equiaxed & Elongated	297	351	Flat
N3 (775°C/200MPa/ 1232 Hours)	18 to 249.5	65.9	Equiaxed	292	348	Flat
N4 (775°C/230MPa/ 645 Hrs)	21 to 321	67.2	Equiaxed & Elongated	298	357	Flat
SR1 (725°C/286MPa/ 1828 Hrs)	20 to 605	79	Equiaxed	343	371	Flat
SR3 (725°C/286MPa/ 1814 Hrs)	20 to 423	72	Equiaxed	329	389	Flat
SR4 (725°C/250MPa/ 3529 Hrs)	25 to 323	77	Equiaxed	325	352	Flat
263-P3 (725°C/286MPa/ 1833 Hrs)	12 to 559	114	Equiaxed	349	366	Flat
263-W1 (725°C/265MPa/ 2376 Hrs)	32 to 534	89	Equiaxed	313	373	Flat
263-W2 (725°C/265MPa/ 1988 Hrs)	31 to 423	111	Equiaxed	325	357	Flat

The grain boundary morphology remains constant as well. The main change that is observed in the creep exposed samples is an increase in hardness in both the head and the gauge. The gauge hardness is always greater than the head hardness showing that the additional strain is

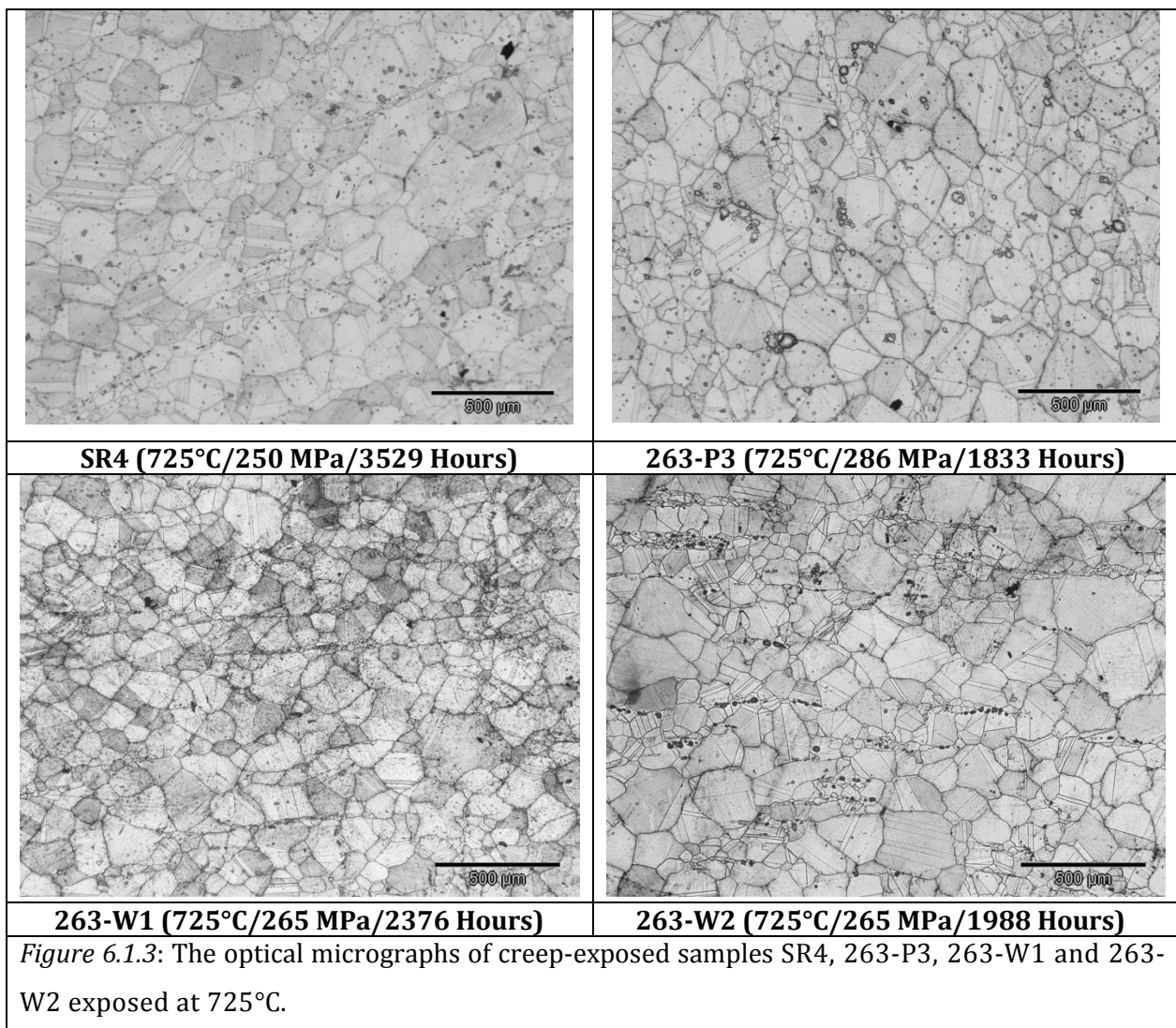
accelerating microstructural precipitation and work hardening in the gauge. It is noticeable that the grain size in the creep exposed samples is smaller than that of the as-hardened parent pipe or the weld pipe.

The following section shows the microstructures of the creep exposed samples. The creep exposed micrographs were found to be equiaxed in SR1 (725°C/286MPa/1828 Hrs), SR3 (725°C/286MPa/1814 Hrs), SR4 (725°C/250MPa/3529 Hrs), 263-P3 (725°C/286MPa/1833 Hrs), 263-W1 (725°C/265MPa/2376 Hrs), and 263-W2 (725°C/265MPa/1988 Hrs). Samples shown elongated as well as equiaxed grains were N1 (725°C/200 MPa/16,172 Hrs), N2 (725°C/230MPa/7,089Hrs) and N3 (775°C/200MPa/1232 Hours). The higher stresses and temperatures have played an important role in recrystallization and growth of the grains.





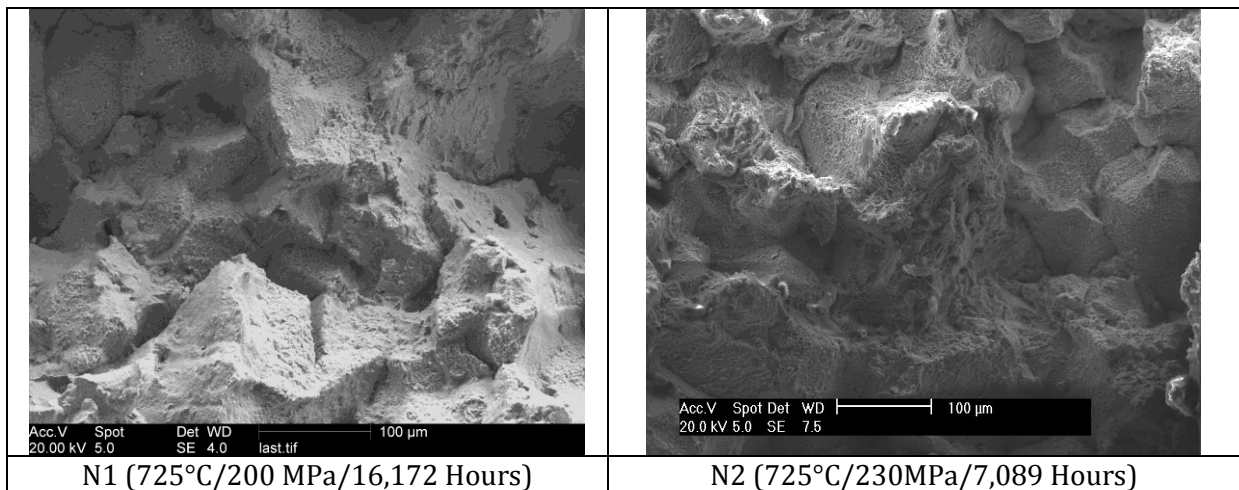
Precipitates were found to precipitate along the direction of the load in samples SR1 and SR3.

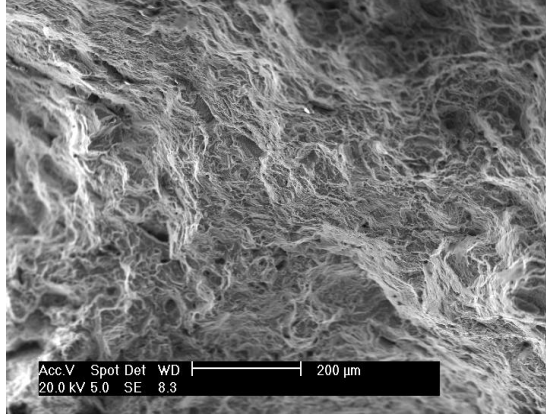
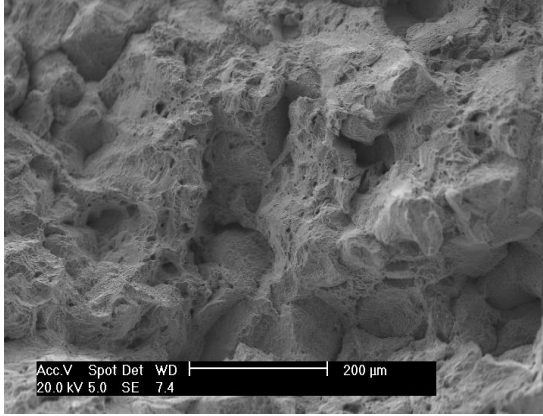
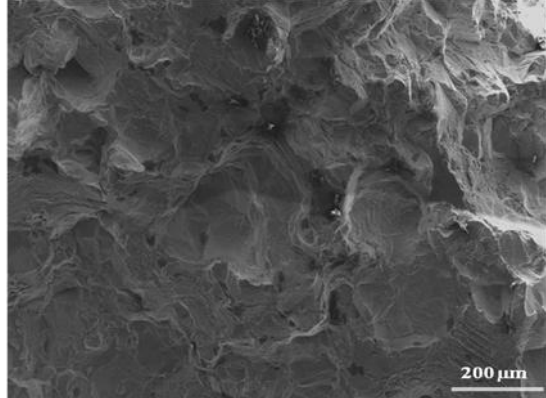
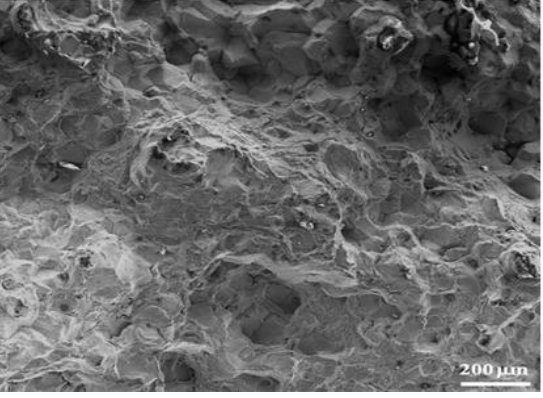
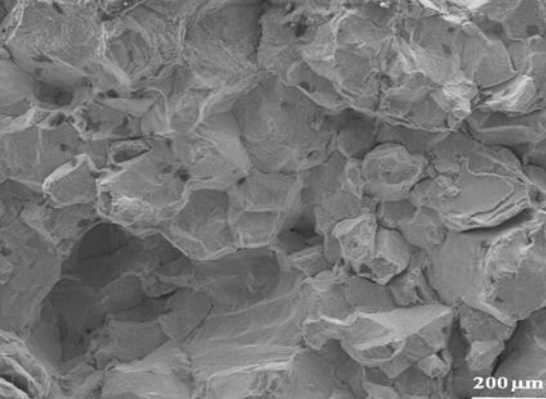
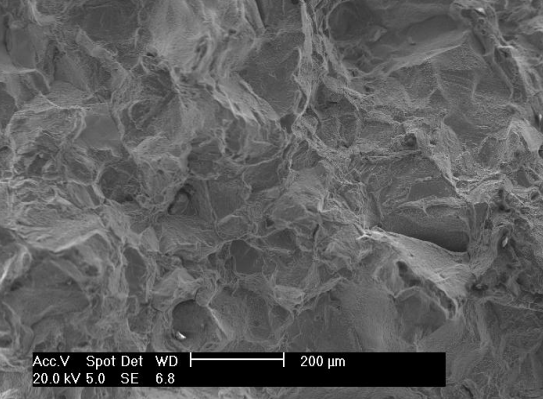
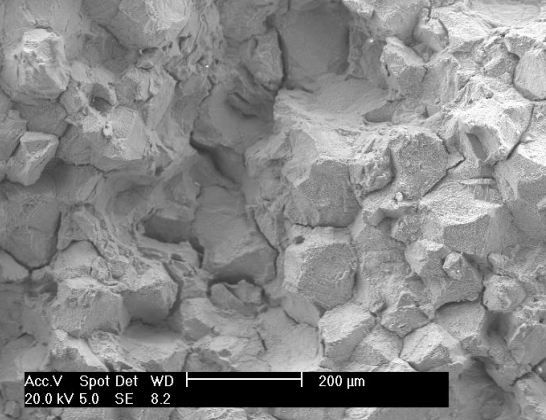
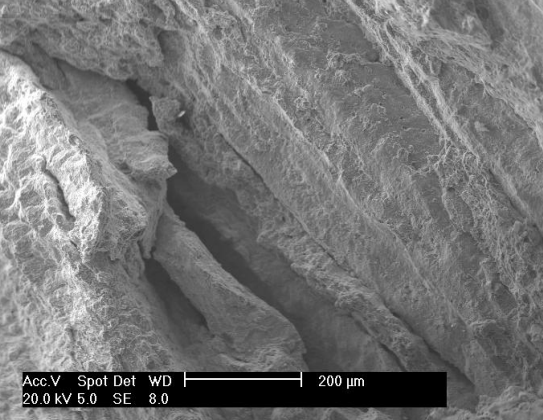


They were exposed at 725°C for ever highest stress level of 286MPa. All samples were exposed to precipitation annealing for 4 to 24 hours at 800°C before creep tests. The different exposure time was found to effect the precipitation behaviour in all creep exposed samples. Therefore, samples have shown different microstructure after the creep exposure.

6.2 Fractography

The failure mechanism of creep exposed specimens was analysed using scanning electron microscopy. The representative fractographs of creep failed samples are shown in following micrographs. The failure mechanisms in creep failed samples are discussed in this section. The fracture modes were observed to depend on the creep exposure conditions in all samples. Samples SR4, N1 and 263-W1 were found to creep failed by intergranular creep mechanism. Both SR4 and N1 samples exposed at 725°C and were precipitation hardened for 8 hours at 800°C. The rest of all samples were failed by a mixed mode of fracture mechanism: intergranular and transgranular. However the prominent mechanism observed in all samples was intergranular fracture mode but there was evidence of a contribution from transgranular failure.



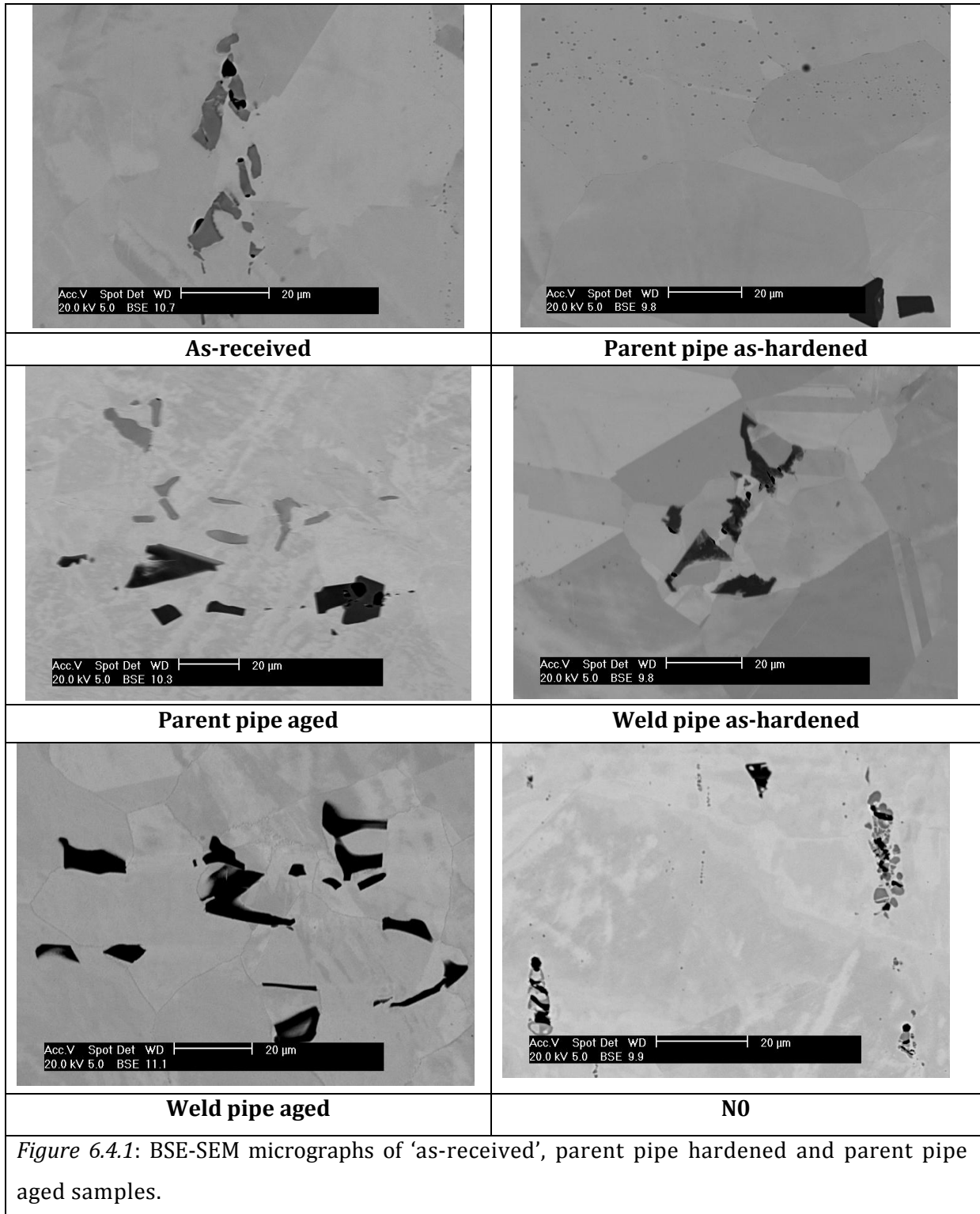
 <p>Acc.V Spot Det WD 200 μm 20.0 kV 5.0 SE 8.3</p>	 <p>Acc.V Spot Det WD 200 μm 20.0 kV 5.0 SE 7.4</p>
<p>N3 (775°C/200MPa/1232 Hours)</p>	<p>N4 (775°C/230MPa/645 Hours)</p>
 <p>200 μm</p>	 <p>200 μm</p>
<p>SR1 (725°C/286MPa/1828 Hours)</p>	<p>SR3 (725°C/286 MPa/1814 Hours)</p>
 <p>200 μm</p>	 <p>Acc.V Spot Det WD 200 μm 20.0 kV 5.0 SE 6.8</p>
<p>SR4 (725°C/250 MPa/3529 Hours)</p>	<p>263-P3 (725°C/286 MPa/1833 Hours)</p>
 <p>Acc.V Spot Det WD 200 μm 20.0 kV 5.0 SE 8.2</p>	 <p>Acc.V Spot Det WD 200 μm 20.0 kV 5.0 SE 8.0</p>
<p>263-W1 (725°C/265 MPa/2376 Hours)</p>	<p>263-W2 (725°C/265 MPa/1988 Hours)</p>

6.3 Phase Identification

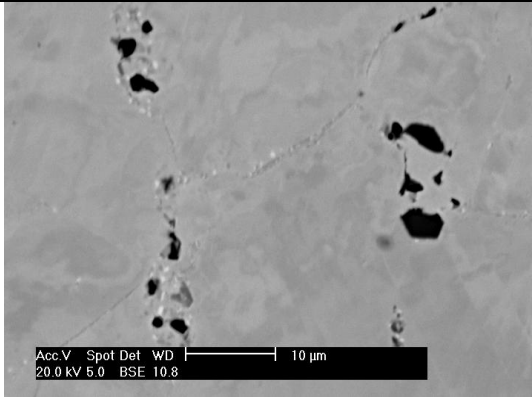
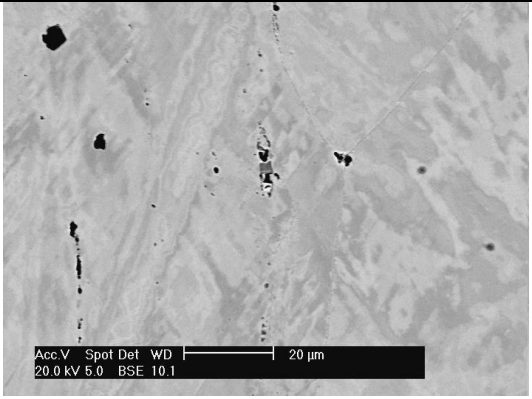
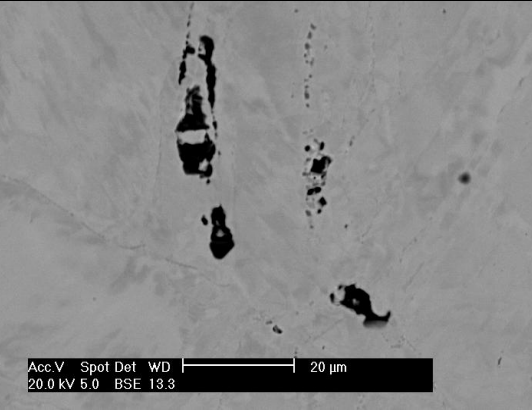
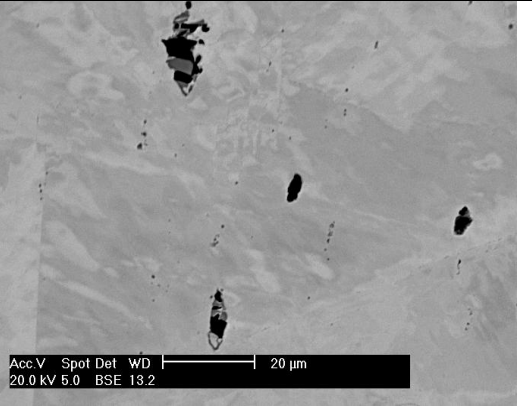
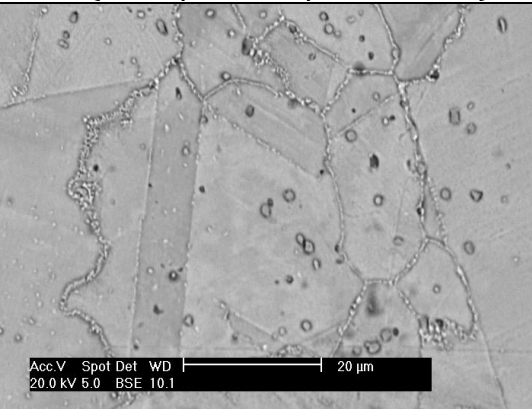
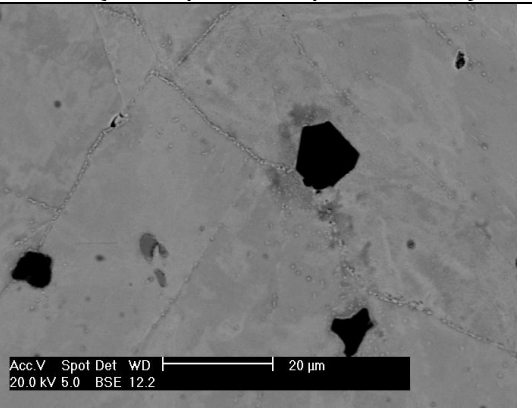
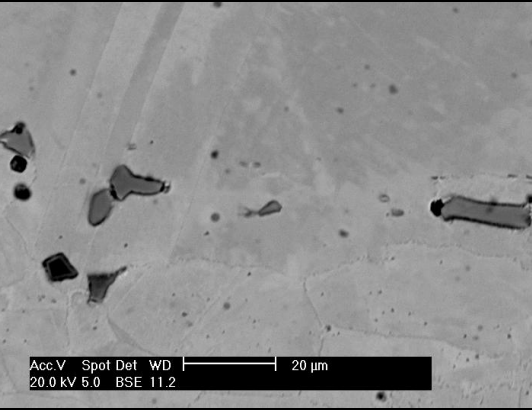
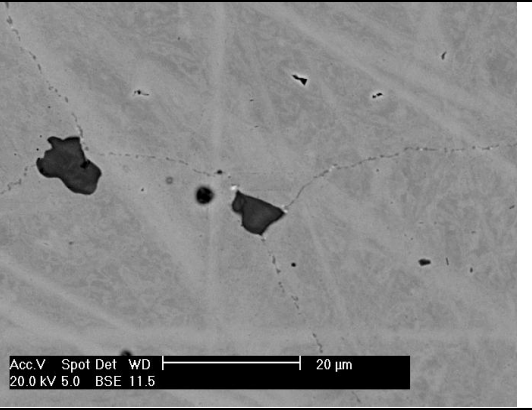
X-ray diffraction patterns of as-received, thermal and creep exposed specimens of Nimonic 263 alloys were analysed to identify the phases, as discussed in section 3.5. The identified precipitates in the specimens were γ' -gamma prime, $M_{23}C_6$, TiN, μ and η -phase. $M_{23}C_6$ is referred as in many places in place of Cr-rich precipitate $Cr_{23}C_6$ as discussed in the previous sections.

6.4 Precipitate Morphology and Location

Precipitate morphology and locations are discussed in this section. BSE-SEM micrographs of as-received, thermal exposed and creep exposed samples are shown in *Figures 6.4.1* and *6.4.2*, respectively. The precipitates found in the specimens were rich in Ti, Cr and Mo. The morphology and location of the precipitates in thermal and creep exposed samples are shown in *Table 6.4.1* and *6.4.2* respectively. The precipitates were found intra- and intergranularly in the alloy. Mo-enriched and Cr-enriched precipitates were found very fine in size along the grain and twins boundaries in creep exposed specimens N1 (725°C/200 MPa/16,172 Hours), N2 (725°C/230MPa/7,089 Hours), N3 (775°C/200MPa/1232 Hours), N4 (775°C/230MPa/645 Hours), P3 (725°C/286 MPa/1833 Hours), SR1 (725°C/286MPa/1828 Hours), SR3 (725°C/286 MPa/1814 Hours), SR4 (725°C/250 MPa/3529 Hours) and W1 (725°C/265 MPa/2376 Hours). η -phase found in the thermal and creep exposed specimens were long rod shape of size minimum of 2 μ m to maximum of 15 μ m and observed near to TiN precipitates. SR1 and SR3 specimens were creep exposed at 725°C under a uniaxial load of 286MPa after hardened for 4 and 8 hours at 800°C respectively. In both specimens extensive precipitation were observed along the grain and twin boundaries.



The MC carbide, rich in Ti and Mo in the form of (Ti, Mo) C was observed in the alloy. The intragranular MC carbides were cylindrical or equiaxed morphology. The MC carbides phase was also observed at the grain and twin boundaries. The intergranular precipitates were rich in chromium and they were mostly $M_{23}C_6$ carbides.

	
<p>N1 (725°C/200 MPa/16,172 Hours)</p>	<p>N2 (725°C/230MPa/7,089 Hours)</p>
	
<p>N3 (775°C/200MPa/1232 Hours)</p>	<p>N4 (775°C/230MPa/645 Hours)</p>
	
<p>SR1 (725°C/286MPa/1828 Hours)</p>	<p>SR3 (725°C/286 MPa/1814 Hours)</p>
	
<p>SR4 (725°C/250 MPa/3529 Hours)</p>	<p>263-P3 (725°C/286 MPa/1833 Hours)</p>

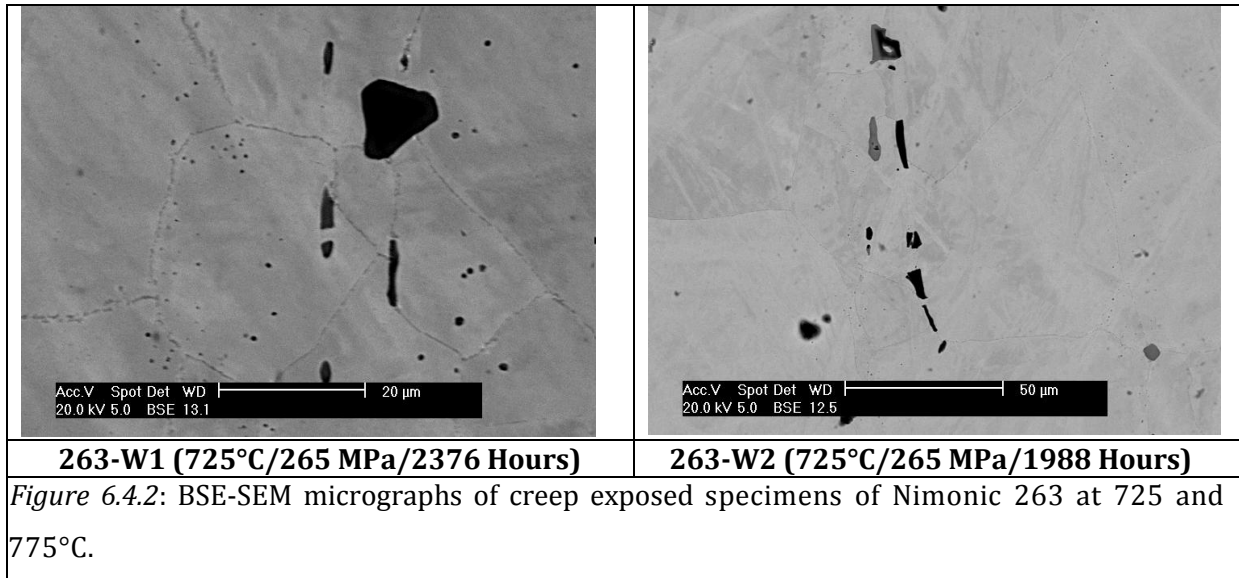


Table 6.4.1: Precipitate morphology and location in as-received & thermal exposed Nimonic 263

Specimen ID	Precipitate Location	Precipitates Morphology		
		Phases	Size	Shape
As-received	Intra- and inter-granularly	η -phase, Ni_3Ti	3-15 μm	Rods shape
		Ti (C,N)	5-18 μm	Regular to totally irregular geometry
		M_{23}C_6	<1-2 μm	
Parent pipe as-hardened	Intra- and inter-granularly	η -phase	2-20 μm	Long rods shape
		Ti (C,N)	1-2 μm	Regular to totally irregular geometry
		M_{23}C_6	<1-10 μm	
Parent pipe aged	Intra- and inter-granularly	η	2-20 μm	Long rods shape
		Ti (C,N)	1-2 μm	Regular to totally irregular geometry
		M_{23}C_6	<1-10 μm	
		Mo-enriched	<0.5-1 μm	
Weld pipe as-hardened	Intra- and inter-granularly	η -phase	5-15 μm	Regular to totally irregular geometry
		Ti (C,N)	4-10 μm	
		M_{23}C_6	<1-5 μm	
Weld pipe aged	Intra- and inter-granularly	η -phase	6-10 μm	Regular to totally irregular geometry
		Ti (C,N)	6-15 μm	
		M_{23}C_6	<1 μm	
N0	Intra- and inter-granularly	η -phase	2-4 μm	Rods shape
		Ti (C,N)	5-7 μm	Regular to totally irregular geometry
		M_{23}C_6	<1-2 μm	

Table 6.4.2: Precipitate morphology and location in creep exposed Nimonic 263 alloys

Specimen ID	Precipitate Location	Precipitates Morphology		
		Phases	Size	Shape
N1	Intra- and inter-granularly	η -phase	2-3.5 μm	Long rods shape
		Ti (C,N)	1-5 μm	Regular to totally irregular geometry
		M_{23}C_6	<1 μm	
		Mo-enriched	<1-1.2 μm	
N2	Intra- and inter-granularly	η -phase	2-2.5 μm	Long rods shape
		Ti (C,N)	1-3 μm	Regular to totally irregular geometry
		M_{23}C_6	<1 μm	
		Mo-enriched	<0.5-1 μm	
N3	Intra- and inter-granularly	η -phase	1-2.5 μm	Regular to totally irregular geometry
		Ti (C,N)	10-15 μm	
		M_{23}C_6	<1 μm	
	Along the GB	Mo-enriched	<1 μm	
N4	Intra- and inter-granularly	η -phase	2-3 μm	Regular to totally irregular geometry
		Ti (C,N)	5-10 μm	
		M_{23}C_6	<1 μm	
	Along the GB	Mo-enriched	<1 μm	
P3	Intra- and inter-granularly	η -phase	2-4 μm	Rods shape
		Ti (C,N)	5-6 μm	Regular to totally irregular geometry
		M_{23}C_6	<1-2 μm	
		Mo-enriched	<1 μm	
SR1	Intra- and inter-granularly	η -phase	2-3.5 μm	Long rods shape
		Ti (C,N)	5-10 μm	Regular to totally irregular geometry
		M_{23}C_6	<1 μm	
		Mo-enriched	<1 μm	
SR3	Intra- and inter-granularly	η	5-12 μm	Long rods shape
		Ti (C,N)	5-10 μm	Regular to totally irregular geometry
		M_{23}C_6	<1 μm	
		Mo-enriched	<0.5-1 μm	
SR4	Intra- and inter-granularly	η -phase	1-8 μm	Regular to totally irregular geometry
		Ti (C,N)	4-8 μm	
		M_{23}C_6	<1 μm	
	Along the GB	Mo-enriched	<1 μm	
W1	Intra- and inter-granularly	η -phase	10-12 μm	Regular to totally irregular geometry
		Ti (C,N)	5-10 μm	
		M_{23}C_6	<1 μm	
	Along the GB	Mo-enriched	<1 μm	
W2	Intra- and inter-granularly	η -phase	8-10 μm	Regular to totally irregular geometry
		Ti (C,N)	5-15 μm	
		M_{23}C_6	<1 μm	

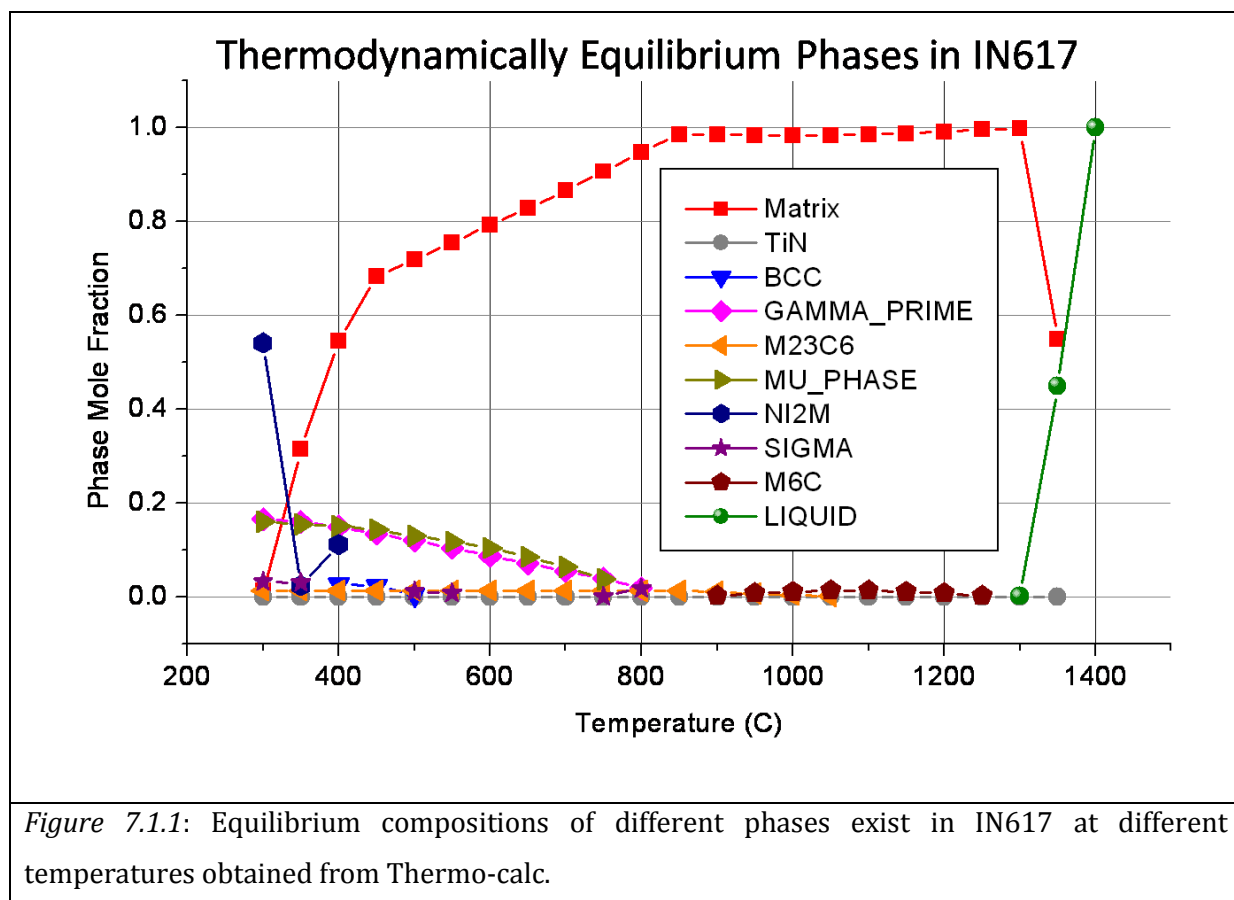
Summary

The microstructural work in this chapter has shown that the thermal and creep exposed samples were differ on grain structure, hardness and precipitation. The hardness of parent pipe aged and as hardened was higher than that of weld pipe aged and as hardened, however all samples has equiaxed grain structures. Their average grain size was approximately same. The creep exposed samples also exhibited the equiaxed grains but a few samples such as N1, N2 and N4 showed equiaxed as well as elongated grains. The hardness of creep exposed samples was higher than the thermally aged samples. The precipitates in thermally aged and creep exposed at 725 and 775°C samples were TiN, $M_{23}C_6$, Mo-rich phase and η -phase. The TiN precipitates were blocky in shape and found randomly in the alloy. They are of size in the range from 2-15 μ m. All the creep exposed samples were found to have η -phase. They were of long rod or cylindrical morphology and found mostly inside the grains. η -phase and TiN precipitates were found together in many places in the alloy matrix. However, TiN phase was in large fraction in as-received alloy. It was found that η -phase was precipitated and grown during the creep exposure conditions. Mo-rich phase was very fine of size less than 1 μ m and observed only along the grain boundaries and near to the large $M_{23}C_6$ phase. The exact nature of the Mo-rich phase as either μ - or M_6C will need to be identified in future work. The morphology of this phase was irregular.

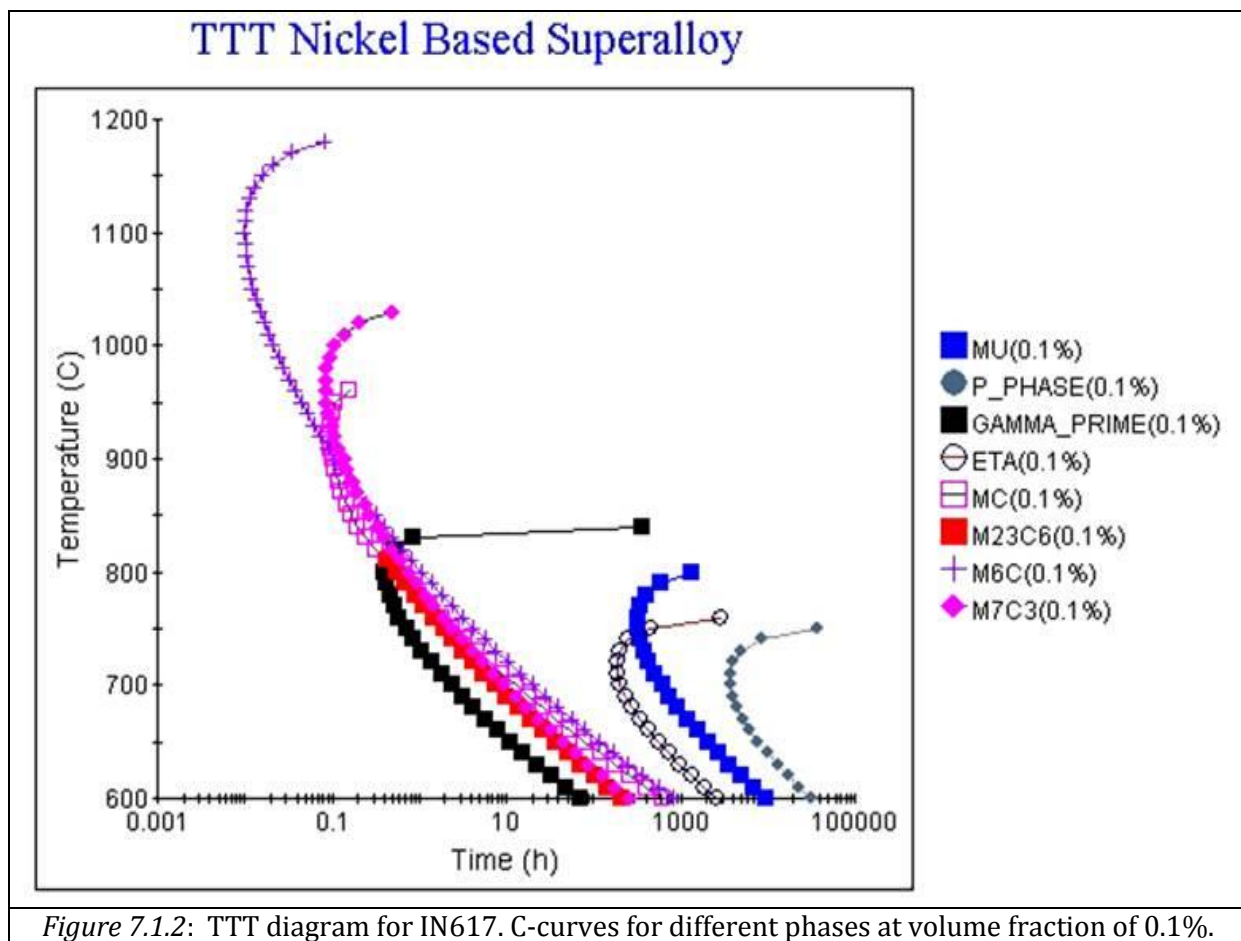
Chapters 4, 5, and 6 presented the experimental results for each of the different alloys studied in this thesis. This chapter gives a discussion of the results and the implications of the findings.

7.1 Discussion for IN617 Alloy

The thermodynamically stable phases that appeared in IN617 at different temperatures can be predicted from the thermodynamic prediction software programs, Thermo-calc (Thermo-Calc Software AB, 2006) and JMatPro (Saunders, 2004 & 2008). The thermodynamic equilibrium phases in alloy IN617 at 650 and 700°C are γ' , $M_{23}C_6$ (Cr-enriched), TiN (Ti-enriched) and μ -phase (Mo-enriched). *Figure 7.1.1* shows the predicted thermodynamic equilibrium phases along with their proportions at different temperatures in IN617.



The experimental results have confirmed the presence of these phases, but μ -phase was only observed for the specimens that had been creep-exposed to longest durations of 45,000 hours at 650°C (T0008) and at 700°C, in both specimens T0151, exposed for even a short duration of 4,000h and T0154, exposed for 32,000h. A time-temperature-transformation (TTT) diagram can be obtained from JMatPro software and is shown in *Figure 7.1.2*. It predicts the different phases to appear in the alloy in a range of temperature and time domains. The thermodynamic prediction shows that μ -phase appears after 2000 hours at 650°C and it is the last phase to appear in this alloy. $M_{23}C_6$ and MC phase appear at around 50 hours to 2,000 hours in between γ' and μ phases. At a temperature of 650°C and creep durations lower than 2,000 hours, no μ -phase can be seen (*Figure 7.1.2*).



μ -phase is not a thermodynamically favoured phase, at lower temperature and time durations, therefore, in the specimen T0003, which was creep-exposed at 650°C for 574 hours,

no μ -phase would be predicted and none was observed in the microstructural studies. The thermodynamic prediction shows that the equilibrium phase γ' appears after 10 hours to 100 hours at 650°C and it is the earliest phase to appear in the alloy, as observed in *Figure 7.1.2*.

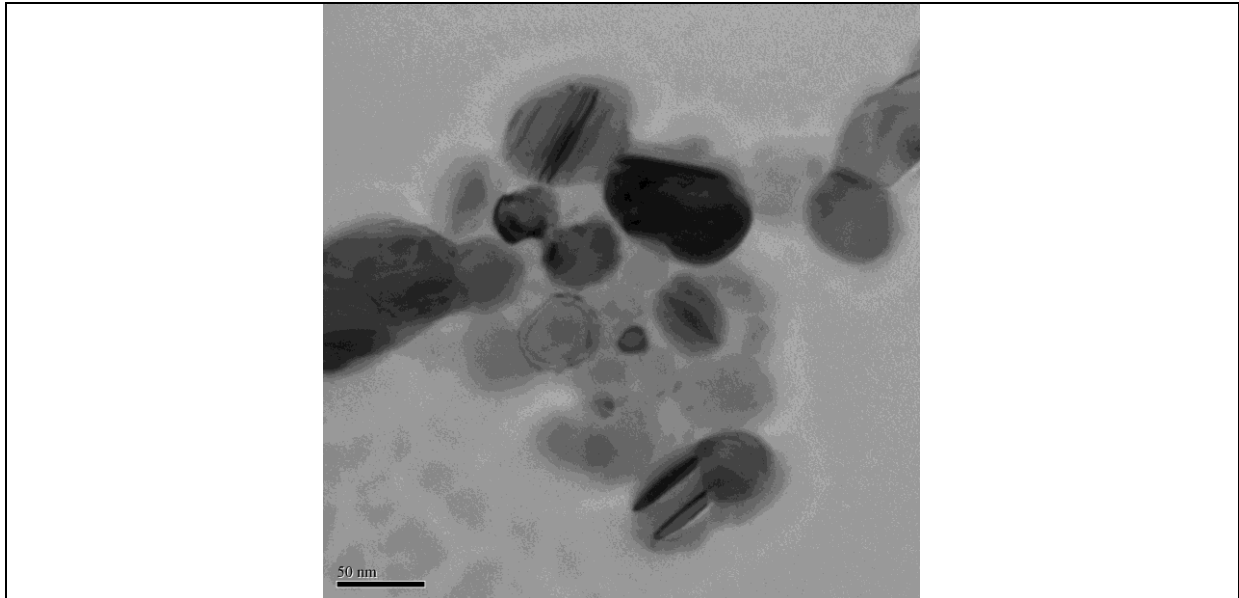
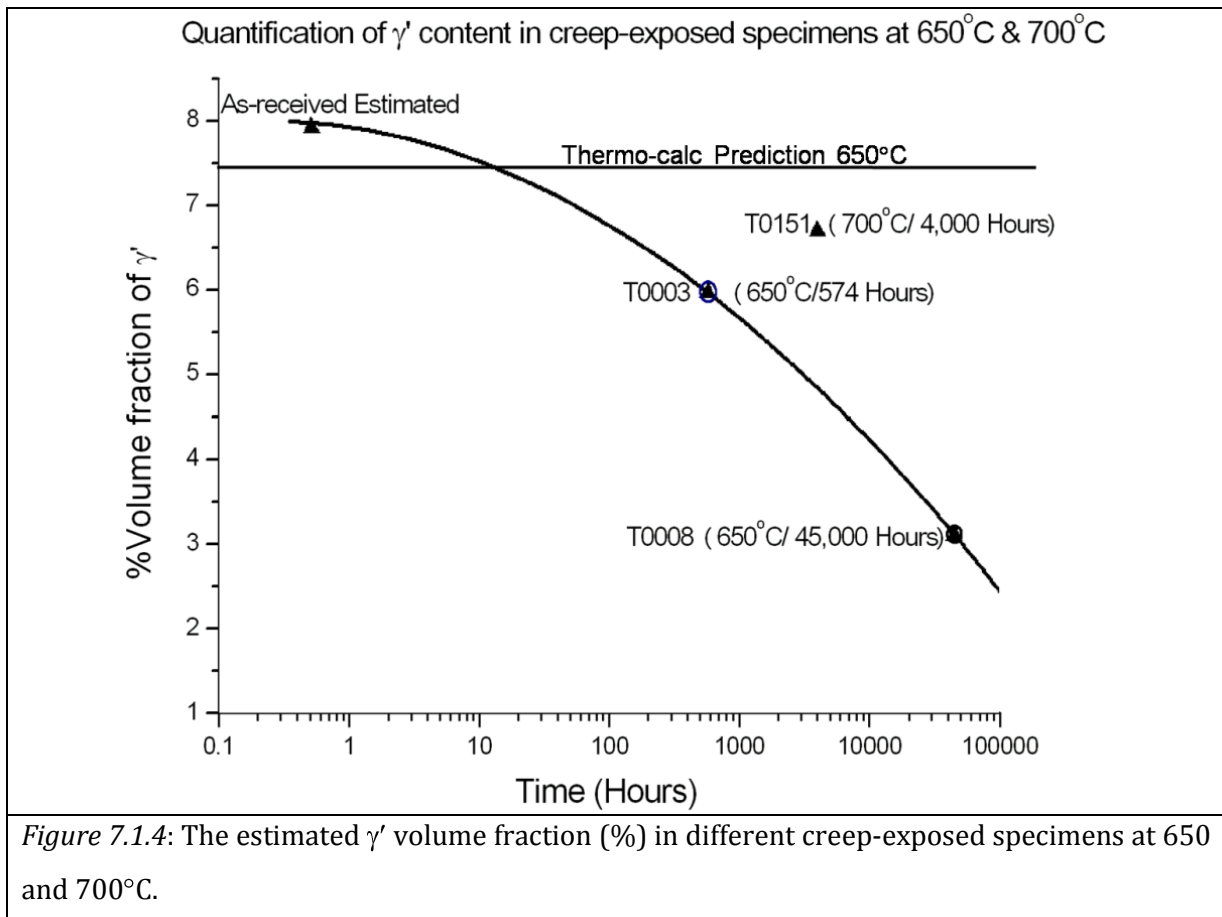


Figure 7.1.3: μ -phase observed in specimen T0151 creep-exposed at 700°C for short durations of 4,000 hours.

Experimentally, it was found that precipitates of γ' were of spherical morphology from 10nm to 70nm in size range and uniformly distributed through-out the matrix. The quantification of γ' content in creep-exposed specimens at 650 and 700°C can be estimated from Thermo-calc and results are shown in *Figure 7.1.4*.

The %volume fraction in 'as-received' specimen was estimated as approximately 8% and it was of fine spherical morphology from 10nm to 25nm. On creep-exposure the γ' precipitates have shown an obvious growth in size range from 10nm to 70nm, the coarsening depends upon the creep duration and temperature. In all creep-exposed specimens at 650°C, γ' precipitates showed no appreciable change in the morphology, but change was observed in size of the precipitates.



This growth of γ' precipitates in specimens was consistent with diffusion-controlled coarsening and was controlled by the volume diffusion of aluminium and titanium in the matrix. The stable shape of γ' precipitates is beneficial to the high temperature strength and creep properties. However, with an increase in the creep-exposure temperature to 700°C, a remarkable change in shape occurred; fine spherical γ' precipitates took a bigger spherical shape with substantial increase in number (T0151). This can be observed in specimen T0151, exposed at 700°C. The %volume fraction in specimen T0151, creep-exposed at 700°C for 4,000 hours durations was estimated as approximately 6.7 %, which is lower than the 'as-received' specimen. This sample showed γ' precipitates morphology, can be observed in *Figure 7.1.5*, as spherical shape, and of size range from 15 to 50nm. The cuboidal shape precipitates also found in the sample and they are of titanium carbo-nitride particles (SADP confirmed it).

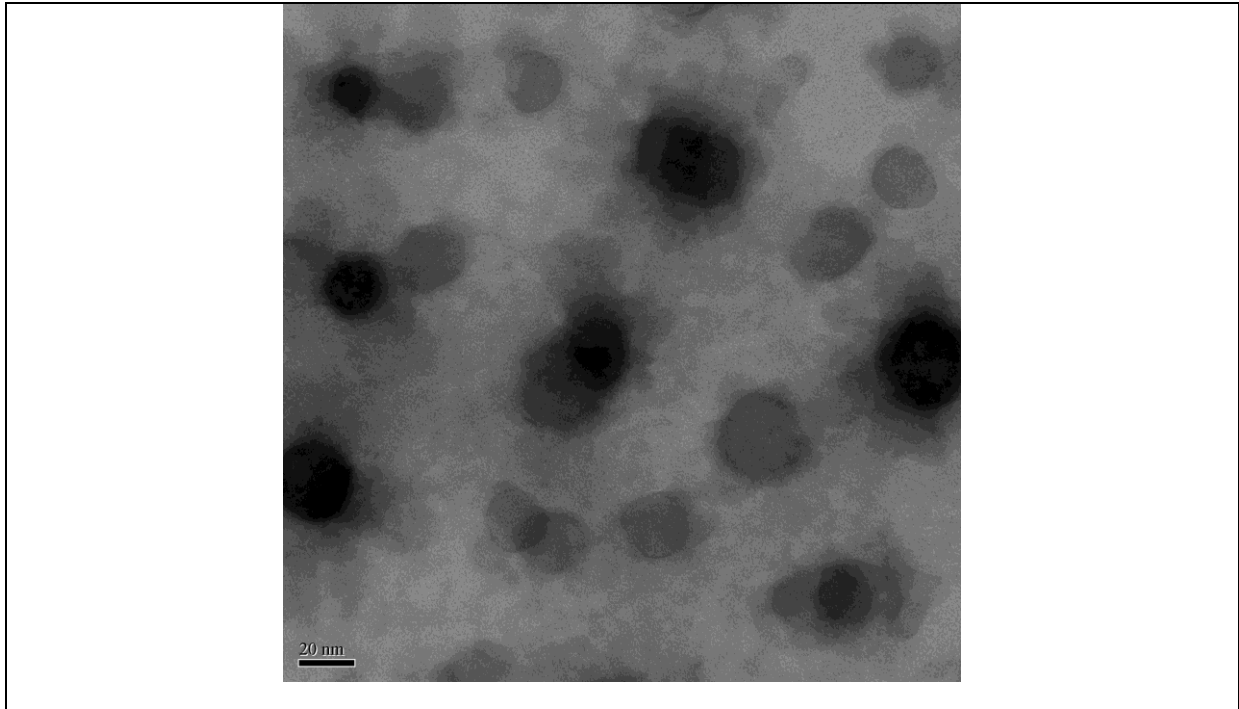
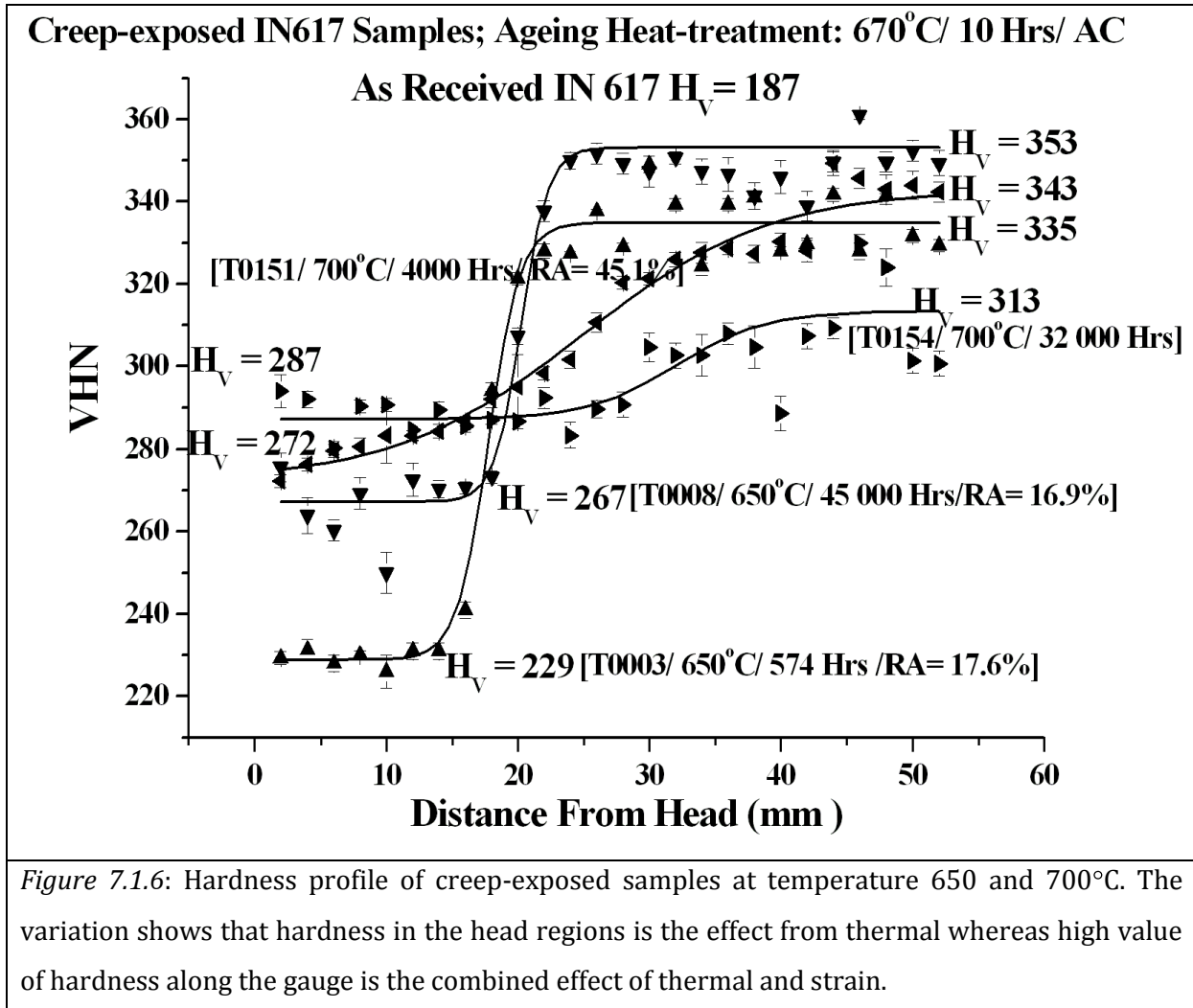


Figure 7.1.5: γ' morphology in specimen T0151 creep-exposed at 700°C for 4,000 hours. The morphology of spherical can be observed in the TEM micrograph.

The hardness of all creep-exposed specimens was higher than for the 'as-received' specimen. The thermally exposed head regions of the samples had lower hardness than the gauges that had been exposed to both stress and temperature. All specimens showed an extensive network of precipitates in both the grain boundaries that were decorated with fine $M_{23}C_6$ (Cr-rich) precipitates, and the grains themselves.

Figure 7.1.6 shows the hardness variation profile of creep-exposed samples at 650 and 700°C from 574 to 45,000 hours. The hardness increases substantially in the head and gauge length from the as-received samples. The high hardness value in head and gauge regions from the as received sample is due to precipitation, dislocations and particle-dislocation interactions. Further, the high hardness value along the gauge length from the head regions is due to extensive precipitations and dislocation density during the exposure effect of temperature and strain.



Sample T0008 sample showed highest value of hardness along the gauge length after 45,000 hours of creep exposure. The reduction in area was approximately 17% lowest among all the samples. In this sample extensive precipitation of carbides was observed. The increase in hardness in the head regions from the as-received arises from precipitation of $M_{23}C_6$ rather than gamma prime, whose volume percent decreases, observed from the thermo-calc studies. The further increase in hardness of the gauge length compared to head is possibly due to work hardening (increase in dislocation density) and extensive precipitations.

Precipitates of $M_{23}C_6$ and TiN/TiC were found to have varying morphology and there was no straight-forward relationship between the morphology of precipitates and their composition. It was observed that the area fraction of $M_{23}C_6$ carbides increases over the

exposure time in the head and gauge region of the specimens. The rises in hardness observed in the head and gauge of the specimens are contributed by the precipitation of $M_{23}C_6$ carbides and also, due to fine precipitation of Ti (C, N) carbo-nitrides. A secondary hardening effect was also observed from the γ' precipitates, dispersed throughout the matrix.

Time-temperature parameters have been devised to assist in correlating and extrapolating stress-rupture data. One particularly useful stress-rupture parameter is the Larson-Miller parameter (Larson and Miller, 1952) given by the *Equation 7.1.1*. Here, the LM parameter relationship is used to correlate the hardness.

$$LM = T[C_{LM} + \log t_r]/1000 \quad (7.1.1)$$

where T is the absolute temperature, C_{LM} is 20, independent of the material. t_r is rupture time in hours. A correlation of the hardness along the head and gauge region, with the Larson-Miller parameter is shown in *Figure 7.1.7*. This figure shows the curve fitting for the hardness value along the gauge length and head at 650 and 700°C. The graph shows that the hardness value for the gauge length increases and for the head remains constant with creep duration.

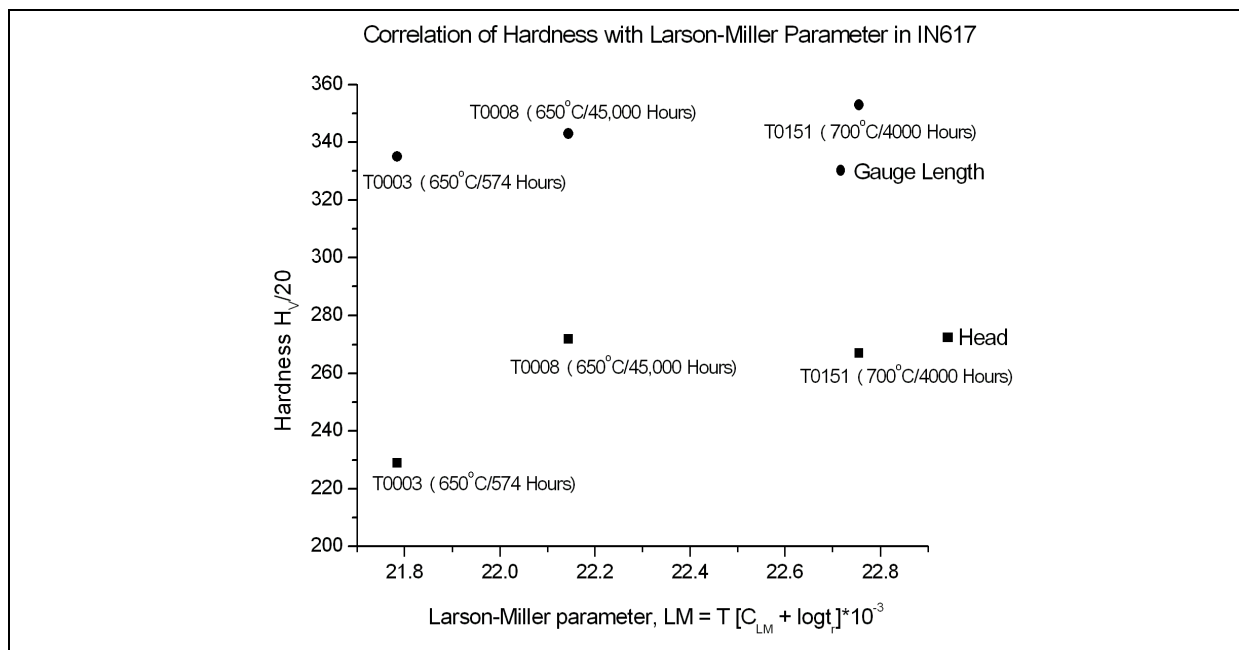
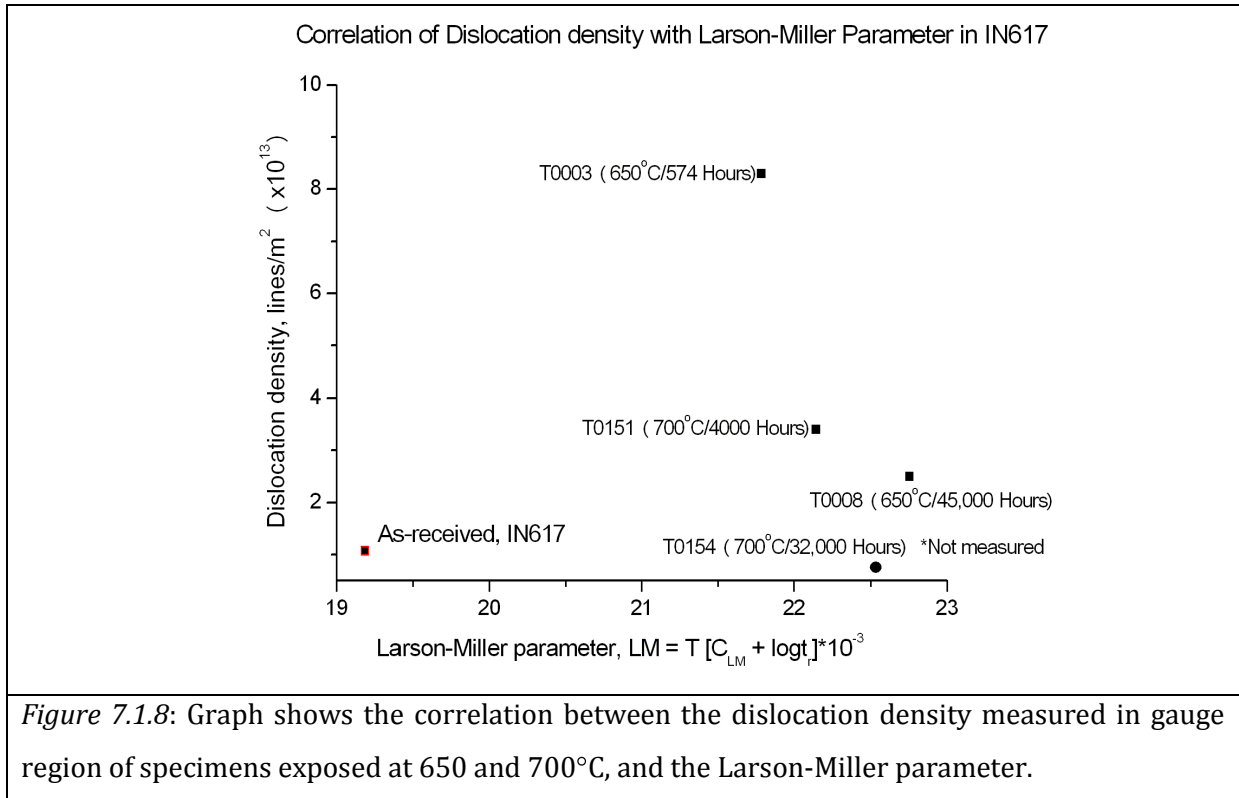


Figure 7.1.7: Graph shows the correlation between the hardness along the thermally exposed head regions and stress and temperature exposed gauge regions, and the Larson-Miller parameter, for IN617 alloys.

Another correlation of the dislocation density with the Larson-Miller parameter is shown in *Figure 7.1.8*. Here the graph shows that the dislocation density remains constant after the long creep exposure.

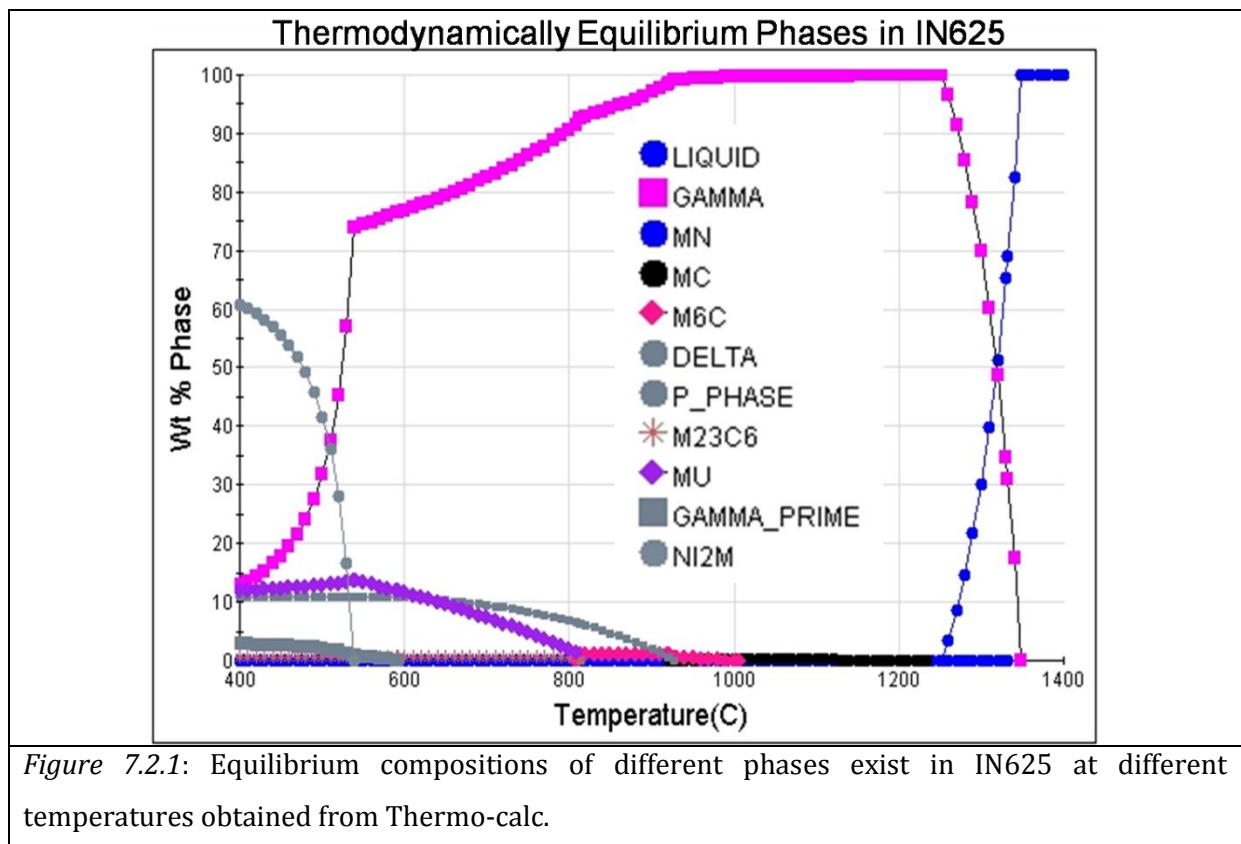


The Larson-Miller approach is a useful tool for comparing creep data at different times and temperatures but care has to be taken that there are not large changes in the creep mechanisms which could be caused by e.g. differences in diffusion rates at different temperatures.

Creep fracture mechanism observed in creep exposed specimens (T0003 & T0008) for 650°C were intergranular creep mechanisms. Although for 700°C creep exposure temperature, in specimens (T0151 & T0154); there was some evidence of a transgranular contribution to the creep failure mechanism.

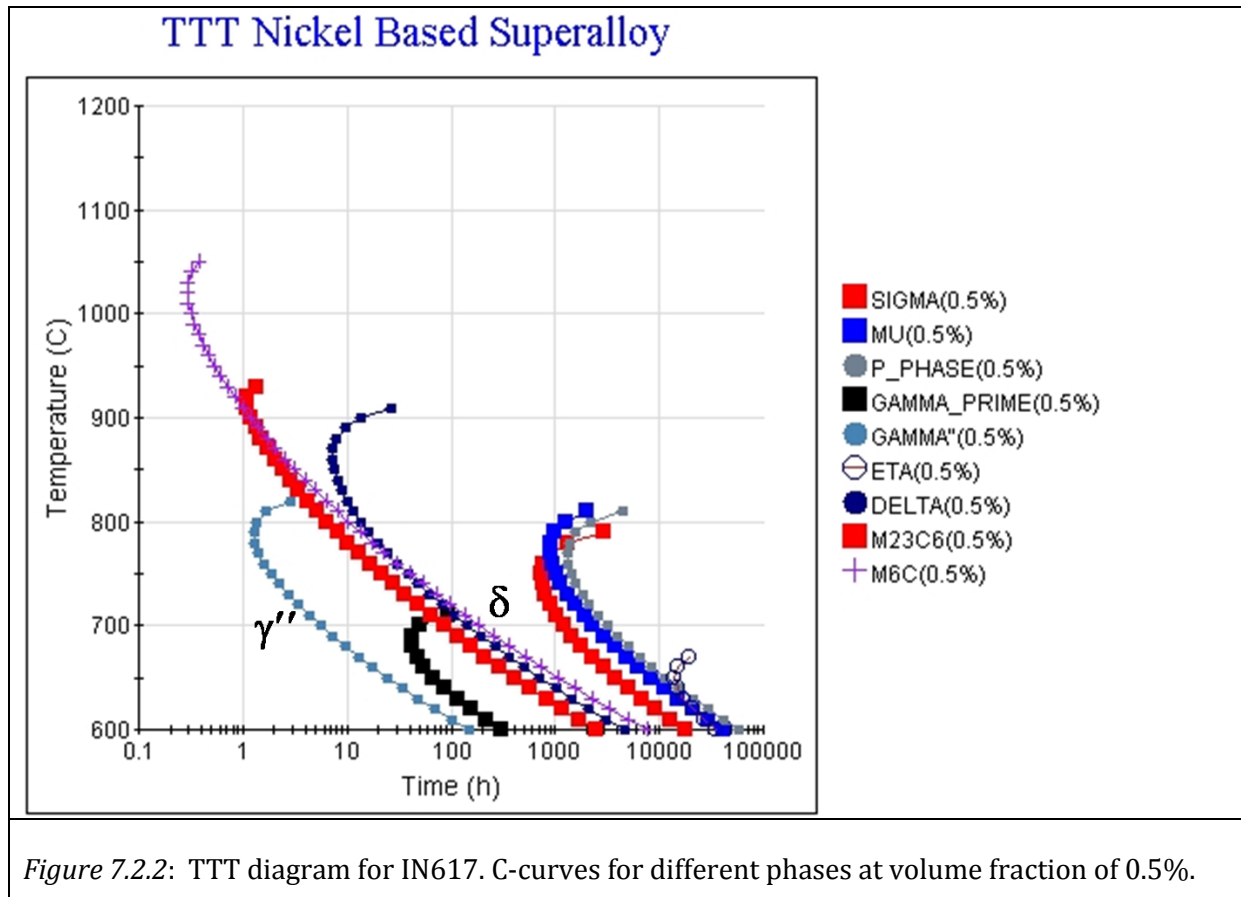
7.2 Discussion for IN625 Alloy

The thermodynamic equilibrium phases in alloy IN625 at different temperatures with their composition is shown in *Figure 7.2.2*. The equilibrium phases in alloy IN625 at 650°C were gamma double prime (γ''), $M_{23}C_6$ (Cr-enriched), TiN (Ti-enriched), NbC (Nb-enriched), and delta (δ) phase. Thermodynamic prediction showed that at 650°C gamma double prime (γ'') phase is a metastable phase and its stable form is δ -phase.

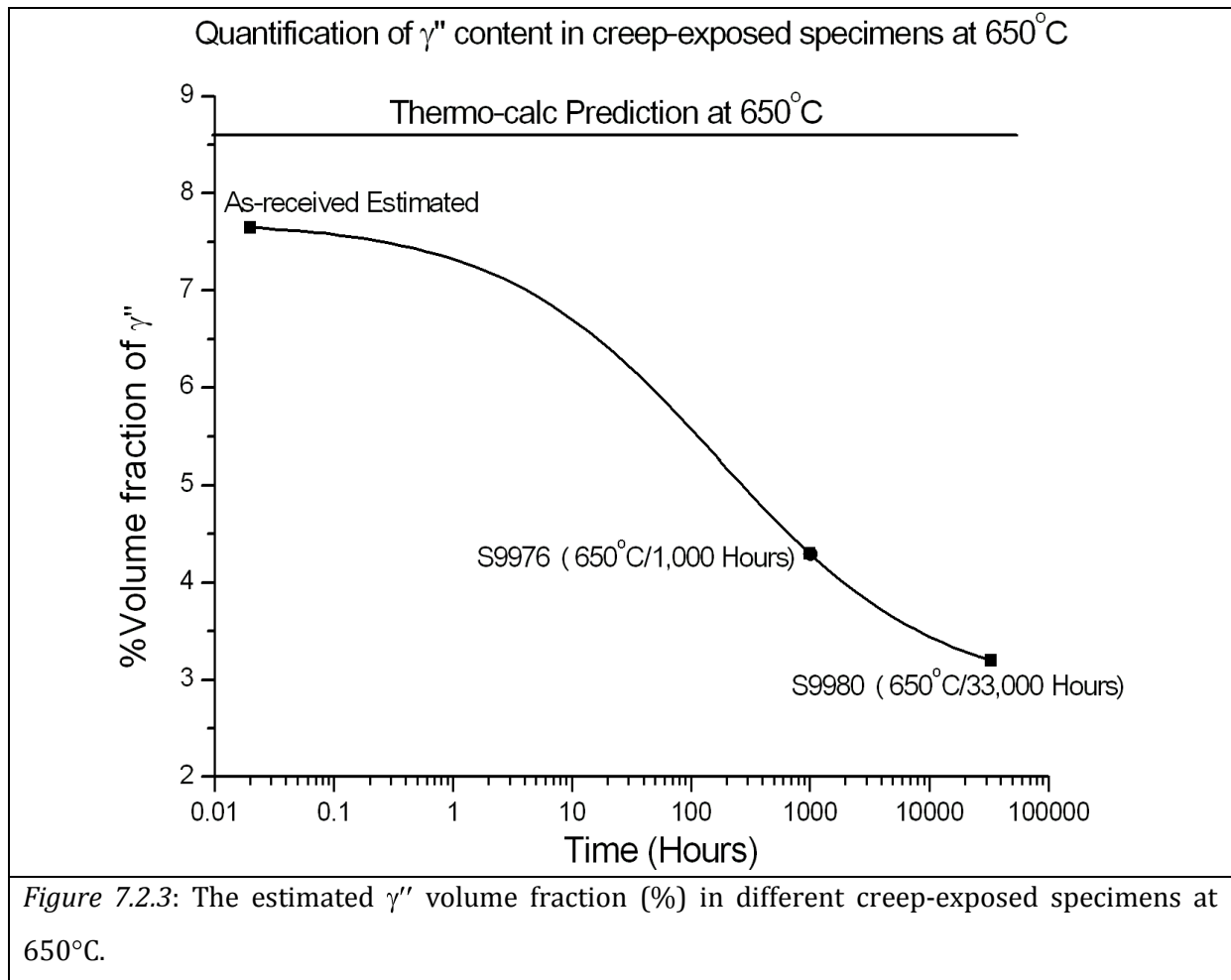


The experimental results have confirmed the presence of these phases at 650°C for short and long durations. A time-temperature-transformation (TTT) diagram was obtained from JMatPro and is shown in *Figure 7.2.2*. The TTT diagram shows the appearance of phases in the alloy after different durations at different temperatures. The thermodynamic prediction shows that the equilibrium phase γ'' appears after 20 hours to 150 hours at 650°C and it is the earliest phase to appear in the alloy, as shown in *Figure 7.2.2*. The γ'' precipitate has an ordered body-centered

tetragonal DO_{22} structure and it gets transformed to the orthorhombic δ -phase upon exposure to creep.



It was observed that γ'' precipitates were of circular and thin ellipsoidal disc morphology of size varying from 5 to 48nm and the precipitates were uniformly distributed through-out the matrix. The quantification of the γ'' content in creep-exposed specimens at 650°C is estimated from Thermo-Calc and shown in *Figure 7.2.3*. The TTT diagram (*Figure 7.2.2*) shows that δ -phase appeared in the alloy after 1000 hours of exposure. On prolonged exposure all γ'' precipitates get transformed to thermodynamic stable δ -phase. The volume fraction of γ'' in specimens S9980 & S9976 were observed as 3.2% and 4.3% respectively. The lower % of γ'' in S9980 was to its longer exposure to 33,000 hours at low stress. δ -phase was observed in both creep exposed specimens S9980 & S9976 but it was not observed in as-received IN625. However, the δ -phase in S9980 was thicker than the S9976.



It was observed that the growth of δ -phase in both specimens was consistent with diffusion controlled coarsening and was controlled by the volume diffusion of niobium, molybdenum, titanium and aluminium. It was observed that the hardness in the gauge length of specimens S9980 and S9976 were 403 and 433Hv/20. The lower hardness value in S9980 was due to the coarsening of the δ -phase, expected as the duration of exposure was longest.

Figure 7.2.4 shows the variation of hardness along the head and gauge length in the creep-exposed sample. A substantial rise in hardness value was observed in head and gauge length from the as-received sample. A rise in hardness in head regions of the sample is due to precipitation of phases and a further rise in hardness in gauge region is due to precipitation as well as work hardening.

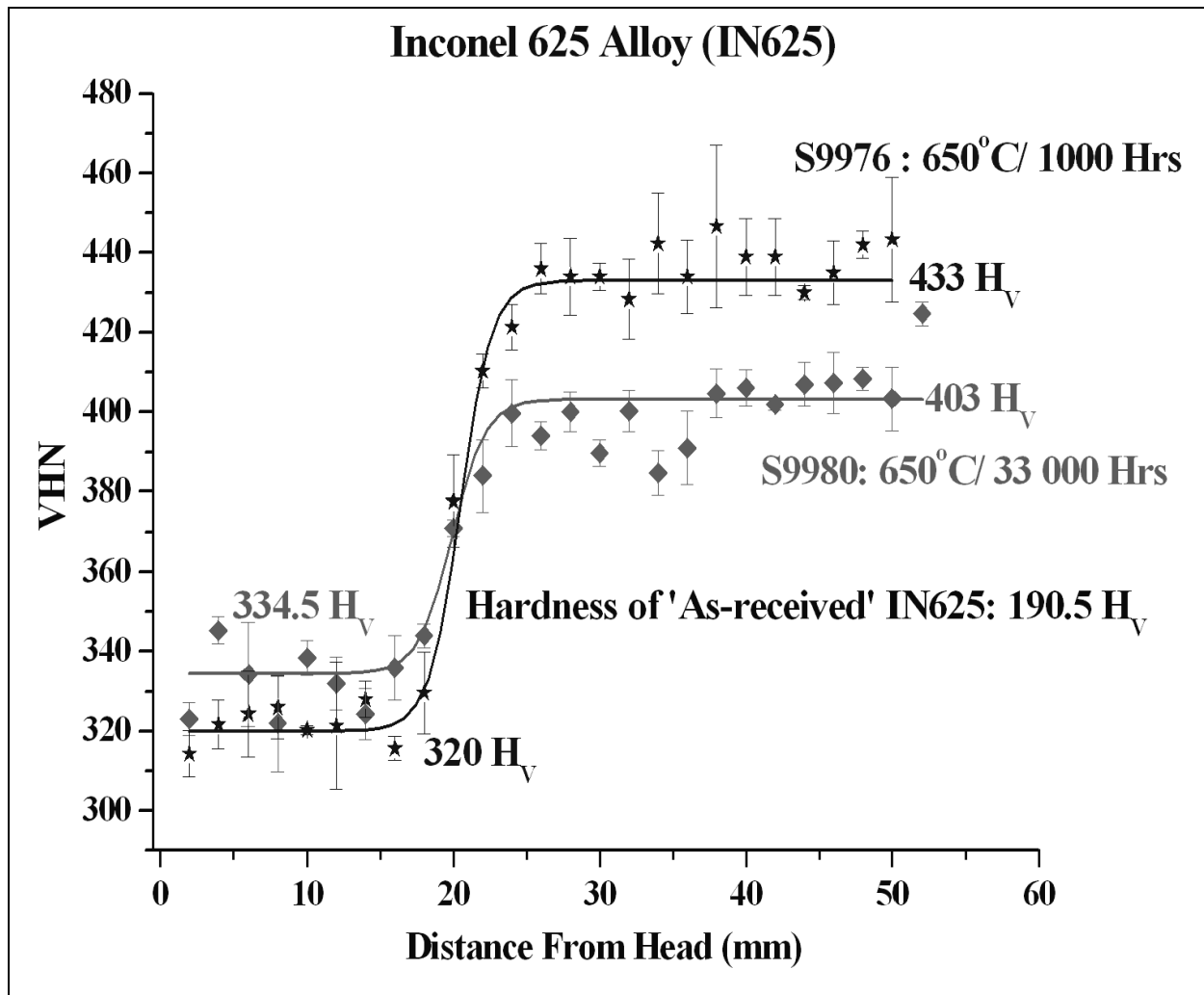
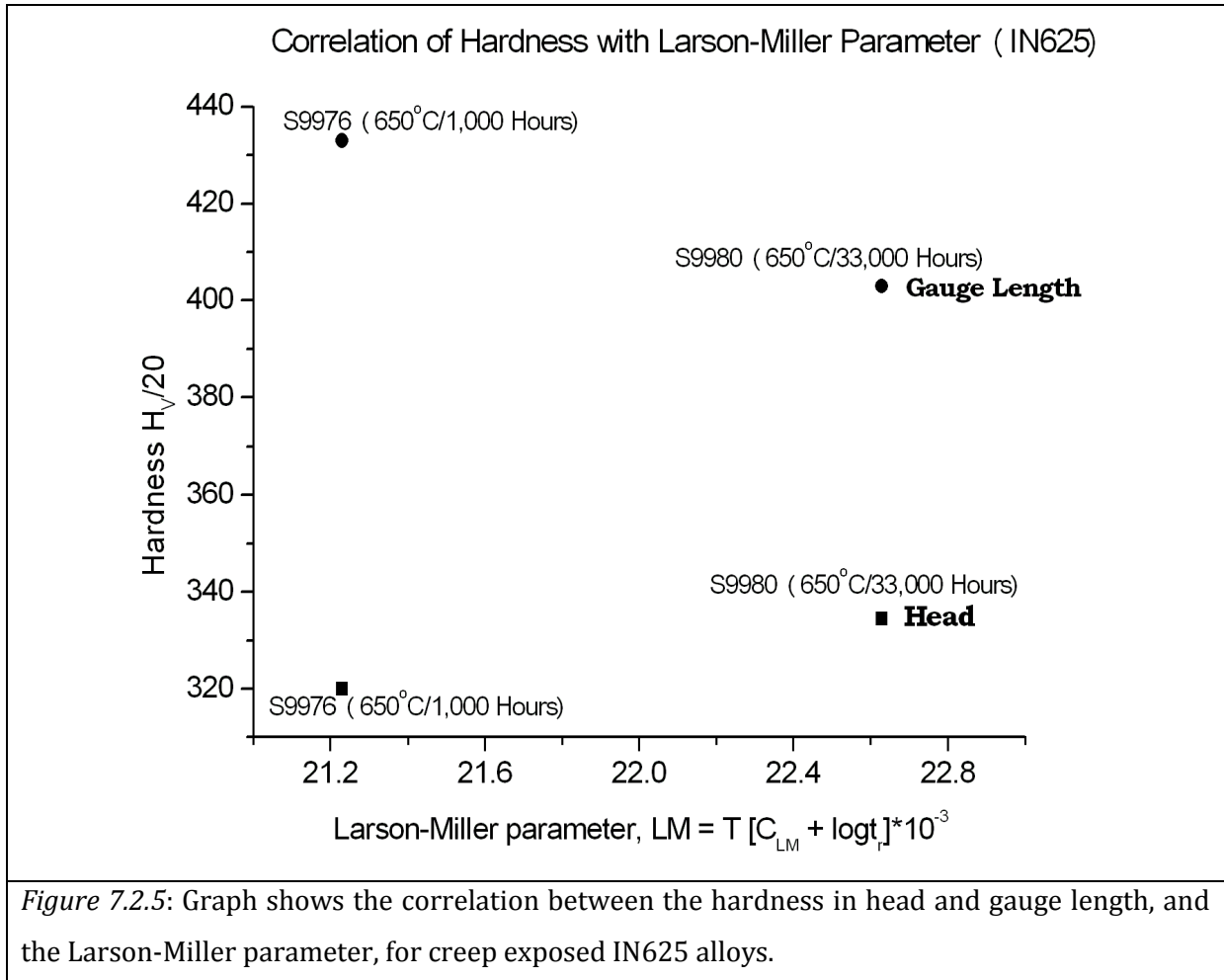
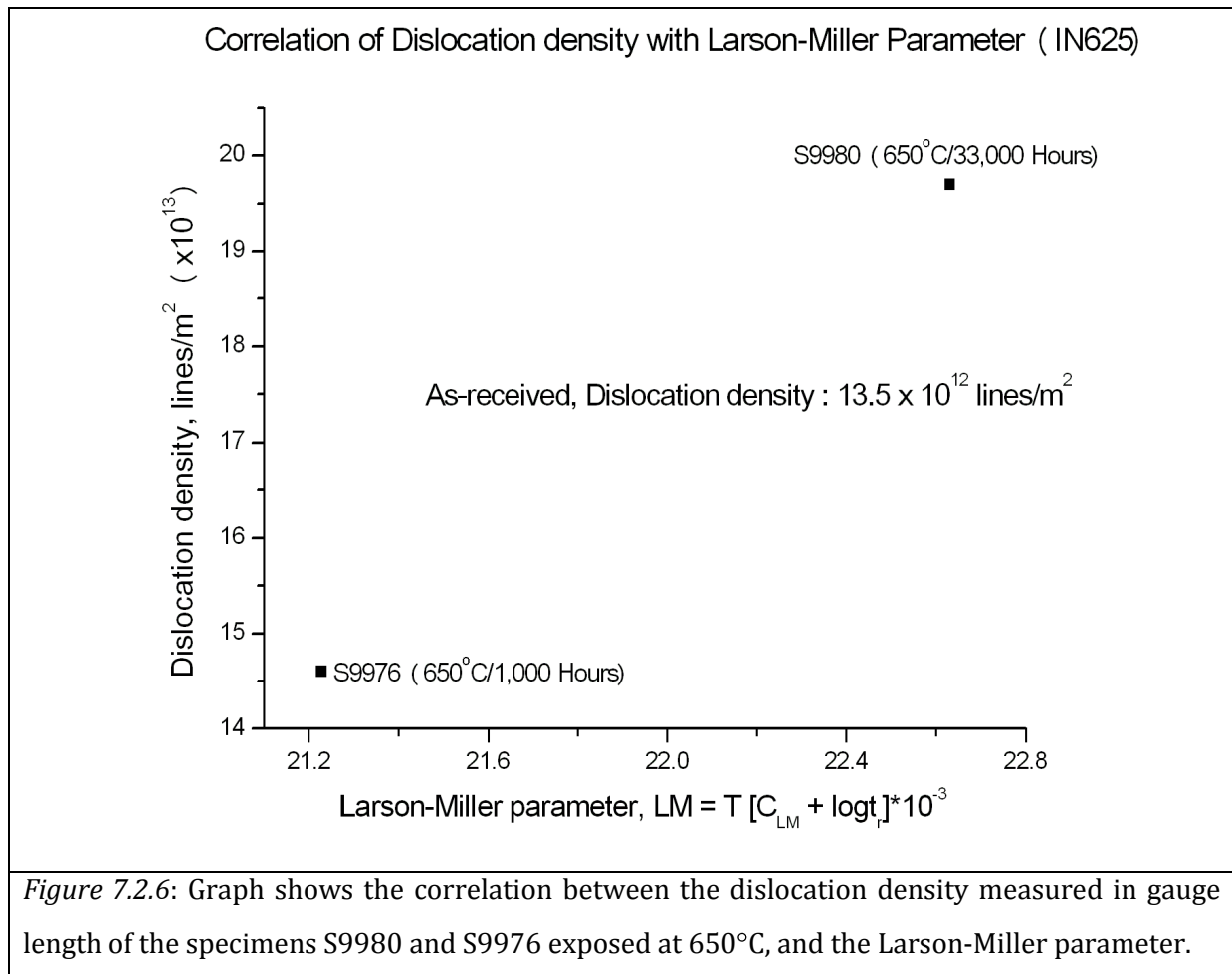


Figure 7.2.4: Hardness profile along head and gauge length in the creep-exposed samples of IN625.

A correlation was made between the hardness along the gauge and head regions and the Larson-Miller parameter (equation 7.1.1), is shown in *Figure 7.2.5*.



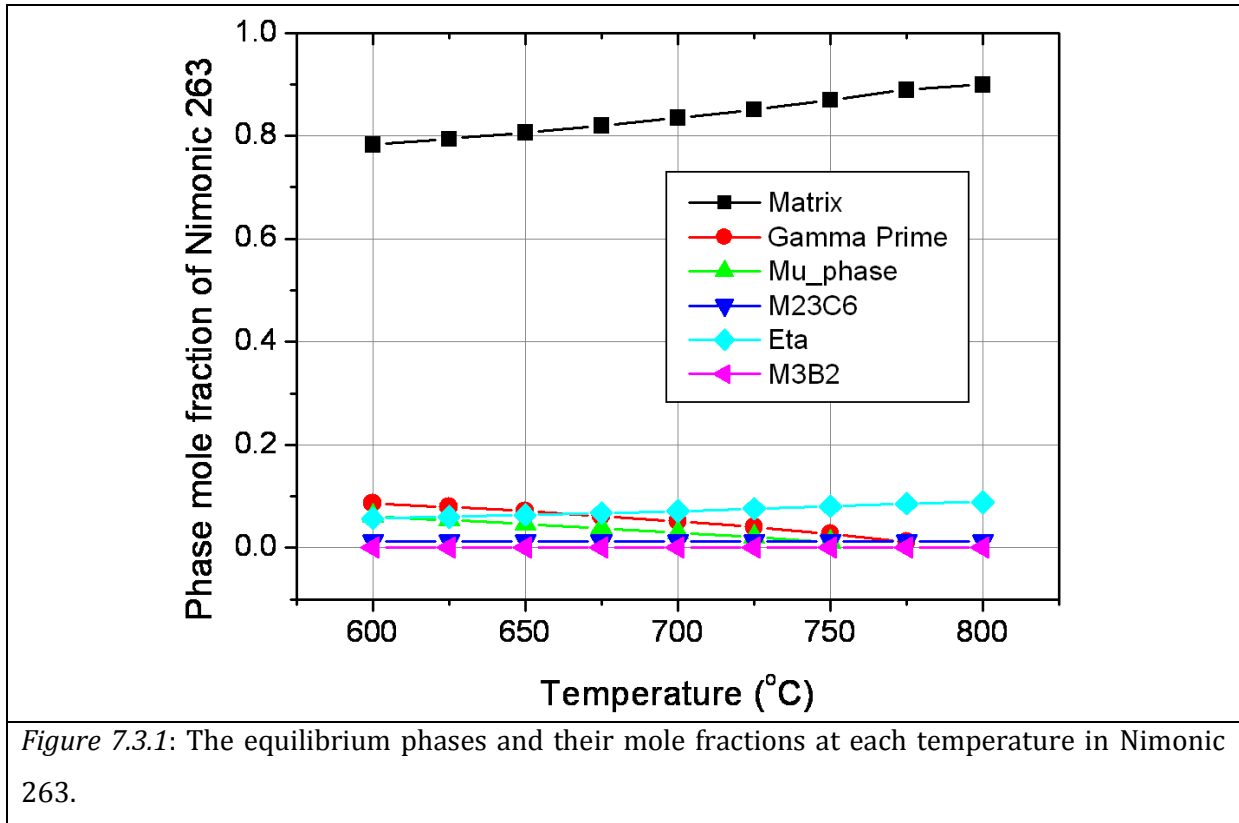
The correlation in the figure shows the hardness in the gauge length decreases from a high value in sample exposed for 1000 hours to a constant value after 33,000 hours and remains constant for further longer exposed conditions. This was expected because of the coarsening of δ -phase from a thin needle shape to a wider lath. However head region shows the rise in the hardness and remains constant for the longer exposed conditions. Another correlation between the dislocation density and the Larson-Miller parameter is shown in *Figure 7.2.6*. This graph shows that rise in the dislocation density and remains constant for the longer exposure conditions.



The fracture mechanism observed in both creep exposed specimens S9980 and S9976 were of a mixed mode creep mechanism.

7.3 Discussion for Nimonic 263 Alloy

Thermodynamic calculations were performed to predict the phase stability in this alloy. *Figure 7.3.1* shows all the predicted equilibrium phases and their mole fractions at each temperature. The formation of η phase is detrimental to the mechanical properties. In *Figure 7.3.1* it can be observed that the weight fraction of γ' and η phase varied inversely. It was found that the η phase was precipitated by the consumption of γ' . Therefore, before the creep tests, the alloy was precipitation-annealed at 800°C for 4-8 hours, to promote the formation of γ' . The experimental observations have confirmed the presence of these phases. The major precipitates were TiN, $M_{23}C_6$, Mo-enriched and η -phase.



It was observed that η -phase had thin plate and needle shape morphology. Very fine $M_{23}C_6$ and Mo-enriched precipitates were observed intergranularly in all samples. The MC carbides, rich in Ti and Mo in the form of (Ti, Mo), were also observed in the samples.

Summary

The microstructural work has shown that the phases present in the alloys correspond closely to thermodynamic predictions. Once the deleterious brittle phases of either mu phase (IN617 and 625) or eta phase (Nimonic 263) form, the mechanical properties of the alloys degrade and creep fracture occurs. Thus, any strategy to optimise the mechanical properties of these alloys for power plant alloys needs to aim to prevent the nucleation and growth of these phases by careful control of the alloy chemistry. Thermo-calc and JMatPro give a useful insight into the precipitation of the different phases.

References:

1. Larson, F.R. and Miller, J., (1952). A time-temperature relationship for rupture and creep stresses. *Trans. ASME* 74, 765–775.
2. Thermo-Calc Software AB (Version 4), (2006). <http://www.thermocalc.com>, SE-113 47: Stockholm, Sweden, (Retrieved on 15th August 2009).
3. Saunders N., Guo Z., Li X., Miodownik A. P., and Schillé J-Ph. (2004). Modelling the material properties and behaviours of Ni-based superalloys, *Superalloys 2004*, Edited by K.A. Green, T.M. Pollock, H. Harada, et al., TMS (The Minerals, Metals & Materials Society), 849-858.
4. Saunders N., Guo Z., Miodownik A. P., and Schillé J-Ph. (2008) Modelling high temperature mechanical properties and microstructure evolution in Ni-based superalloys, <http://www.thermotech.co.uk/resources/NiAlloys-2008.pdf>, UK, (Retrieved on 15th August 2009).

Optical microscopy, scanning electron microscopy and transmission electron microscopy have been used to study the phase precipitation and microstructural evolution in Ni-base superalloys IN617, IN625 and Nimonic 263. There are two areas in particular where this thesis makes a new contribution to the literature in that I have found no previous report of either dislocation densities for these alloys or μ -phase precipitates.

The experimental observations on phase precipitation and microstructural evolution in creep-exposed alloys are summarized as follows:

I. IN617

- i. Prior to creep-exposure, the grain morphology of the 'as-received' IN617 sample was equiaxed. Creep exposure led to a significant change in the grain morphology. Elongated grains were observed in the specimen exposed to 700°C.
- ii. The hardness increases substantially in the head and gauge lengths the as-received sample. The hardness in the head arises from precipitation of mainly $M_{23}C_6$ carbides rather than gamma prime.
- iii. The rise in hardness along the gauge length observed in the creep-exposed samples was associated with the additional precipitation in the matrix and at the grain boundaries, during creep-exposure. The major precipitates at temperature 650°C were γ' , $M_{23}C_6$ and TiN. In the creep-exposed samples, precipitates were randomly distributed throughout the matrix. After a long duration of creep exposure at 650°C, μ -phase was found to precipitate. The major precipitates at 700°C were γ' , $M_{23}C_6$, TiN and μ -phase. The work hardening due to increase in dislocation density was the also contributed to increase in hardness in the gauge length.

- iv. Precipitates were found to have varying morphology from a regular to an irregular morphology.
- v. It was observed that $M_{23}C_6$ increased in volume fraction over time and expected to contribute to strength of alloy.
- vi. Main solid solution strengthening (SSS) elements are Cr (22%) which goes into $M_{23}C_6$ and μ -phase, and Co (12%) and Mo (9%) which go into μ -phase.
- vii. μ -phase was by far the largest contributor to the reduction in SSS. Thermodynamically, it precipitates out very late. Only seen in 45000 hour sample at 650°C. Predicted to reach >8% vol fraction if given time to completely precipitate out.
- viii. μ -phase was found to nucleate near to the grain boundary carbides. μ -phase had a globular morphology and its structure was found with stacking faults and twins.
- ix. The precipitation strengthening phase was γ' , whose volume fraction was ~8% in the as-received IN617 alloy. The morphology of γ' precipitates was spherical in 'as-received' and in the creep-exposure samples the morphology was spherical. The γ' precipitates were found to increase in diameter from an initial diameter of 10nm to final 65nm after creep exposure.
- x. Gamma prime and TiN were expected to precipitate out quickly in first 10-100 hours but normally found in as-received sample. Gamma prime has largest observed volume fraction of any precipitate in 4-8% range and smallest in size so probably the only possibly significant contributor to precipitate hardening.
- xi. Coarsening of gamma prime would increase the creep rate, even if their smaller volume fraction.
- xii. Thermodynamic trend indicated a decrease in gamma prime and increase in TiN. TiN particles showed large (1-10 μ m) and fairly stable in size. Size and volume fraction were too small to contribute to precipitate hardening
- xiii. Creep failure occurred at 650°C usually by an intergranular creep mechanism although for higher temperature creep exposure there was some evidence of a transgranular

contribution to the creep failure mechanism. A higher exposure temperature led to extensive grain boundary cavitation.

- xiv. The dislocation density in the creep-exposed samples was of the order of 10^{13} lines/m².
- xv. Slip (dislocation motion) was the deformation mechanism in the IN617 alloy.
- xvi. Average grain size is not seen to change much over time at 650°C. There probably grain growth suppressed by GB precipitates ($M_{23}C_6$). Grain size determines growth rate of $M_{23}C_6$ as requires Cr to diffuse from inner grain to boundary.
- xvii. Elongated grains were observed at 700°C after 4000h, with a drop in grain size and also fine equiaxed grains were observed in some regions after 32000h.

II. IN625

- xxviii. A complex microstructural evolution was observed in IN625 after creep-exposure tests. Creep tests led to the significant changes in the microstructure. The grains were decorated with needle shaped orthorhombic δ -phase.
- xix. The morphology of the δ -phase was needle-like and consisted of thin plates oriented in two-near orthogonal directions.
- xx. The volume fraction of precipitation strengthening phase γ'' in the as-received alloy was observed to be approximately 8%. The morphology of γ'' was observed to transform from an irregular morphology to a thin disc after creep-exposure. On prolonged exposure this phase transformed to the thermodynamically stable δ -phase.
- xxi. The creep failure mechanism observed in both creep exposed specimens S9980 and S9976 was a mixed mode, intergranular and transgranular creep mechanism.
- xxii. The dislocation density in the creep-exposed samples was of the order of 10^{13} lines/m².
- xxiii. Twinning and slip were the deformation mechanisms in the IN625 alloy.

III. Nimonic 263

- xxiv. The major precipitates were found to be TiN, $M_{23}C_6$, Mo-enriched precipitates and η -phase.
- xxv. η -phase was found to occur with TiN precipitates and of long rod morphology of size $20\mu\text{m}$.
- xxvi. Mo-enriched precipitates were very fine in size less than $1\mu\text{m}$ and found along the grain boundaries and also, near to the large $M_{23}C_6$ precipitates.
- xxvii. MC carbides rich in Ti and Mo in the form of (Ti, Mo) C were found in the creep-exposed alloys.
- xxviii. $M_{23}C_6$ precipitates were observed mostly along the grain boundaries.

Suggestions for future work

The phases identified in the thermal and creep exposed Nimonic 263 specimens were Ti, Cr and Ti-Ni enriched. An extensive transmission electron microscopy is required to identify their exact nature of phases in the thermally and creep exposed Nimonic 263 alloys. It was observed that carbon extraction replica is one of the promising TEM specimen preparation techniques which enabled help in this study to identify the exact mechanism of transformation of γ' to TiN. Thus, it would be appropriate to analyse a satisfactory number of extracted replicas in the TEM to find the exact phase transformation mechanisms for Nimonic 263. EBSD maps are required to map the grain orientations and morphology in the creep exposed alloys particularly for the alloys exposed at high temperature for long durations.

μ -phase was observed in IN617 after long durations at 650°C and at 700°C, and since it is a detrimental TCP phase, it degrades the creep properties by either or both loss of solid solution strengthening elements from the matrix, and crack initiation through brittle μ -phase precipitates. The modelling on thermodynamics of IN617 alloy shows that μ -phase is a dominant grain boundary precipitate. However, the thermodynamic calculations do not account for effects of strain; since the strains during the creep have considerable effect on the precipitation in terms of formation kinetics and volume fractions. Future work on modelling could be undertaken to study the predictions calculations by better understanding the transformation kinetics of the μ -phase, in the alloy. The following parameters could be considered for an improved thermodynamic model.

- The grain morphology and grain boundary structure,
- Combined effects of strain, time and temperature,
- Precipitate transformation kinetics

This thesis forms part of a wider TSB project on modelling the microstructural evolution of nickel-based superalloys for understanding the microstructure of these alloys for long term application in steam power plant. The nature of the data collected in this thesis has been to a

large extent defined by the required inputs to the modelling programme. It is clear that any model of microstructural evolution in power plant alloys needs to take account of the dominant strengthening mechanism, i.e. the role of the solid solution strengthening in IN617 and IN625 as well as the role of the precipitates and changes to grain size and morphology. The dislocation densities and role of μ -phase have given important guidance to the development of the complementary microstructural models.